



HAL
open science

Statistical size effects on compressive strength of concrete

Chi Cong Vu

► **To cite this version:**

Chi Cong Vu. Statistical size effects on compressive strength of concrete. Materials and structures in mechanics [physics.class-ph]. Université Grenoble Alpes, 2018. English. NNT : 2018GREAU030 . tel-04114469

HAL Id: tel-04114469

<https://theses.hal.science/tel-04114469>

Submitted on 2 Jun 2023

HAL is a multi-disciplinary open access archive for the deposit and dissemination of scientific research documents, whether they are published or not. The documents may come from teaching and research institutions in France or abroad, or from public or private research centers.

L'archive ouverte pluridisciplinaire **HAL**, est destinée au dépôt et à la diffusion de documents scientifiques de niveau recherche, publiés ou non, émanant des établissements d'enseignement et de recherche français ou étrangers, des laboratoires publics ou privés.

THÈSE

Pour obtenir le grade de

DOCTEUR DE LA COMMUNAUTE UNIVERSITE GRENOBLE ALPES

Spécialité : **Sciences de la Terre et de l'Univers et de
l'Environnement (CESTUE)**

Arrêté ministériel : 25 mai 2016

Présentée par

Chi Cong VU

Thèse dirigée par **Jérôme WEISS** et
codirigée par **Olivier PLE** et **David AMITRANO**

préparée au sein de l'**Institut des Sciences de la Terre**
dans l'**École Doctorale Terre, Univers, Environnement**

Effets d'échelle statistiques sur la résistance à rupture en compression du béton

Statistical size effects on compressive strength of concrete

Thèse soutenue publiquement le **16 octobre 2018**
devant le jury composé de :

M. Damien Vandembroucq

Directeur de Recherche, CNRS-PMMH, ESPCI Paris, Président

M. Gilles Pijaudier-Cabot

Professeur, Université de Pau et des pays de l'Adour, Rapporteur

M. Daniel Bonamy

Physicien, CEA-SACLAY, Rapporteur

Mme. Stéphanie Deschanel

Maître de Conférences, INSA Lyon, Examinatrice

M. Jérôme Weiss

Directeur de Recherche, CNRS-ISTerre, Université Grenoble Alpes
(UGA), Directeur de thèse

M. Olivier Plé

Professeur, CNRS-LOCIE, Université Savoie Mont Blanc (USMB),
Co-directeur de thèse

M. David Amitrano

Maître de Conférences, CNRS-ISTerre, Université Grenoble Alpes
(UGA), Co-directeur de thèse



Statistical size effects on compressive strength of concrete

Acknowledgements

This thesis reports a research project carried out at Institut des Sciences de la Terre (ISTerre) and IUT Grenoble of University of Grenoble Alpes (UGA), and Laboratoire Optimisation de la Conception et Ingénierie de l'Environnement (LOCIE) of University of Savoie Montblanc (USMB). The financial support provided by the AGIR-POLE-PAGE program from UGA is greatly appreciated.

First and foremost, I would like to express my appreciation to my advisor Jérôme WEISS for his continuous support of my Ph.D. project, for his patience, availability, and immense knowledge. His guidance helped me pass every single work in all the time of this study. I am also grateful for our valuable scientific and non-scientific conversations that have been driving me in the right way during the last three years. I will keep all of them as a pleasant memory. Besides, I would like to express my sincere gratitude to my supervisors Olivier PLÉ and David AMITRANO who were always available to help me resolve all problems and difficulties related to experiments as well as analyzing data. It was a great opportunity for me to work under the pleasant, positive and constructive guidance of these three men. They have set examples of excellent and very kind researchers, mentors and instructors. Once again, thank you so much.!

I would like to acknowledge and thank the jury members for their interest and participation in my thesis. Special thanks go to Mr. Gilles PIJAUDIER-CABOT and Mr. Daniel BONAMY for accepting to be the referees of this thesis and for their constructive comments, ideas to improve the quality of my thesis script. I am also very grateful to Mrs. Stéphanie DESCHANEL and Mr. Damien VANDEMBROUCQ for examining my thesis. Thank you Damien for your participation in all “comité de suivi de thèse” meetings during the last three years and especially accepting to be the president of my jury.

I also wish to thank the researchers and students of the team “Mécanique des failles” of ISTerre who helped enormously and encourage constantly me as well as my family during all the time in Grenoble. I would also like to thank Mrs. Coralie AUBERT, engineer from ISTerre in Grenoble and Mr. Vincent WATON, engineer from IUT Chambéry, and other technicians of ISTerre and IUT Grenoble for their technical supports throughout all my experiments.

In the following paragraphs, I would like to thank my family and Vietnamese friends in Vietnamese.

Đầu tiên, tất nhiên rồi, con xin cảm ơn Bố Mẹ, những người đã cho con cuộc sống này, dạy dỗ, động viên, ủng hộ con cả vật chất lẫn tinh thần trong suốt 30 năm qua cũng như nhiều chục năm về sau nữa. Niềm vui của Bố Mẹ chính là động lực thúc đẩy con cố gắng mỗi ngày. Cảm ơn Tâm đã luôn hỗ trợ anh trong suốt quá trình học tập và nghiên cứu, chúc em (ku) luôn thành công trên con đường (ku) em đã chọn.

Em xin chân thành cảm ơn Ban chủ nhiệm, các Thầy Cô giáo Bộ môn Công nghệ và Quản lý Xây dựng (bmthicong), Trường Đại học Xây dựng, đã tạo điều kiện và giúp đỡ trong suốt thời gian học tập tại Pháp. Cảm ơn Tuấn (TuanVuAnh), đã nhiệt tình giúp đỡ khi tôi vắng mặt tại Bộ môn (“sau tất cả, mình lại trở về với nhau...!” ^^).

Công việc nghiên cứu của bố Bún và cuộc sống của gia đình Bún sẽ không thể dễ dàng nếu không có sự giúp đỡ của rất nhiều anh, chị, em và bạn bè tại Grenoble. Bố cháu xin được cảm ơn (i) các ISTerriennes: C. Quyên, E. Thu và đặc biệt là C. Vân đã luôn động viên và hỗ trợ trong suốt thời gian làm việc tại ISTerre; (ii) chi hội phụ huynh: Lan Anh-Quang (Alexis), Linh-Quân (Rom), Trang-Long (Tết), Uyên-Khôi (Mía), C.Vân-A.Ngọc (Nhi), Hoàn-Bình (Louis-Léo), Gđ. Chị Ly (Théo), Gđ. Chị Ngọc-Montpellier (Titi-Hậu Đậu) đã luôn luôn có mặt giúp đỡ trong các công việc và đặc biệt đã góp phần làm phong phú vốn ẩm thực của gia đình Bún; và (iii) hội 10 chai: a. Kiên, Dũng, Trung và “những cái chai còn sót lại”: Hoàng Trần (nam thần ...), Thảo-Bảo, Giang-Minh, Thu An-Văn Bình, đã luôn luôn (un peu trop !) “motivé” giúp đỡ “Công An” chuyển đồ, xin CAF và đặc biệt là tiêu thụ một lượng lớn thực phẩm (bia) của Carré4 cũng như sòng bạc khổng lồ (GéantCasino) - cảm ơn mọi người rất nhiều.

Con cũng muốn cảm ơn Bố Khải, Mẹ Ngọc vì đã luôn động viên vợ chồng con và đặc biệt đã tin tưởng (chuyên) giao cho con người con sẽ cảm ơn cuối cùng dưới đây. Trước khi làm việc này, xin cảm ơn con gái, Phương Linh (Annie-Bún), cảm ơn con vì đã cho Bố biết rằng (i) Ông Bà nội con đã yêu thương Bố vô vàn như thế nào; (ii) một con “Khi” nhỏ bé lại có thể cung cấp một năng lượng (niềm vui-hạnh phúc) lớn như vậy để Bố Mẹ cố gắng mỗi ngày; và (iii) Bố - một con người dù đã tiến hóa rất lâu rồi nhưng vẫn còn một cái “đuôi” - Bố yêu con !

Cuối cùng, tất nhiên rồi, cảm ơn em, Thúy-An, người đã mang đến và chăm sóc cho “thế giới nhỏ” của anh. Cảm ơn em vì đã luôn tin tưởng, động viên anh trong mỗi công việc anh làm, giúp anh cân bằng (giảm/tăng ?) áp lực sau mỗi ngày làm việc; làm cho cuộc sống của gia đình mình dễ dàng hơn, vui hơn và (ồn ào hơn ? ^^). Sẽ còn (nguyên) những khó khăn chờ đón gia đình mình khi trở về, nhưng sự tin tưởng và tình thương yêu sẽ giúp chúng ta từ từ vượt qua những trở ngại đấy...!

Sẽ chẳng lời nào để diễn tả đủ và hết sự biết ơn những người đã giúp đỡ gia đình Bún, cuối cùng xin chúc tất cả mọi người sức khỏe, may mắn, học tập tốt, lao động tốt, xin hẹn gặp lại tại VIỆT NAM.!

Grenoble, November 20th 2018

Chi-Cong VU

Abstract

Size effects on mechanical strength, i.e. the fact that larger structures fail under lower stresses than smaller ones, already highlighted by Leonardo da Vinci and Edméé Mariotte centuries ago, remain nowadays a crucial problem to establish structural design rules and safety regulations from an upscaling of laboratory data. These size effects are generally explained either from a deterministic energetic approach that predicts a non-vanishing asymptotic strength but, by construction, does not account for fluctuations around the mean strength and their size dependence, or from a statistical approach based on the weakest-link theory that implies a vanishing strength towards large scales.

Recently, an alternative framework has been proposed based on an interpretation of compressive failure of heterogeneous materials as a critical transition from an intact to a failed state. This critical interpretation releases the underlying hypotheses of the weakest-link theory, pure brittleness and the independence of damage events, while predicting a non-vanishing asymptotic mean strength (σ_∞) but vanishing intrinsic fluctuations at large scales. The application this framework to the statistical size effects on compressive strength of concrete, a typical quasibrittle material of tremendous importance in civil engineering, is investigated in this thesis.

From an extensive series of uniaxial compression experiments (527 tests) carried out on concrete samples with four different sizes and three different microstructures, we demonstrate (i) the failure of the weakest-link theory in this case, and instead (ii) the pertinence of the critical framework to account for size effects on compressive strength of concrete, in terms of average strength, associated fluctuations, and probability of failure. From a detailed analysis of the microstructural disorder of our materials, we show that the pore structure, rather than the concrete mix, plays a significant role on size effects on strength. In this framework, the asymptotic strength (σ_∞) represents the genuine characteristic compressive strength (f_{ck}) of the material, a key property for the dimensioning large-scale structures from an upscaling of small-scale laboratory mechanical tests and for the quality control of concrete.

As a consequence of the leading role of the pore structure in controlling the size effects on compressive strength of low-porosity concretes, when estimating the characteristic (asymptotic) strength from a series of tests with a single sample size, a condition on this size with respect to the characteristic scale of pore structure is proposed to be fulfilled.

Keywords: size effect, compressive strength, concrete, autocorrelation function, critical transition, finite-size scaling, strength variability, quasibrittle material, characteristic strength.

Résumé

Les effets d'échelle sur la résistance mécanique des matériaux, i.e. le fait que plus un échantillon de matière est grand, plus, en moyenne, sa contrainte à rupture sera faible, déjà soulignées par Leonardo da Vinci et Edmée Mariotte il y a des siècles, demeurent de nos jours un problème crucial pour établir des règles de sécurité et de conception de grandes structures à partir de données de laboratoire. Ces effets d'échelle sont généralement expliqués soit par une approche déterministe qui prédit une résistance asymptotique non nulle mais, par construction, ne tient pas compte des fluctuations de la résistance moyenne et de leur dépendance vis-à-vis de la taille, ou d'une approche statistique basée sur la théorie du maillon le plus faible qui implique une résistance nulle pour un système de taille infini.

Récemment, un cadre alternatif a été proposé sur la base d'une interprétation de la rupture en compression des matériaux hétérogènes comme une transition de phase critique entre un état intact et un état rompu. Cette interprétation libère les hypothèses de base de la théorie du maillon le plus faible comme la fragilité extrême et l'indépendance entre événements de microfracturation et prédit qu'un système de taille infinie conservera une résistance mécanique non nulle (σ_∞) mais une variabilité associée de la résistance nulle. En appliquant ce cadre critique, les effets d'échelle statistique sur la résistance en compression du béton, un matériau quasi-fragile typique et important en génie civil, sont étudiés dans cette thèse.

A partir d'une importante série d'expériences de compression uniaxiale (527 essais) qui a été réalisée sur des échantillons du béton de quatre tailles différentes et trois microstructures différentes, nous démontrons (i) l'échec de la théorie du maillon le plus faible dans ce cas; et au lieu de cela (ii) la pertinence du cadre critique pour tenir compte des effets d'échelle sur la résistance à rupture en compression du béton, en termes de valeur moyenne, de fluctuation associées et de probabilité de défaillance. A partir d'une analyse détaillée de la microstructure de nos matériaux, nous montrons que la structure des pores, plutôt que les agrégats, joue un rôle important sur les effets d'échelle sur la résistance à rupture en compression. Dans ce cadre, la résistance asymptotique (σ_∞) représente la véritable résistance caractéristique en

compression (f_{ck}), qui est une propriété essentielle pour la conception de structures à grande échelle et pour le contrôle de la qualité du béton.

En conséquence du rôle important de la structure des pores sur les effets d'échelle sur la résistance en compression des bétons à faible porosité, lors de l'estimation de la résistance caractéristique à partir d'une série d'essais avec une seule taille d'échantillon, une condition sur cette taille par rapport à la taille caractéristique de la structure des pores est proposée.

Mot-clés: effet d'échelle, résistance en compression, fonction d'autocorrélation, transition de phase critique, lois d'échelle de taille finie, variabilité de résistance, matériau quasi-fragile, résistance caractéristique.

Contents

Acknowledgements	iii
Abstract.....	v
Résumé.....	vii
Contents	ix
List of Figures.....	xiii
List of Tables	xxi
Notations.....	xxiii
Chapter 1 Introduction.....	1
1.1 Context and motivation.....	1
1.2 Objectives and methodology	9
1.3 Organization of the thesis	10
Chapter 2 Experimental program.....	13
2.1 Outline of experimental program.....	13
2.2 Materials and mix proportions	14
2.3 Specimen preparation	15
2.4 Uniaxial compression test.....	18
2.5 Calibration of the measured displacement.....	19
Chapter 3 Microstructural characteristics	23
3.1 Introduction.....	23
3.2 Autocorrelation Function analysis	24
3.3 Image analysis procedure.....	25
3.4 Global autocorrelation length	27
3.5 Characterization of the pore structure.....	30
3.5.1 Image of pore structure	30
3.5.2 Pore size distribution and porosity	31
3.5.3 Autocorrelation length of pore structures	34

3.6	Conclusion	38
Chapter 4	Properties of hardened concrete samples	41
4.1	Introduction.....	41
4.2	Density.....	42
4.3	Moisture content	42
4.4	Elastic Young's modulus	45
4.4.1	Static modulus of elasticity.....	45
4.4.2	Dynamic modulus of elasticity	48
4.4.3	Static versus dynamic elastic moduli.....	51
4.5	Conclusion	53
Chapter 5	Compressive failure of concrete as a critical phase transition	55
5.1	Introduction.....	56
5.2	Acoustic Emission measurement	58
5.2.1	Principles of Acoustic Emission technique	58
5.2.2	Acoustic Emission signal parameter.....	59
5.3	Acoustic Emission experimental work	62
5.3.1	Acoustic Emission equipment	62
5.3.2	Acoustic Emission test set-up parameters	66
5.3.3	Testing setup.....	68
5.4	Experimental results	69
5.4.1	Evolution of AE activity toward failure	70
5.4.2	Probability distribution of AE energy.....	76
5.4.3	Interpretation of AE duration.....	80
5.4.4	Probability distribution of AE duration and AE amplitude.....	83
5.5	Discussion and Conclusion.....	87
Chapter 6	Statistical size effects on compressive failure strength of concrete.....	93
6.1	Uniaxial compressive behavior of concrete.....	94
6.2	The failure of weakest-link theory to account for statistical size effects on compressive strength.....	96
6.3	Compressive failure interpreted as a critical transition and associated finite size scaling.....	100
6.4	Finite size effects on compressive strength of concrete	103
6.5	The role of microstructural disorder on finite-size effects	109
6.6	Discussion and Conclusion.....	111
Chapter 7	Revising the concept of characteristic compressive strength of concrete.....	115

7.1	Introduction.....	115
7.2	Relationship between compressive strength and Young's modulus.....	118
7.3	Characteristic compressive strength of concrete	121
7.3.1	Asymptotic versus characteristic compressive strength	122
7.3.2	Recommendations for the determination of the asymptotic compressive strength.....	126
7.4	Conclusion	129
Chapter 8	Conclusion and perspectives	131
8.1	Conclusions and main results	131
8.2	Perspectives	134
Appendix A	Weibull-type size effect	137
Appendix B	Results of Acoustic Emission experiments.....	141
Appendix C	Application to published experimental strength data	161
Appendix D	Examples of application for Chapter 7.....	165
Bibliography	169

List of Figures

Fig. 1.1. Illustration of different size effect laws to capture the dependence of nominal stress at failure, σ_f , on structure size, L , of beams with (a) initial notches; and (b) no notch. (modified from (Bazant, 2004a)).....3

Fig. 1.2. Examples of applications of the SEL (Eq. (1.1)) and the MFSL (Eq. (1.2)) to fit the experimental size effect data of different concrete structures (reprinted from (Van Vliet, 2000)).....4

Fig. 1.3. Applications of size effect laws for fitting the size dependence of compressive peak stresses of different concrete mixtures and different shapes of sample (after (Carpinteri et al., 1999)). Fig. (a), (b) and (c) used the experimental data of (Blanks and McNamara, 1935) for three different concrete mixtures. Fig. (d) is after (Xu and He, 1990). R is the correlation coefficient, quantifying the error of the non-linear fitting.6

Fig. 2.1. Grading curves of aggregates for three concrete mixtures.14

Fig. 2.2. Concrete specimens used for the experimental investigations: (a) Geometries of the four different sizes of concrete specimens; (b) Cross sections of the three different concrete mixtures.16

Fig. 2.3. Different steps in preparing the concrete specimens. (a) Cylindrical cardboard molds with different sizes and constituent materials for casting concrete samples; (b) The hardened concrete samples during the air-dried curing process.....17

Fig. 2.4. Uniaxial compression testing setups. (a) Compression machine A used for three larger concrete specimen sizes (cylinders 70x140mm; 110x220mm and 160x320mm); (b) Compression machine B used for the smallest size (cylinders 40x80mm).18

Fig. 2.5. The relationship of the total displacement (Δ_t), the displacement of the reference sample (Δ_{ref}), and the elastic deformation of loading machine (Δ_{fr}) with the applied loads for the calibration tests carried out with (a) the compression machine A and (b) the compression machine B.21

Fig. 2.6. Comparisons of stress-strain curves of different samples before and after calibrating the measured displacement: (a) for the Aluminum sample; (b) for a 160-mm sample of M-concrete. Dashed lines are the curves before calibration and solid lines are the curves after calibration.22

Fig. 3.1. Sectioning of concrete samples with identification of polished surfaces.....26

Fig. 3.2. 2D Autocorrelation function analysis of concretes samples (see text for details). ...26

Fig. 3.3. Autocorrelation function for 3 different compositions of concrete; (upper) original scanned image of concrete ; (lower) digital image of ACF; (a) F-concrete; (b) M-concrete; (c) C-concrete.	27
Fig. 3.4. Global autocorrelation length, ξ_g , for all concrete specimens.	28
Fig. 3.5. Autocorrelation function of concrete: (a) for different sections of sample M-160x320 mm; (b) Different sizes of sample for the F-concrete group; (c) Different compositions of concrete with the same sample size (160x320 mm).	29
Fig. 3.6. Image analysis procedure of the pore structure: (a) concrete sample surface after grinding and polishing; (c) scanned image of pores after the contrast enhancement operation; (d) binary image of pores obtained after thresholding.....	30
Fig. 3.7. Comparison of the pore structure for three different concrete mixtures; (a) F-110x220mm; (b) M-110x220mm; (c) C-110x220mm. Top figures are the original scanned images and bottom figures are the corresponding binary images of pores.....	31
Fig. 3.8. Size distribution of pores per unit volume for different concrete samples. (a) F-concrete; (b) M-concrete; (c) C-concrete and (d) All concrete samples.....	33
Fig. 3.9. An example of Autocorrelation function (ACF) of the pore structures; where ϕ_a is the area fraction of pores, the asymptotic value of ACF is equal to the square of the area fraction of pore, ϕ_a^2 , and $X_{0,p}$ is the integral range where $ACF(X_{0,p}) = \phi_a^2$	35
Fig. 3.10. Autocorrelation length of pore structure, ξ_p , for all concrete specimens.....	36
Fig. 3.11. Autocorrelation function of pore structure in concrete samples: (a) for different sections of sample M-160x320mm; (b) different sizes of sample for the C-concrete group; (c) different composition of concrete with the same size (110x220mm).....	37
Fig. 3.12. Relationship between the autocorrelation length (a) ξ_g and the maximum aggregate size, d_{max} ; (b) ξ_p and d_{max} ; and (c) ξ_p and the product of the porosity, p_o (absolute value) and the maximum pore diameter, $d_{p,max}$. Black dashed-lines are the linear fits.	39
Fig. 4.1. Properties of hardened concrete samples as a function of the sample diameter: (a) Density; (b) Moisture content.	44
Fig. 4.2. Illustration of the method of estimation of the tangent elastic modulus, Y_t , where the red curve is the stress-strain curve, the blue curve is 5Hz differentiated stress-strain curve, $d\sigma/d\varepsilon$, and the black curve is the 40-point moving average of the blue curves.	46
Fig. 4.3. The values of tangent elastic moduli, Y_t , for all of concrete samples.	46
Fig. 4.4. The values of static elastic moduli for all concrete samples: (a) Secant modulus, Y_s ; and (b) The relationship between the secant modulus, Y_s , and tangent modulus, Y_t	47
Fig. 4.5. Testing equipment for the acoustic pulse velocity measurement.....	48
Fig. 4.6. Size-dependent of the elastic properties of concretes: (a) P-wave velocity; (b) Dynamic modulus of elasticity.	50
Fig. 4.7. The relationship between static and dynamic elastic moduli of concrete. (a) Y_t vs. Y_d ; and (b) Y_s vs. Y_d	52

Fig. 5.1. Principle of recording procedure of Acoustic Emission signals (reprinted from (Kocur, 2012)).....	58
Fig. 5.2. AE versus other NDT methods (a) Principle of AE technique and (b) Principle of Soundwave-based NDT methods (e.g. ultrasound method).	59
Fig. 5.3. Continuous and burst AE signal (after (Wevers and Lambrihs, 2009)).....	60
Fig. 5.4. Schematic diagram of AE parameters (modified from (Pollock, 1989)).	61
Fig. 5.5. A cut-away of a typical piezoelectric AE sensor (source: NDT Resource Centre)...	63
Fig. 5.6. Wide-band AE sensor of type PICO used in this work and its dimensions.	63
Fig. 5.7. Manufacturer’s calibration certificate for an example of AE sensor of type PICO used in this research.	64
Fig. 5.8. Coupling position of AE sensors: (a) for the smallest size (40x80-mm samples) and (b) for the larger sizes (70x140-mm, 110x220-mm and 160x320-mm samples).	65
Fig. 5.9. The setting parameters of MISTRAS-2001 AE system (modified from (Mistras, 2001)).....	67
Fig. 5.10. Experimental setup used for uniaxial compression tests combined with AE monitoring (AE test). (a) Instrumentation setup; (b) Equipment setup on the compression machine A for large specimens (70x140 mm, 110x220 mm and 160x320 mm); (c) Equipment setup on the compression machine B for small specimens (40x80 mm).....	69
Fig. 5.11. A typical stress-strain curve of uniaxial compression test for the definition of the control parameter Δ , where σ_f is the peak stress.	70
Fig. 5.12. Evolution of the AE activity during a stress-controlled compression test on a sample of diameter $\phi = 160$ mm of M-concrete. (a) Blue curve: load; black curve: cumulated AE energy; red: AE energy release rate, sampled at 100Hz. (b) Blue curve: cumulated AE events; black curve: cumulated AE amplitude; red: AE amplitude; pink curve: cumulated AE duration. In this study, the value of AE amplitude is converted into Voltage from its value in dB by using Eq. (5.1).	73
Fig. 5.13. Evolution of AE event rate $dN/d\Delta$ for (a) different sample sizes of F-concrete; and (b) the three different materials. Curves were averaged over all sensors and all samples of a given sample size (a), and on all sensors and samples (whatever the sample size) of a given material (b). Other sample sizes for M- and C-concretes give similar results (see Fig. B.4, Table. B.2 and Table. B.3 in Appendix B).	74
Fig. 5.14. The AE energy release rate $dE/d\Delta$ for (a) different sample sizes of M-concrete, and (b) for three different concrete mixtures. Curves were averaged over all sensors and all samples of a given sample size (a), and on all sensors and samples (whatever the sample size) of a given material (b). Other sample sizes for F- and C-concretes give similar results (see Fig. B.5 and Table. B.1 and Table. B.3 in Appendix B).	75
Fig. 5.15. (a) Cumulative distribution cdf of AE energies at different distances to failure Δ , for a test on a 110-mm sample of M-concrete. (b) Data collapse of the same data in a rescaled plot. Other sample sizes and materials give similar results (see Appendix B).	79
Fig. 5.16. Near failure (red diamonds), and stress-integrated (blue circles) cumulative distribution of AE energies for a test on a 160 mm sample of M-concrete. Other sample sizes and materials give similar results.....	80

Fig. 5.17. Conditional average maximum AE amplitude $\langle V_{\max} T \rangle$ for (a) different sample sizes of C-concrete, and (b) the three different materials. Curves of data points were averaged over all sensors and all samples of a given size (a), and on all sensors and samples (whatever the size) of a given material (b). Black dashed lines are the reference curves according to Eq. (5.22), with $V_{th} = 34dB$ and $\tau = 100\mu s$. Other sample sizes and materials give similar results (see Fig. B.6, Table. B.1 and Table. B.2 in Appendix B).....	82
Fig. 5.18. Cumulative distributions <i>cdf</i> of AE durations, T , for different bins of the control parameter Δ for a test on a 40-mm sample of C-concrete. Similar results are observed with other sample sizes and materials (see Appendix B).	85
Fig. 5.19. Cumulative distributions <i>cdf</i> of maximum AE amplitudes, V_{\max} , for different bins of the control parameter Δ for a test on a 40-mm sample of C-concrete. Similar results are observed with other sample sizes and materials (see Appendix B).....	86
Fig. 5.20. Probability density functions of AE energy for the whole AE events dataset for (a) four different sample sizes of F-concrete and (b) for three different concrete mixtures. The <i>pdfs</i> were normalized by their maximum value. Curves on the left were averaged over all sensors and all samples of a given sample size, and on the right on all sensors and samples (whatever the sample size) of a given material. Other sample sizes for M- and C-concretes give similar results (see Fig. B.1 in Appendix B).....	87
Fig. 5.21. Probability density functions of AE duration of the whole AE events catalog for (a) four different sample sizes of C-concrete and (b) for three different concrete mixtures. The functions were normalized by their maximum value. Curves on the left were averaged over all sensors and all samples of a given sample size, and on the right on all sensors and samples (whatever the sample size) of a given material. Other sample sizes for F- and M-concretes give similar results (see Fig. B.2 in Appendix B).....	88
Fig. 5.22. Probability density functions of AE amplitude for (a) four different sample sizes of F-concrete and (b) for three different concrete mixtures. The functions were normalized by their maximum value. Curves on the left were averaged over all sensors and all samples of a given sample size, and on the right on all sensors and samples (whatever the sample size) of a given material. Other sample sizes for F- and M-concretes give similar results (see Fig. B.3 in Appendix B).....	88
Fig. 6.1. Stress-strain curves of different concrete specimens: (a) for different specimen sizes of F-concrete (45 curves for each size); (b) for different concrete mixtures with the same sample size ($\phi \times h = 110 \times 220$ mm) (42-46 curves for each concrete mixture).....	95
Fig. 6.2. Sample size effect on compressive strength for the different types of concrete.	95
Fig. 6.3. Rescaled Weibull distributions of compressive failure strength of concrete; (a) F-concrete; (b) M-concrete ; and (c) C-concrete.....	98
Fig. 6.4. Rescaled Gumbel distributions of compressive strength of concrete; (a) F-concrete; (b) M-concrete; and (c) C-concrete.	99
Fig. 6.5. Normal probability plot of the distributions of compressive strength for the different sample sizes and the three different concrete mixtures.	100
Fig. 6.6. Finite-size effect on the mean value of uniaxial compressive strength. (a) F-concrete; (b) M-concrete; (c) C-concrete. Main graphs show the mean compressive strength, $\langle \sigma_f \rangle$ as a function of specimen size. Black symbols are the experimental data obtained from the uniaxial compressive tests, with the associated standard deviation $\delta(\sigma_f)$. Red curve is the fitting by Eq.	

(6.3). Insets show the same data and fits in a $[\langle\sigma_f\rangle vs. \phi^{-1/\nu_{FS}}]$ graph. In this smaller graph, the fitting by Eq. (6.3) becomes a straight line and the asymptotic strength σ_∞ is determined.	106
Fig. 6.7. Finite-size effect on the standard deviation of uniaxial compressive strength. (a) F-concrete; (b) M-concrete; (c) C-concrete. Main graphs show the standard deviation of compressive strength, $\delta(\sigma_f)$ as a function of specimen size. Black symbols are the experimental data obtained from the uniaxial compressive tests. Red curve is the fitting by Eq. (6.4). Insets show the same data and fits in a $[\delta(\sigma_f) vs. \phi^{-1/\nu_{FS}}]$ graph where Eq. (6.4) is a straight line.	107
Fig. 6.8. Finite-size effects on the uniaxial compressive strength of concrete: (a) for the mean strength, $\langle\sigma_f\rangle$ and (b) for the standard deviation of strength, $\delta(\sigma_f)$. Main graphs show the relationship between $\langle\sigma_f\rangle$ and $\delta(\sigma_f)$ with the ratio of sample size ϕ to the length scales L_m and L_δ , respectively. Black dashed-lines are the fits by Eq. (6.3) for the mean strength (a), and Eq. (6.4) for the standard deviation of strength (b). Insets show the same data and fits on $[\langle\sigma_f\rangle vs. (\phi/L_m)^{-1/\nu_{FS}}]$ and $[\delta(\sigma_f) vs. (\phi/L_\delta)^{-1/\nu_{FS}}]$ plots where the fits by Eq. (6.3) and Eq. (6.4) are the straight lines.	108
Fig. 6.9. Relationship between the global autocorrelation length, ξ_g and the length scales (a) L_m ; and (b) L_δ . Black dashed-lines are the linear fits.	110
Fig. 6.10. Relationship between the autocorrelation length of the pore structure, ξ_p and the length scales (a) L_m ; and (b) L_δ . Black dashed-lines are the linear fits.	110
Fig. 6.11. Illustration of size effect on the compressive failure strength for the different concrete mixtures.	113
Fig. 7.1. Relationships between the compressive strength and elastic modulus of concrete samples: (a) for F-concrete; (b) for M-concrete; (c) for C-concrete and (d) for all of concrete samples. Closed symbols are the static elastic moduli Y_t , open symbols are the secant moduli Y_s and unfilled symbols with error bars are the dynamic elastic moduli Y_d	120
Fig. 7.2. Normal distribution curve for the compressive strength of concrete samples (modified from (Pillai and Menon, 2009)).	122
Fig. 7.3. Comparison between the asymptotic strength, σ_∞ , determined from the finite-size scaling of the mean strength (Eq. (6.3)), and the estimated values of characteristic strength, f_{ck} , following the Eurocode 2 (filled symbols) and ACI-318 (open symbols): (a) F-concrete; (b) M-concrete and (c) C-concretes.	125
Fig. 7.4. Relationship between the length scale (L_m) and the product $p_0 \times d_{p,max}$	128
Fig. A.1. Various cases on which the weakest-link theory is applied: (a) one-dimensional discrete chain; (b) unidimensional bar (after (Bazant and Planas, 1998; Torrenti et al., 2013)).	138
Fig. B.1. Probability density functions of AE energy for the whole AE events dataset for four different sample sizes of (a) M-concrete and (b) C-concrete. The <i>pdfs</i> were normalized by their maximum value. Curves were averaged over all sensors and all samples of a given sample size.	141

Fig. B.2. Probability density functions of AE duration of the whole AE events catalog for four different sample sizes of (a) F-concrete and (b) C-concrete. The functions were normalized by their maximum value. Curves were averaged over all sensors and all samples of a given sample size.	142
Fig. B.3. Probability density functions of AE amplitude for four different sample sizes of (a) F-concrete and (b) M-concrete. The functions were normalized by their maximum value. Curves were averaged over all sensors and all samples of a given sample size.....	142
Fig. B.4. Evolution of AE event rate $dN/d\Delta$ for different sample sizes of (a) M-concrete; and (b) C-concrete. Curves were averaged over all sensors and all samples of a given sample size.	143
Fig. B.5. The AE energy release rate $dE/d\Delta$ for different sample sizes of (a) F-concrete, and (b) C-concrete. Curves were averaged over all sensors and all samples of a given sample size.	144
Fig. B.6. Conditional average maximum AE amplitude $\langle V_{\max} T \rangle$ for different sample sizes of (a) F-concrete, and (b) M-concrete. Curves of data points were averaged over all sensors and all samples of a given size (a). Black dashed lines are the reference curves according to the equation: $\langle V_{\max} T \rangle = V_{th} \exp(T/\tau)$ (Eq. (5.22)), with $V_{th} = 34dB$ and $\tau = 100\mu s$	145
Fig. B.7. Cumulative distribution (<i>cdf</i>) of AE energies, E , at different distances to failure (Δ) for tests on four different sample sizes of F-concrete : (a) 40x80 mm; (b) 70x140 mm; (c) 110x220 mm; and (d) 160x320 mm. Insets: data collapses of the same data, presented in the corresponding main graph, in a rescaled plot.	146
Fig. B.8. Cumulative distribution (<i>cdf</i>) of AE durations, T , at different distances to failure (Δ) for tests on four different sample sizes of F-concrete : (a) 40x80 mm; (b) 70x140 mm; (c) 110x220 mm; and (d) 160x320 mm. Insets: data collapses of the same data, presented in the corresponding main graph, in a rescaled plot.	147
Fig. B.9. Cumulative distribution (<i>cdf</i>) of peak AE Amplitudes, V_{\max} , at different distances to failure (Δ) for tests on four different sample sizes of F-concrete : (a) 40x80 mm; (b) 70x140 mm; (c) 110x220 mm; and (d) 160x320 mm. Insets: data collapses of the same data, presented in the corresponding main graph, in a rescaled plot.	148
Fig. B.10. Cumulative distribution (<i>cdf</i>) of AE energies, E , at different distances to failure (Δ) for tests on four different sample sizes of M-concrete : (a) 40x80 mm; (b) 70x140 mm; (c) 110x220 mm; and (d) 160x320 mm. Insets: data collapses of the same data, presented in the corresponding main graph, in a rescaled plot.	149
Fig. B.11. Cumulative distribution (<i>cdf</i>) of AE durations, T , at different distances to failure (Δ) for tests on four different sample sizes of M-concrete : (a) 40x80 mm; (b) 70x140 mm; (c) 110x220 mm; and (d) 160x320 mm. Insets: data collapses of the same data, presented in the corresponding main graph, in a rescaled plot.	150
Fig. B.12. Cumulative distribution (<i>cdf</i>) of peak AE Amplitudes, V_{\max} , at different distances to failure (Δ) for tests on four different sample sizes of M-concrete : (a) 40x80 mm; (b) 70x140 mm; (c) 110x220 mm; and (d) 160x320 mm. Insets: data collapses of the same data, presented in the corresponding main graph, in a rescaled plot.	151
Fig. B.13. Cumulative distribution (<i>cdf</i>) of AE energies, E , at different distances to failure (Δ) for tests on four different sample sizes of C-concrete : (a) 40x80 mm; (b) 70x140 mm; (c)	

110x220 mm; and (d) 160x320 mm. Insets: data collapses of the same data, presented in the corresponding main graph, in a rescaled plot.152

Fig. B.14. Cumulative distribution (*cdf*) of AE durations, T , at different distances to failure (Δ) for tests on four different sample sizes of **C-concrete**: (a) 40x80 mm; (b) 70x140 mm; (c) 110x220 mm; and (d) 160x320 mm. Insets: data collapses of the same data, presented in the corresponding main graph, in a rescaled plot.153

Fig. B.15. Cumulative distribution (*cdf*) of peak AE Amplitudes, V_{\max} , at different distances to failure (Δ) for tests on four different sample sizes of **C-concrete**: (a) 40x80 mm; (b) 70x140 mm; (c) 110x220 mm; and (d) 160x320 mm. Insets: data collapses of the same data, presented in the corresponding main graph, in a rescaled plot.154

Fig. C.1. Finite-size effect on the mean compressive strength. (a) B-8 concrete mixture; (b) B-9 concrete mixture; (c) B-10 concrete mixture. Main graphs show the mean compressive strength, $\langle\sigma_f\rangle$ as a function of specimen size. Black symbols are the experimental data reported by (Blanks and McNamara, 1935). Red curve is the fitting by Eq. (6.3). Insets show the same data and fits in a $[\langle\sigma_f\rangle \text{ vs. } \phi^{-1/\nu_{FS}}]$ graph. In this smaller graph, the fitting by Eq. (6.3) becomes a straight line and the asymptotic strength σ_∞ is determined.162

List of Tables

Table 2.1. Mixture proportions for 1m ³ of concrete	15
Table 2.2. Properties of reference samples used for the displacement calibration tests.....	20
Table 3.1. Pore structure parameters, averaged over all sections and samples sizes, for the three different concrete mixtures.	34
Table 3.2. The values of the microstructural characteristics length scales, ξ_g and ξ_p , and integral ranges of the ACF, $X_{0,g}$ and $X_{0,p}$, averaged over all sections and sample sizes, for the 3 different concrete mixtures.	36
Table 4.1. Density and moisture of three different concrete mixtures	44
Table 4.2. Elastic properties of the three concrete mixtures.....	49
Table 5.1. Summary of the hardware-setup values for AE testing.....	68
Table 5.2. Summary of the scaling exponents for the distributions of AE durations, of AE energies released, and of AE amplitudes as well as for the rate of AE events, and of AE energy release for three different concrete mixtures and comparison with the corresponding values of Mean-Field Depinning/Stick-Slip (Baro et al., 2018; Dahmen, 2017; Ertas and Kardar, 1994; Leblanc et al., 2013; Salje and Dahmen, 2014).	91
Table 6.1. Compressive strength of concrete samples.....	97
Table 6.2. Finite-size scaling parameters obtained for the three concrete mixtures.....	105
Table 7.1. Correlation coefficient between the compressive strength (σ_f) and static moduli Y_t and Y_c for different concrete samples.....	121
Table 7.2. The estimated parameters of the finite-size scaling of characteristic strength expressed according to equation (7.4).	124
Table. B.1. Summary of the scaling exponents for the distributions of AE durations, of AE energies released, and of AE amplitudes as well as for the rate of AE events, and of AE energy release for four different sample sizes of F-concrete and comparison with the corresponding values of Mean-Field Depinning/Stick-Slip (Baro et al., 2018; Dahmen, 2017; Ertas and Kardar, 1994; Leblanc et al., 2013; Salje and Dahmen, 2014).	155
Table. B.2. Summary of the scaling exponents for the distributions of AE durations, of AE energies released, and of AE amplitudes as well as for the rate of AE events, and of AE energy release for four different sample sizes of M-concrete and comparison with the corresponding	

values of Mean-Field Depinning/Stick-Slip (Baro et al., 2018; Dahmen, 2017; Ertas and Kardar, 1994; Leblanc et al., 2013; Salje and Dahmen, 2014).....	157
Table B.3. Summary of the scaling exponents for the distributions of AE durations, of AE energies released, and of AE amplitudes as well as for the rate of AE events, and of AE energy release for four different sample sizes of C-concrete and comparison with the corresponding values of Mean-Field Depinning/Stick-Slip (Baro et al., 2018; Dahmen, 2017; Ertas and Kardar, 1994; Leblanc et al., 2013; Salje and Dahmen, 2014).....	159
Table C.1. Concrete mixture data, geometrical specimen sizes and mean compressive strengths for the experiments reported by (Blanks and McNamara, 1935).	163
Table D.1. Example of application of the checking procedure proposed in section 7.3.2 for our three concrete mixtures	165
Table D.2. Example of application of the checking procedure proposed in section 7.3.2 for three assumed cases of C-concrete	166

Notations

L	Sample (structure) size
d_{\max}	Maximum aggregate size
h	Height (length) of the cylindrical concrete sample
ϕ	Diameter of the cylindrical concrete sample
F	Load (force)
Δ_t	Displacement measured from the compressive machine (total displacement)
Δ_{sp}	Displacement of specimen
Δ_{fr}	Elastic deformation of loading frame
Y_{ref}	Elastic modulus of reference sample
S	Cross-section area
ACF	Autocorrelation Function
ξ_g	Global autocorrelation length
ξ_p	Pore autocorrelation length
X_0	Integral range of Autocorrelation Function
$d_{p,\max}$	Maximum pore diameter
α_p	Power-law exponent of pore size distribution
d_p	Diameter of pore
d_{pm}	The largest two-dimensional diameter of an equivalent circular pore
p_o	Porosity
ϕ_a	Area fraction of pore
ρ	Density of concrete sample
m	Mass of concrete sample

V	Volume of sample
w_c	Moisture content
Y_t	Tangent modulus of elasticity
Y_s	Secant modulus of elasticity
σ	Stress
ε	Strain
V_p	P-wave velocity
ν	Poisson's ratio
Y_d	Dynamic modulus of elasticity
V_{\max}	Peak Acoustic Emission (AE) amplitude in Voltage
Δ	Reduced control parameter
σ_f	Peak stress
E	Acoustic Emission (AE) energy
T	Acoustic Emission (AE) duration
N	Number of AE events
p	Exponent of AE event rate
α	Exponent of AE energy rate
β	Exponent of a non-truncated power law distribution of AE signal parameter
θ	Exponent of the stress-integrated power law distribution of AE signal parameter
γ	Exponent of AE signal parameter cut-off
ξ	Correlation length
σ_∞	Asymptotic compressive strength
L_m	Finite-size length scale of mean strength
L_δ	Finite-size length scale of strength variability
f_{ck}	Characteristic compressive cylinder strength of concrete
f_{cm}	Mean value of concrete cylinder compressive strength
f'_c	Specified compressive strength of concrete
s	Standard deviation of concrete cylinder compressive strength
k	Acceptance constant of compressive strength

Chapter 1

Introduction

1.1 Context and motivation

Engineering structures are generally designed on the basis of size-independent hypotheses for material strength (as in Eurocode (EN 1992, 2004) for concrete structures), meaning that geometrically similar structures of different sizes are assumed to fail at the same applied stress. Hence, the failure stress obtained from laboratory mechanical tests on small samples could be used to predict the behavior of large structures. However, the size-dependence of material strength is one of the oldest mentioned problems of mechanics, already highlighted by Leonardo da Vinci in the 1500s: large structures fail under stresses lower (in average) than the failure stress of geometrically similar but smaller ones. Since Leonardo, this problem has been increasingly and extensively studied for various materials and different loading conditions (Bazant and Planas, 1998), because of its great impact for the establishment of safety regulations and the assessment of structural integrity. Various theories and models have been proposed and developed to explain these size effects of strength, which can be classified into two broad, fundamentally different categories: (i) Deterministic size effects and (ii) Statistical size effects.

An energetic, deterministic size effect, caused by the stress redistribution and the associated energy released before the complete failure of the structure, has been proposed and thoroughly studied by Bazant and co-workers for the so-called quasi-brittle materials such as concrete, fiber composites, rocks, tough ceramics, sea ice, etc.,. In these materials, failure is preceded by the formation of a fracture process zone (FPZ), and size effects on strength arise when the FPZ size becomes non negligible compared with the structure size (Bazant, 1984).

Corresponding to two kinds of quasi-brittle structure, two types of energetic size effect can be distinguished (Bazant, 2004a, 1999; Bazant and Chen, 1997).

The first type occurs in notched samples or structures where large cracks have grown in a stable manner before global failure (i.e. reinforced concrete structures). In this case, the size effect of strength was proposed in the form of a size effect law (SEL) (Bazant, 1984) as:

$$\sigma_f = Bf_t \left(1 + \frac{L}{D_0}\right)^{-1/2} \quad (1.1)$$

where, σ_f is the nominal stress at failure; f_t represents the tensile strength of the material; L is the structure size; B (dimensionless constant) and D_0 (transitional size) are constants estimated from experiments which are related to the relative size of the Fracture Process Zone (FPZ), and to the initial notch (or crack) size in the structure. For $L \gg D_0$, Eq. (1.1) yields $\sigma_f \sim L^{-1/2}$, which is the form of size effect arising from linear elastic fracture mechanics (LEFM) (see Fig. 1.1a). This means that when the size of the structure is very large compared with the size of the FPZ, the structure displays a fully brittle behavior. If $L \leq D_0$, we have $\sigma_f \rightarrow Bf_t$, which is the value of the nominal stress at failure according to the strength criterion (Bazant and Kazemi, 1990). This case corresponds to a non-brittle structure, or plastic materials with no size effect of strength (Bazant, 1998).

The rest type of energetic size effect happens in structures without notches or preexisting large cracks (e.g. plain concrete structures), the relationship between the strength (nominal stress at failure, σ_f) and the structure size L was formulated in the form of an un-notched size effect law (called USEL below) (Bazant, 1999, 1998; Bazant et al., 2007; Bazant and Yavari, 2005):

$$\sigma_f = \sigma_\infty \left(1 + \frac{rD_b}{L}\right)^{1/r} \quad (1.2)$$

where r is a positive constant theoretically bounded between 1 and 2 (Bazant, 1998), D_b is the constant that can be regarded as the thickness of the boundary layer of cracking (see Fig. 1.1b) and σ_∞ is the strength for a very large structure ($L \gg D_b$).

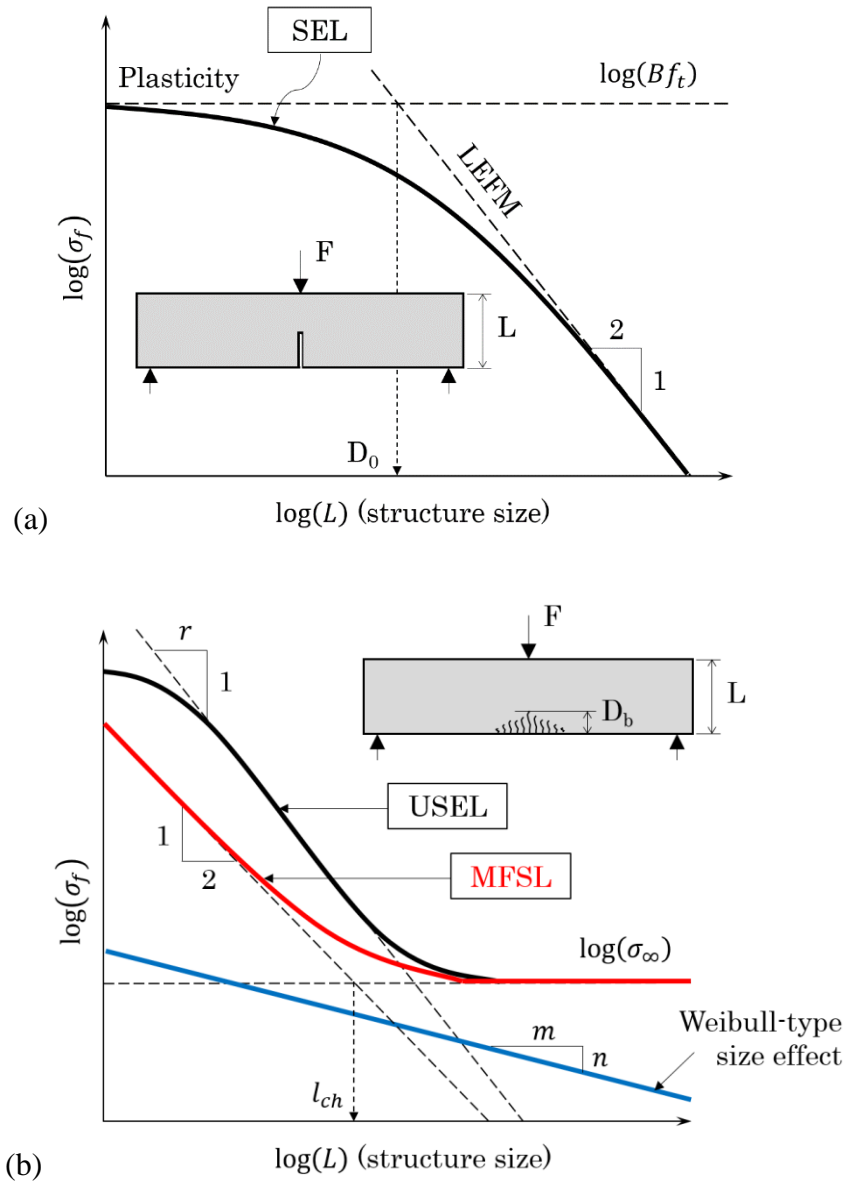


Fig. 1.1. Illustration of different size effect laws to capture the dependence of nominal stress at failure, σ_f , on structure size, L , of beams with (a) initial notches; and (b) no notch. (modified from (Bazant, 2004a)).

In the special case $r = 2$, the USEL (Eq. (1.2)) is similar to the multifractal scaling law (MFSL) proposed by Carpinteri and co-workers (Carpinteri, 1994a, 1994b, Carpinteri et al., 1999, 1995), based on geometrical arguments of a fracture surface at ultimate load:

$$\sigma_f = \sigma_\infty \left(1 + \frac{l_{ch}}{L}\right)^{1/2} \quad (1.3)$$

Where σ_∞ and l_{ch} represent the nominal strength of an infinitely large specimen and an internal material length, respectively. In equation (1.3), σ_∞ and l_{ch} are determined from the best fit of

the experimental data. The prediction of size effect following to the MFSL is contrary to that of the SEL (Eq. (1.1)) which should only be applied for the case of notched structures (see Fig. 1.2).

These size effect formulations above have been extensively used to interpret experimental data from different quasibrittle materials (rocks, concrete, composites, etc.) and structures under various loading conditions (tension, three-/four- point bending, compression, splitting failure, etc.) (see the reviews in (Bazant, 2004a, 1999), (Carpinteri et al., 1999, 1995; Carpinteri and Pugno, 2005) and (Torrenti et al., 2013)). Some examples of application of SEL and MFSL to interpret the experimental size effect of direct or indirect tensile strength data of different concrete structures are shown in Fig. 1.2.

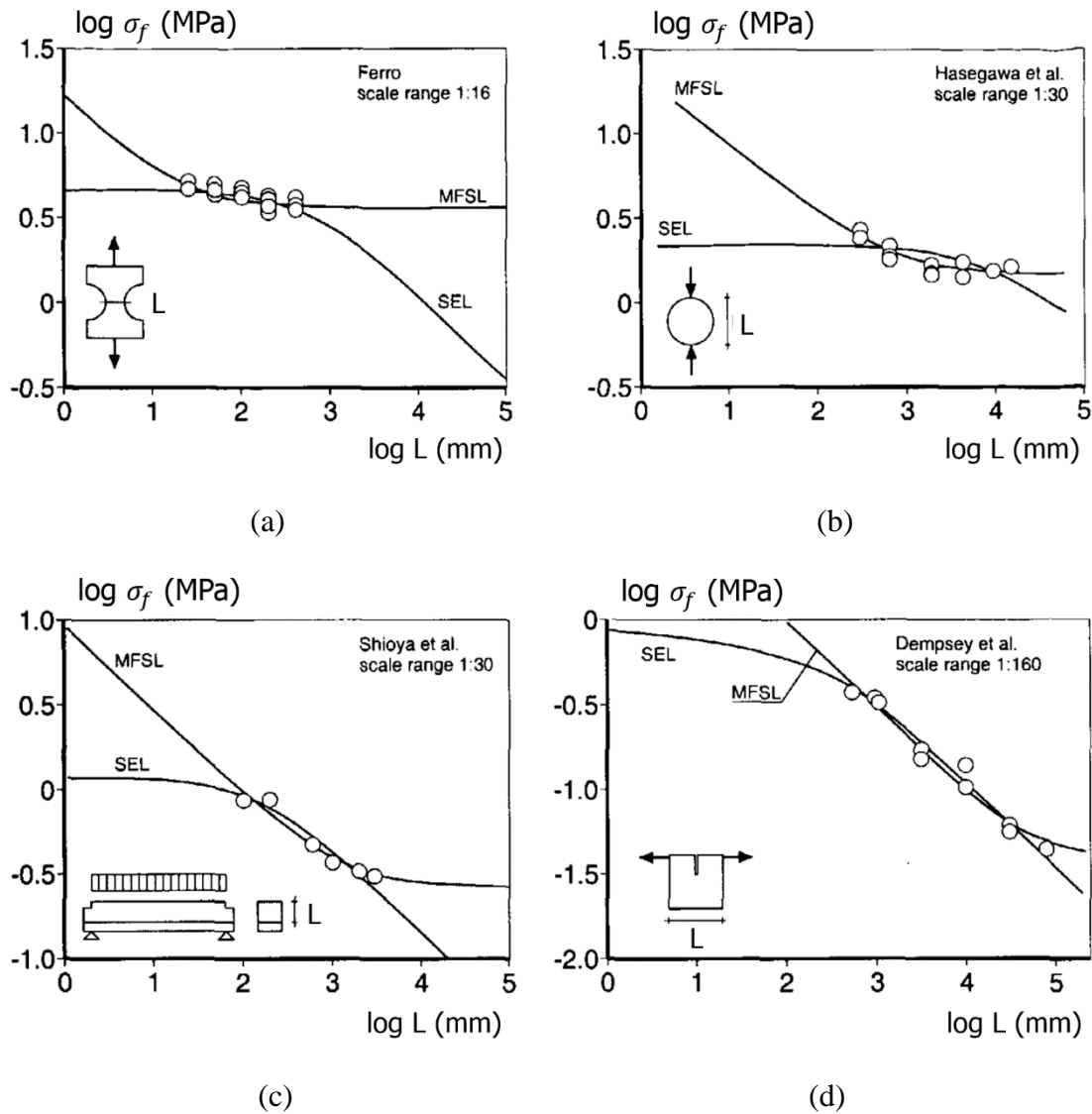


Fig. 1.2. Examples of applications of the SEL (Eq. (1.1)) and the MFSL (Eq. (1.2)) to fit the experimental size effect data of different concrete structures (reprinted from (Van Vliet, 2000)).

Although established from the experiments of direct or indirect tension loading, the size effect formulations above are normally used to predict the size dependence of compressive strength of heterogeneous materials (Burtcher and Kollegger, 2004, 2003; Carpinteri et al., 1999; Ferro and Carpinteri, 2008; Sener et al., 1999). As shown in Fig. 1.3, both SEL (Eq. (1.1)) and MFSL (Eq. (1.3)) are in good agreement with the size effect of compressive peak stresses of concrete data. These observations are consistent with the fact that the size effect laws are not clearly distinguished in the laboratory scale. However, the opposite trends of the two curves are evident outside the range of the experimental data. In particular, according to the MFSL prediction (or the case of $r = 2$ in USEL (Eq. (1.2)), a plain concrete sample of plain concrete infinite size will have a finite value of compressive strength (see Fig. 1.3). The existence of a non-zero compressive strength have been also confirmed from an intensive tests performed by (del Viso et al., 2008; Muciaccia et al., 2017; Yi et al., 2006).

In conclusion, beyond the possible pertinence of the underlying theoretical frameworks (which are strongly different for USEL and MFSL), this raises important points, namely: (i) the role of a characteristic (or internal) length scale related to the presence of material inhomogeneities (disorder); and (ii) the existence of an asymptotic strength for very large structure sizes ($\sigma_f \rightarrow \sigma_\infty = \text{const}$ for $L \rightarrow +\infty$ in the above scaling laws) (see Fig. 1.1b). We will see below that we recover these two characteristics from our dataset, although we will propose a fully different theoretical interpretation.

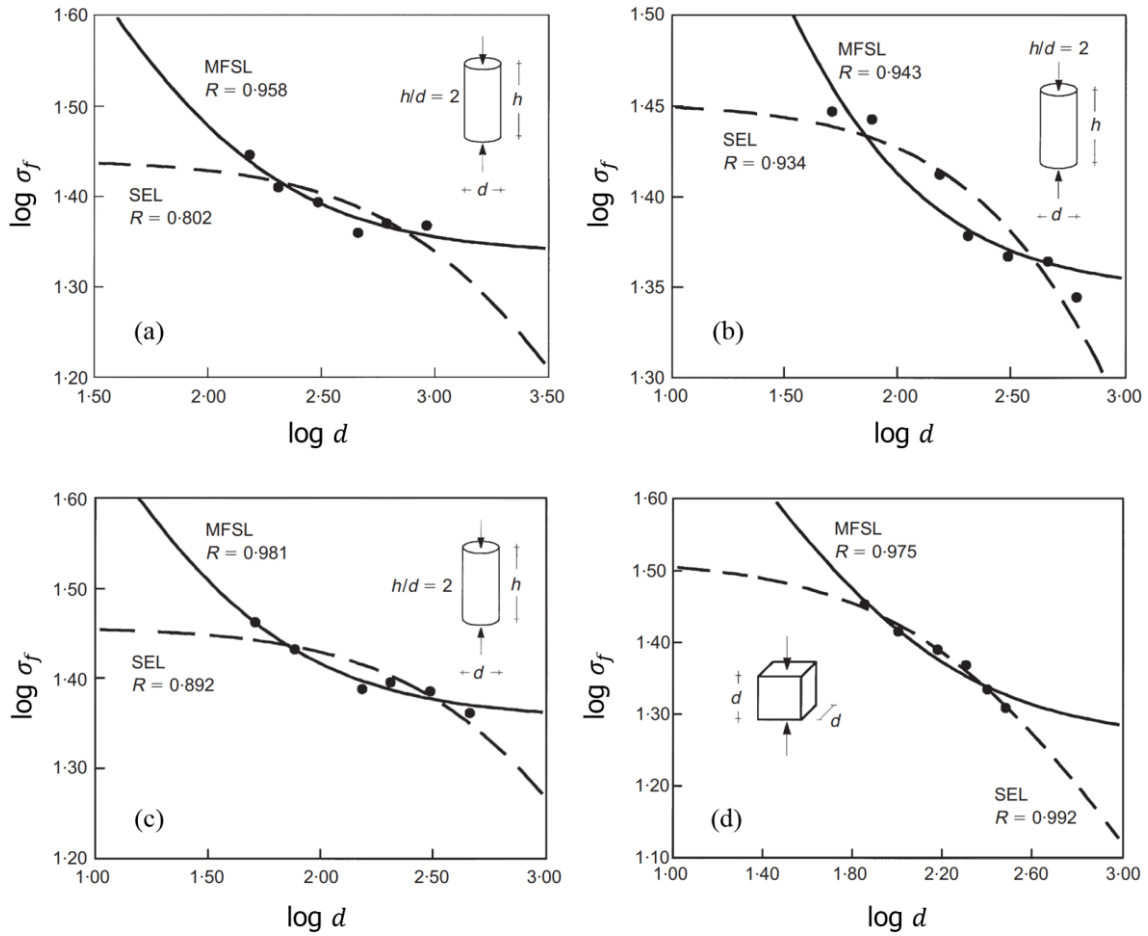


Fig. 1.3. Applications of size effect laws for fitting the size dependence of compressive peak stresses of different concrete mixtures and different shapes of sample (after (Carpinteri et al., 1999)). Fig. (a), (b) and (c) used the experimental data of (Blanks and McNamara, 1935) for three different concrete mixtures. Fig. (d) is after (Xu and He, 1990). R is the correlation coefficient, quantifying the error of the non-linear fitting.

A limitation of the aforementioned deterministic size effects is that, by construction, they do not give any prediction for a possible size dependence of the strength variability, $\delta(\sigma_f)$, and more generally for the failure probability of the structure under a stress σ , $P_f(\sigma)$. This introduces the second broad category of theoretical concepts, i.e. statistical size effects. Traditionally, the statistical size effects are modeled with a weakest-link approach. This hypothesis was first qualitatively introduced by Mariotte (Mariotte, 1686), and then formalized by Weibull (Weibull, 1951, 1939a, 1939b) and several others (Fisher and Tippett, 1928; Gumbel, 1958; Tippett, 1925), mainly mathematicians. According to the weakest-link concept, a structure is considered as being equivalent to a chain of N independent links and the whole chain will fail as soon as the “weakest” link occurs to break. Translated to failure mechanics, this assumes that the structure contains a population of non-interacting pre-existing defects,

and global failure occurs as soon as crack propagation is triggered from the weakest-link, which is associated with the largest defect. Combining these two fundamental hypotheses, pure brittleness and the absence of mechanical interactions, with linear elastic fracture mechanics (LEFM) stating that a crack will initiate from a flaw of size s at a stress $\sigma_c \sim s^{-1/2}$, one can derive the failure probability of the structure under an applied stress σ , $P_f(\sigma)$, from the distribution of preexisting defect sizes (Alava et al., 2009; Bazant et al., 1991; Weibull, 1951, 1939a). Assuming a power law tail for this distribution, $P_f(\sigma)$ is given by (Weibull, 1951, 1939b):

$$P_f(\sigma, V) = 1 - \exp \left[\left(-\frac{V}{V_0} \right) \left(\frac{\sigma}{\sigma_0} \right)^m \right] \quad (1.4)$$

, whereas Gumbel statistics (Gumbel, 2004, 1958) are obtained with the assumption that the tail of the defect sizes distribution decays faster than a power law:

$$P_f(\sigma, V) = 1 - \exp \left[\left(-\frac{V}{V_0} \right) \exp \left(\frac{\sigma}{\sigma_0} \right) \right] \quad (1.5)$$

In the two last equations, V is the volume of the structure, V_0 is the representative volume element (RVE) for the defect population, σ_0 is a reference stress that can be interpreted as the mean strength for a volume V_0 , and m is the so-called Weibull's modulus. A brief review of the weakest-link concept and Weibull theory is described in Appendix A.

In case of Weibull statistics, the mean value $\langle \sigma_f \rangle$ and the associated standard deviation $\delta(\sigma_f)$ of strength should scale with the system size L as (Bazant et al., 1991; Torrenti et al., 2013; Van Vliet, 2000; Weiss et al., 2014a):

$$\langle \sigma_f \rangle(L) \sim \delta(\sigma_f)(L) \sim L^{-n/m} \quad (1.6)$$

where n is the topological dimension ($V \sim L^n$). Relation (1.6) implies that a system of infinite size will have a vanishing strength (see Fig. 1.1b), a fundamental difference with the deterministic size effects mentioned above.

Weibull statistics have been applied to tensile strength statistics of brittle materials like glass fibers (Andersons et al., 2002; Baran et al., 1999; Gurvich et al., 1997; Phani, 1987), carbon fibers (Asloun et al., 1989; Wang and Shao, 2014; Weibull, 1951, 1939a), or ceramics (Bao and Jin, 1993; VandenBorn et al., 1991). In these cases, the underlying hypotheses of the weakest-link theory (brittleness and independence of the breaking events) appear reasonable,

owing to the aspect ratio of the samples (fibers, i.e. an almost 1D situation) as well as the nature of the materials. Indeed, the FPZ size is considered to be negligible compared with the structure size, and final failure takes place almost at one point ahead of the crack tip (Bazant et al., 1991). Hence, the whole structure displays an elastic behavior until abrupt failure occurs without precursory phenomena.

In contrast, for quasibrittle materials like concrete and/or loading configurations inhibiting extensive mode I crack propagation, such as compression, terminal failure results from a complex, progressive microfracturing process involving an initiation phase, elastic interactions and stress redistributions, as well as friction along rough surfaces (Weiss et al., 2014a). The presence of such precursors to failure (Alava et al., 2009; Bertalan et al., 2014) makes the weakest link theory inappropriate for those (Bazant, 2004a, 2004b, 1998; Bazant and Xiang, 1997; Weiss et al., 2014a). In the energetic size effect framework (Eq. (1.2)), this progressive microcracking is considered to be confined within a FPZ whose (fixed) size is not negligible compared with the structure size and is related to a characteristic length scale of the microstructural disorder (Bazant, 1999; Bazant et al., 1991; Bazant and Yavari, 2005). However, acoustic emission (Lockner et al., 1991) as well as X-ray tomography (Renard et al., 2017) measurements during compressive rock failure have shown that the correlation length ξ of microcracking and damage increases continuously during loading to reach the system size ($\xi \approx L$) near terminal failure. As proposed recently, this argues for an interpretation of compressive failure as a critical phase transition from an intact to a failed state (Weiss et al., 2014a), allowing to derive finite-size scaling laws for the mean compressive strength as well as the associated variability. Unlike deterministic size effects, this critical framework is statistical by nature, but, unlike the weakest-link theory, releases the hypotheses of pure brittleness and independence, instead takes into account elastic interactions between microcracking events and stress redistributions. As detailed in (Weiss et al., 2014a), it predicts a non-vanishing asymptotic strength ($\sigma_\infty > 0$) (but a vanishing strength variability $\delta(\sigma_f)$ towards large sizes) as well as a link between a microstructural length scale (the RVE of the disorder) and the scales which size effects become significant. Hence, on those respects, our framework share superficial similarities with the deterministic size effects mentioned above, although the underlying physics strongly differs.

Following this critical interpretation of compressive failure, we were able to interpret numerous published data on the size dependence of the average strength $\langle \sigma_f \rangle$ of various materials including different rocks, coal, ice, and concrete (Weiss et al., 2014a, 2014b). However, because the number of identical tests performed on a given material at a given size

were generally strongly limited, a thorough analysis of the associated variability $\delta(\sigma_f)$ and of the probability of failure $P_f(\sigma)$ was not possible. In addition, microstructural characterization was cursory, not allowing to clarify the role of the microstructural disorder. Those points represent important goals of the present study.

1.2 Objectives and methodology

This work was designed to address three major objectives as follows:

- 1) The first and foremost objective of this work is to get more insight into the role of heterogeneities on the statistical size effects of compressive strength as well as the critical behavior of compressive failure of heterogeneous materials.
- 2) The second one is to experimentally validate the interpretation of compressive failure of heterogeneous materials as a critical phase transition from an intact state to a failed state. This includes (i) the investigation of the influence of sample size as well as the microstructural disorder on the critical behavior of failure under compression loading, and (ii) the determination of the critical exponents.
- 3) Last but not least, this study aims at reevaluating the concept of the characteristic compressive strength of materials, the most valuable property used in structural design, by taking into account the statistical size effects on the mean value and associated variability of compressive strength.

In order to achieve these goals, a campaign of compression experiments was carried out on a large number of concrete specimens with four different sizes and three different mixtures.

Concrete is chosen in the present work for the following reasons:

- As a composite material, concrete has a high degree of heterogeneity and a complex microstructure (Carpinteri et al., 1999; Mehta and Monteiro, 2006).
- In civil engineering, concrete is commonly used to withstand compression loadings as its compressive strength much larger than tensile or flexural strengths (Mehta and Monteiro, 2006; Neville, 2004). However, in most current building codes, the size effect on compressive strength is not taken into account in calculating and designing concrete structures (Torrenti et al., 2013).
- Concrete is an artificial material, normally produced by mixing together Portland cement with sand, crushed stone or gravel, and water (Mehta and Monteiro, 2006).

Therefore, we can define the desired (input) parameters (e.g. size distribution and type of aggregate) in the fabrication stage of our concrete specimens.

1.3 Organization of the thesis

After this introduction, the thesis is composed of seven chapters. The contents of each chapter are briefly described in the following.

Chapter 2 deals with the experimental program that has been followed throughout this project. In this chapter, detailed descriptions are given in terms of the constituent materials used for concrete mixing, the fabrication procedure and the geometry of concrete specimens used for this work. We also describe the details of the uniaxial compression test including the loading configuration and setup, the testing procedure and the displacement calibration.

Chapter 3 is devoted to the investigation of the microstructural characteristics of our undamaged concrete specimens. For this purpose, an image analysis program is applied to (i) quantify the associated characteristic length scales via the Autocorrelation Function analysis (ACF) on scanned images of internal sections, and (ii) to characterize the pore structure existing in the hardened concrete samples.

In Chapter 4, the influence of the material microstructure and the sample size on the properties of concrete are analyzed. This analysis includes the density, the moisture state and the elastic properties of the hardened concrete specimens.

As the heart of this thesis, the next three chapters address the three main research objectives.

Chapter 5 describes experimental evidences supporting the interpretation of compressive failure of concrete as a critical phase transition. This work is done by using Acoustic Emission (AE) measurements performed during the compressive loading on tested specimens with different concrete mixtures and different sample sizes. From the analysis of AE signal parameters, the acceleration of the rate of number and energy released of fracturing events, the distributions of AE energies, durations and amplitudes toward the failure, and the divergence of the fracturing correlation length and time near failure are exposed. These results enables us to (i) confirm the pertinence of the critical interpretation of compressive failure; (ii) determine the associated critical exponents; and (iii) examine the influence of sample size as well as of the microstructural disorder on the critical behavior of compressive failure of concrete.

Chapter 6 presents the results of the uniaxial compressive tests conducted on all of our concrete samples with different sizes and different compositions. From those, the statistical size effects on the compressive strength of concrete, in terms of average strength, associated fluctuations, and probability of failure are explored. In this chapter, the rationality of the finite-size scaling laws for the mean strength and its associated variability derived from the critical interpretation of compressive failure (Chapter 5) is checked with the experimental strength data. The role of the microstructural disorder on the statistical size effects of compressive strength is also discussed.

As a consequence of the results of Chapter 6, Chapter 7 revisits some specific aspects in classical design rules of concrete structures by taking into account the statistical size effects on compressive strength. This work focus on (i) the concept of characteristic compressive strength of concrete and (ii) the relationship between the compressive strength and the modulus of elasticity. The standards EN 1992 (EN 1992, 2004) and ACI 318 (ACI 318-05, 2005) are referenced for this chapter.

The final chapter gives conclusions and perspectives of the present work.

Additional theoretical background and experimental results related to previous chapters are exposed in the associated appendices.

Chapter 2

Experimental program

2.1 Outline of experimental program

The experimental program for this research consists of three major parts. The aims of the first part are to examine the mechanical behavior under compression loading and to collect the values of compressive failure strength for different concrete samples. For this purpose, a series of 527 uniaxial compression tests were performed on concrete specimens with three different mixtures and four different sample sizes. In addition, 30 compression tests with the Acoustic Emission recording (AE tests) were performed for the second part of the experimental work, in order to investigate the critical behavior of compressive failure of concrete samples. The third part of the experimental study was to examine the microstructural characteristics of hardened concrete samples. This work was done from image analysis performed on the internal sections of 12 undeformed concrete samples (one sample for each size and each concrete mixture). The details of the image analysis and AE experiments will be described in Chapter 3 and Chapter 5, respectively.

In the following sections of this chapter, the details of the constituent materials of the concrete mixtures, the manufacturing procedure and the geometry of testing specimens used throughout the work are detailed. We also present the details of the uniaxial compression test including the loading configuration and setup, the testing procedure and the displacement calibration of concrete specimen.

2.2 Materials and mix proportions

The cement used in all mixes was CEM I 52.5N type Portland cement, satisfying the standard (NF EN 197-1, 2012). In this study, locally available natural sand was used as the fine aggregate, while coarse aggregates were natural gravel. All the aggregates were clean and their specific properties conform to the regulation (NF EN 12620, 2008). The size distribution of aggregates was investigated from a sieving analysis, following the standard (NF EN 933-1, 2012). The gradation curves of aggregates used in this work are shown in Fig. 2.1. Ordinary potable water available in the laboratory was used for the mixing and curing of concrete.

Following the French standard (NF EN 206-1, 2004), the weight method was applied to prepare three different concrete mixtures based on three different aggregate sizes (see Fig. 2.1 and Table 2.1). The maximum aggregate size, d_{\max} , were 3.15mm (sand), 16mm (medium gravel) and 25mm (coarse gravel). The corresponding abbreviations for identifying each concrete group are: Fine aggregate (F), Medium aggregate (M) and Coarse aggregate (C) (see Fig. 2.2b). The volume fraction of aggregates for all mixes was kept constant at $0.7\text{m}^3/\text{m}^3$ of concrete and the finesse modulus of aggregates for the three mixtures are reported in Table 2.1. The water-to-cement ratio was also set constant for all specimens in each concrete mixture. The details of each mixture proportion for 1m^3 of concrete are summarized in Table 2.1.

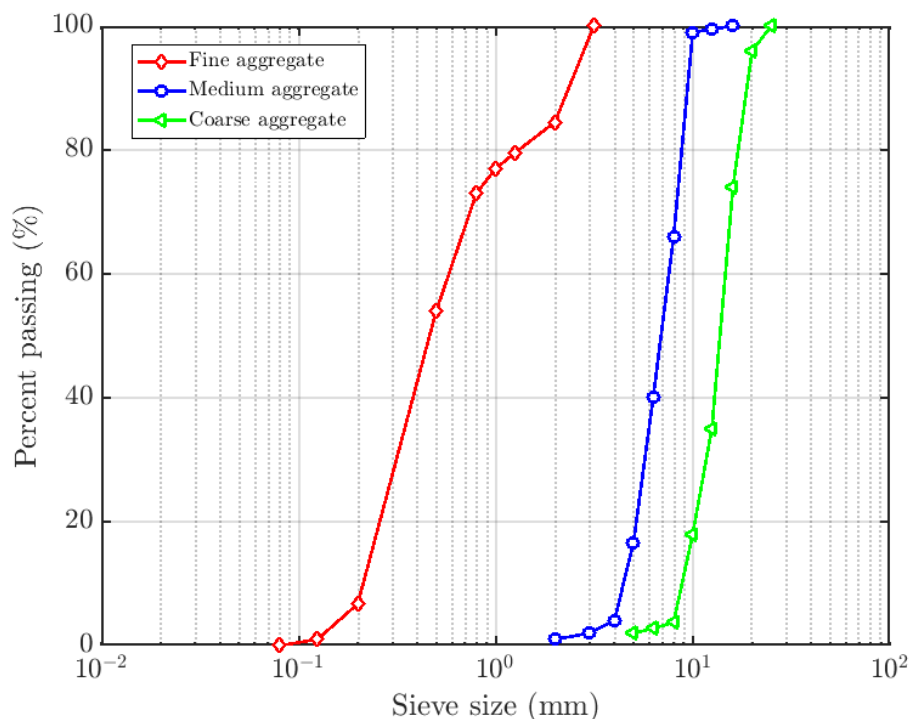


Fig. 2.1. Grading curves of aggregates for three concrete mixtures.

Table 2.1. Mixture proportions for 1m³ of concrete

Concrete mixture	Water (kg)	Cement (kg)	W/C	Sand (kg)	Medium aggregate (kg)	Coarse aggregate (kg)	Maximum aggregate size (mm)	Finesse modulus
F	225	450	0.50	1350	0	0	3.15	3.24
M	195	335	0.58	800	1065	0	16	6.95
C	195	335	0.58	800	0	1065	25	9.21

2.3 Specimen preparation

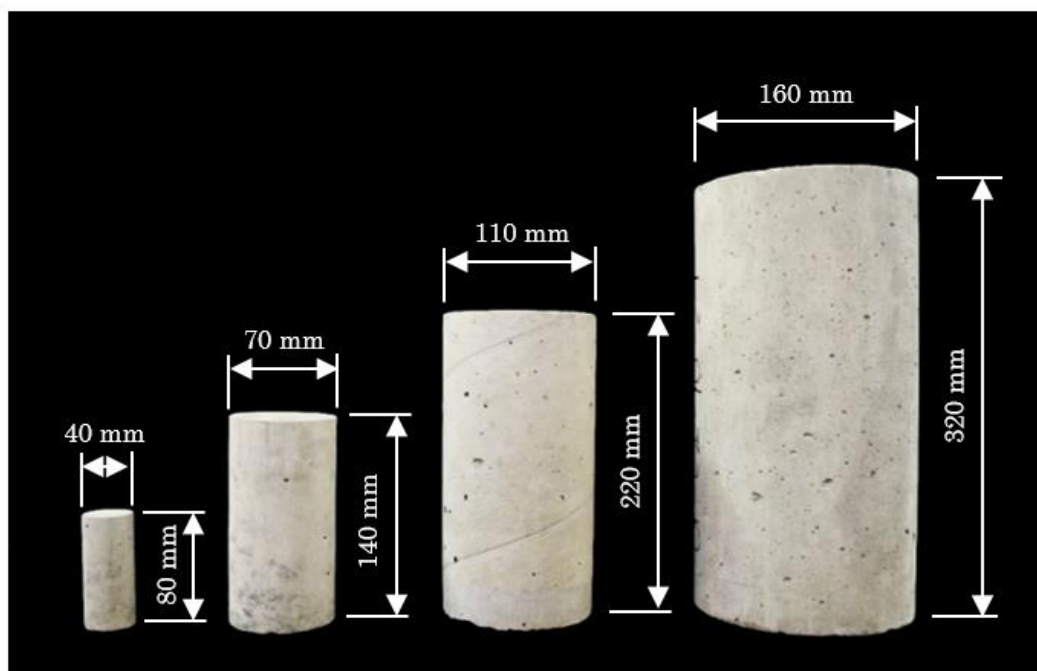
In this work, all concrete specimens were cylinders with a fixed height-to-diameter ratio $h/\phi = 2$ and, for each concrete mixture, the diameter (ϕ) ranged as follows: 40, 70, 110 and 160 mm (see Fig. 2.2b). About 45 samples for each sample diameter (ϕ) and aggregate size (d_{max}), for a total of 539 concrete specimens, were produced. Among these, 12 samples were selected for analyzing the initial microstructure (Chapter 3) and 527 remaining samples were used for the compression tests (Chapter 5 and Chapter 6).

All concrete samples were cast according to the procedure of normal weight concrete described in (NF EN 206-1, 2004). During mixing, cement and aggregates were firstly blended in dry conditions and water then added in the mixer. To minimize the influence of the casting process on strength variability, all samples for each composition were fabricated from the same batch of concrete. The concrete mixtures were poured in cylindrical cardboard molds (see Fig. 2.3a) and compacted by an internal vibrator combined with an external vibrating table to improve the consolidation of the samples.

After casting, all concrete specimens were cured initially for 48 hours by covering the molds with a plastic sheet in a moisture room. After demolding, the specimens were continually cured in a water basin at a temperature of approximately 20°C for 2 months.

The compression axis during loading was perpendicular to the direction of casting. To ensure planar surfaces when applying loading and avoid flexural stresses, all the specimens were cut by diamond grinding discs. Sawing of the concrete specimens was carried out at the age of 56 days. After sawing, the concrete specimens were immediately immersed again in the water basin for an additional month, then stored in air-dried condition at the laboratory temperature until the testing day (Fig. 2.3b). According to the recommendation of the regulation (NF EN 12390-3, 2012), loading tests should be performed after a minimum age of

28 days. In this work, all the loading tests were carried out five months after concrete preparation.



(a)



F-Concrete

M-Concrete

C-Concrete

(b)

Fig. 2.2. Concrete specimens used for the experimental investigations: (a) Geometries of the four different sizes of concrete specimens; (b) Cross sections of the three different concrete mixtures.



(a)



(b)

Fig. 2.3. Different steps in preparing the concrete specimens. (a) Cylindrical cardboard molds with different sizes and constituent materials for casting concrete samples; (b) The hardened concrete samples during the air-dried curing process.

2.4 Uniaxial compression test

A series of 527 uniaxial compressive tests was carried out under a load control protocol, following the procedure recommended by the regulation (NF EN 12390-3, 2012). As the samples were very different in size, two load-control uniaxial compression machines (of different stiffness and loading capacity), complying with the standard (NF EN 12390-4, 2000), were used. Machine A (Fig. 2.4a) with a capacity of 3000kN was used for the three larger sample sizes (70x140-mm; 110x220-mm and 160x320-mm cylinders). The stiffness of this machine is 2.9 times stiffer than that of the largest samples. For the remaining size (40x80mm-samples), the uniaxial compression tests were conducted with machine B (Fig. 2.4b). This machine has a capacity of 300kN and its stiffness is 3.5 times larger than the stiffness of the small samples.

A constant stress rate of 0.5MPa/s, corresponding to a strain rate ranging from 2.4×10^{-5} /s to 3.2×10^{-5} /s was applied on the concrete samples placed between two steel-hardened platens of the compression machine until the specimen failed. Loads were continuously measured by the load cell positioned at the top platen (see Fig. 2.4a) and directly

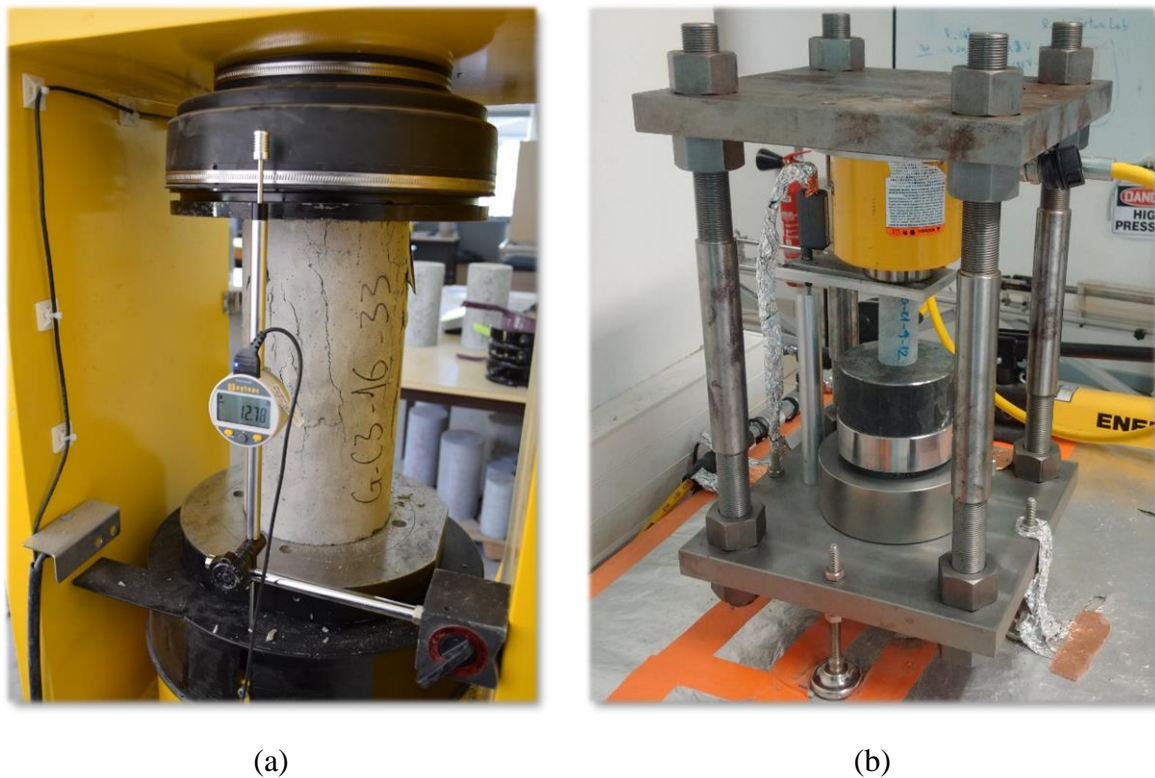


Fig. 2.4. Uniaxial compression testing setups. (a) Compression machine A used for three larger concrete specimen sizes (cylinders 70x140mm; 110x220mm and 160x320mm); (b) Compression machine B used for the smallest size (cylinders 40x80mm).

transmitted to the data acquisition system. When the load fell below 50% of the peak load, loading was automatically stopped. While the bottom steel platen was fixed, the top one could rotate. This enables the upper platen to adjust to the geometrical imperfections of the specimens.

During loading, the load (F) and the axial displacement (Δ_t) were continuously monitored and recorded at a 5Hz frequency. The axial displacement of the bottom platen (Δ_t) was measured by one Linear Variable Differential Transducer (LVDT) attached on the frame of the machine.

2.5 Calibration of the measured displacement

When a concrete specimen is loaded, both the specimen and the machine deform. As a result, the measured displacement (Δ_t) generally comprises not only the true axial shortening of the specimen (Δ_{sp}), but also the elastic deformation of the loading frame (Δ_{fr}) as a function of the applied load. Therefore, to obtain the value of Δ_{sp} , the elastic deformation Δ_{fr} has to be subtracted from the total displacement (Δ_t) by using the following equation:

$$\Delta_{sp} = \Delta_t - \Delta_{fr} \quad (2.1)$$

According to Eq. (2.1), the elastic loading frame deformation (Δ_{fr}) can be determined if we know the value of displacement (Δ_{sp}). This is done by performing a compression test on the reference sample of known elastic modulus. The value of (Δ_{fr}) can then be calculated as follows:

$$\Delta_{fr} = \Delta_t - \frac{F \cdot h}{Y_{ref} \cdot S} \quad (2.2)$$

where F is the applied load, Y_{ref} is the Young's modulus of the reference sample, h and S are the height and the cross-sectional area of the reference sample, respectively. Note that Eq. (2.2) is only valid in the elastic phase of the reference sample.

In this study, we used an aluminum cylinder of 110x220 mm and a stainless steel cylinder of 40x80 mm to evaluate the elastic deformation of machine A (Fig. 2.4a) and machine B (Fig. 2.4b), respectively. The properties of these two reference samples are summarized in Table 2.2. With large elastic limits ($> 250\text{MPa}$), these reference samples remain in the elastic stage under loadings applied in this study. In other words, using the reference samples enables us to

predict the relationships between the loading frame deformation (Δ_{fr}) and the applied load (F).

The calibration tests were carried out on the reference samples by using the same testing configuration as for the compression tests performed on concrete samples (section 2.4). The maximum loads at the end of the calibration tests were set up to cover the maximum loads for the compression tests of our concrete samples but to be smaller than the elastic limit of the reference samples (Table 2.2). Fig. 2.5 shows the relationship between the three displacements (Δ_t ; Δ_{ref} and Δ_{fr}) with the applied load (F) for two calibration tests carried out with two compression machines. The true displacement of the reference sample (Δ_{ref}) was calculated by using Hooke's law as $\Delta_{ref} = F \cdot h / (Y_{ref} \cdot S)$ and the elastic deformation of loading frame (Δ_{fr}) was computed from equation (2.2).

Table 2.2. Properties of reference samples used for the displacement calibration tests

Properties		Aluminum sample	Stainless steel sample
Diameter, ϕ	(mm)	110	40
Height, h	(mm)	220	80
Modulus of elasticity, Y_{ref}	(GPa)	75	200
Strength	(MPa)	390	620
Elastic limit	(MPa)	260	310
Density	(kg/m ³)	2800	7900

The applied Δ_{fr} vs. F load data recorded from the calibration tests were then arranged into the successive load intervals of width 2000N. We assumed a linear relation $\Delta_{fr} - F$ in each interval:

$$\Delta_{fr}(j) = k_j \cdot F + m_j \quad (2.3)$$

where k_j and m_j are constants, extracted from the linear fitting of $\Delta_{fr} - F$ data in j^{th} load interval. Applying Eq. (2.3) for all of the load intervals, we constructed a calibration table which consists of the consecutive class intervals of applied load and the corresponding values (k_j, m_j).

Using this calibration table for the compression tests of concrete specimens, we can calculate the elastic deformation of the compression machine (Δ_{fr}) at any applied load and correct the true displacement of concrete sample (Δ_{sp}). Fig. 2.6 shows the comparisons of stress-strain curves of different samples before and after calibrating the measured displacement. In this figure, we also plotted the value of the elastic modulus (Y_t) approximately estimated from the stress-strain curve (see Chapter 4 for more details). It is observed that the elastic modulus after calibration, of course, is much larger than before calibration. In particular, the value of the estimated elastic modulus for the aluminum sample obtained after the correction of measured displacement ($Y_t = 74.8$ GPa) (see Fig. 2.6a) is very close to the specified value (reported in Table 2.2), confirming the suitability of the calibration procedure. A similar result was obtained for the steel sample and machine B. Note that this calibration procedure does not have any impact on the measure of the compressive strength of the samples (see Fig. 2.6b). In the rest of this thesis, when mentioning the displacement (or deformation) of concrete specimen, it is understood as the value after calibration.

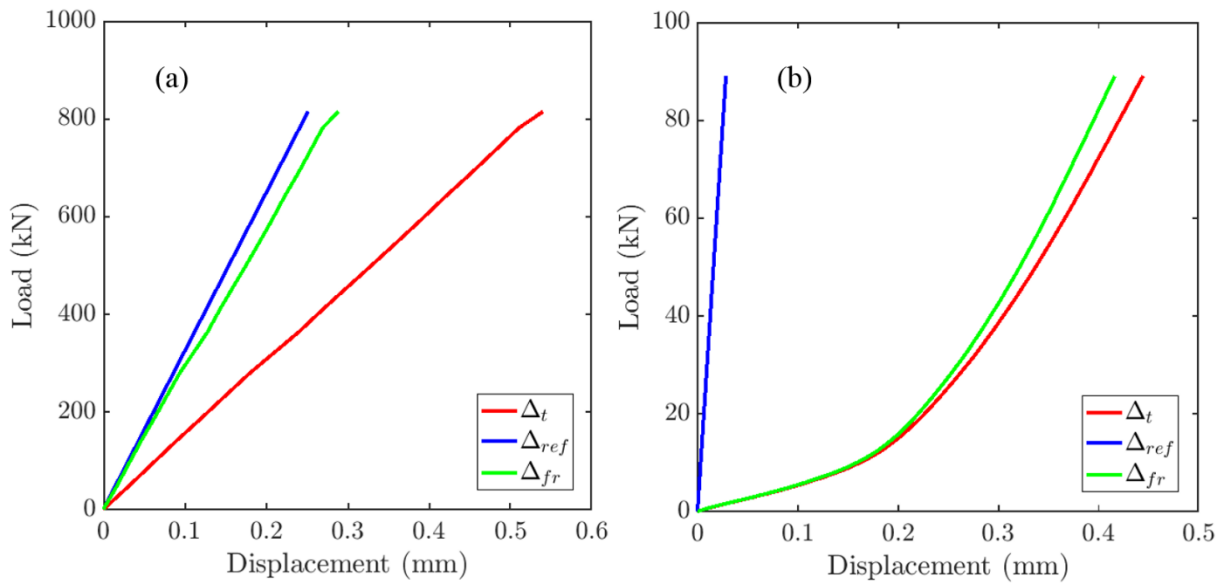


Fig. 2.5. The relationship of the total displacement (Δ_t), the displacement of the reference sample (Δ_{ref}), and the elastic deformation of loading machine (Δ_{fr}) with the applied loads for the calibration tests carried out with (a) the compression machine A and (b) the compression machine B.

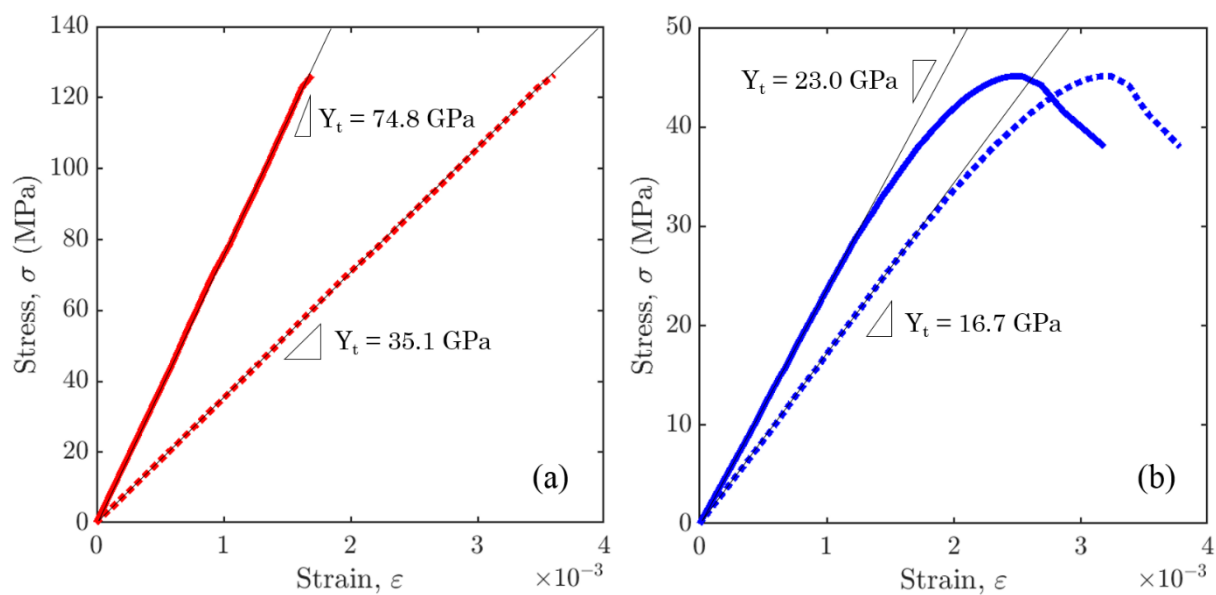


Fig. 2.6. Comparisons of stress-strain curves of different samples before and after calibrating the measured displacement: (a) for the Aluminum sample; (b) for a 160-mm sample of M-concrete. Dashed lines are the curves before calibration and solid lines are the curves after calibration.

Chapter 3

Microstructural characteristics¹

3.1 Introduction

Concrete is a complex heterogeneous material in which aggregates with a certain size distribution are mixed together with cement and water to form a hardened material. The internal structure of hardened concrete is hence influenced by various factors, including component properties, aggregate size, shape and texture, and preparation conditions (Masad et al., 1999). Therefore, studying the mechanical behavior of concrete requires an accurate description of its microstructure, as effective elastic properties (Jeulin and Ostoja-Starzewski, 2001; Torquato, 1991) as well as fracture of heterogeneous materials (Alava et al., 2006) depend on disorder characteristics (size, shape and spatial distribution of heterogeneities).

In this chapter, we present an image analysis procedure to capture the microstructural characteristics of our undamaged concretes from internal sections within specimens of different sizes and compositions. To analyze the internal structure of our (undeformed) concretes and quantify the associated characteristic length scales, we performed an Autocorrelation Function analysis (ACF) on scanned images of internal sections (Kanit et al., 2003). This allowed estimating a “global” autocorrelation length, ξ_g , describing the internal microstructure as a whole, as well as an autocorrelation length of pore structure, ξ_p .

¹ The content of this chapter has been presented in the article:

Vu, C. C., Weiss, J., Plé, O., Amitrano, D., Vandembroucq, D. (2018), Revisiting statistical size effects on compressive failure of heterogeneous materials, with a special focus on concrete, *Journal of the Mechanics and Physics of Solids*, 121, p.47–70. doi:10.1016/j.jmps.2018.07.022

Following this introduction, the next section recalls the principles of the ACF analysis. A brief description of the image analysis procedure used in this study is provided in section 3.3. Section 3.4 is devoted to determine the global autocorrelation lengths, ξ_g . The characterization parameters of the pore structure of concrete samples are investigated in section 3.5. Conclusions for this chapter are summarized in section 3.6.

3.2 Autocorrelation Function analysis

The two-dimensional autocorrelation function (ACF) of an image statistically characterizes the spatial pattern within that image and represents a powerful tool for microstructural analysis (Pfleiderer et al., 1993). The main advantage of this method is that the segmentation of the images, to extract microstructural features (aggregates, pores, grains, etc.), is not mandatory, thus avoiding possible biases associated with the identification of feature boundaries. ACF is sensitive to the size, shape, orientation and spatial organization of the features, but not on their location. It gives: (i) a quantitative description of the microstructure in general terms, and (ii) an objective determination of a representative volume element (RVE) of the material in terms of microstructural disorder (Kanit et al., 2003).

The ACF describes the correlation of an image with itself (Heilbronner, 1992) and is defined by:

$$f(x, y) \otimes f(x, y) = \int_{-\infty}^{+\infty} \int_{-\infty}^{+\infty} f(x', y') \cdot f(x + x', y + y') dx' dy' \quad (3.1)$$

where $f(x, y)$ is the two-dimensional gray value function defining the image, \otimes is the convolution or correlation operator, (x, y) are the image coordinates, and (x', y') represent the distance (or lag) from the corresponding (x, y) position.

The ACF is generally introduced in the context of Fourier analysis and Fast Fourier Transforms (FFT) which is mathematically equivalent to Eq. (3.1) but computationally more efficient (Gonzalez and Woods, 2002; Jahne, 2005). On the image plane, a region of interest (ROI), which must be square to allow the use of FFT algorithms, is selected and digitized (Heilbronner and Barrett, 2014; Pfleiderer et al., 1993). Following Heilbronner (Heilbronner, 2002; Heilbronner and Barrett, 2014), we used the following procedure to calculate the ACF:

- 1- The ROI is selected and digitized;
- 2- The mean gray value is subtracted:

$$g(x, y) = f(x, y) - \langle f(x, y) \rangle \quad (3.2)$$

3- The two-dimensional discrete Fourier transform is given by:

$$g(u, v) = \frac{1}{N} \sum_{x=0}^{N-1} \sum_{y=0}^{N-1} g(x, y) \cdot \exp[-2\pi i(ux + vy)] \quad (3.3)$$

where N is the size of the matrix, $g(u, v)$ is the discrete transform, and u and v are the frequencies in x - and y - directions;

- 4- The transform is calculated using the theorem of separability, meaning that two consecutive 1D FFTs are used to transform the rows and columns of the image matrix;
- 5- The Fourier transform of the ACF is obtained by multiplying the Fourier transform of the image, $g(u, v)$, with its complex conjugate $g^*(u, v)$;
- 6- The ACF value is finally obtained by a two-dimensional inverse discrete Fourier transform.

3.3 Image analysis procedure

One sample was selected from each composition and each size sets of specimens. These samples were then cut into four pieces (see Fig. 3.1). In order to obtain good quality images, the sample surfaces were first ground flat using hand pressure on a water-cooled wheel topped with more and more grit size of metal-bonded diamond plates, and then polished using successively finer grit resin-bonded diamond plates. A water rinse was applied after polish to thoroughly clean the fresh surface. The quality of polish was considered acceptable as the reflectivity of the surface was uniform, without striations from the grinding materials.

Color images of the sample sections were acquired with a flatbed scanner, using 24-bit color (RGB) digital imaging with a resolution of 1200dpi (corresponding to a 21.17 μ m pixel size). The RGB image was split into three gray scale images (corresponding to Red, Green, Blue channel), and the ACF was averaged over the three different channels (see Fig. 3.2).

For circular sections, as FFT algorithms require square ROIs, 90 different square ROIs, rotating around the center of the circular image, were examined and their ACF averaged. For rectangular sections, two square ROIs were combined to pave to entire image.

The entire image analysis procedure used to calculate the ACF of each concrete sample is summarized in Fig. 3.2.

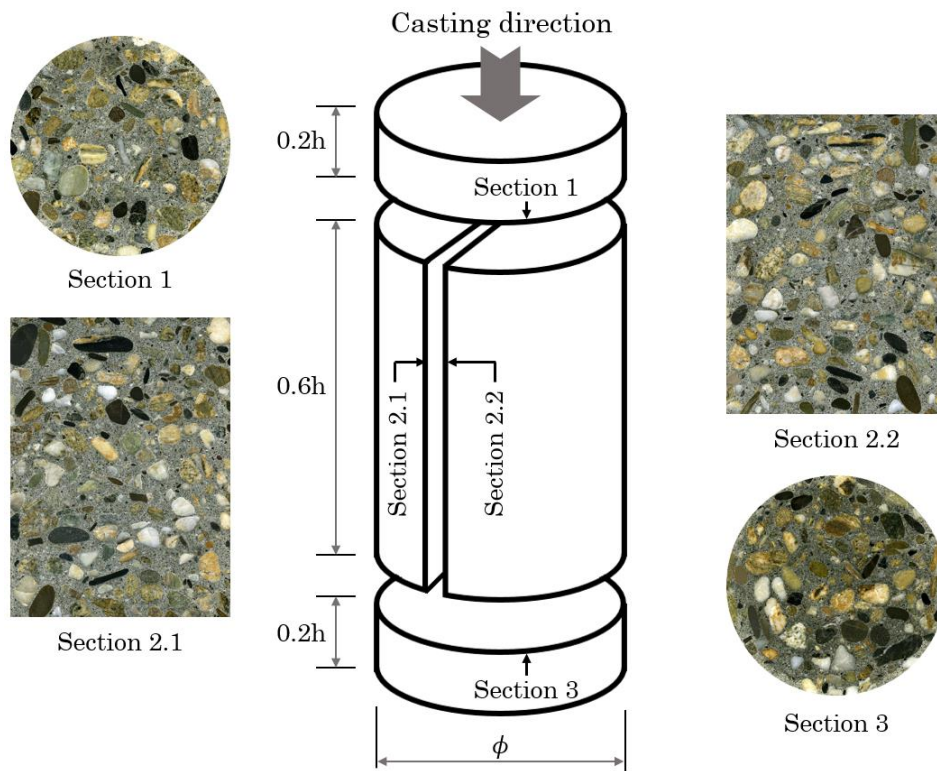


Fig. 3.1. Sectioning of concrete samples with identification of polished surfaces.

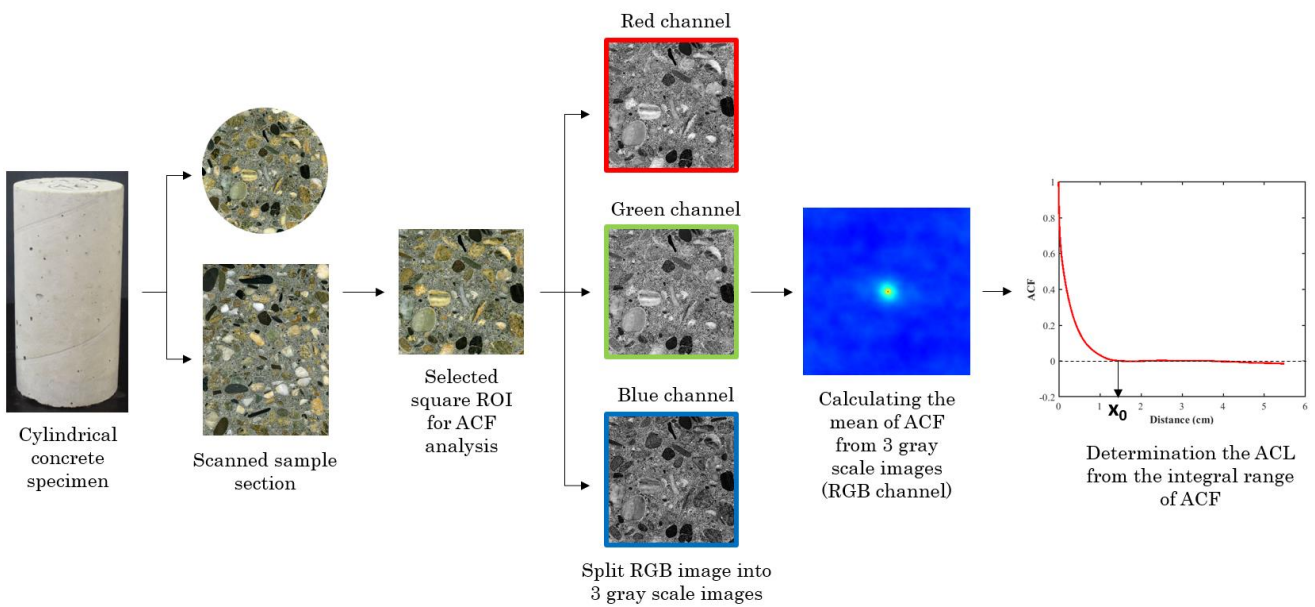


Fig. 3.2. 2D Autocorrelation function analysis of concretes samples (see text for details).

3.4 Global autocorrelation length

The ACF for 3 different concrete mixtures with the same sample size ($\phi \times h = 110 \times 220$ mm) are displayed on Fig. 3.3.

The different microstructures are easily recognizable on the ACF plots, with the extent of the central stain clearly correlated with the aggregate gradation (F-, M- and C-concretes). We then define the characteristic microstructural length scale as the Autocorrelation length, ξ_g , calculated from an integration of the ACF:

$$\xi_g = \int_0^{X_{0,g}} (ACF(r) - ACF(X_{0,g})) dr \quad (3.4)$$

where $X_{0,g}$ corresponds to the integral range over which the ACF remains positive (Kanit et al., 2003; Matheron, 1971), i.e. $ACF(X_{0,g})$ (see Fig. 3.2).

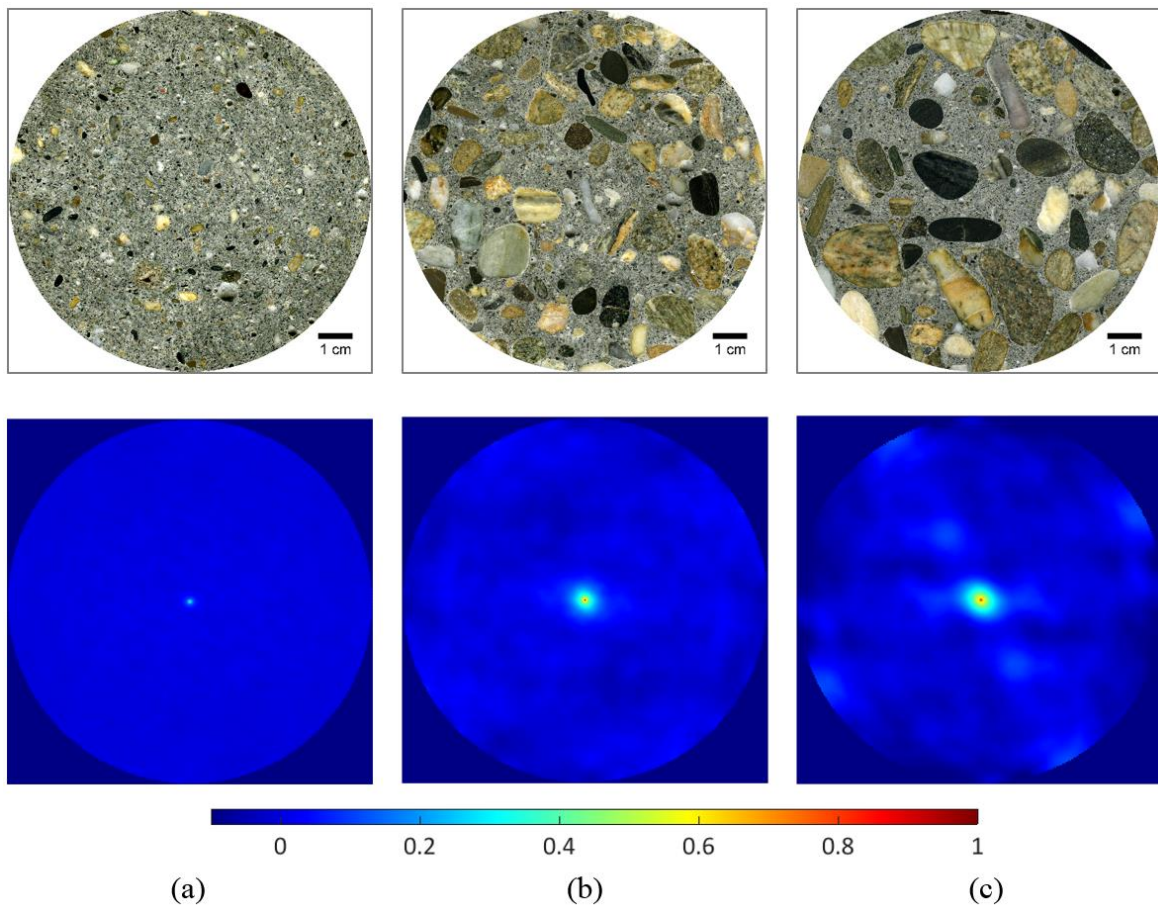


Fig. 3.3. Autocorrelation function for 3 different compositions of concrete; (upper) original scanned image of concrete ; (lower) digital image of ACF; (a) F-concrete; (b) M-concrete; (c) C-concrete.

Owing to the possibly anisotropic shape of the aggregates, the ACF values might be slightly anisotropic, especially for large aggregates (C-concrete) and small samples (e.g. Fig. 3.3c). In this study, we do not quantify this anisotropy. Therefore, the ACL value was estimated by averaging the ACL over all directions around the central point. The results are summarized on Fig. 3.5, from which we can conclude that:

(i) different sections of the same concrete sample show very similar ACF and ACL, meaning that there is no segregation of the internal concrete microstructure (Fig. 3.5a),

(ii) for a given concrete mixture, the ACF and the corresponding ξ_g -value do not exhibit any significant sample size effect (Fig. 3.4 and Fig. 3.5b),

(iii) as expected, there is a clear correlation between ξ_g (reported in Table 3.2) and the aggregate size (Fig. 3.5c and Fig. 3.12a), meaning that the latter largely controls the microstructural characteristics of the material and,

(iv) the ACL of the C-concrete (3.5 mm) is about one order of magnitude smaller than the diameter of the smallest samples (40 mm). This suggests that, in terms of microstructural characteristics, even the smallest samples can be considered as being larger than the RVE of the material, whatever the type of concrete.

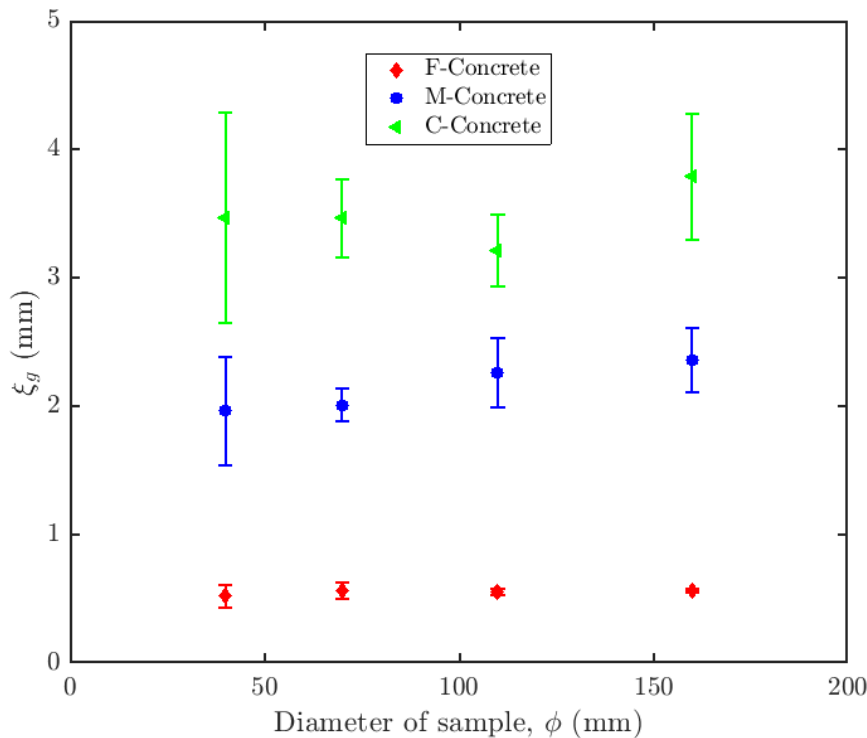


Fig. 3.4. Global autocorrelation length, ξ_g , for all concrete specimens.

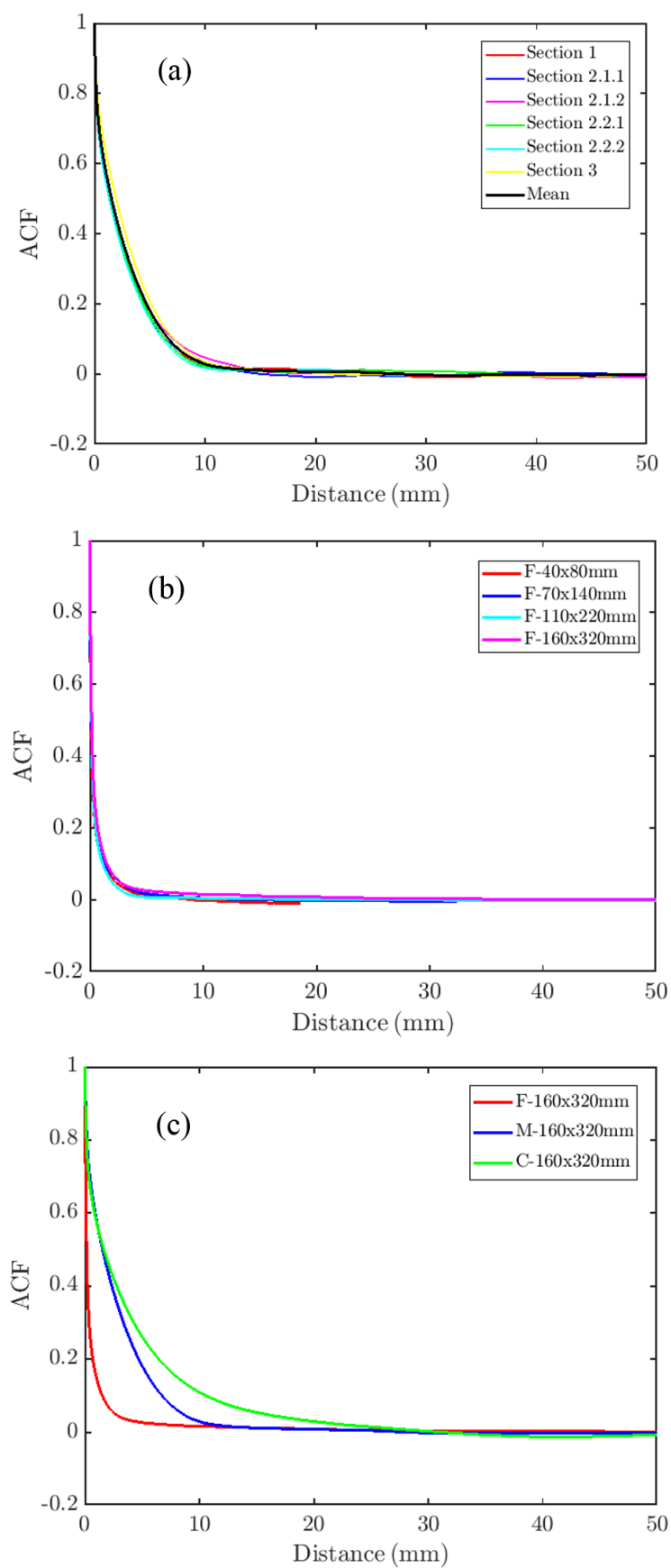


Fig. 3.5. Autocorrelation function of concrete: (a) for different sections of sample M-160x320 mm; (b) Different sizes of sample for the F-concrete group; (c) Different compositions of concrete with the same sample size (160x320 mm).

3.5 Characterization of the pore structure

The strength of concrete can be significantly affected by the volume of all pores: capillary pores, gel pores and air voids (entrained and entrapped air voids) (Neville, 2004). Hence, the porosity and size distribution of pores must be quantified (Fonseca and Scherer, 2015). Due to their small sizes (ranging from 0.5nm to 1 μ m), gel and capillary pores are hard to detect by optical methods and have little impact on the strength of concrete (Mehta and Monteiro, 2006). Thus, we just focus here on air voids (referred as pores in the following). In the present work, an image analysis procedure was used to characterize the pore structure of our undamaged concrete samples based on the procedure presented in (ASTM C 457/C 457M-16, 2016; Jakobsen et al., 2006).

3.5.1 Image of pore structure

After the scanning process for color image of cross-section concrete sample (section 3.3), to image the pore structure, these sectional surfaces were treated to enhance the contrast between the pores and other components (aggregates, cement paste). This work was done by filling the depressions with a calcium carbonate paste. After this preparation, the sectional surfaces were scanned by a flatbed scanner at a resolution of 1200dpi (equivalent to 21.17 μ m/pixel). Thanks to the white color of the calcium carbonate paste, the pores were easily distinguished from the solid phases (aggregates and hardened cement paste) after applying a manual contrast enhancement (Fig. 3.6c) and thresholding (Fig. 3.6d). Fig. 3.7 illustrates a comparison of the pore structures for three different concrete mixtures.

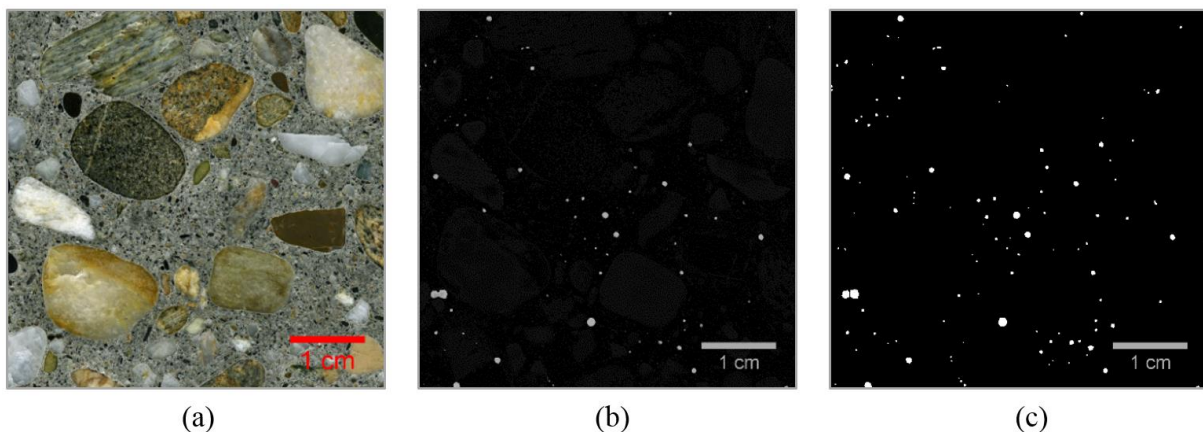


Fig. 3.6. Image analysis procedure of the pore structure: (a) concrete sample surface after grinding and polishing; (c) scanned image of pores after the contrast enhancement operation; (d) binary image of pores obtained after thresholding.

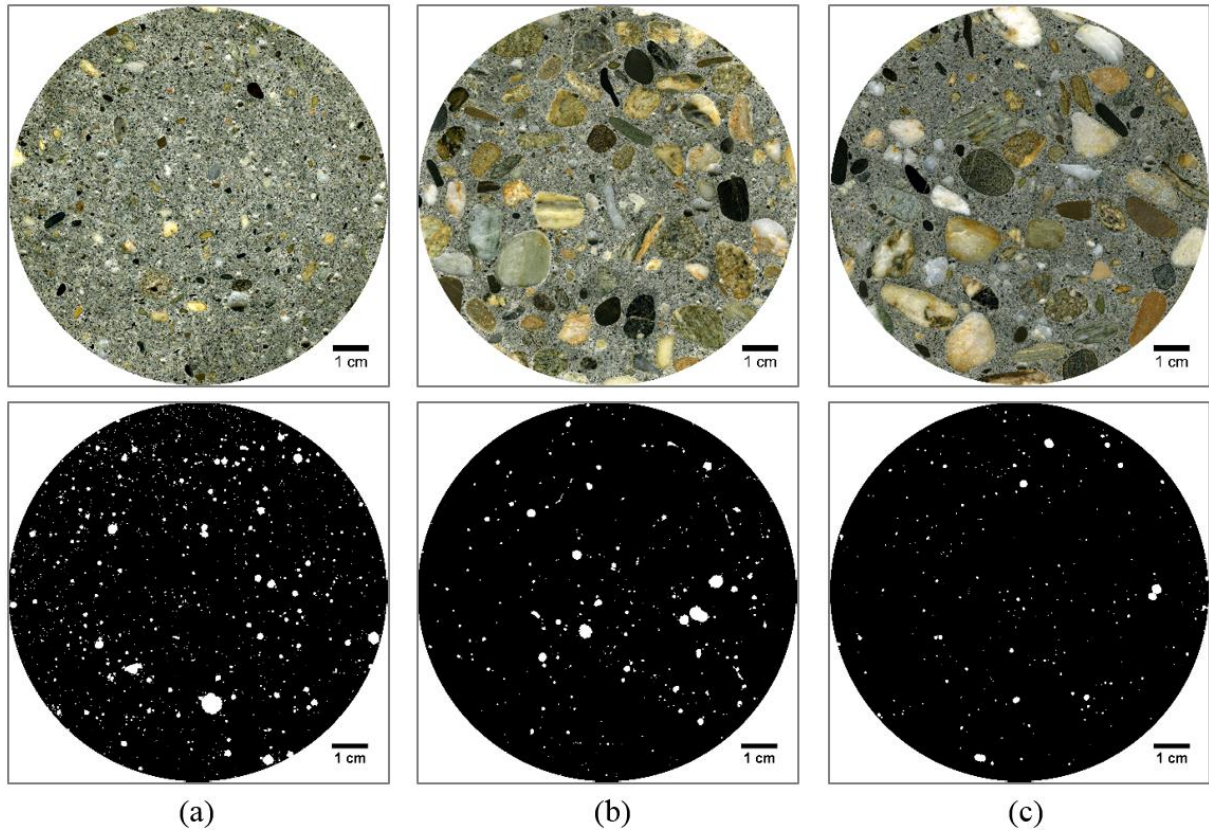


Fig. 3.7. Comparison of the pore structure for three different concrete mixtures; (a) F-110x220mm; (b) M-110x220mm; (c) C-110x220mm. Top figures are the original scanned images and bottom figures are the corresponding binary images of pores.

3.5.2 Pore size distribution and porosity

Whereas gel and capillary voids are irregular in shape, air voids are generally spherical-like (Mehta and Monteiro, 2006; Neville, 2004). This is consistent with the cross-sections of Fig. 3.7. Therefore, to obtain the three-dimensional (3D) pore size distribution, a stereological 2D→3D conversion method for a polydispersed system of spheres (Saltykov, 1967; Underwood, 1970) was applied in this research. From the binary image of pores (Fig. 3.7), the cross-sectional areas of individual pores were calculated and classified into n size (diameter) intervals. A value of $n = 14$ was chosen to obtain a large enough number of pores in each interval. We noted $(N_A)_i$ the number of pores per unit area in each size interval i . The corresponding diameter range for the i^{th} interval is $[d_{pm} \times 10^{-0.1(i-2)}, d_{pm} \times 10^{-0.1(i-1)}]$, where d_{pm} is the largest 2D diameter of an equivalent circular pore. Following the Saltykov's method (Saltykov, 1967; Underwood, 1970), we assumed that the largest 2D pore areas correspond to the largest spheres. It means that the diameter of the largest 2D pore area is equal

to that of the largest 3D spherical pore in the sample volume. Smaller 2D areas of diameter $(d_p)_i$ can result from cutting the spheres having a diameter $(d_p)_j$ larger than or equal to $(d_p)_i$. Then, from the geometric probability distribution of the distances from a random cutting plane to the centers of spheres, we obtain the expression:

$$(N_v)_j = \frac{1}{(d_p)_j} \sum_{i=j}^n \alpha_i (N_A)_i \quad (3.5)$$

where the j 's refer to sphere diameters and the i 's refer to area diameters; i and j are integer values from 1 to n , and n is equal to the total number of diameter class intervals; $(N_v)_j$ is the number of spherical pores per unit volume in the diameter class j ; $(d_p)_i$ is the diameter of the largest areas observed on the cutting plane, this diameter depends on the number of size class intervals, and corresponds to the sphere diameter class j ; $\sum_j (N_A)_{i,j}$ represents the number per unit area of pore diameter class $(d_p)_i$, which can be obtained from spheres of different diameter $(d_p)_j$; α_i is the coefficient corresponding to the area's diameter class $(d_p)_i$, this coefficient can be obtained from the probability of a cutting plane intersecting a sphere of diameter $(d_p)_j$ to yield areas of diameter $(d_p)_i$. Using the values of the coefficients α_i given in (Saltykov, 1967; Shen et al., 2006; Underwood, 1970), the 3D pore size distribution was determined for each concrete sample.

Fig. 3.8 presents the (cumulative) probability distribution of pore sizes for different concrete samples. We observe: (i) an absence of sample size effect on the pore size distribution for a given type of concrete; (ii) that the pore size distributions have a power law shape, $P(> d_p) \sim d_p^{-\alpha_p}$, with an exponent α_p slightly varying with the material (see Fig. 3.8).

From these distributions, the average diameter and the total porosity were estimated and reported in Table 3.1 for the different concrete samples. We note that the number of pore per m^3 , the mean as well as the maximum pore diameter, and the total porosity, all decrease with increasing aggregate size (see Fig. 3.7 and Table 3.1). In this study, the maximum pore diameter, $d_{p,max}$, was calculated by averaging the values of d_{pm} of all four different sections (Fig. 3.1) of a given size, and of all sections and samples (whatever the size) of a given concrete mixture.

The main cause of porosity present in hardened concretes is due to the presence of free water during the mixing of concrete. During the batching procedure, because air and water do not mix, air trapped in fresh concrete is in the form of gas bubbles surrounded by a thin liquid

film and suspended in the mix water (Mehta and Monteiro, 2006). The more water used for preparing concrete, the more free water will remain after complete hydration, thus the more air bubbles are trapped when concrete hardens. This explains why the F-concrete, which has the largest water-cement ratio, shows the highest pore sizes and porosity (see Fig. 3.7 and Table 3.1).

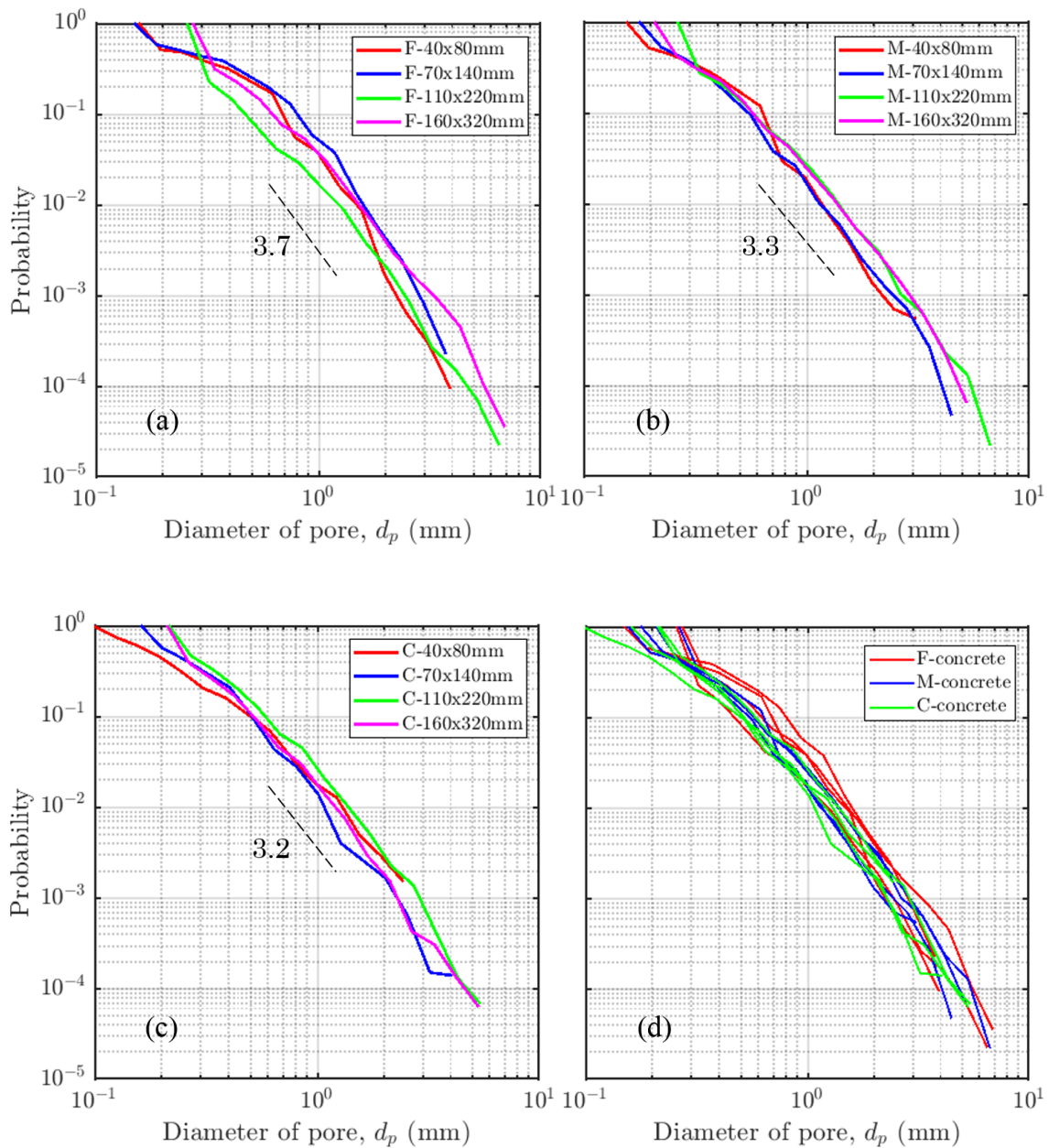


Fig. 3.8. Size distribution of pores per unit volume for different concrete samples. (a) F-concrete; (b) M-concrete; (c) C-concrete and (d) All concrete samples.

Table 3.1. Pore structure parameters, averaged over all sections and sample sizes, for the three different concrete mixtures.

Concrete mixture	Mean pore diameter, $\langle d_p \rangle$ (mm)		Maximum pore diameter, $d_{p,max}$ (mm)		Porosity, p_o (%)	
	Mean	SD	Mean	SD	Mean	SD
	F	0.33	0.24	6.9	1.8	4.8
M	0.31	0.21	6.7	1.2	1.6	0.4
C	0.28	0.20	5.4	1.3	1.5	0.3

3.5.3 Autocorrelation length of pore structures

With the same procedure described above for ξ_g (section 3.3) but performed on the binary images of the pores (Fig. 3.7), the autocorrelation length of the pore structure, ξ_p , was obtained. For the binary image, the value of $g(x, y)$ in Eq. (3.2) is equal to 1 for the white phase (pores) and 0 for the black phase (aggregates, cement paste) (see Fig. 3.7). In this case, the initial value of the ACF of the pore structure is ϕ_a at $r = 0$ (see Fig. 3.9), where ϕ_a is the area fraction of pore (the white phase in Fig. 3.7), while it reaches the asymptotic limits of ϕ_a^2 for very large distance ($r \rightarrow +\infty$) (Jiao et al., 2008; Kanit et al., 2003; Moon et al., 2014; Torquato, 1991). We define the characteristic length scale of pore structure as the autocorrelation length, ξ_p , computed from an integration of the ACF of pore structure:

$$\xi_p = \int_0^{X_{0,p}} \left(ACF(r) - ACF(X_{0,p}) \right) dr \quad (3.6)$$

where $X_{0,p}$ corresponds to the integral range over which the ACF of pore structure remains larger than ϕ_a^2 (Kanit et al., 2003), hence, $ACF(X_{0,p}) = \phi_a^2$ was used in this study.

Fig. 3.10 shows the values of ξ_p for each concrete sample, averaged over 4 different sections. For a given concrete mixture, there is no clear trend for the evolution of ξ_p with sample size, meaning that there is no significant size effect on the characteristic length of the pore structure of our concretes (e.g. C-concrete samples (Fig. 3.11b)). Unlike for the global autocorrelation length, ξ_g (in Fig. 3.4), the F-concrete shows the highest ξ_p -value (see Fig. 3.10 and Fig. 3.11c). Moreover, different sections of the same sample display very similar ACF

and ACL of pore structure (Fig. 3.11a), meaning that the pore structures were uniformly distributed in the volume of hardened concrete sample. The length scale, ξ_p , and the integral range of ACF, $X_{0,p}$, of the pore structures for the three different concrete mixtures are summarized in Table 3.2.

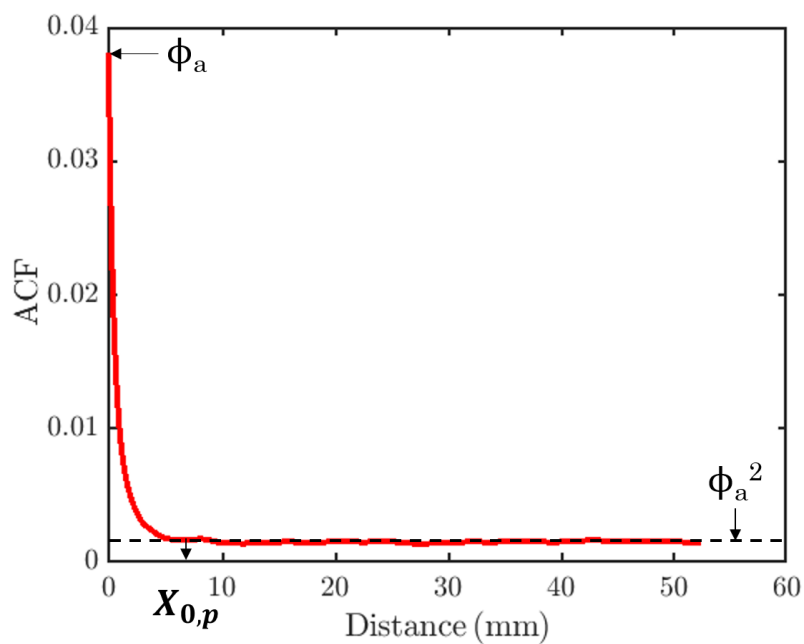


Fig. 3.9. An example of Autocorrelation function (ACF) of the pore structures; where ϕ_a is the area fraction of pores, the asymptotic value of ACF is equal to the square of the area fraction of pore, ϕ_a^2 , and $X_{0,p}$ is the integral range where $ACF(X_{0,p}) = \phi_a^2$.

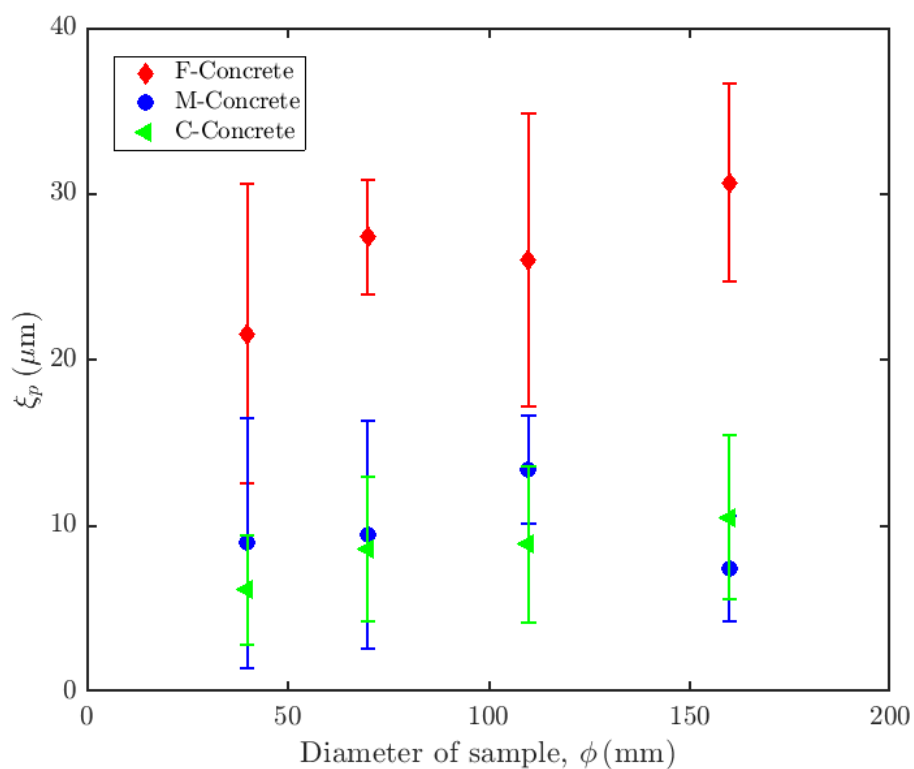


Fig. 3.10. Autocorrelation length of pore structure, ξ_p , for all concrete specimens.

Table 3.2. The values of the microstructural characteristics length scales, ξ_g and ξ_p , and integral ranges of the ACF, $X_{0,g}$ and $X_{0,p}$, averaged over all sections and sample sizes, for the 3 different concrete mixtures.

Concrete mixture	ξ_g (mm)		$X_{0,g}$ (mm)		ξ_p (μm)		$X_{0,p}$ (mm)	
	Mean	SD	Mean	SD	Mean	SD	Mean	SD
F	0.6	0.1	7.0	3.7	26.4	7.5	6.9	4.9
M	2.1	0.3	13.7	4.9	9.8	5.7	4.4	2.2
C	3.5	0.5	19.0	9.3	8.5	4.4	6.0	3.3

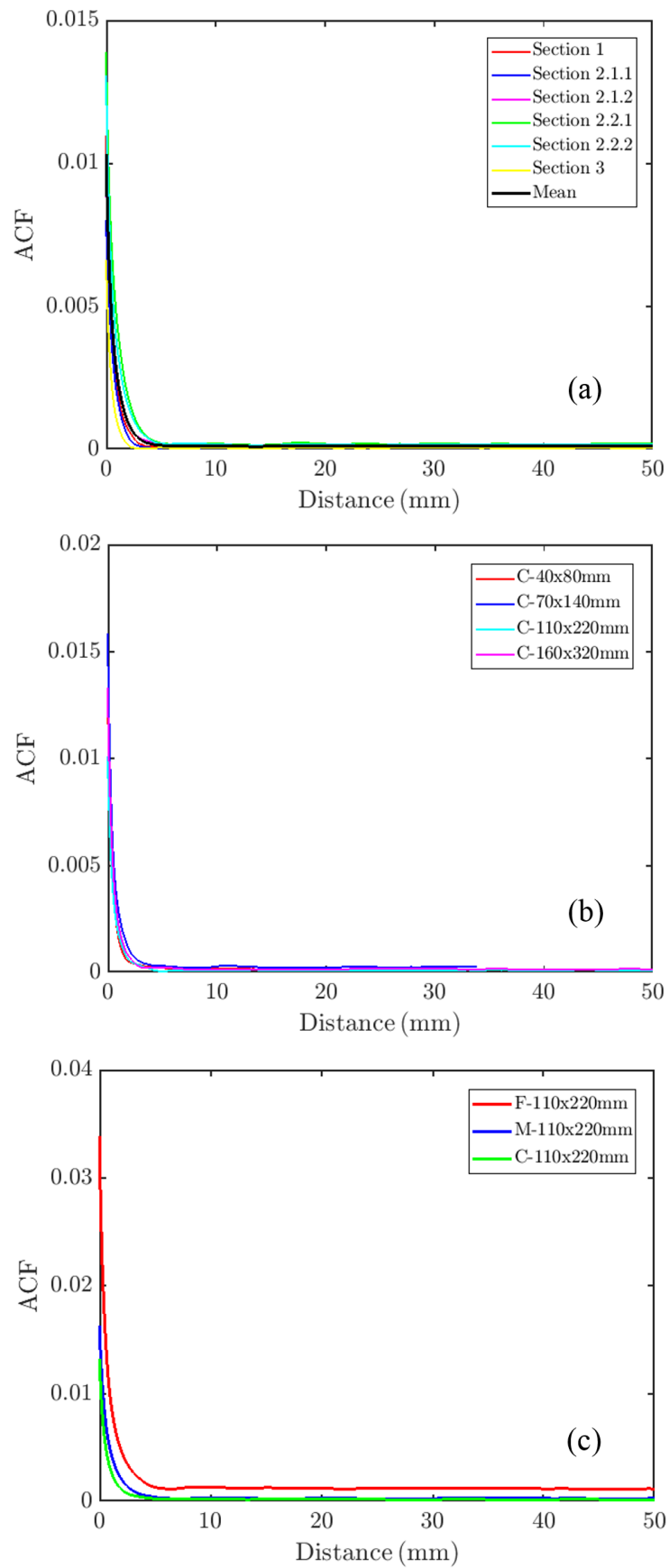


Fig. 3.11. Autocorrelation function of pore structure in concrete samples: (a) for different sections of sample M-160x320mm; (b) different sizes of sample for the C-concrete group; (c) different composition of concrete with the same size (110x220mm).

3.6 Conclusion

In this chapter, the microstructural disorder of our undamaged concretes has been characterized from an image analysis conducted on internal sections within concrete samples of different sizes and compositions. We have also performed the Autocorrelation Function analysis (ACF) on the scanned images of sample surfaces to analyze the internal structure of concretes. This work enabled us to estimate two values of the Autocorrelation lengths which were used to define the associated characteristic microstructural disorder length scales of our concrete specimens. Details are as follows:

- The global autocorrelation length, ξ_g , derived from the ACF analysis performed on the color image of sample surfaces (section 3.4) can be used to describe the internal microstructural disorder as a whole. Moreover, as displayed in Fig. 3.12a, a positive correlation of ξ_g with the maximum aggregate size, d_{\max} , enables us to indicate that the global autocorrelation length, ξ_g , can also be used to represent the structure of aggregates.
- The autocorrelation length, ξ_p , estimated from the ACF analysis realized on the binary image of pores (section 3.5) is considered as the characteristic length scale of the pore structure. As shown in Fig. 3.12c, a clear correlation between ξ_p and the product of the total porosity, p_o , and the maximum pore diameter, $d_{p,max}$, is observed. This demonstrates that the pore autocorrelation length, ξ_p , captures both the total numbers and the size of pores in hardened concrete sample.

An important result obtained in this chapter is that both the global, ξ_g , and the pore, ξ_p , autocorrelation lengths as well as the corresponding integral ranges $X_{0,g}$ and $X_{0,p}$ are (i) independent of the sample size and (ii) much smaller than the smallest sample size, whatever the type of concrete. (Kanit et al., 2003) argued that the integral range of a microstructure is an adequate measurement of the corresponding RVE size. Hence, our results indicate that all samples tested in this work, including the smallest ones, are larger than the RVE of the corresponding concrete in terms of microstructure and disorder.

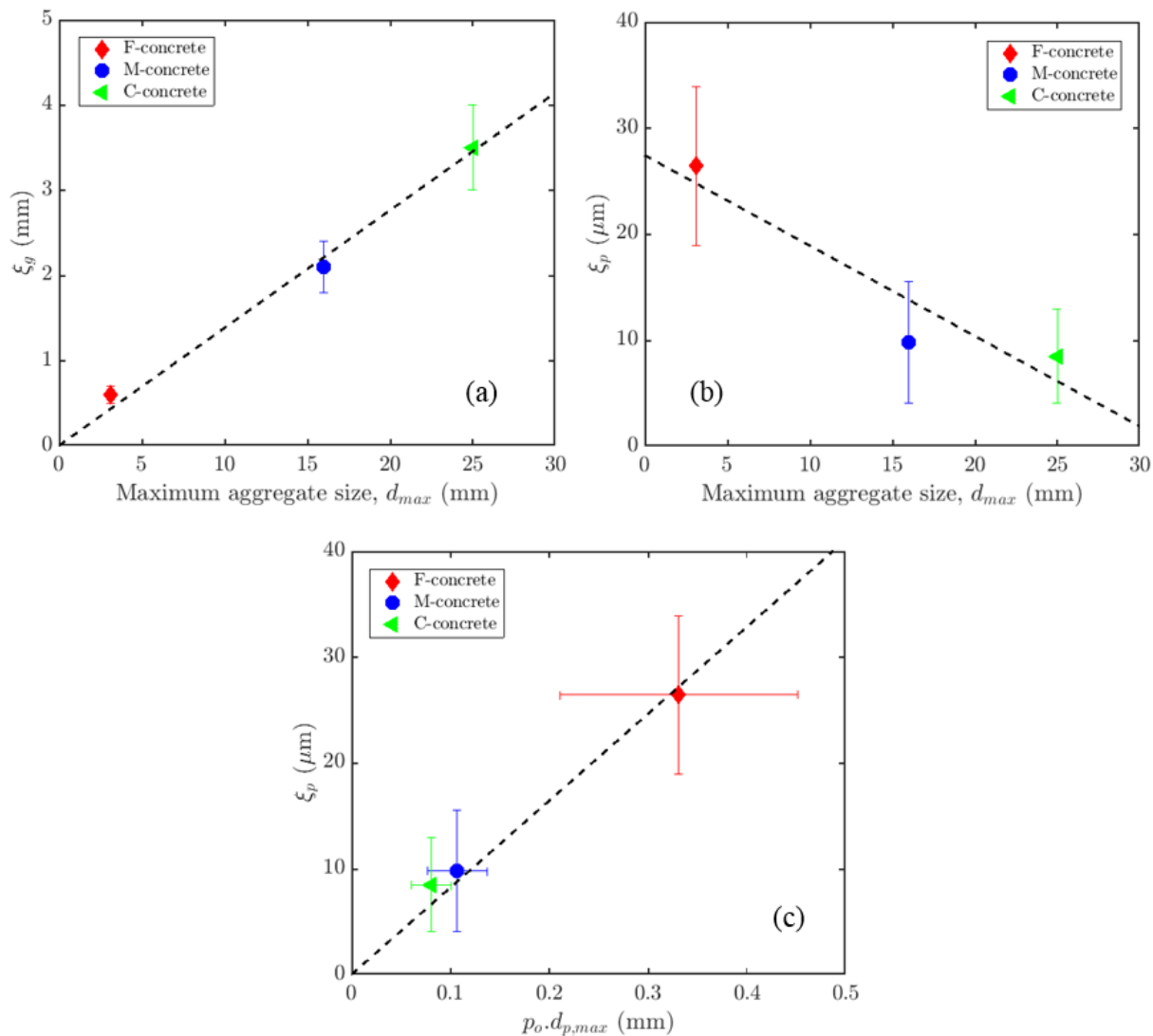


Fig. 3.12. Relationship between the autocorrelation length (a) ξ_g and the maximum aggregate size, d_{max} ; (b) ξ_p and d_{max} ; and (c) ξ_p and the product of the porosity, p_o (absolute value) and the maximum pore diameter, $d_{p,max}$. Black dashed-lines are the linear fits.

Chapter 4

Properties of hardened concrete samples²

4.1 Introduction

As a multiphase heterogeneous material, the response of concrete to applied stress is a result of complex interactions and is affected by various factors (Mazars et al., 1991). According to (Mehta and Monteiro, 2006), these factors can be classified into four categories: (1) characteristics and proportions of materials, (2) curing conditions, (3) loading parameters, and (4) specimen parameters.

Within each concrete mixture, all the samples were produced from the same batch as well as using the same casting and curing process (section 2.3). As an identical loading protocol was applied for all the tests (section 2.4), we can neglect the influence of the loading parameters on compressive strength. Regarding specimen parameters, this includes the sample size, and geometry, the microstructural characteristics, the density and the moisture state of hardened concrete (Jeulin and Ostoja-Starzewski, 2001; Mehta and Monteiro, 2006; Torquato, 1991). As all our cylindrical concrete samples were prepared with a constant of height/diameter ratio ($h/\phi = 2$), the effect of specimen geometry is thus ignored in this study. The microstructural characteristics of our concretes have been already investigated in the previous chapter. Therefore, in continuation of the characterization of the sample parameters, this chapter is devoted to examine the density and moisture state as well as the elastic Young's modulus of

² The content of this chapter has been presented in the article:

Vu, C. C., Plé, O., Weiss, J., Amtrano, D. (2018), Revisiting the concept of characteristic compressive strength of concrete, submitted to *Cement and Concrete Research*.

the hardened concrete samples. The influences of sample size and microstructure on these properties are also described.

4.2 Density

Before each loading test, the dimensions and the weight of the sample were measured. An average diameter, ϕ , was computed from six measures (two for each end of sample and two in the middle of the sample length). The average length, h , was obtained from three measurements. Following the standard (NF EN 12390-7, 2012), the density, ρ , of the hardened concrete sample is simply given by:

$$\rho = \frac{m}{V} \quad (4.1)$$

where m is the mass of the concrete sample and V the volume ($V = h \frac{\pi \phi^2}{4}$).

Fig. 4.1a shows the mean density and its standard deviation for all concrete samples. It is observed that: (i) for a given concrete mixture, the densities for all sample sizes are similar. In other words, there is no significant sample size effect on density; (ii) there is a clear correlation between the density and the aggregate gradation (F-, M- and C-concretes) (see Fig. 4.1a and Table 4.1), with an increasing density when increasing the aggregate size, as expected; and (iii) the densities range from 2180kg/m³ to 2400kg/m³, i.e. all our concrete samples comply with the definition of normal-weight concrete (EN 1992, 2004; Mehta and Monteiro, 2006; Neville, 2004; NF EN 206-1, 2004).

4.3 Moisture content

In hardened concrete, water is presented in various states: (i) chemically bounded water within the hydration products, (ii) adsorbed or physically bounded water in gel pores (gel water), and (iii) free water in capillary pores (capillary water) (Hilsdorf, 1967). These different types of water content control the moisture state inside hardened concrete samples and have a considerable effect on the mechanical properties of concrete (Bartlett and MacGregor, 1994; Mehta and Monteiro, 2006; Neville, 2004). In general, the moisture content, which depends on the microstructural characteristics of the material and environmental conditions such as temperature, relative humidity, and air velocity (Mehta and Monteiro, 2006), is used to quantitatively characterize the moisture state of concrete.

In this study, the moisture content, w_c , of the concrete samples was investigated from the following procedure:

- 1- After loading, 10 deformed concrete samples were collected for each sample size and each concrete mixture, and weighted. This weight is noted m_1 ;
- 2- The deformed concrete samples were kept in a drying oven at $(105\pm 5)^\circ\text{C}$ for a minimum duration of 3 days, according to the regulation (NF EN 12390-7, 2012). After this 3-days period, the mass of the dried specimens was measured every 2 hours. When no significant change of the mass was detected over three consecutive measurements, the sample was considered as totally dry and its weight called m_2 ;
- 3- The moisture content of hardened concrete sample is defined as the mass ratio of water to solid phases in the sample (Ifsttar, 1994): $w_c = \frac{(m_1 - m_2)}{m_2} \times 100\%$

The mean value and standard deviation of moisture contents for all concrete samples are displayed in Fig. 4.1b. For a given concrete group, no significant sample size dependence can be observed. In contrast with the density (see Fig. 4.1a), the largest moistures are observed for the F-concrete (see Fig. 4.1b and Table 4.1). The moisture content is generally affected by the environmental humidity, the cement content and the porosity of the hardened cement paste (Mehta and Monteiro, 2006). In our case, all loading tests were performed on the concrete samples during a short period (an average of 50 loading tests per day). Hence, the environmental conditions can be considered similar for all of concrete samples. The F-concrete was prepared with the largest water-to-cement ratio in the mix (see Table 2.1), possibly hold the more water free in the hardened sample after the hydration process (see section 3.5). This is the main reason to explain why the F-concrete samples show the highest moisture content.

Compressive strength is known to increase with decreasing moisture in hardened concrete (Neville, 2004; Pihlajavaara, 1974). However, owing to the low moisture contents ($< 5.5\%$) observed in our concrete samples (see Table 4.1), this factor is not expecting to play a significant role on strength in this study (Bartlett and MacGregor, 1994; Neville, 2004).

Table 4.1. Density and moisture content of three different concrete mixtures

Concrete mixture	Density, ρ (kg/m ³)		Moisture content, w_c (%)	
	Mean	SD	Mean	SD
F	2184.0	20.5	5.3	0.4
M	2391.4	14.7	3.2	0.2
C	2403.8	18.2	3.2	0.3

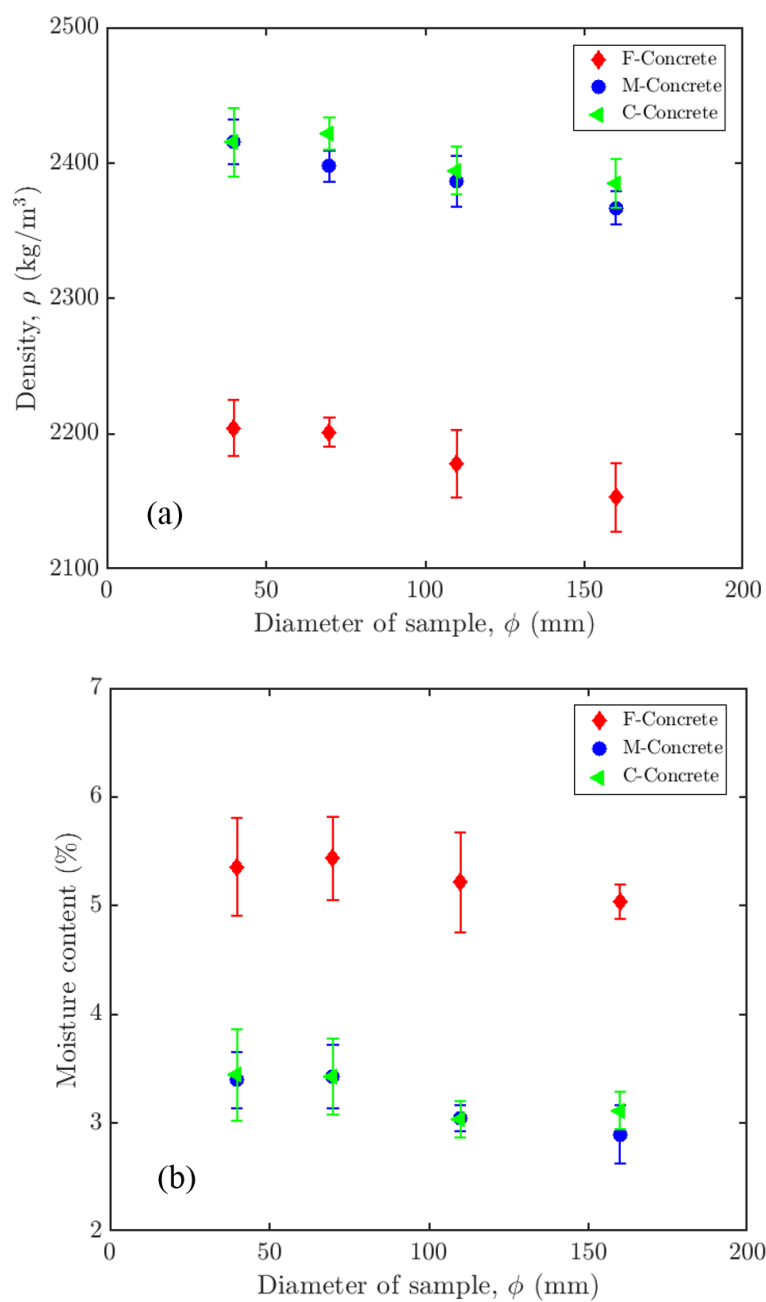


Fig. 4.1. Properties of hardened concrete samples as a function of the sample diameter: (a) Density; (b) Moisture content.

4.4 Elastic Young's modulus

As presented in Chapter 3, the internal characteristic length scales are independent of the sample size and much smaller than the smallest sample size, regardless of concrete mixture. This means that all tested specimens are statistically representative for the microstructure of our concretes. Therefore, linear properties, and particularly effective elastic properties, should be size-independent (Kanit et al., 2003). We test this idea here from the study on the modulus of elasticity, one of the important elastic properties in terms of structural design, quality assurance and quality control of concrete structures. This study covers both the static and dynamic elastic (Young's) moduli as well as the relationship between them.

4.4.1 Static modulus of elasticity

The static elastic Young's modulus is defined as the ratio of axial stress to axial strain for a material subjected to uniaxial load (Neville, 2004). Various estimation of this static modulus from the stress-strain curve have been proposed, such as the secant modulus (ACI 318-05, 2005; EN 1992, 2004; NF EN 12390-13, 2014), the chord modulus (ASTM C469/C469M-14, 2014) or the tangent modulus (Fib Mode Code, 2013; Mehta and Monteiro, 2006). In this work, both the tangent and secant elastic moduli for all concrete samples were determined. The deformation of a concrete specimen is calculated as the ratio of the displacement, Δ_{sp} , (see section 2.4) to the specimen height ($\varepsilon = \Delta_{sp}/h$). An example of a stress-strain curve for our concrete samples is displayed in Fig. 4.2.

In order to estimate the tangent elastic modulus of concrete, we defined the tangent modulus, $(Y_t)_i$ at a data point i from a differentiation of the stress-strain curve:

$$(Y_t)_i = \frac{\sigma_{i+1} - \sigma_i}{\varepsilon_{i+1} - \varepsilon_i} \quad (4.2)$$

A 40 data points moving average of this $(Y_t)_i$ curve was then performed, and the maximum value of this moving average is taken as the tangent modulus, Y_t , of the concrete sample examined (see Fig. 4.2). The values of tangent moduli, Y_t , for different sizes and compositions of concrete are shown in Fig. 4.3.

In this study, the secant modulus, Y_s was calculated by the slope of a line drawn from the origin to 40% of the peak stress (EN 1992, 2004). The variations of secant moduli, Y_s , with sample size for the three concrete mixtures are presented in Fig. 4.4a. As shown in Fig. 4.4b, the secant modulus, Y_s , is observed to be approximately equal to the tangent modulus, Y_t ,

regardless of concrete mixture and sample size, meaning that below 40 % of the peak load, all our concretes remain essentially in the elastic stage.

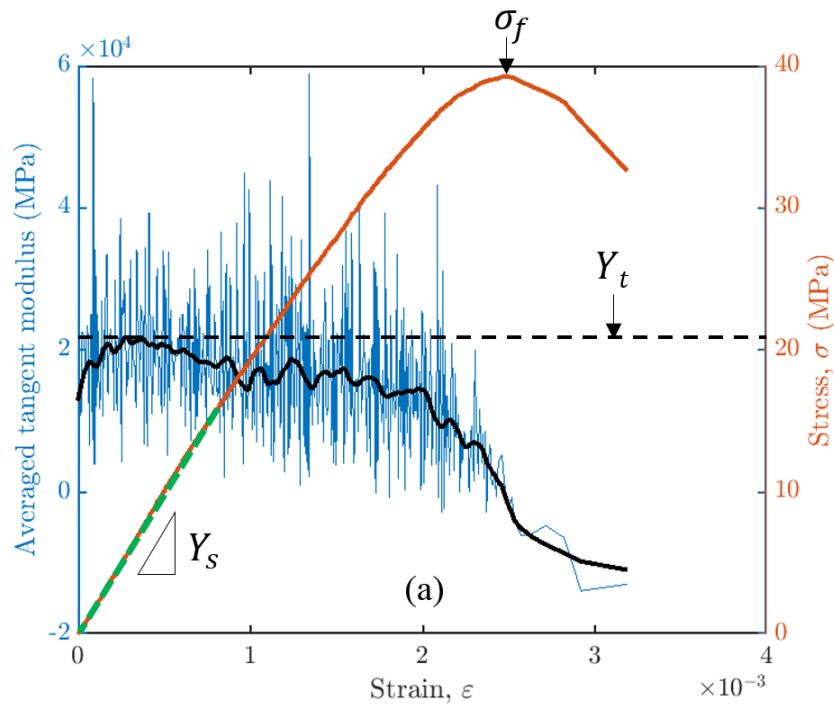


Fig. 4.2. Illustration of the methods of estimation of the tangent elastic modulus (Y_t), where the red curve is the stress-strain curve, the blue curve is 5Hz differentiated stress-strain curve ($d\sigma/d\varepsilon$) and the solid black curve is the 40-point moving average of the blue curve; and of the secant elastic modulus (Y_s) which is calculated by the slope of a line (dashed green line) drawn from the origin to 40% of the peak stress σ_f .

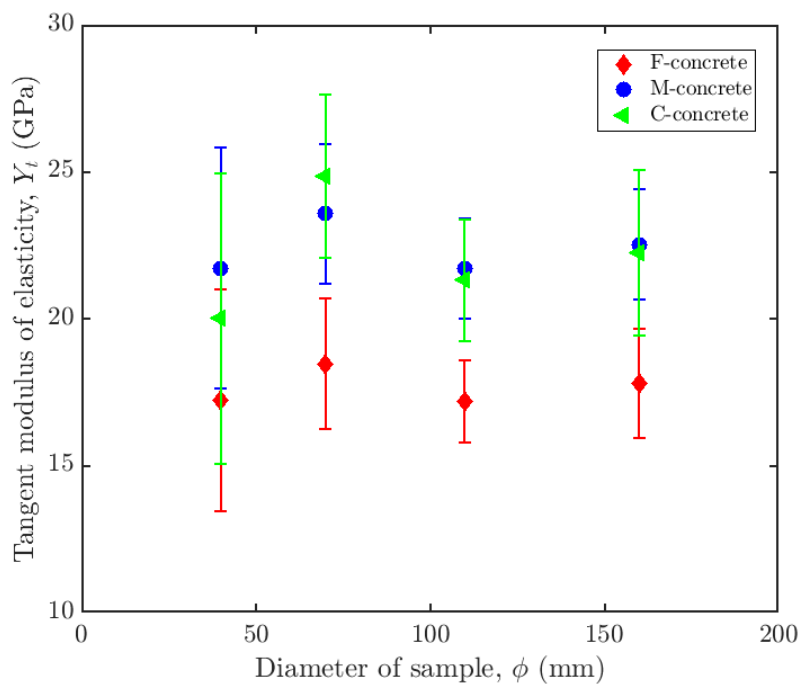
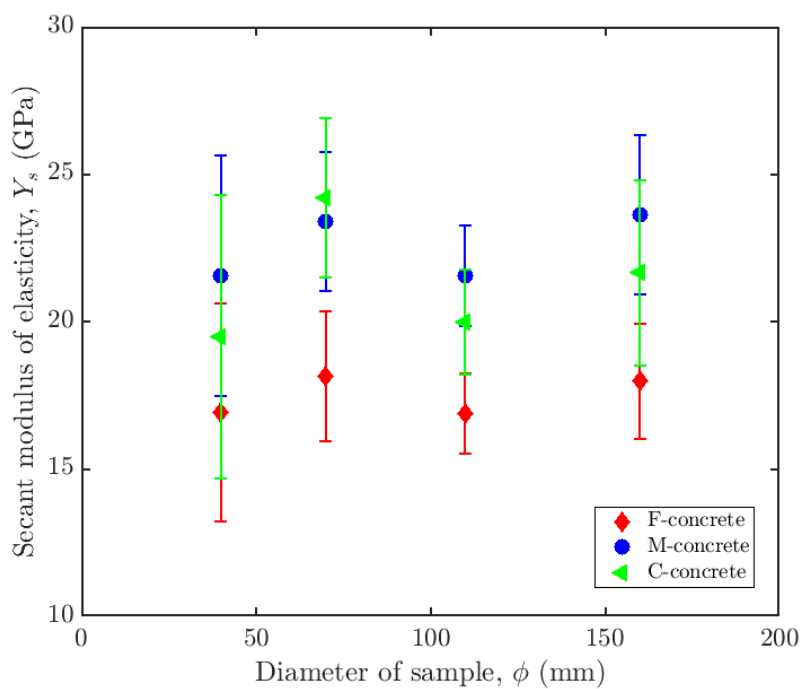
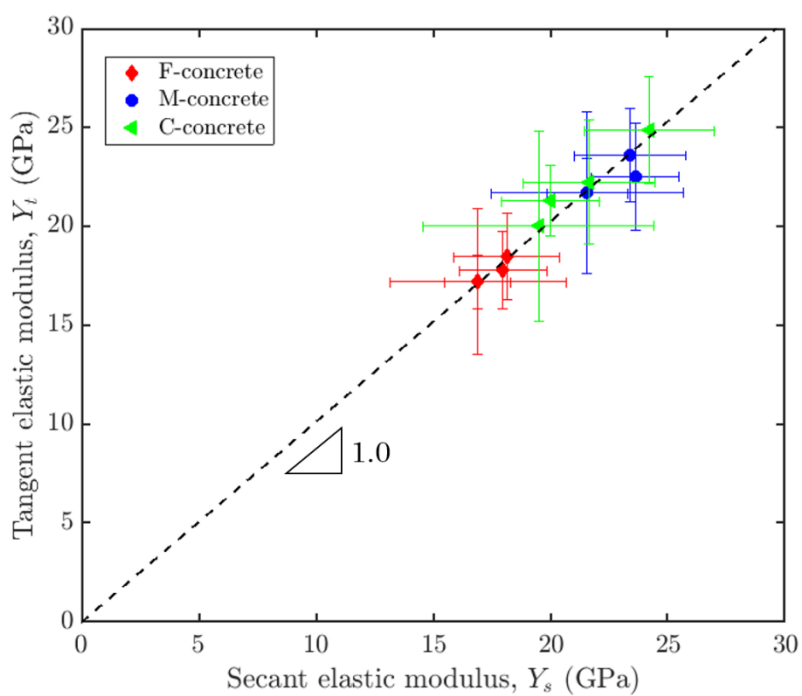


Fig. 4.3. The values of tangent elastic moduli, Y_t , for all of concrete samples.



(a)



(b)

Fig. 4.4. The values of static elastic moduli for all concrete samples: (a) Secant modulus, Y_s ; and (b) The relationship between the secant modulus, Y_s , and tangent modulus, Y_t .

4.4.2 Dynamic modulus of elasticity

According to (ASTM C597-02, 2002), the dynamic Young's modulus of concrete can be estimated from the P-wave velocity, V_p , of a compression wave travelling through an elastic concrete body, the Poisson's ratio, ν , and the density of the concrete sample, ρ :

$$Y_d = V_p^2 \left[\frac{\rho(1 + \nu)(1 - 2\nu)}{1 - \nu} \right] \quad (4.3)$$

In this study, based on the principles of ultrasonic testing described in (ASTM C597-02, 2002), the transit time, Δt , of the P-wave through the concrete sample was measured by using an Acoustic Emission (AE) equipment. The velocity, V_p , was then calculated as $V_p = h/\Delta t$. These non-destructive measurements were carried out on undamaged concrete samples before compression testing. Three samples were selected from each size and type of concrete, for a series of 36 AE tests performed. A couple of piezoelectric transducers (AE sensors) with a frequency bandwidth of 20-1200 kHz was used to detect the P-wave arrival. A sketch of the testing equipment is shown on Fig. 4.5.

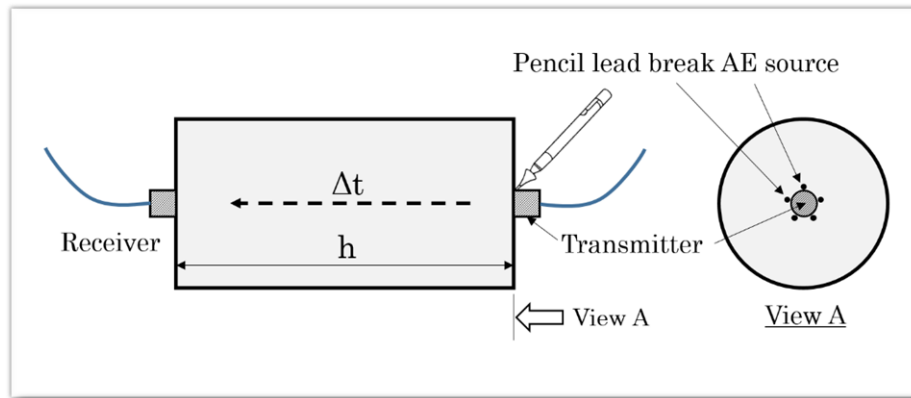


Fig. 4.5. Testing equipment for the acoustic pulse velocity measurement

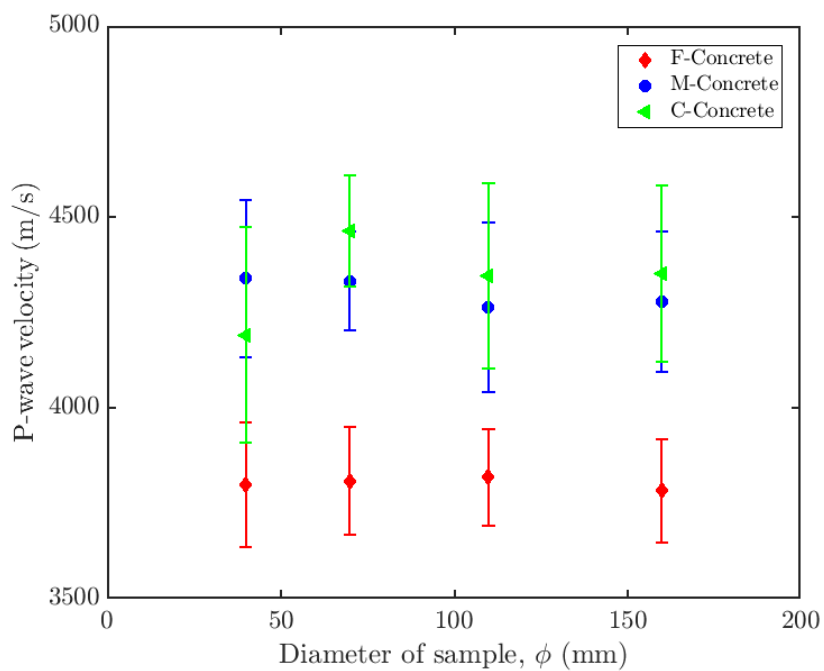
Pulses of longitudinal stress waves were generated by breaking a pencil lead (AE source) very close to one of two AE sensors (see Fig. 4.5). The remaining AE sensor, acting as a “receiver”, then picked up a signal due to the propagated stress waves at the opposite end of the concrete cylinder (see Fig. 4.5). Δt was calculated from the difference of arrival time of the P-wave between the two sensors. Five different pencil lead break tests were performed around each of the AE sensors (see Fig. 4.5 - view A), for a total of 10 values of P-wave velocity determined for each concrete sample. As the S-waves were hardly distinguishable from the P-

waves on the AE waveforms, the measurement of the shear modulus, and so of the Poisson's ratio, was not possible. To estimate the Young's modulus from Eq. (4.3), a value $\nu = 0.18$ was considered for all concrete samples (in agreement with ASTM standards falling between 0.15 and 0.20 (ASTM C597-02, 2002; Mehta and Monteiro, 2006; Neville, 2004)) and the measured values of density ρ (reported in Table 4.1) were used. P-wave velocities and dynamic elastic moduli for different sizes and compositions of concrete specimens are presented in Fig. 4.6a and b, respectively.

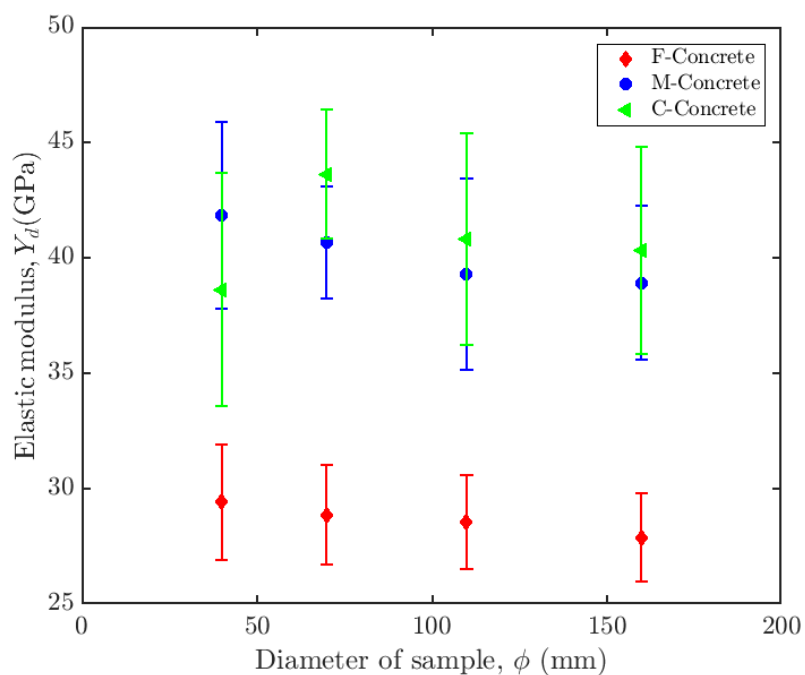
As expected, the highest values of both the mean and the associated variability of the P-wave velocities (Fig. 4.6a), static (Fig. 4.3) and dynamic elastic moduli (Fig. 4.6b) are observed for the coarser materials (M- and C-concretes), while the smallest values are obtained for the finer ones (F-concrete). The values of these properties for the three different concrete mixtures are summarized in Table 4.2. For a given concrete mixture, we did not observe any significant size effect on mean elastic moduli or their standard deviations. This absence of sample size effect on the elastic properties means that all the concrete samples tested, including the smallest ones (40x80mm-samples), are large enough in terms of microstructural characteristics to be statistically representative of the linear (e.g. elastic) mechanical properties of the materials.

Table 4.2. Elastic properties of the three concrete mixtures

Concrete group	Velocity,		Static elastic modulus				Dynamic elastic modulus,	
	V_p (m/s)		Y_t (GPa)		Y_s (GPa)		Y_d (GPa)	
	Mean	SD	Mean	SD	Mean	SD	Mean	SD
F	3803.0	141.1	17.7	2.3	17.5	2.5	28.7	2.2
M	4308.1	189.8	22.4	2.5	22.3	2.9	40.4	3.7
C	4342.5	243.7	22.0	3.1	21.2	3.8	40.9	4.6



(a)



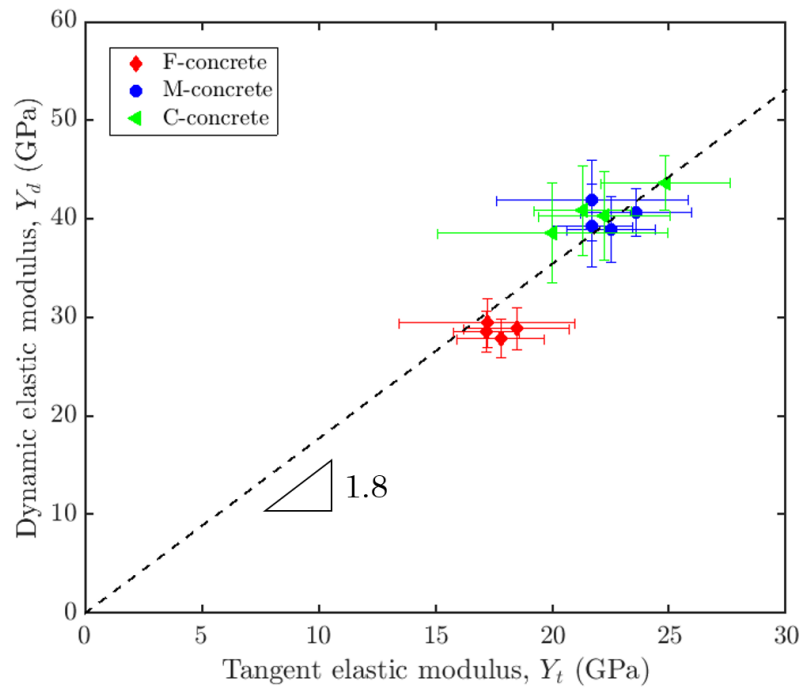
(b)

Fig. 4.6. Size-dependent of the elastic properties of concretes: (a) P-wave velocity; (b) Dynamic modulus of elasticity.

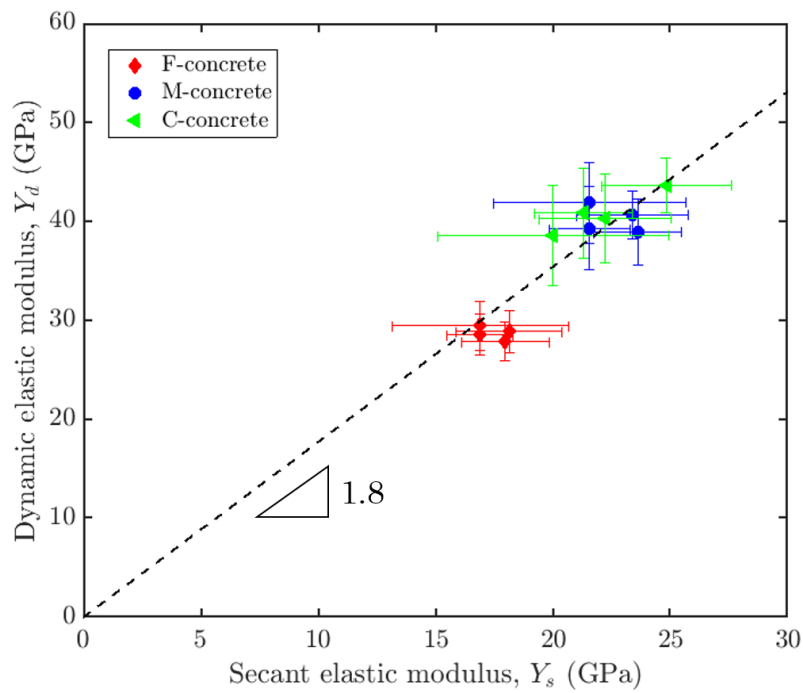
4.4.3 Static versus dynamic elastic moduli

On Fig. 4.7, the dynamic elastic modulus, Y_d , is observed to be systematically larger than both the static moduli Y_t and Y_s , regardless of sample size and concrete mixture, with a proportionality coefficient of 1.8 ($Y_d \sim 1.8Y_{t,s}$). Nevertheless, it is noteworthy that the values of both static elastic moduli, Y_t and Y_s , in this study were obtained from the deformation of the whole length of the concrete sample (see section 2.4). As recommended in (RILEM TC 148-SSC, 2000), the strain should be measured over the central third of the specimen length for a proper determination of static moduli $Y_{t,s}$. On the other hand, (Mansur et al., 1995) demonstrated that the static elastic modulus estimated by the strain measured from the central region of the concrete specimen is approximately 1.35 times higher than the strain measured between the loading platens (as in our case). Hence, if we use the correction factor of 1.35 for the all values of $Y_{t,s}$, the linear relation in Fig. 4.7 becomes $Y_d \sim 1.33Y_{t,s}$. This is consistent with empirical relationships between static and dynamic moduli presented in (Lydon and Balendran, 1986; Neville, 2004).

By means of a nondestructive technique, the dynamic modulus is investigated before loading and so without microcracking occurring in the concrete sample during the measurement. As a result, the dynamic modulus samples the genuine elastic properties of the material, while the static modulus can be affected by permanent non-linear deformations resulting from damage and microcracking (Linger, 1963; Neville, 2004). Because of this, the dynamic modulus is considered to be approximately equal to the initial tangent modulus determined in the static test (Mehta and Monteiro, 2006; Neville, 2004). This explains why the elastic dynamic modulus, Y_d , (or initial tangent modulus) is generally higher than the elastic static modulus, Y_t and/or Y_s .



(a)



(b)

Fig. 4.7. The relationship between static and dynamic elastic moduli of concrete. (a) Y_t vs. Y_d ; and (b) Y_s vs. Y_d .

4.5 Conclusion

In this chapter, the density and moisture state as well as the elastic Young's modulus of our concrete specimens have been investigated. From the study results of these properties, the following conclusions can be drawn:

- For a given concrete group, the density and moisture content of the hardened samples were not affected by the sample size. This allows to conclude that all loading tests for each concrete mixture were performed under similar initial conditions.
- There is no significant dependence of elastic properties including both the static and dynamic elastic moduli, as well as the velocity of compression wave (P-wave), on the sample size within a given concrete mixture. These results are in full agreement with the former expectation that all samples, including the smallest ones, are statistically representative of the microstructure of our concretes (Chapter 3), and so are larger than the RVE for the linear (elastic) properties. In other words, there is no size effects on elasticity.
- The ratio of the dynamic modulus of elasticity to the static modulus for all specimens, regardless of concrete mixture and sample size, is always greater than unity. However, this ratio directly depends on the methodologies applied for measuring the deformation of specimens during the loading and for estimating the static elastic modulus. This means that there is no simple conversion between the dynamic modulus which is known as the genuine elastic modulus of the material, and an estimate of the static modulus which is used in structural design.

Chapter 5

Compressive failure of concrete as a critical phase transition

Based on

Vu, C. C., Amitrano, D., Plé, O., Weiss, J. (2018), Compressive failure as a critical transition: Experimental evidences and universality, submitted to *Physical Review Letters*. ArXiv preprint arXiv: 1807.06386.

Classical fracture and failure theories do not consider material disorder and assume a brutal failure without precursors. The role of internal disorder on fracture has been extensively analyzed over the last decades, mostly from theoretical and numerical models. Yet, the exact nature of the process remains highly debated. Here we show, from experimental data on an emblematic disordered material, concrete, that compressive failure can be interpreted as a critical transition between an intact and a failed state. The associated critical exponents are found to be independent of sample size and microstructural disorder and close to mean-field depinning values. Although compressive failure differs from classical depinning in several respects, including the nature of the elastic redistribution kernel, an analogy between the two processes allows deriving (finite)-size effects on strength that match our extensive dataset.

5.1 Introduction

Historically, fracture and failure theoretical frameworks or criteria, such as Griffith theory or the Coulomb failure criterion, do not consider material disorder. Consequently, they predict an abrupt global failure, without any precursory phenomenon. In that sense, failure can be interpreted as a first-order transition from an intact to a failed state (Alava et al., 2006; Girard et al., 2012). Materials heterogeneity has been however considered for a long time, especially to account for failure strength variability and associated size effects (Weibull, 1939a). Nevertheless, this weakest-link approach is based on strong assumptions such as the absence of mechanical interactions between defects and between rupture events, or a global failure dictated by the activation of the largest flaw (the weakest-link). These assumptions might appear reasonable for weakly disordered materials under tension, especially in the case of a pre-existing large crack or notch. However, in case of large enough disorder, the quasi-static propagation of such a crack can be interpreted as a dynamical critical transition (Barés et al., 2013; Bonamy et al., 2008; Bonamy and Bouchaud, 2011). The limitations of these classical frameworks appear even clearer for highly disordered un-notched systems and/or loading conditions stabilizing crack propagation, such as compression (through the presence of friction). In those cases, it is known for a long time that failure is a *process*, involving the nucleation, interaction, propagation and coalescence of many microcracks (Lockner et al., 1991; Reches and Lockner, 1994), hence characterized by precursory phenomena. The presence/absence of precursors to failure and faulting has obvious consequences in terms of natural hazards forecasting, for e.g. earthquakes (de Arcangelis et al., 2016; Jaumé and Sykes, 1999), cliff collapses (Amitrano et al., 2005) or landslides (Crosta and Agliardi, 2003).

The failure of heterogeneous media has been extensively studied over the last 30 years (Alava et al., 2006; Herrmann and Roux, 1990), essentially on the basis of theoretical and numerical models such as fiber-bundle (FBM) (Pradhan et al., 2010), random-fuse (RFM), random-spring (RSM) (Nukala et al., 2005), or progressive damage (PDM) (Amitrano et al., 1999; Girard et al., 2012, 2010) models. However, the nature of the associated transition remains controversial. In the limit of infinite disorder, fracture can be mapped onto the percolation problem (Roux et al., 1988). For bounded disorder, FBM with equal-load sharing, corresponding to a mean-field approximation, exhibit a critical behavior with the rate of bundle breaking per increasing stress diverging at the critical point (the failure) (Pradhan et al., 2010). A critical transition was also reported for a PDM of compressive faulting, with the average damage avalanche size, the correlation length of damage (Girard et al., 2010), or the largest

damage cluster (Girard et al., 2012), all progressively increasing during the loading history and diverging at failure. This interpretation is also consistent with a mapping of the faulting problem onto the depinning transition (Fisher et al., 1997). On the other hand, for RFM and RSM with large (but finite) disorder, the damage process was found to resemble percolation, i.e. to be uncorrelated up to the vicinity of failure, and then to brutally localize at failure, thus suggesting instead a first-order transition (Nukala et al., 2005, 2004). Besides the nature of the transition, this raises the question of the role of the disorder strength on failure precursors.

This debate calls for experimental data, which are still sparse and disparate. Power law distributions of acoustic emission (AE) energies released by damage and microcracking, $P(E) \sim E^{-\beta}$, have been frequently reported and presented as evidences of “criticality” in a broad sense. However, for highly porous (Baró et al., 2013; Nataf et al., 2014) or cellular (Mäkinen et al., 2015) materials under compression, the AE event rate dN/dt or the energy distribution do not exhibit significant trends as approaching failure, possibly as the result of a transient hardening mechanism (Baro et al., 2018), whereas the (stable) power law *pdf* of energies is accompanied by Omori-like aftershocks triggering. In contrast, in low-porosity rocks, a progressive localization of damage before faulting under compression has been revealed from either AE (Lockner et al., 1991; Schubnel et al., 2007) or X-ray tomography (Renard et al., 2018, 2017). In this last case, the damage rate, defined as the rate of increasing crack-induced porosity, as well as the size of the largest microcrack, were found to power-law diverge as approaching global failure, arguing for an interpretation of compressive faulting as a critical transition (Renard et al., 2018). Criticality was also argued for the flexural failure of composite materials from a divergence of the AE energy release (Guarino et al., 1998).

Despite these various hints, experimental studies are still lacking to ascertain this critical interpretation of compressive failure, to determine the critical exponents, to check their universal character and to precise the role of internal disorder. Finding more experimental evidences to support these points is the main purpose of this chapter.

The rest of this chapter is organized as follows. In section 5.2, a brief description of AE technique is presented. Section 5.3 details the experimental set-up including AE equipment and setting parameters for the AE measurements used in this study. From the experimental results, the critical behavior of compressive failure of concrete is investigated in section 5.4. Conclusion of this chapter are summarized in section 5.5.

5.2 Acoustic Emission measurement

5.2.1 Principles of Acoustic Emission technique

Acoustic Emission (AE) is a natural phenomenon that happens in a wide range of materials and structures under various kinds of stimulus (change in load, temperature, pressure, etc.) (Grosse and Ohtsu, 2008; Mindess, 2004; Pollock, 1989). According to the (ASTM E1316-06a, 2006), AE is defined as *"the class of phenomena whereby transient elastic waves are generated by the rapid release of energy from localized sources within a material, or the transient elastic waves so generated"*. Sources of AE vary from the initiation and growth of cracks, frictional sliding, slip and dislocation movements, and phase transformations in metals (Grosse and Ohtsu, 2008; Ohtsu, 2010; Ouyang et al., 1991; Vives et al., 1994). Based on the theory of elastic waves, the basic principle of AE technique is very similar to that used for earthquakes in seismology, but applied on a smaller geometric scale (range from some millimeters of sample up to several tenth meters of real structure) (Grosse and Ohtsu, 2008; Prosser, 2001), hence to much higher frequencies (hundreds of kHz to MHz for AE, Hz and below for earthquakes).

When a structure is subjected to a sufficiently large stimulus (e.g. stress), the elastic waves are released from the sources (e.g. due to cracking). These waves propagate through the elastic medium towards its surface and are then recorded by the transducers (AE sensors), previously placed on the surface of structure. These AE sensors allow to transform the detected stress waves into electrical signals. After pre-amplification, the AE signals are transmitted to the acquisition system and finally are stored for the analysis. The basic principle of the AE technique is illustrated in Fig. 5.1.

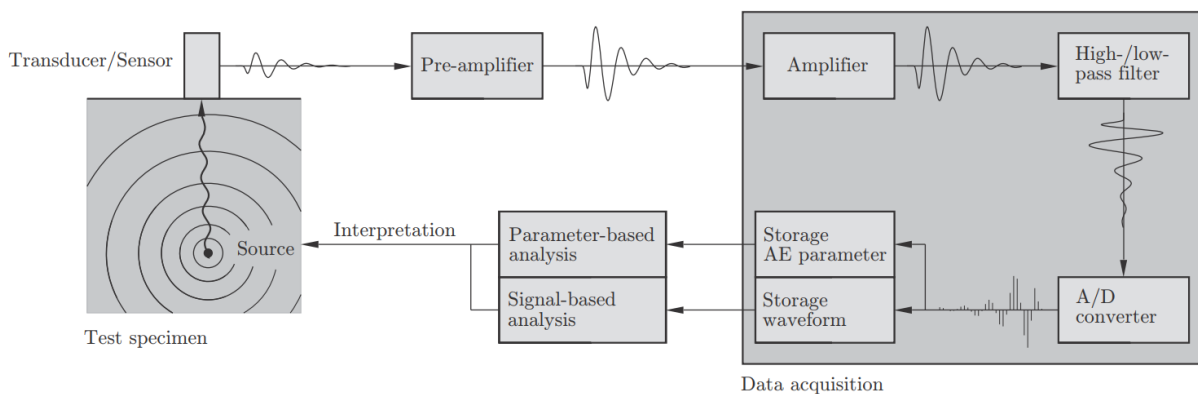


Fig. 5.1. Principle of recording procedure of Acoustic Emission signals (reprinted from (Kocur, 2012))

The AE technique can be considered as a non-destructive testing (NDT) method in the case of a material tested under a working load without any additional loads (Grosse and Ohtsu, 2008). For example, it has been applied as a NDT measurement for investigating the P-wave velocity of our concretes in section 4.4.2. However, unlike most other NDT methods (e.g. ultrasonic) which are implemented either before or after the damage occurs in the structure (Fig. 5.2b), the AE technique is usually applied during loading to track microcrack nucleation and propagation in the structure (Fig. 5.2a) (Grosse et al., 2003). If a defect is present but does not grow (or grows too slowly to generate inertial effects), no AE is received. The possibility of observing the damage process during the entire load history without disturbing the specimen is a crucial advantage of the AE technique in comparison with other NDT methods (Grosse et al., 2003; Grosse and Ohtsu, 2008).

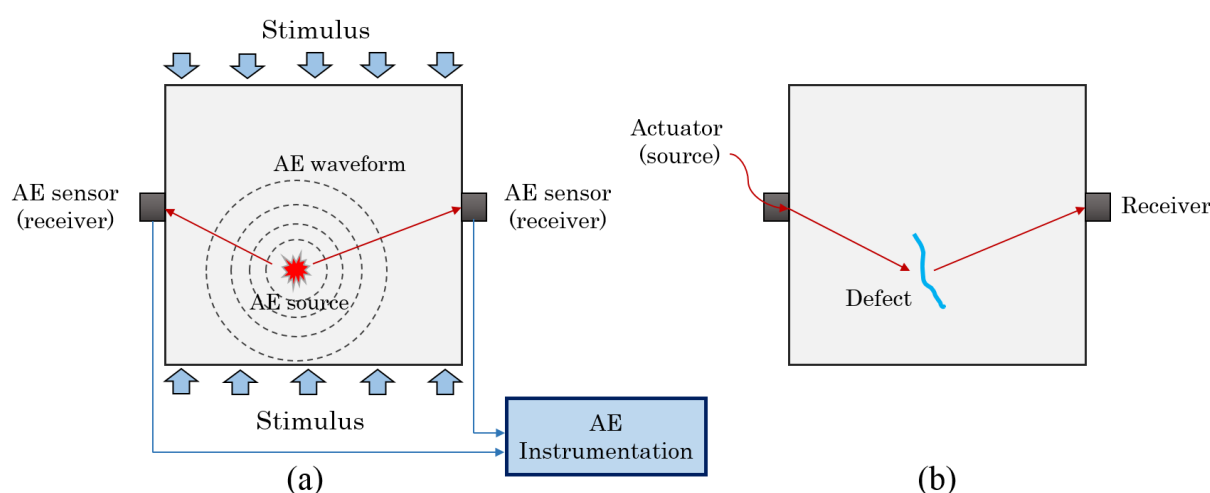


Fig. 5.2. AE versus other NDT methods (a) Principle of AE technique and (b) Principle of Soundwave-based NDT methods (e.g. ultrasound method).

5.2.2 Acoustic Emission signal parameter

When a waveform of an acoustic event reaches the surface of a structure, the AE signal is detected by the AE sensors. Two basic types of AE signals can be generated: continuous and burst (transient) signals (Fig. 5.3). Continuous signals may originate from undesired sources such as mechanical rubbing in the testing systems, environmental noises, etc. Burst-type emissions originate from a variety of sources, but primarily involve some form of damage (e.g. crack) growth as observed in a sample (Mindess, 2004). Therefore, the first step in AE detection is the setup of a threshold level in voltage amplitude (see Fig. 5.4). Consequently,

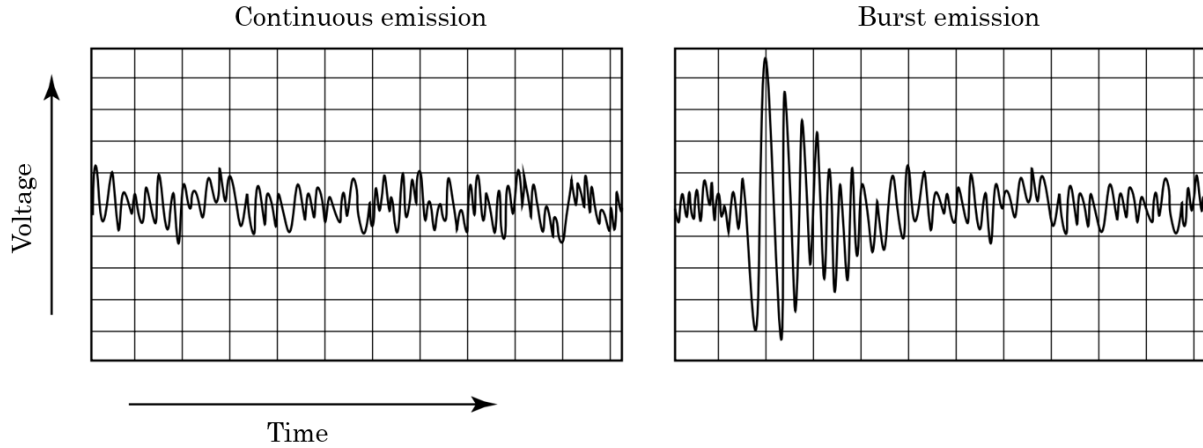


Fig. 5.3. Continuous and burst AE signal (after (Wevers and Lambrighs, 2009)).

only signals overcoming the threshold are detected as AE events while the signals below are considered as the background noise.

The AE signal parameters which are extracted from the AE signals with respect to the threshold setting are depicted in Fig. 5.4. According to the definitions introduced in (ASTM E1316-06a, 2006; Grosse and Ohtsu, 2008; Mistras, 2001), the most widely used AE signal parameters are defined as follow:

- **Hit**: a signal that exceeds the threshold and causes a system channel to record data. In Fig. 5.4, one waveform corresponds to one “hit”;
- **Counts**: the number of times the AE signal exceeds a preset threshold during any selected portion of a test;
- **Amplitude**: the highest peak voltage attained by an AE waveform. The AE amplitudes are expressed on a decibel (logarithmic) scales as follow:

$$\text{Signal peak amplitude (dB)} = 20 \log_{10} \left(\frac{V_{max}}{V_{ref}} \right) \quad (5.1)$$

where:

$V_{ref} = 1\mu V$ is the reference voltage at the sensor output (before amplification)

V_{max} = the peak voltage of the measured AE signal

In the present work, peak amplitudes exceeding a defined threshold value are considered as AE events, and signals below the threshold are considered as noise.

- **Duration:** the elapsed time from the first threshold crossing to the last. The duration is directly measured in microseconds;
- **Rise time:** the time from the first threshold crossing to the peak amplitude of the AE signal. Governed by wave propagation processes between the source and the sensor, this parameter can be used for several types of signal qualification or noise elimination;
- **Energy:** the total elastic energy released by an emission event. AE energy can be measured using two different methods (i) the Measured Area under the Rectified Signal Envelope (MARSE) - relative energy (see Fig. 5.4) and (ii) an absolute energy. In the MARSE technique, the relative value of energy is proportional to the true measure of the total energy of an AE hit. The absolute energy is a true energy of an AE hit measured in attoJoule (aJ). This energy is derived from the integral of the squared voltage divided by the reference resistance over the duration of the AE waveform packet (Mistras, 2001; Pollock, 1989). The absolute energy is recorded and used in our analysis throughout this study.

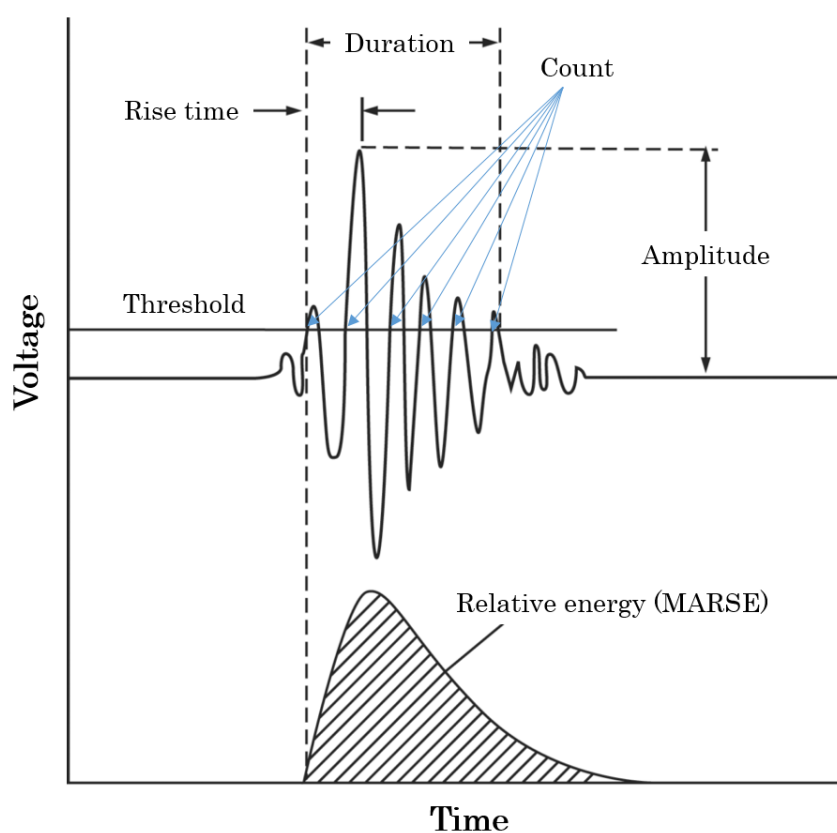


Fig. 5.4. Schematic diagram of AE parameters (modified from (Pollock, 1989)).

5.3 Acoustic Emission experimental work

This section describes the details of the AE experimental work based on the combination of uniaxial compression tests with AE measurements. Hereafter, this kind of experiment is referred as an AE test. As a part of a total of 527 loading experiments (section 2.4), 30 concrete samples with different sizes and compositions were used for the AE tests. For a given concrete mixture, four AE tests for 40-mm samples and two tests for 70-, 110- and 160-mm samples, were performed in this study. In this section, we firstly explore the specified aspects of the main AE equipment, then highlight some noteworthy parameters that need to be set up before performing an AE experiment, and finally the testing procedure is introduced.

5.3.1 Acoustic Emission equipment

Generally, the main AE instrumentation consists of transducers (AE sensors), a set of amplifiers, a signal acquisition-processing device, a personal computer (PC), as well as connecting coaxial cables and analysis software (Mistras, 2001). A simple layout of AE measurement chain is illustrated in Fig. 5.1. In this research, the AE system used is the MISTRAS-2001 AE system manufactured by Physical Acoustics Corporation (PAC). In what follow, we describe some specific aspects of the main components of this AE system used throughout this study.

5.3.1.1 Acoustic Emission sensors

A crucial element in the AE equipment is the transducer (sensor). The main function of AE sensors is to convert the surface displacements generated by elastic waves into an electrical signal for processing by the measuring equipment. The schematic diagram of a typical AE sensor used in AE tests is shown in Fig. 5.5.

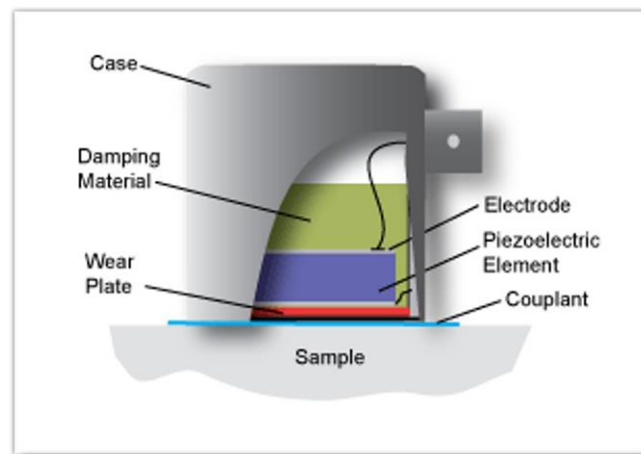


Fig. 5.5. A cut-away of a typical piezoelectric AE sensor (source: NDT Resource Centre).

The active element of a AE sensor is a thin disk of piezoelectric material which is generally a special ceramic such as lead-zirconate-titanate (PZT) (Grosse and Ohtsu, 2008; Ohtsu, 2015; Pollock, 1989). In this study, the wide-band AE sensors of type PICO produced by PAC were used. They allow to measure in the frequency range from 10 kHz up to 1.85 MHz with a peak frequency of approximately 900 kHz (Fig. 5.7). In particular, their small size (Fig. 5.6) and light weight (1 gram) make them easy to couple on our small samples (i.e. 40-mm samples in our case).

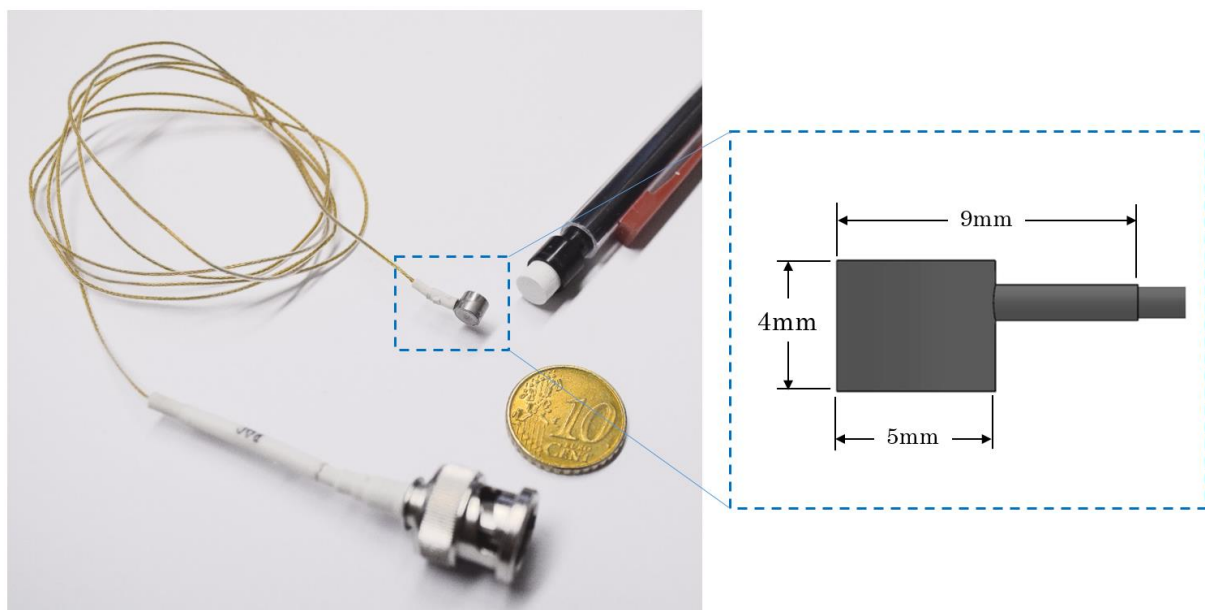


Fig. 5.6. Wide-band AE sensor of type PICO used in this work and its dimensions.

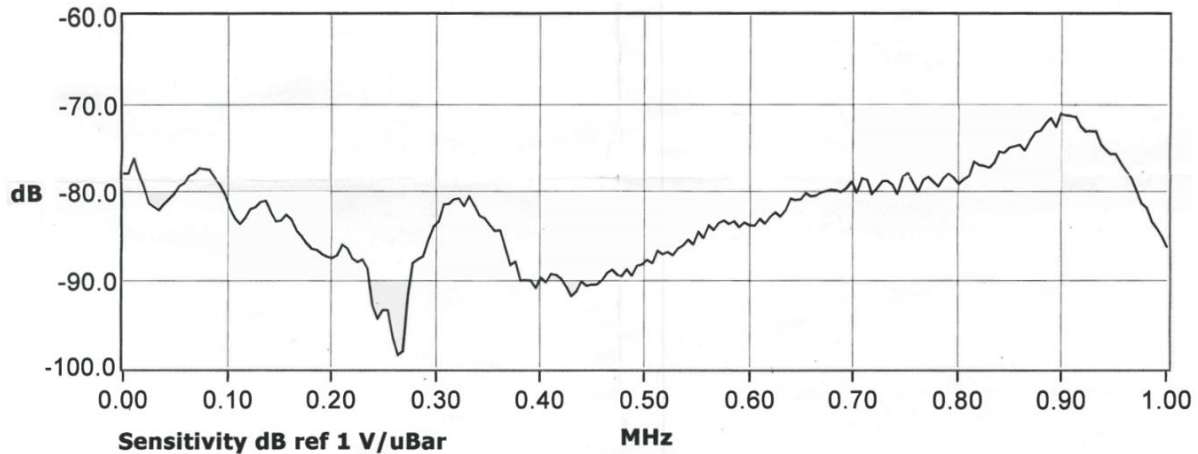


Fig. 5.7. Manufacturer's calibration certificate for an example of AE sensor of type PICO used in this research.

5.3.1.2 Coupling of transducers

A correct coupling of the AE sensors to the surface of the sample is very important for obtaining a good signal transmission. During the test, the long term stability of the couplant and the environmental conditions, should be considered to select the right couplant for the AE test (ASTM E650–97, 1997). There are several types of couplant used for AE testing such as liquid, gel, grease and adhesive glue. Here we used the Silicone adhesive glue (Silcoset 151) for coupling the AE sensors with the concrete samples, because it can provide a thin layer and easily removes any air gap at the interface between the sensor and the sample surface. This kind of couplant allows to obtain an excellent sound transmission which is comparable with greased based, but offers an easier sensor removal after the testing (Theobald et al., 2008). Moreover, this silicone adhesive glue also works very well on rough surfaces (like lateral surface of concrete sample) and has a good resistance to bond failure if surface displacement occurs during the test. Hence, it is more suitable than the gel or liquid couplants for vertical coupling application in our case.

In order to ensure a proper coupling, the contacting surface between the AE sensors and the sample should be planar, smooth and clean before its application. For this aim, some small areas on the lateral surfaces of the samples were ground and polished by an angle grinder with less and less grit size of metal-bonded discs.

For the purpose of recording the AE signals, a set of 2 AE sensors were coupled opposite to each other on the smallest samples (40x80 mm) (see Fig. 5.8a), while 4 AE sensors were

used for the larger samples (70x140 mm, 110x220 mm and 160x320 mm) (see Fig. 5.8b). The coupling position of AE sensors is shown in Fig. 5.8.

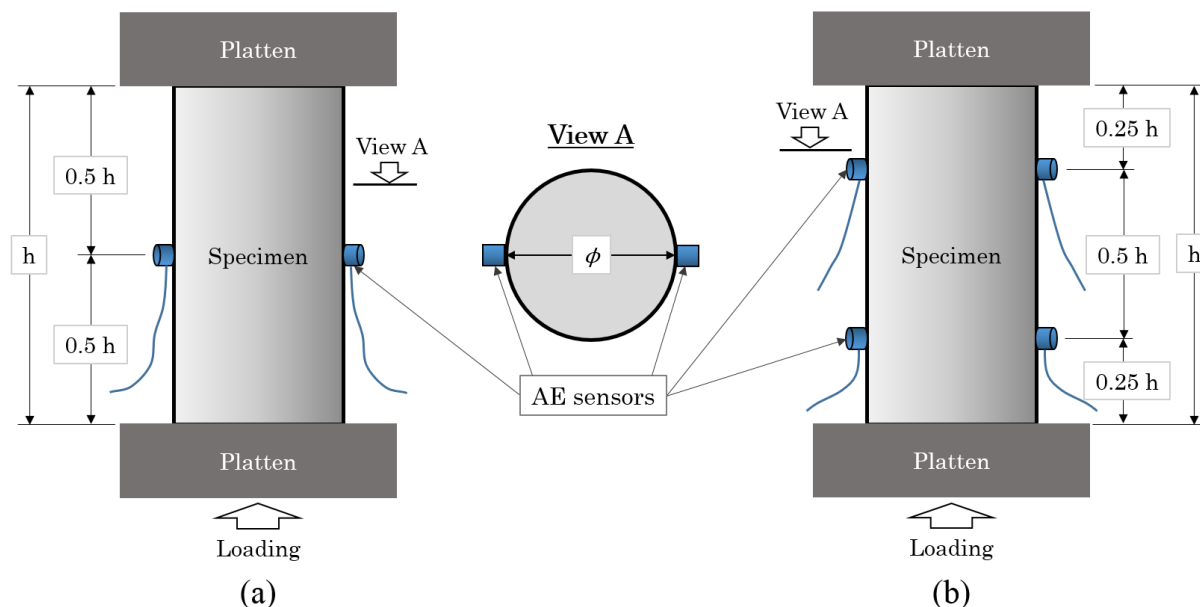


Fig. 5.8. Coupling position of AE sensors: (a) for the smallest size (40x80-mm samples) and (b) for the larger sizes (70x140-mm, 110x220-mm and 160x320-mm samples).

5.3.1.3 Acoustic Emission preamplifier

Because the AE signals detected by AE sensor are weak, they are generally amplified by a preamplifier, and then processed by a data acquisition system (Mistras, 2001; Ohtsu, 2015). A gain of preamplifier employed for concrete is around 40-60 dB and a band-pass filter 10 kHz - 2 MHz is recommended (Ohtsu, 2015). Here we used the 2/4/6 preamplifier produced by PAC for our AE tests. This preamplifier has gains of 20 dB, 40 dB and 60 dB and a filter frequency range of 10-2000 kHz. A gain of 40 dB was applied in all the experiments.

5.3.1.4 Data acquisition system

The AE signals from the loaded specimen are converted into electrical signals by the AE sensors, then amplified by preamplifiers and recorded by the Acoustic Emission Digital Signal Processor (AEDSP-32/16) cards. This kind of AEDSP board provides a wide bandwidth ranging from 10 kHz to 2 MHz. In this study, a sampling rate of 4 MHz was fixed for all the tests. A parametric input is an external voltage proportional to test parameter (i.e. external load in this study), which is recorded simultaneously with the AE signals.

The MISTRAS-2001 system is equipped with software packages named AEWin to collect and process data. The AEWin runs and records the AE signals while the testing is

performed. Before starting an AE experiment, some parameters have to be defined in order to provide the AEWin software with the correct information to extract the AE parameters. Further details about these specific parameters are given in the following section.

5.3.2 Acoustic Emission test set-up parameters

As mentioned above, when recording the AE data using the AEWin software, several specific parameters have to be defined so as to provide the hardware setup of software before the testing. These hardware set-up parameters were then held into the file called “Layout” file that can be read only by the AEWin software. This layout file was used for all AE tests without any changes in the present study.

Hardware settings include the amplitude threshold, gain, sampling rate, pre-trigger, hit length, Peak Definition Time (PDT), Hit Definition Time (HDT) and Hit Lock-out Time (HLT). These variables can be set individually for each channel.

The threshold level applied in AE measurements is often 30-50 dB in concrete (Ohtsu, 2015, 2010), while for an equipment with a high sensitivity, a threshold in the range 25-35 dB is recommended (Mistras, 2001). In this work, the AE threshold level was set at 30 dB for all the AE tests.

PDT, HDT and HLT are the time parameters of the signal measurement process. The illustration of these parameters can be seen in Fig. 5.9. A proper set of time parameters enables a correct identification of individual AE signals. For this reason, we performed some Pencil Lead Break (PLB) tests which are similar to Hsu-Nielsen (H-N) pencil test described in (ASTM E976-10, 2010), on some concrete specimens to determine the timing parameters. Based on the measurement of the transit time Δt of the P-wave between two AE sensors placed on the two ends of cylindrical sample (see Fig. 4.5), the velocity of P-wave, V_p , is calculated as $V_p = h/\Delta t$, where h is the height of sample (more details for this test are described in section 4.4.2).

The correct value of PDT enables the system to determine the peak time (i.e. the rise time) of the signal (see Fig. 5.9). If it is too short, the AEWin software will chose an incorrect value of rise time. The value of *PDT* can be determined by dividing the AE sensors spacing (the diameter of sample, ϕ , in our case) by the value of V_p (Mistras, 2001) as follows:

$$PDT = \phi/V_p \quad (5.2)$$

The maximum measured value of V_p , of approximately 4400 m/s (see Table 4.2 and Fig. 4.6a), was observed on the C-concrete sample. For the smallest size (40-mm samples), the value of

PDT given by Eq. (5.2) is equal to $9.1 \mu\text{sec}$. In the MISTRAS-2001 AE system, the PDT is at least $10 \mu\text{sec}$ (Mistras, 2001). Consequently, we chose a PDT of $10 \mu\text{sec}$ for all the AE tests.

The HDT defines the duration that the acquisition system will wait to determine the end of a hit (see Fig. 5.9). In most PAC systems, the value of HDT must be at least twice as long as PDT and more than $20 \mu\text{sec}$. However, the HDT should be set as short as possible to reduce the risk that two separate events will be treated as a single hit (Mistras, 2001). Therefore, we used a HDT of $20 \mu\text{sec}$ in all the AE tests.

The HLT is the time that the system uses, having recorded a signal, to set itself up and be ready to record the following hit. The recommended value of $20 \mu\text{s}$ for most of AE system produced by PAC (Mistras, 2001) was chosen for HLT in this study.

Following the recommendation in (Mistras, 2001), for the setting of analog filter, the high limit is calculated by dividing the sampling rate by three. With a sampling rate of 4 MHz (section 5.3.1.4), we fixed the filter high to 1.2 MHz and the values of the filter low to 20 kHz. During the recording of the data using the AEWin software, all the sensors are automatically set up in an independent trigger mode, meaning that each channel has its own trigger. The pre-trigger values tells the software how long to record the waveform (in μsec) before the trigger point (or the point at which the threshold is exceeded). In this work, a pre-trigger value of $50 \mu\text{sec}$ was set up for all the channels. The value of other hardware set-up parameters used in this study are summarized in Table 5.1.

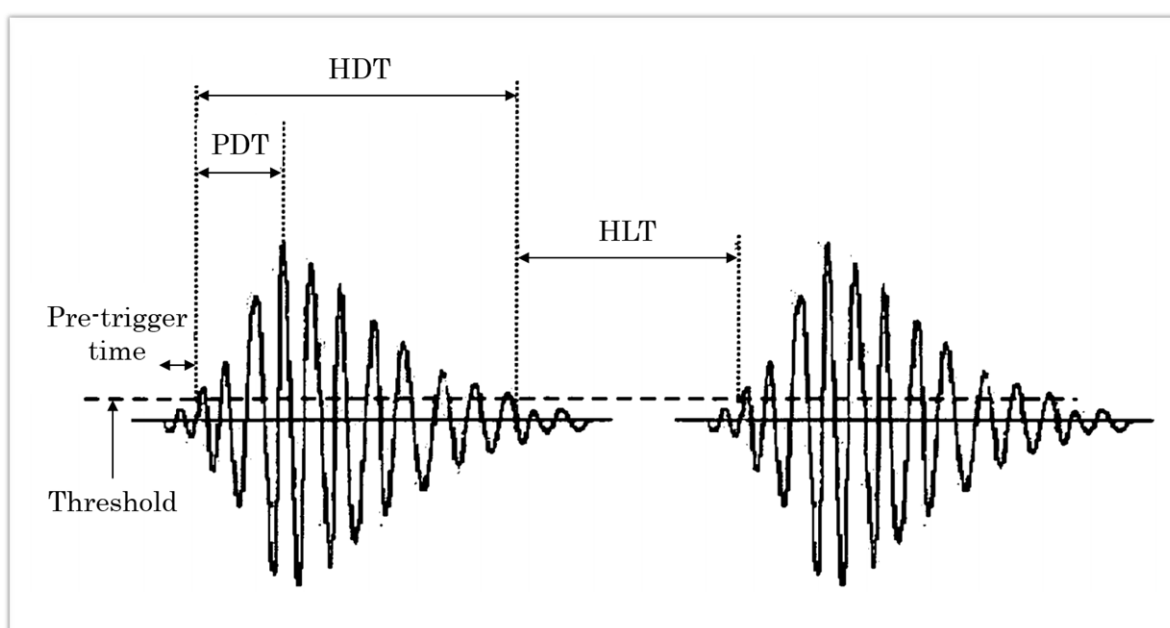


Fig. 5.9. The setting parameters of MISTRAS-2001 AE system (modified from (Mistras, 2001)).

Table 5.1. Summary of the hardware-setup values for AE testing

Parameter	Value
Peak definition time (PDT)	10 μs
Hit definition time (HDT)	20 μs
Hit lockout time (HLT)	20 μs
Sampling rate	4 MSPS
Pre-trigger	50 μs
Hit length	10 <i>k</i>
Threshold	30 <i>dB</i>
Gain	40 <i>dB</i>
Analog filter	20 kHz - 1.2 MHz
Time driven rate	10 <i>ms</i>

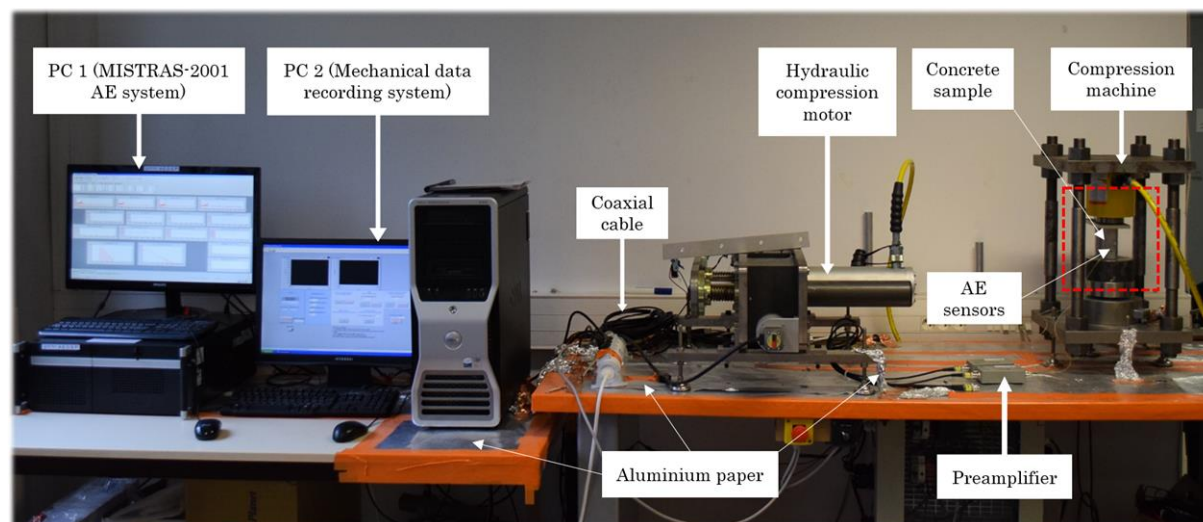
5.3.3 Testing setup

Fig. 5.10 shows the testing system which includes the compression testing system and the AE monitoring equipment. As already mentioned in section 2.4, due to the sample size range considered in this work, two different compression machines with different stiffness and load capacity (Machine A (Fig. 2.2c) and Machine B (Fig. 2.2d), were used in this study. However, this did not impact the AE measurements, as the AE equipment worked independently from the compression machine.

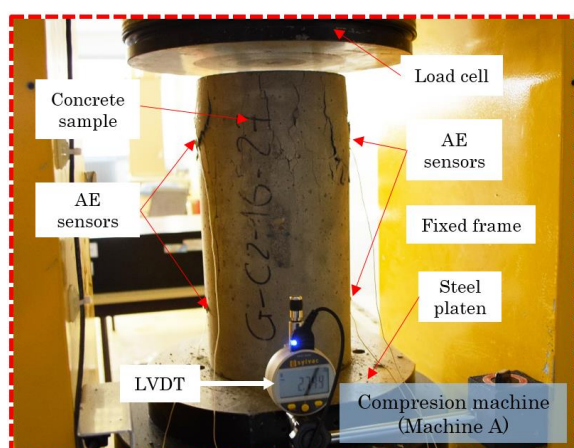
During the loading test, the passive AE signals generated within the deformed concrete sample were continuously monitored and stored in PC-1 by a MISTRAS-2001 AE system while the mechanical data (i.e. load, axial displacement of sample) was saved in PC-2 (see Fig. 5.10a). Electromagnetic interference noise, resulting from ground loops of AE cables or poorly connected ground power, may affect the quality of the AE signal (Pollock, 1989). To suppress this kind of noise, layers of aluminum were placed below the testing system and all of the testing equipment was electrically isolated (see Fig. 5.10a).

After the AE sensors are installed and connected to the monitoring equipment, system sensitivity is checked before loading begins. This involves the breaking of pencil lead near the sensor to verify the response from an acoustic signal (ASTM E976-10, 2010). This test is carried out to ensure that all the AE sensors have been properly coupled to the sample prior

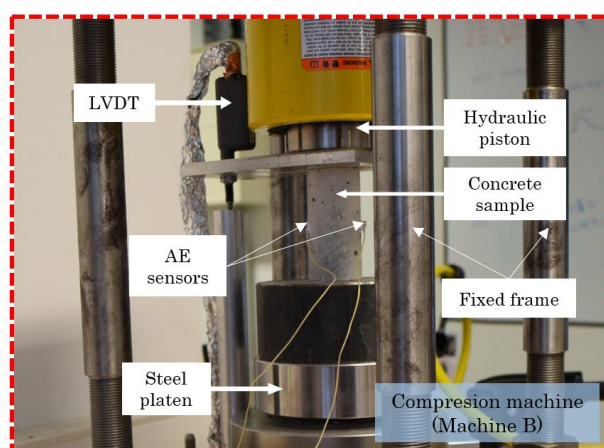
testing. In our case, an AE sensor that is well coupled should record a signal covering of at least 70 dB to display the entire dynamic range of the sensor. Therefore, if a sensor response is below 70 dB, it is recoupled and the connection is checked again.



(a)



(b)



(c)

Fig. 5.10. Experimental setup used for uniaxial compression tests combined with AE monitoring (AE test). (a) Instrumentation setup; (b) Equipment setup on the compression machine A for large specimens (70x140 mm, 110x220 mm and 160x320 mm); (c) Equipment setup on the compression machine B for small specimens (40x80 mm).

5.4 Experimental results

In this section, a critical interpretation of compressive failure of concrete is rationalized based on the analysis of the evolutions of AE activities (damage and microcracking events) in terms of number, peak amplitude, duration and dissipated energy as approaching catastrophic failure.

For this purpose, the evolution of these AE parameters are plotted as a function of the reduced control parameter, Δ , defined here as the distance to failure:

$$\Delta = \frac{(\sigma_f - \sigma)}{\sigma_f} \quad (5.3)$$

where σ_f is the peak/failure stress (see Fig. 5.11). The critical point is therefore identified as the peak load. The control parameter varies from $\Delta = 1$ at the beginning of loading to $\Delta = 0$ at the critical point.

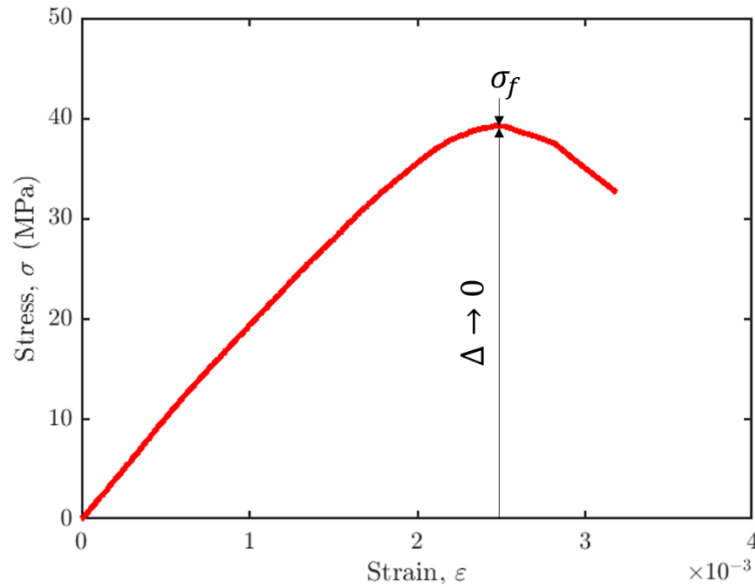


Fig. 5.11. A typical stress-strain curve of uniaxial compression test for the definition of the control parameter Δ , where σ_f is the peak stress.

In this study, the values of the scaling exponents for different AE parameters were firstly estimated from an individual AE dataset (1 AE sensor on 1 sample). Then, these exponents were averaged over:

- all AE sensors and all samples to determine the exponents of a given size;
- all AE sensors and all samples (whatever the size) to determine the exponents of a given material disorder (concrete mixture).

5.4.1 Evolution of AE activity toward failure

In Fig. 5.12, we show the evolution of the intermittent AE activity as a function of the control parameter (Δ) until the peak load (critical point) for a typical uniaxial compression test. It can be seen that both the total energy release and the maximum energy of events, E , seem to

accelerate towards failure (Fig. 5.12a). Similar results are also obtained for the AE duration, T , number of AE events, N , and maximum AE amplitude, V_{\max} (see Fig. 5.12b). According to (Guarino et al., 1998), the divergences of these AE parameters as approaching failure ($\Delta \rightarrow 0$) can be regarded as a signature of a critical behavior. To examine this apparent criticality, we focus here on the evolutions of the AE events rate and AE energy release rate toward the critical point. For this aim, we divided the whole AE events recorded until failure into several bins of the control parameter Δ . The binning is equally spaced in a log scale and sized to ensure a large enough number of AE events in each bin.

For each bin of Δ :

- the representative value of the control parameter is calculated as the center of this bin;
- the AE event rate ($dN/d\Delta$) is computed by dividing the total number of AE events (dN) recorded over this bin by the bin width ($d\Delta$); and,
- the AE energy rate ($dE/d\Delta$) is defined as the total energy released (dE) by all AE events in this bin of Δ , normalized by the bin width ($d\Delta$).

Fig. 5.13 shows the evolutions of AE event rate ($dN/d\Delta$) up to the failure for different sample sizes and different materials. It is observed that $dN/d\Delta$ diverges on approaching the failure as a power law dependency of Δ with an exponent p :

$$\frac{dN}{d\Delta} \sim \Delta^{-p} \quad (5.4)$$

The value of exponent p is estimated from a linear regression on a log-scale plot (Fig. 5.13) and the error on the slope is given for a 95% confidence level. We find the overall exponent $p = 0.70 \pm 0.05$ for all of concrete samples regardless of size (Fig. 5.13a) and of material disorder (Fig. 5.13b). Such time-reversed Omori's law (Utsu et al., 1995) has been reported for the compressive failure of porous sandstones ($14\% \leq p_0 \leq 24\%$) (Ojala et al., 2004; Schubnel et al., 2007), though with a varying p – value, possibility depending on the strain-rate (Ojala et al., 2004). In our low-porosity quasi-brittle materials (see section 3.5.2), under our stress-controlled protocol, the p – value was found to be independent of both external and internal (disorder-related) scales.

As shown in Fig. 5.14, we also find that the AE energy rate $dE/d\Delta$ diverging towards failure appears to follow a power law scaling of Δ as:

$$\frac{dE}{d\Delta} \sim \Delta^{-\alpha} \quad (5.5)$$

An acceleration of the AE energy release rate prior the macro failure according to the expression (5.5) has been confirmed by many authors, while the value of power exponent α and its controlling factors are still controversial (see reviews in (Baro et al., 2018)). However, a value $\alpha \leq 1$ is often reported from the results of AE experiments (Baro et al., 2018; Wang et al., 2008; Yin et al., 2004). As presented by (Yin et al., 2004), the power-law exponent of AE energy rate (similar meaning to α in Eq. (5.5)) possibly depends on the loading confinement, the applied strain rate or the density of the material. In contrast, from the results of AE tests carried out on different natural and artificial porous materials ($17\% \leq p_0 \leq 40\%$), (Baro et al., 2018) have demonstrated that the measured exponent ($\alpha \sim 1$) does not depend on the materials (porosity and density), the stress rate and the sample sizes.

In our case, the α –value was estimated from a linear fit of data on a log-log scale (Fig. 5.14) with a 95% confidence interval. The values of α for different sample sizes and different concrete mixtures are summarized in Table 5.2 and Appendix B. Overall, we find a value $\alpha = 1.3 \pm 0.1$, independently of sample size (Fig. 5.14a) and of material disorder (Fig. 5.14b).

From the equations (5.4) and (5.5), the evolution of the average AE energy per event, dE/dN , can be written as follows:

$$\frac{dE}{dN} \sim \Delta^{-\alpha+p} \quad (5.6)$$

As mentioned above, both the scaling exponents p and α are independent of the sample sizes and of the concrete mixtures. Therefore, we can deduce that the average AE event energy is diverging towards failure as $dE/dN \sim \Delta^{-0.6}$ with an exponent 0.6 ± 0.1 independent of sample size as well as material disorder. On the other hand, the average value of AE energy for each window of Δ can be analyzed from the probability density functions of E . Therefore, the study of the probability distribution of AE energy (E) is necessary to fully characterize the evolution of AE activity towards the failure. This analysis is detailed in the following section.

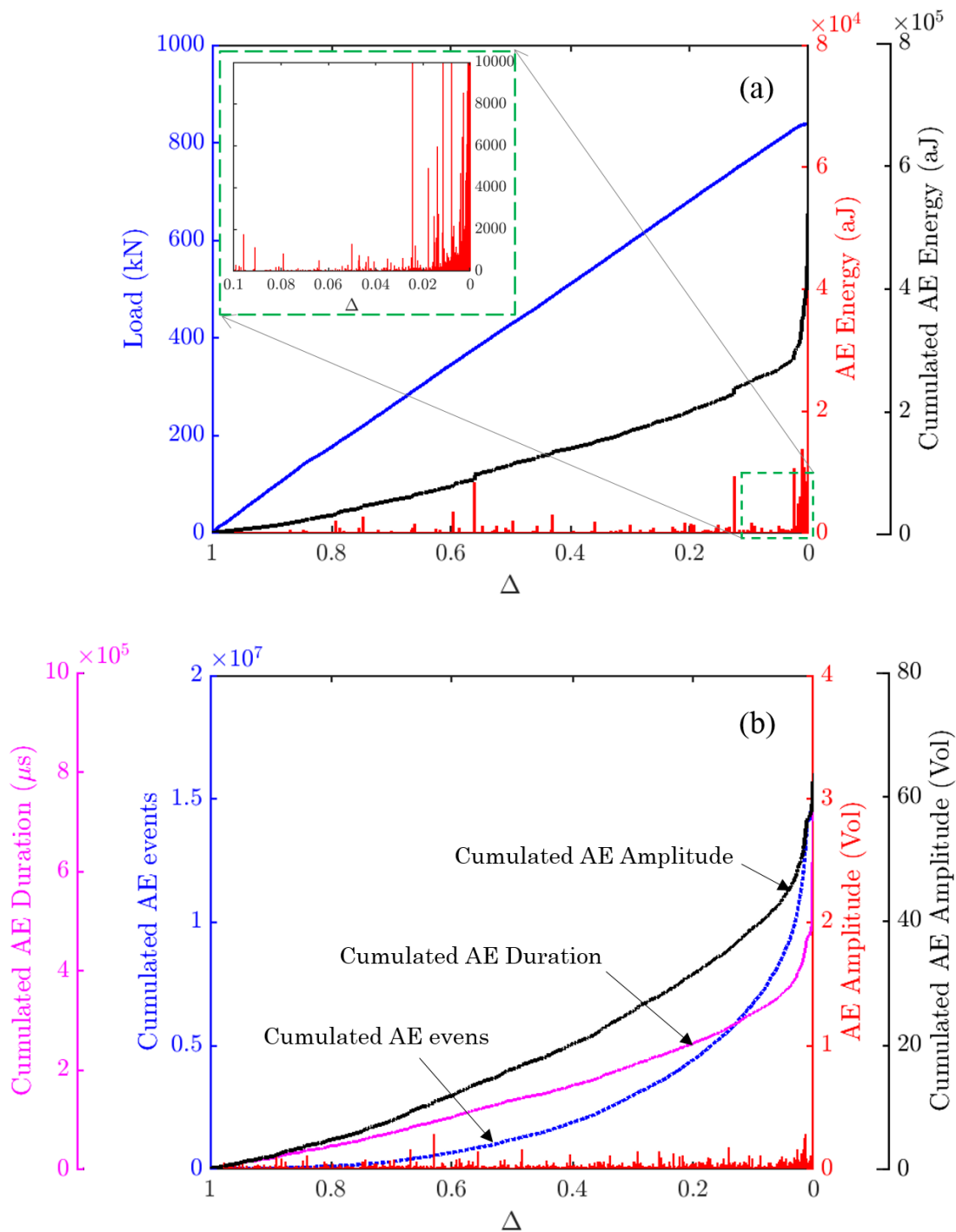


Fig. 5.12. Evolution of the AE activity during a stress-controlled compression test on a sample of diameter $\phi = 160\text{mm}$ of M-concrete. (a) Blue curve: load; black curve: cumulated AE energy; red: AE energy release rate, sampled at 100Hz. (b) Blue curve: cumulated AE events; black curve: cumulated AE amplitude; red: AE amplitude; pink curve: cumulated AE duration. In this study, the value of AE amplitude is converted into Voltage from its value in dB by using Eq. (5.1).

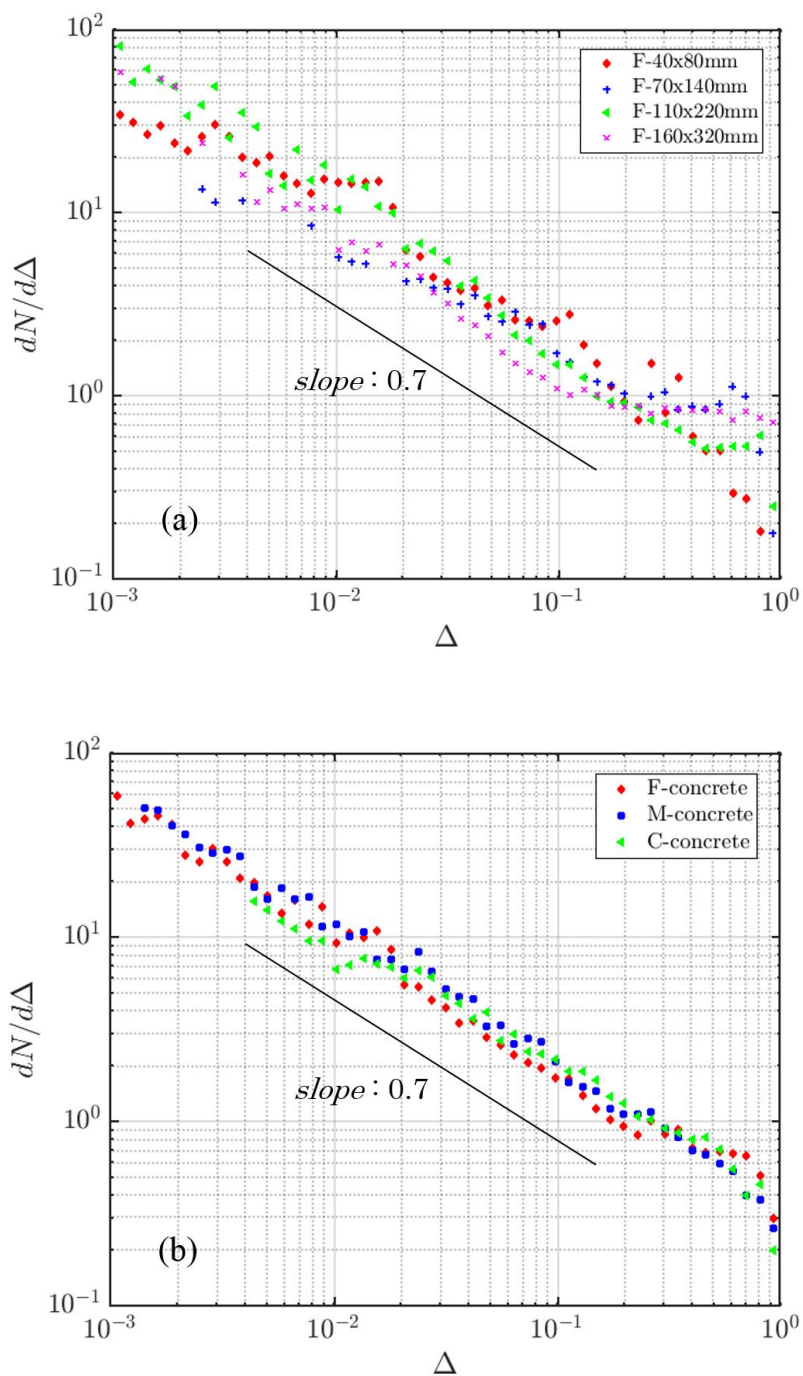


Fig. 5.13. Evolution of AE event rate $dN/d\Delta$ for (a) different sample sizes of F-concrete; and (b) the three different materials. Curves were averaged over all sensors and all samples of a given sample size (a), and on all sensors and samples (whatever the sample size) of a given material (b). Other sample sizes for M- and C-concretes give similar results (see Fig. B.4, Table. B.2 and Table. B.3 in Appendix B).

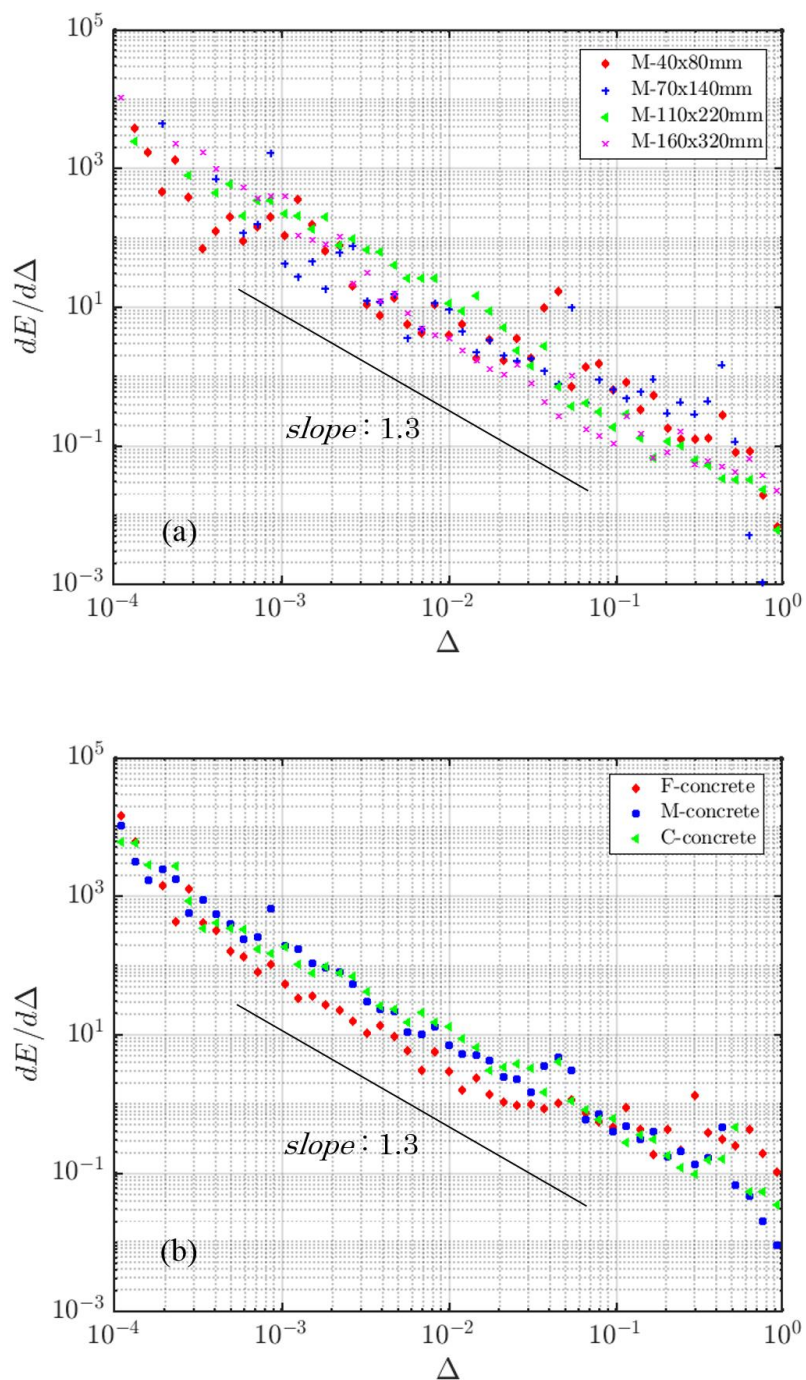


Fig. 5.14. The AE energy release rate $dE/d\Delta$ for (a) different sample sizes of M-concrete, and (b) for three different concrete mixtures. Curves were averaged over all sensors and all samples of a given sample size (a), and on all sensors and samples (whatever the sample size) of a given material (b). Other sample sizes for F- and C-concretes give similar results (see Fig. B.5 and Table. B.1 and Table. B.3 in Appendix B).

5.4.2 Probability distribution of AE energy

We now study the statistical distribution of AE energy, E , for different values of the control parameter Δ before the failure. For this analysis, all the AE events recorded up to the peak stress were firstly arranged into ten bins of Δ containing the same number of events. We then calculate the AE energy distribution of each bin. In each bin of Δ , (i) the number of AE events was not less than 300 events to ensure a good statistical analysis and (ii) the representative value of Δ was defined as the median value of this bin.

Fig. 5.15 shows a progressive evolution of the distribution of AE energies as approaching the failure. In the early stages of loading, the energy cumulative distribution (*cdf*), $P(> E)$, is clearly truncated towards large energies, but the associated upper cut-off is increasing as fracturing goes on. Close to failure ($\Delta \rightarrow 0$), a power law *cdf* is recovered, $P(> E) \sim E^{-\beta_E+1}$, over ~ 5 orders of magnitude, without detectable upper cut-off (Fig. 5.16). We therefore conjecture an evolution of the probability density function (*pdf*) as follows:

$$P(E) \sim E^{-\beta_E} f\left(\frac{E}{E^*}\right) \quad (5.7)$$

where $f\left(\frac{E}{E^*}\right)$ rapidly vanishes for $\frac{E}{E^*} > 1$, and a cut-off energy, E^* , diverging at the critical point is assumed as a function of Δ according to the following equation:

$$E^* \sim \Delta^{-\gamma_E} \quad (5.8)$$

We recover a non-truncated power law distribution at failure, $P(E) \sim E^{-\beta_E}$, while the sweeping of an instability (Sornette, 1994) predicts another power law $P(E) \sim E^{-\theta_E}$ for the stress-integrated *pdf* (see Fig. 5.16). The relationship between these two last exponents with the exponent γ_E (Eq. (5.8)) is given by (Girard et al., 2010):

$$\theta_E = \beta_E + \frac{1}{\gamma_E} \quad (5.9)$$

, or:

$$\gamma_E = \frac{1}{\theta_E - \beta_E} \quad (5.10)$$

In this study, for each dataset (1 AE sensor on 1 sample), the power-law exponents β_E and γ_E were determined from a maximum likelihood methodology (Clauset et al., 2009). β_E is

estimated such that the Eq. (5.7) fits the AE energy distribution of the AE events closest to the failure (i.e. 100 AE events used in this study), while θ_E is estimated from that of the whole AE events dataset recorded over the entire failure process, from the onset of loading until the failure (Fig. 5.16). Substituting these two exponents into Eq. (5.10), the value of exponent γ_E was then determined. With these three estimated exponents, the hypothesis of the evolution for the probability density function (*pdf*) of AE energies (Eq. (5.7)) and the scaling for the cut-off E^* (Eq. (5.8)) are confirmed from a data collapse analysis (see an example in Fig. 5.15). This data collapse was done by plotting all curves of AE energy distributions for different values of Δ (Fig. 5.15a) in a rescaled plot with $x = E \cdot \Delta^{\gamma_E}$ and $y = P(E) \cdot \Delta^{-\beta_E \cdot \gamma_E}$ (Fig. 5.15b). Some other examples of the evolution of the AE energies distribution for different sample sizes and different concrete mixtures are presented in Appendix B. We also find the overall values $\beta_E = 1.4 \pm 0.1$, $\theta_E = 1.75 \pm 0.1$ and $\gamma_E = 3.3 \pm 0.9$ not varying significantly with the sample size and the material disorder (see Table 5.2 and Appendix B).

Assuming, for the sake of simplicity, a circular rupture of “radius” r as the AE source model, and an AE energy (E) proportional to the radiated seismic energy, E , for both mode I (Evans, 1979) or shear failure events (Hanks, 1977; Scholz, 2002) should scale as:

$$E \sim \Delta \sigma \times r^3 \quad (5.11)$$

Considering further a size-independent stress drop $\Delta \sigma$ (Hanks, 1977), the relation (5.11) yields the scaling for the cut-off rupture radius is given by:

$$r^{*3} \sim E^* \sim \Delta^{-\gamma_E} \quad (5.12)$$

Further identifying r^* with the correlation length ξ of the fracturing/faulting process, one gets a divergence $\xi \sim \Delta^{-\nu}$ with $\nu = \gamma_E/3 = 1.1 \pm 0.3$ when approaching the critical point ($\Delta \rightarrow 0$).

In the previous section, the rapid increase of AE activity towards the failure has been demonstrated by the evolution of both the AE event rate ($dN/d\Delta$) (Fig. 5.13) and the AE energy release rate ($dE/d\Delta$) (Fig. 5.14). This is also confirmed by a clear power-law behavior of AE energy distribution for the AE events closest to the failure and by the divergence of the cut-off, E^* as approaching the failure (Fig. 5.15) in this section. We now expect to relate the evolution of AE energy rate ($dE/d\Delta$) to the distribution of E . The average AE energy release, $\langle E \rangle$, can be estimated from the probability density function of E as:

$$\langle E \rangle = \int_{E_m}^{+\infty} E \cdot P(E) dE \quad (5.13)$$

, where E_m is the minimum AE Energy at a given Δ (lower cut-off). Substituting the relation (5.7) into Eq. (5.13), one gets:

$$\langle E \rangle = \int_{E_m}^{+\infty} E^{1-\beta_E} \cdot f\left(\frac{E}{E^*}\right) dE \quad (5.14)$$

Assuming that $P(E)$ is brutally truncated at E^* , we obtain:

$$\langle E \rangle \sim \int_{E_m}^{E^*} E^{1-\beta_E} \cdot f\left(\frac{E}{E^*}\right) dE \quad (5.15)$$

When approaching the failure, the cut-off value E^* is much larger than E_m , and the exponent β_E is always larger than 1. Hence, neglecting the tail, we obtain:

$$\langle E \rangle_{(\Delta \rightarrow 0)} \sim (E^*)^{2-\beta_E} \left[1 - \left(\frac{E_m}{E^*}\right)^{2-\beta_E} \right] \quad (5.16)$$

Close to the failure where $E^* \gg E_m$, one thus gets:

$$\langle E \rangle_{(\Delta \rightarrow 0)} \sim (E^*)^{2-\beta_E} \quad (5.17)$$

Combining the relations (5.8) and (5.17), the evolution of the average AE energy can be approximated as:

$$\langle E \rangle_{(\Delta \rightarrow 0)} \sim \Delta^{-\gamma_E(2-\beta_E)} \quad (5.18)$$

From the Eq. (5.6) and Eq. (5.18), we obtain the connection between the critical exponents of AE energies distribution and the exponents of the evolution AE activities as follows:

$$\gamma_E(2 - \beta_E) = \alpha - p \quad (5.19)$$

Our results are qualitatively consistent with this analysis, with both $\frac{dE}{d\Delta}$ and E^* diverging towards failure. However, a poor agreement between the two sides of Eq. (5.19) is obtained, with $\gamma_E(2 - \beta_E) = 1.98 \pm 0.63$ while $\alpha - p = 0.6 \pm 0.1$. The origin of this discrepancy is still partly obscure, and might be related to the impact of the lower cut-off E_m , or to the simplifying assumption of a brutal cut-off above E^* in the integration above. Nevertheless, our

analysis shows that all the signatures of AE activity are power-law diverging towards the critical point.

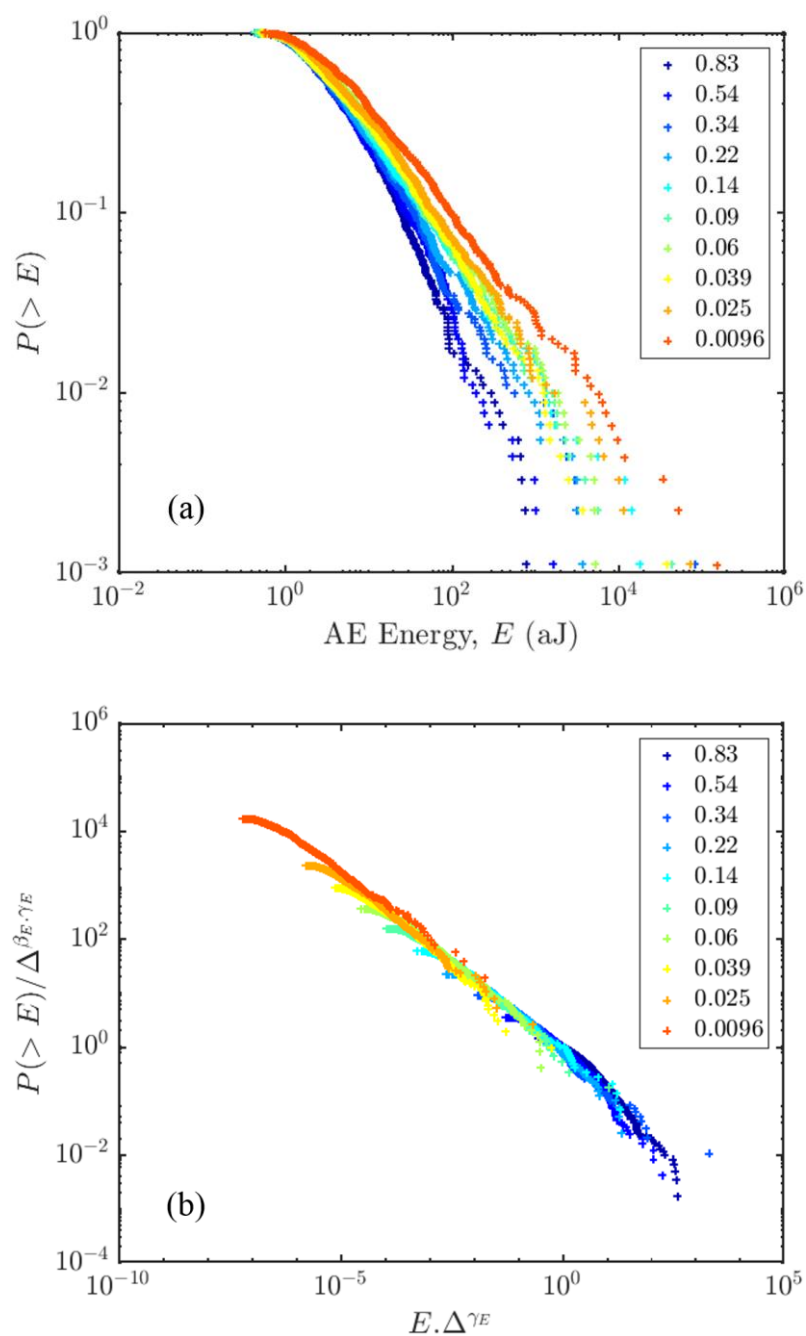


Fig. 5.15. (a) Cumulative distribution (*cdf*) of AE energies at different distances to failure (Δ), for a test on a 110-mm sample of M-concrete. (b) Data collapse of the same data in a rescaled plot. Other sample sizes and materials give similar results (see Appendix B).

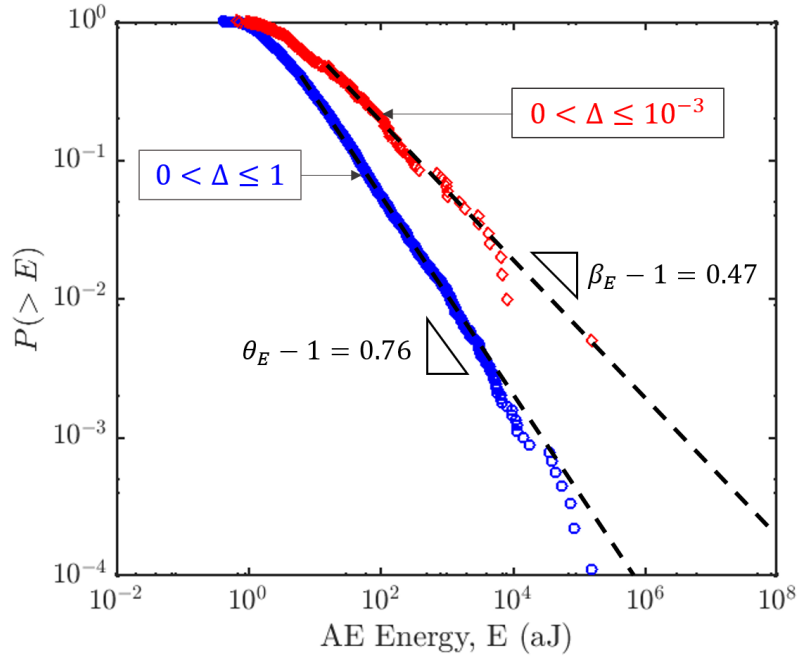


Fig. 5.16. Near failure (red diamonds), and stress-integrated (blue circles) cumulative distribution of AE energies for a test on a 160 mm sample of M-concrete. Other sample sizes and materials give similar results.

5.4.3 Interpretation of AE duration

The interpretation of the AE duration, T , in terms of duration of the fracturing event itself is not always straightforward (e.g. (Baro et al., 2018)). Indeed, the duration is typically defined as the time over which the envelope of the AE signal $V(t)$ remains above a chosen threshold V_{th} (see Fig. 5.4). As the result of scattering of the wave generated at the source by internal disorder and/or reflections at free surface, a coda can develop after the initial pulse (e.g. (Deschanel et al., 2017)). If the material damping is low, this coda will strongly influence the measured duration of the event, which hence will lose its physical meaning in terms of genuine duration of the source mechanism. In this case, we expect an exponential decay for the amplitude of the signal as:

$$V(t) = V_{max} \exp\left(\frac{t_0 - t}{\tau}\right) \quad (5.20)$$

where τ is the attenuation time scale, essentially dictated by material properties, and t_0 the event arrival time. Assuming a short rise time, i.e. $(t = t_0) \approx V_{max}$, the relation (5.20) yields:

$$T = \tau(\log(V_{max}) - \log(V_{th})) \quad (5.21)$$

From the Eq. (5.21), the conditional average of maximum amplitude, $\langle V_{\max}|T \rangle$, is given by:

$$\langle V_{\max}|T \rangle = V_{th} \exp(T/\tau) \quad (5.22)$$

In order to examine the link between T and $\langle V_{\max}|T \rangle$, the AE events recorded before the failure were firstly sorted in equally log-scaled bins of T . The values of $\langle V_{\max}|T \rangle$ and T were then computed by averaging over all AE events in each bin. It is noted that the value of maximum amplitude V_{\max} is expressed in Voltage converted from Eq. (5.1).

The relationship between the AE duration, T , and the conditional average maximum AE amplitude $\langle V_{\max}|T \rangle$ for different sample sizes of C-concrete and for different three concrete mixtures are shown in Fig. 5.17a and Fig. 5.17b, respectively. Following to the expression (5.22), the average maximum amplitude should to be $\langle V_{\max} \rangle \rightarrow V_{th}$ for $T \ll \tau$, and grow exponentially for $T > \tau$. This prediction is recovered for duration below $100\mu\text{s}$, but another scaling is observed above, $\langle V_{\max}|T \rangle \sim T^\delta$, with $\delta = 0.95 \pm 0.05$ (see Fig. 5.17). This argues for an attenuation timescale of about $100\mu\text{s}$, and so, for larger timescales, the voltage signal $V(t)$ is a good proxy of the seismic moment release rate, or, in other words, of the avalanche velocity $v(t)$ (Baro et al., 2018). Note that the measured value of δ is in good agreement with mean-field depinning ($\delta=1$; (Leblanc et al., 2013)). The increasing scatter observed at large durations likely comes from (i) poorer statistics for large events and (ii) an increasing probability to merge few successive events into an apparently single one when the average AE activity becomes very large near failure. The δ –values of different materials are summarized in Table 5.2 and those of different sample sizes for three concrete mixtures are reported in Appendix B.

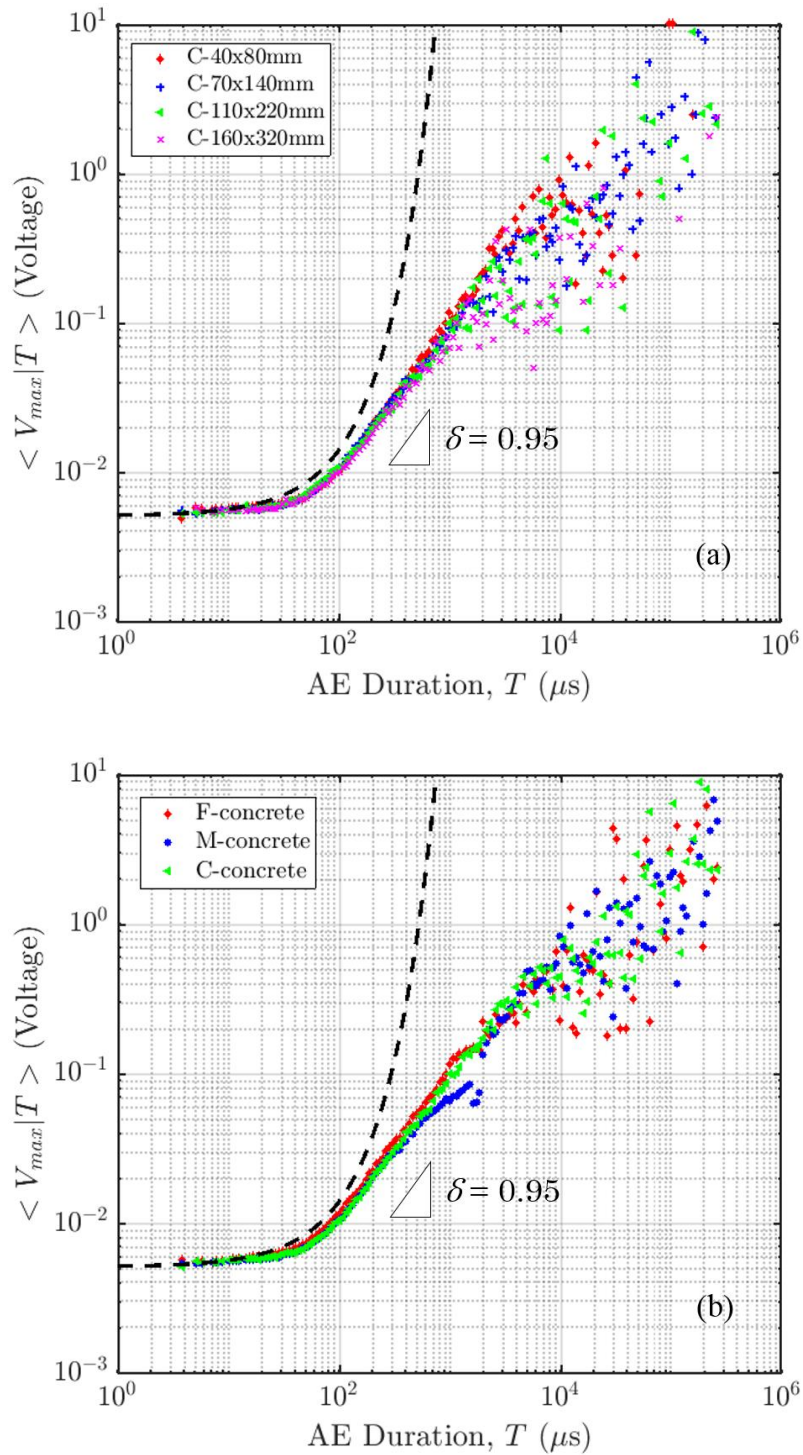


Fig. 5.17. Conditional average maximum AE amplitude $\langle V_{\max}|T \rangle$ for (a) different sample sizes of C-concrete, and (b) the three different materials. Curves of data points were averaged over all sensors and all samples of a given size (a), and on all sensors and samples (whatever the size) of a given material (b). Black dashed lines are the reference curves according to Eq. (5.22), with $V_{th} = 34dB$ and $\tau = 100\mu s$. Other sample sizes and materials give similar results (see Fig. B.6, Table. B.1 and Table. B.2 in Appendix B).

5.4.4 Probability distribution of AE duration and AE amplitude

According to (Vives et al., 1994; Yu and Clapp, 1987), the peak amplitude, V_{\max} and the duration, T , of an AE signal can provide information about the size and the lifetime of an avalanche event (often called an AE hit in specialized AE work). Therefore, an effective way to study the associated avalanche distribution is to measure the distributions of AE amplitude and AE duration (Papanikolaou et al., 2011).

We now consider the statistical distributions of AE duration, T , and maximum AE amplitude, V_{\max} , for different values of the control parameter Δ toward the failure. This analysis is done by sorting out all AE events recorded before the peak stress into ten bins of Δ . We then calculate the distribution of each bin. Noted that the bin values of Δ used here are similar to those used for analyzing the distribution of AE Energy. Similar to the distribution of AE energy (section 5.4.2), we assume that the distribution for both AE duration and maximum AE amplitude is expressed by a scaling as follows:

$$P(x) \sim x^{-\beta_x} g\left(\frac{x}{x^*}\right) \quad (5.23)$$

where $x = T$ or V_{\max} and the cut-off x^* is expected to diverge as $x^* \sim \Delta^{-\gamma_x}$.

Using the same methodology applied to determine the exponents of AE energies distribution (Section 5.4.2), the exponent β_x is extracted from the power-law fitting of the distribution of the AE events very close to the failure (see an illustrated example in Fig. 5.16). The value of exponent γ_x is calculated from the following equation:

$$\gamma_x = \frac{1}{\theta_x - \beta_x} \quad (5.24)$$

in which, θ_x is the exponent estimated from the power-law distribution of the whole AE events dataset recorded up to the failure (see Fig. 5.16). As mentioned in the preceding section, at smaller timescales (i.e. $T < 100\mu\text{s}$ (Fig. 5.17)), the measured AE durations, influenced by wave scattering and seismic coda, are not a good proxy of avalanche duration. Therefore, we only consider the distribution of the AE durations larger than $100\mu\text{s}$ in this study.

A typical cumulative distribution (*cdf*) of the AE durations, T , and the peak AE amplitudes, V_{\max} for different bins of the control parameter, Δ are shown in Fig. 5.18a and Fig. 5.19a, respectively. The overall estimated values of exponents for the distribution of:

- AE duration are $\beta_T = 2.0 \pm 0.3$; $\theta_T = 2.9 \pm 0.2$ and $\gamma_T = 1.1 \pm 0.5$, and

- Maximum AE amplitude are $\beta_V = 2.0 \pm 0.1$; $\theta_V = 2.9 \pm 0.4$ and $\gamma_V = 1.2 \pm 0.6$.

All the power-law exponents β_x and θ_x were estimated by using a maximum likelihood methodology (Clauset et al., 2009). The exponent values of the distributions of AE duration and AE amplitude for all of our concrete mixtures (all sensors and all sample sizes) are summarized in Table 5.2. It is observed that these three exponents in both cases are independent of the sample sizes and the concrete groups (see Table 5.2 and Appendix B).

Fig. 5.18b, and Fig. 5.19b show the same data given in Fig. 5.18a, and Fig. 5.19a, respectively, after rescaling the vertical axis as $P(x)/\Delta^{\beta_x \gamma_x}$ and the horizontal axis as $x \cdot \Delta^{\gamma_x}$. The collapses of both the maximum AE amplitude and AE duration distributions for different Δ are clearly observed with the exponent values reported above. This allows to validate the hypotheses of the power law behavior of the probability distribution (Eq. (5.23)) as well as the divergence of the cut-off values as the function of Δ near the failure ($x^* \sim \Delta^{\gamma_x}$) for both the AE durations and the maximum AE amplitudes. According to (Leblanc et al., 2013), from the values of critical exponents obtained on the experimental data presented in this chapter, the dynamic exponent of the critical transition could be deduced as $z = \gamma_T/\nu \approx 1.0 \pm 0.5$.

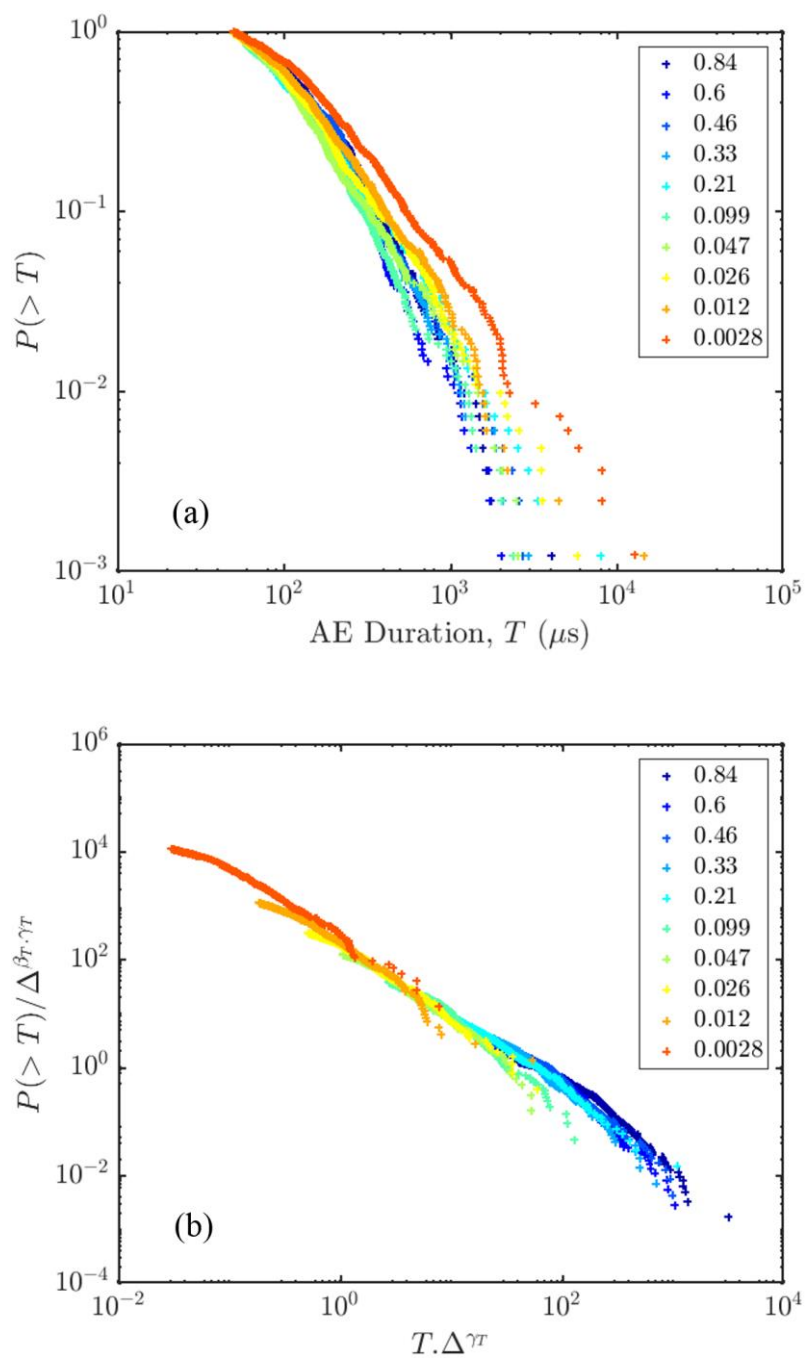


Fig. 5.18. Cumulative distributions (*cdf*) of AE durations, T , for different bins of the control parameter Δ for a test on a 40-mm sample of C-concrete. Similar results are observed with other sample sizes and materials (see Appendix B).

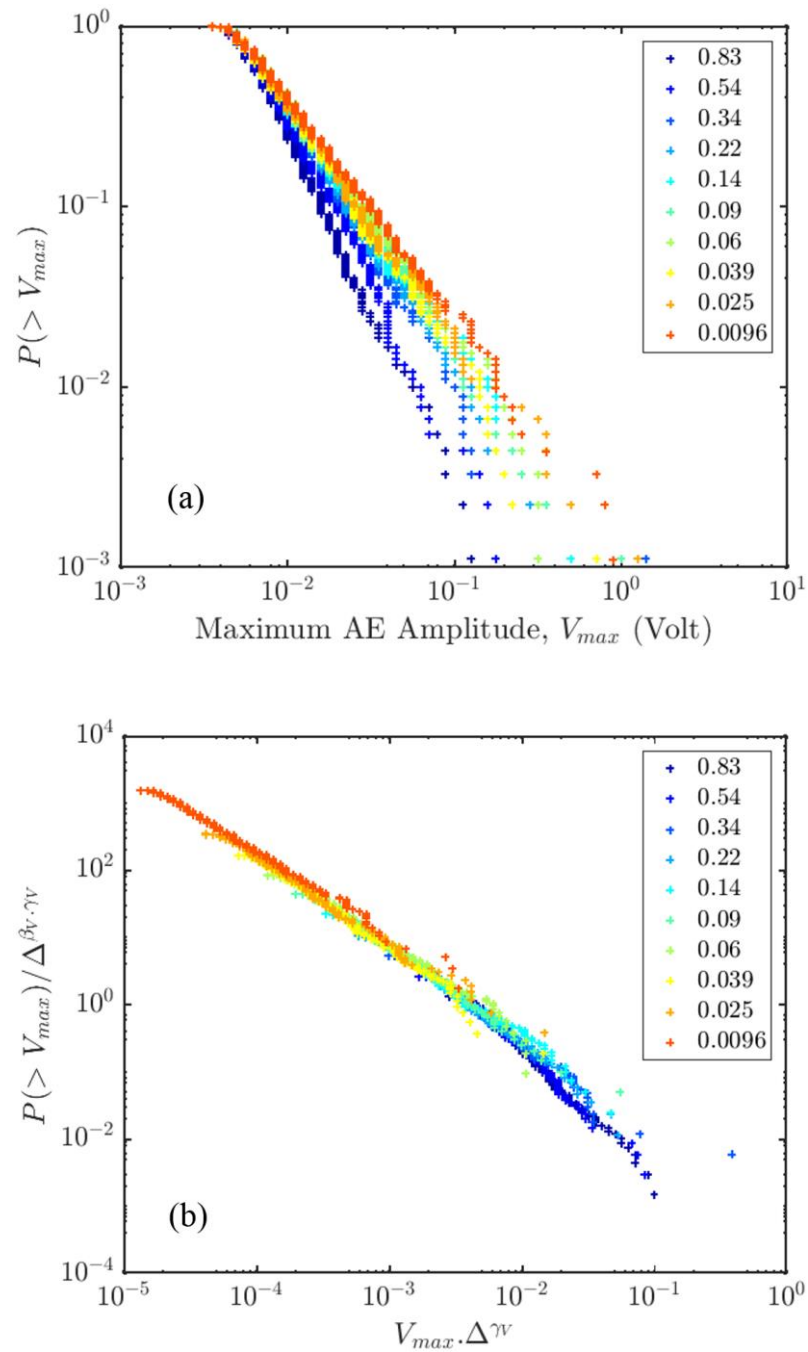


Fig. 5.19. Cumulative distributions (*cdf*) of maximum AE amplitudes, V_{max} , for different bins of the control parameter Δ for a test on a 40-mm sample of C-concrete. Similar results are observed with other sample sizes and materials (see Appendix B).

5.5 Discussion and Conclusion

In this chapter, based on the analysis of AE signal parameters recorded during uniaxial compression tests carried out on the three different types of concrete and four different sample sizes, we have demonstrated the power law behavior of (i) the distribution of microseismic energies, durations and amplitudes near failure; (ii) the divergence of the rate of fracturing events, energies released, and of the fracturing correlation length, as well as of the associated duration as approaching failure. These results are strong evidences for an interpretation of the compressive failure of non-porous disordered materials as a critical transition, where the failure stress identifies as the critical point. This is further supported by the universality of the critical exponents relatively to sample size and disorder.

Theoretically, this critical interpretation could be checked from a finite-size scaling analysis of the probability density functions (*pdf*) of energy, duration, and amplitude obtained from samples of different sizes. We did not find, however, a fully convincing L -dependence in our data (see Fig. 5.20a; Fig. 5.21a and Fig. 5.22a), most likely because (i) the size range explored was limited ($L_{\max}/L_{\min} = 4$) and (ii) the necessarily limited experimental data statistics make the analysis of extremes difficult.

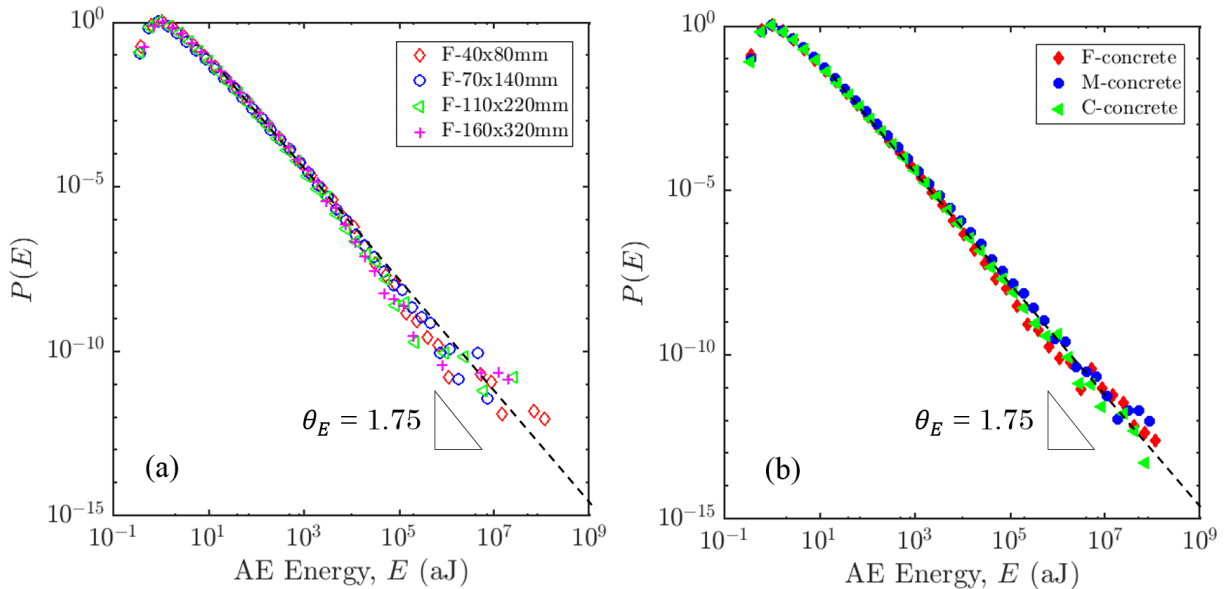


Fig. 5.20. Probability density functions of AE energy for the whole AE events dataset for (a) four different sample sizes of F-concrete and (b) for three different concrete mixtures. The *pdfs* were normalized by their maximum value. Curves on the left were averaged over all sensors and all samples of a given sample size, and on the right on all sensors and samples (whatever the sample size) of a given material. Other sample sizes for M- and C-concretes give similar results (see Fig. B.1 in Appendix B).

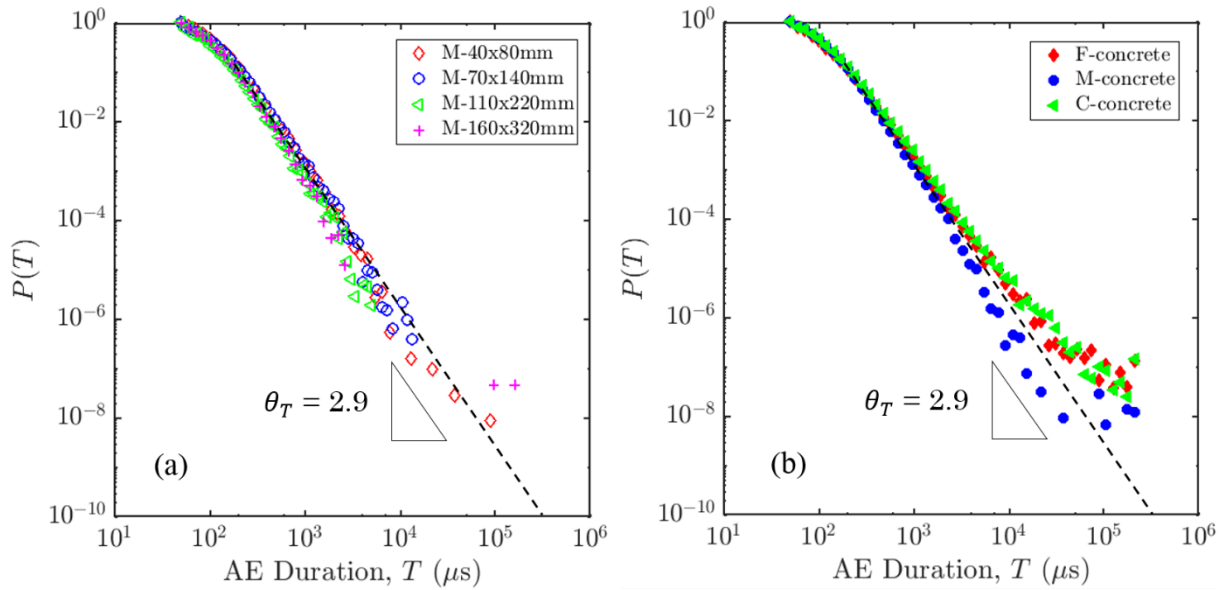


Fig. 5.21. Probability density functions of AE duration of the whole AE events catalog for (a) four different sample sizes of C-concrete and (b) for three different concrete mixtures. The functions were normalized by their maximum value. Curves on the left were averaged over all sensors and all samples of a given sample size, and on the right on all sensors and samples (whatever the sample size) of a given material. Other sample sizes for F- and M-concretes give similar results (see Fig. B.2 in Appendix B).

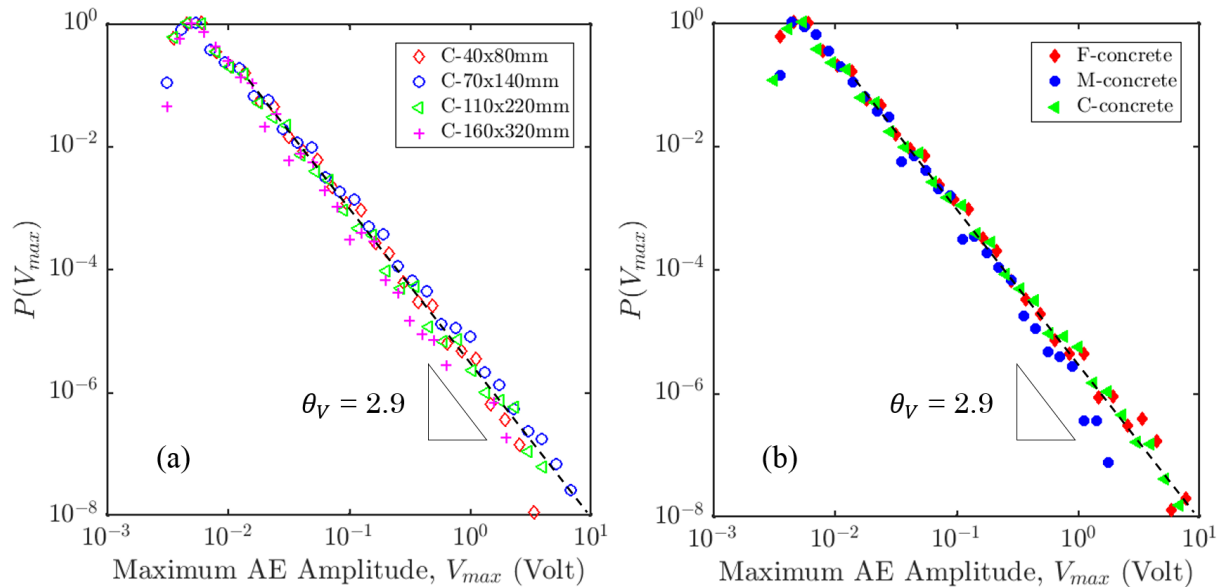


Fig. 5.22. Probability density functions of AE amplitude for (a) four different sample sizes of F-concrete and (b) for three different concrete mixtures. The functions were normalized by their maximum value. Curves on the left were averaged over all sensors and all samples of a given sample size, and on the right on all sensors and samples (whatever the sample size) of a given material. Other sample sizes for F- and M-concretes give similar results (see Fig. B.3 in Appendix B).

From these results, the nature of the critical transition, and its possible affiliation to a particular universality class, can be further discussed. A mapping of the problem of stick-slip along an existing fault to the depinning of an elastic interface was proposed 20 years ago (Fisher, 1998; Fisher et al., 1997). More recently, a similar analogy was proposed in case of compressive failure to account for statistical size effects on strength (Weiss et al., 2014a). Indeed, quasi-brittle failure shares fundamental ingredients with the depinning transition, including a local threshold mechanism, disorder, and elastic interactions. Our results reveal a similar phenomenology of avalanches as approaching the critical point, with experimental exponents remarkably close to mean-field depinning ones (Ertas and Kardar, 1994; Leblanc et al., 2013; Salje and Dahmen, 2014) (see Table 5.2). On the other hand, several differences between the two problems can be stressed. First, the time-reversed Omori's scaling of the avalanche rate ($dN/d\Delta \sim \Delta^{-p}$) is not present in classical depinning, meaning that an additional exponent, p , is required to describe the failure transition. In addition, the nature of the elastic interaction kernel differs. Unlike for depinning, it is non-convex in our case (Démery et al., 2017; Weiss et al., 2014a), allowing localization of damage along a fault, much like for the yielding transition in amorphous plasticity (Lin et al., 2014; Tyukodi et al., 2016). It is non-negative either, meaning that it has unstable modes, differing on this point from the yielding transition (Démery et al., 2017). Although these differences preclude a direct affiliation of our problem onto the universality class of classical depinning, the scaling of the fracturing correlation length, $\xi \sim \Delta^{-\nu}$, with an exponent ($\nu = 1.1 \pm 0.3$) (see Table 5.2) very close to mean-field depinning ($\nu_{MF} = 1$) (Ertas and Kardar, 1994), suggests that some theoretical results could be tentatively transposed to our problem.

In the next chapter, based on the critical phase transition interpretation of compressive failure, the size effects on compressive strength of concrete (section 6.1) are statistically analyzed. We expect that the finite-size scaling laws derived from the critical interpretation can provide an accurate prediction of the statistical size effects on compressive strength of quasi-brittle materials like concrete.

Table 5.2. Summary of the scaling exponents for the distributions of AE durations, of AE energies released, and of AE amplitudes as well as for the rate of AE events, and of AE energy release for three different concrete mixtures and comparison with the corresponding values of Mean-Field Depinning/Stick-Slip (Baro et al., 2018; Dahmen, 2017; Ertas and Kardar, 1994; Leblanc et al., 2013; Salje and Dahmen, 2014).

Quantity	Form	Exponent	Concrete group			All groups	Mean-field values
			F-concrete	M-concrete	C-concrete		
Duration distribution	$P(T) \sim T^{-\beta_T} g(\Delta^{\gamma_T} T)$	β_T	2.1 ± 0.2	2.0 ± 0.3	2.0 ± 0.3	2.0 ± 0.3	2
		γ_T	1.2 ± 0.5	1.1 ± 0.4	1.1 ± 0.5	1.1 ± 0.5	1
Stress-integrated duration distribution	$P_{int}(T) \sim T^{-\theta_T}$	θ_T	2.9 ± 0.2	2.9 ± 0.2	2.9 ± 0.2	2.9 ± 0.2	3
Energy distribution	$P(E) \sim E^{-\beta_E} f(\Delta^{\gamma_E} E)$	β_E	1.5 ± 0.1	1.4 ± 0.1	1.4 ± 0.1	1.4 ± 0.1	4/3
		γ_E	3.2 ± 1.1	3.3 ± 0.8	3.4 ± 0.8	3.3 ± 0.9	3
Stress-integrated energy distribution	$P_{int}(E) \sim E^{-\theta_E}$	θ_E	1.80 ± 0.10	1.75 ± 0.05	1.75 ± 0.05	1.75 ± 0.10	5/3
Amplitude distribution	$P(V) \sim V^{-\beta_V} g(\Delta^{\gamma_V} V)$	β_V	2.0 ± 0.1	2.0 ± 0.2	2.0 ± 0.1	2.0 ± 0.1	2
		γ_V	1.2 ± 0.5	1.2 ± 0.8	1.2 ± 0.6	1.2 ± 0.6	1
Stress-integrated amplitude distribution	$P_{int}(V) \sim V^{-\theta_V}$	θ_V	2.9 ± 0.4	2.9 ± 0.5	2.9 ± 0.4	2.9 ± 0.4	3
Conditional average maximum amplitude vs Duration	$\langle V_{max} T \rangle \sim T^\delta$	δ	0.95 ± 0.05	0.90 ± 0.05	0.95 ± 0.05	0.95 ± 0.05	1
Rate of AE event	$dN/d\Delta \sim \Delta^{-p}$	p	0.70 ± 0.05	0.70 ± 0.05	0.65 ± 0.05	0.70 ± 0.05	None
Rate of AE Energy	$dE/d\Delta \sim \Delta^{-\alpha}$	α	1.2 ± 0.1	1.3 ± 0.1	1.3 ± 0.1	1.3 ± 0.1	2
Derived exponents							
Correlation length	$\xi \sim \Delta^{-\nu}$	ν				1.1 ± 0.3	1
Dynamic exponent	$T^* \sim \xi^z$	z				1.0 ± 0.5	1

Chapter 6

Statistical size effects on compressive failure strength of concrete

Based on

Vu, C. C., Weiss, J., Plé, O., Amtrano, D., Vandembroucq, D. (2018), Revisiting statistical size effects on compressive failure of heterogeneous materials, with a special focus on concrete, *Journal of the Mechanics and Physics of Solids*, 121, p.47–70. doi:10.1016/j.jmps.2018.07.022

The role of microstructural disorder on failure (a strongly non-linear process) and strength is fundamentally different from that on linear (elastic) properties. This difference is particularly striking when considering the weakest-link approach to failure, ruled by extreme value statistics, whereas linear properties average out at scales larger than the disorder correlation length (see Chapter 3 and Chapter 4). In this chapter, we show that the weakest-link approach fails to describe the compressive failure of a heterogeneous material like concrete, and that the average compressive strength saturates at a non-zero value towards large scales. However, this does not mean that a RVE can be considered in terms of damage and failure properties, as the associated strength variability is scale-dependent over the entire scale range. We rationalize these scaling properties of mean strength and associated variability from an interpretation of compressive failure as a critical transition (Weiss et al., 2014a). This critical scenario is associated with a damage correlation length growing during loading to reach the system size near failure (Chapter 5), a behavior actually at the root of the finite-size effects described here. In this context, the definition of a RVE for damage becomes meaningless.

The structure of this chapter is as follows, section 6.1 presents a brief description the uniaxial compressive behavior and the value of the compressive strength of concrete collected from the compression tests. Section 6.2 shows the results from the analysis of compressive strength distribution of our concretes. The focus of this section is to demonstrate the irrelevance of the weakest-link theory to capture the statistical size effects on the compressive strength. Derived from the interpretation of compressive failure of concrete as a critical phase transition which is validated by the results of Acoustic Emission experiments presented in Chapter 5, the finite size scaling laws for both mean value of the compressive strength and its associated variability are described in section 6.3. We then apply these scaling laws to account for the statistical size effects on the compressive strength of our concretes in section 6.4. The role of microstructural disorder on finite-size effects are discussed in section 6.5. Final discussions and conclusions is given in section 6.6.

6.1 Uniaxial compressive behavior of concrete

The stress-strain curves for four different sample sizes of F-concrete and for three different compositions of concrete with the same sample size ($\phi \times h = 110 \times 220$ mm) are shown on Fig. 6.1a and Fig. 6.1b, respectively. As expected, the initial, elastic part of the stress-strain curves is steeper for larger aggregate sizes (M and C concrete mixture), following the hierarchy of elastic moduli shown in Table 4.2. Overall, the ascending part of the loading curves appears more linear towards small sample sizes and large internal (disorder) scales.

The compressive strength of concrete (σ_f) is defined as the maximum stress that the concrete sample can withstand (ASTM C39/C39M-14, 2014; Mehta and Monteiro, 2006; NF EN 12390-3, 2012), hence is calculated by dividing the maximum load, F_{max} , carried by the concrete specimen during the test by the average cross-sectional area ($\sigma_f = 4F_{max}/\pi\phi^2$) (see Fig. 6.1a).

For a specified concrete mixture and each sample size, the mean value and the standard deviation of compressive strength were calculated from the approximately 44 tested samples. These values are summarized in Table 6.1. We observe that the mean compressive strength, $\langle \sigma_f \rangle$, decreases with increasing sample size (diameter of sample, ϕ) (see Fig. 6.1a and Fig. 6.2) and increasing aggregate size, d_{max} (see Fig. 6.1b and Fig. 6.2). These extrinsic (system size related) and intrinsic (internal disorder related) size effects are associated with similar trends for the strength variability (standard deviation $\delta(\sigma_f)$) (see Fig. 6.2).

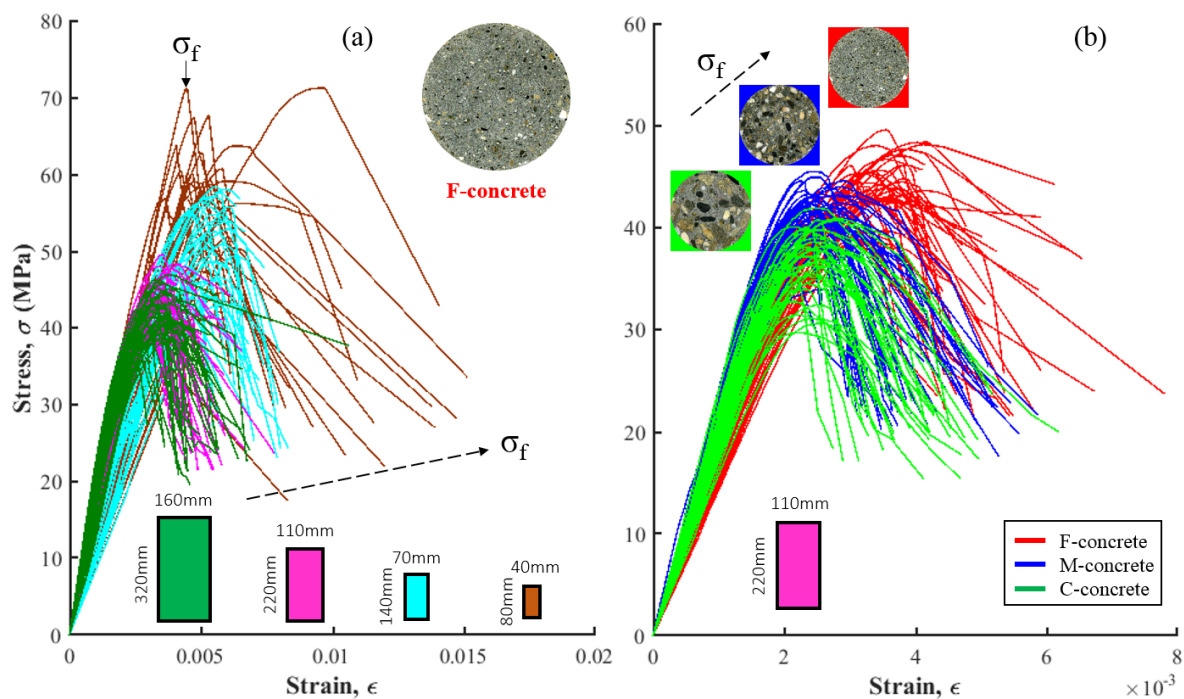


Fig. 6.1. Stress-strain curves of different concrete specimens: (a) for different specimen sizes of F-concrete (45 curves for each size); (b) for different concrete mixtures with the same sample size ($\phi \times h = 110 \times 220$ mm) (42-46 curves for each concrete mixture).

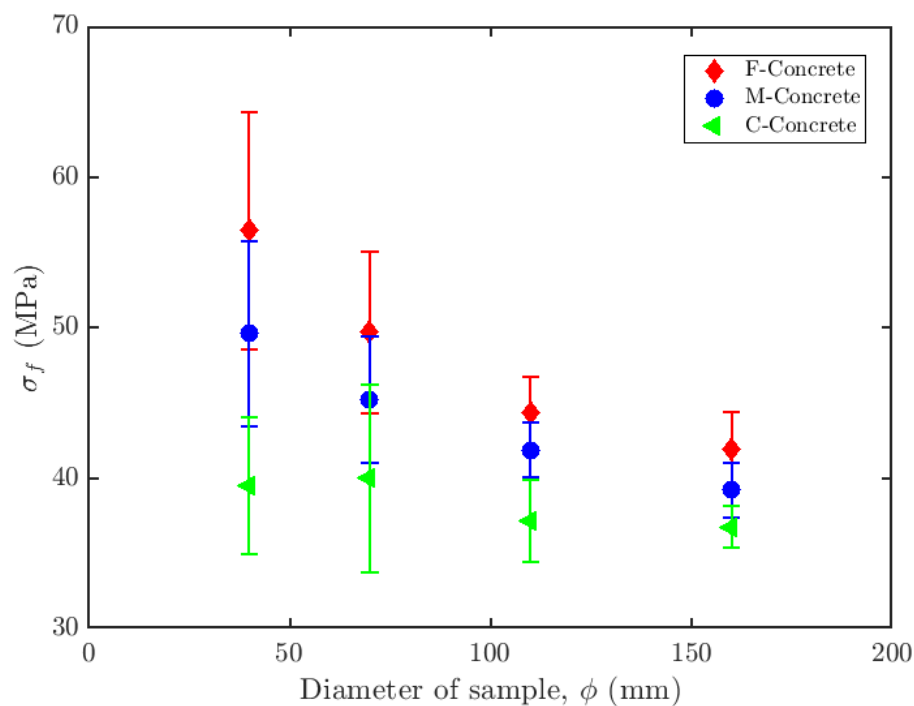


Fig. 6.2. Sample size effect on compressive strength for the different types of concrete.

6.2 The failure of weakest-link theory to account for statistical size effects on compressive strength

As stressed in Chapter 1, the weakest-link theory of failure relies on two fundamental assumptions, namely the independence of local crack initiation events, as well as pure brittleness meaning that the nucleation of any elementary crack at the microscale triggers immediately macroscopic failure. In this framework, depending on the hypothesis for the distribution of preexisting defect sizes, Weibull (Eq. (1.4)) (Weibull, 1951, 1939a) or Gumbel (Eq. (1.5)) (Gumbel, 2004, 1958) statistics are expected for the failure strength distribution $P_f(\sigma_f, L)$. Taking $L = \phi$ and $V \sim \phi^3$ (as $\phi/h = 0.5$ is kept constant in our samples), we can define the rescaled parameter, $W(\sigma_f)$ as follow:

$$W(L, \sigma_f) = \ln \left[-\ln \left(1 - P_f(\sigma_f) \right) \frac{1}{L^3} \right] \quad (6.1)$$

Combining Eq. (6.1) in one hand, and Eq. (1.4) or Eq. (1.5) in the other hand, $W(L, \sigma_f)$ should scale as $W(L, \sigma_f) \sim m \times \ln(\sigma_f)$ for Weibull statistics, or as $W(L, \sigma_f) \sim \left(\frac{\sigma_f}{\sigma_u} \right)$ for Gumbel statistics and, more importantly, should collapse for series of tests performed on the same material. The distributions of compressive strength for our three types of concrete, rescaled in Weibull or Gumbel diagrams, are shown in Fig. 6.3 and Fig. 6.4, respectively. Whatever the material, the compressive strength statistics obtained for different sample sizes do not collapse onto a single straight line, either in Weibull or Gumbel rescaled plots. This demonstrates the irrelevance of extreme value statistics, and so of the weakest-link framework, to account for the compressive failure of heterogeneous quasibrittle materials like concrete. In such double-logarithmic plots, strength distributions might appear roughly linear, however with an apparent m – (Weibull statistics, Fig. 6.3) or σ_u – value (Gumbel statistics, Fig. 6.4) strongly varying with the sample size considered (e.g. m – value varying between 7 and 30 for C-concrete). This is of course in contradiction with the weakest-link approach which assumes scale-independent parameters.

Fig. 6.5 shows the distributions of compressive strength for all sample sizes and all types of concrete in a normal probability plot. A clear collapse of the data along a straight line is observed for all concrete samples regardless of sample size and concrete mixture. We calculated the skewness and kurtosis for each individual distribution (fixed sample size and type of concrete) and found always small values (<1), without any specific trend with sample size (see Table 6.1). For the same individual distributions, we performed Shapiro-Wilk tests

with $\alpha = 0.01$ and found that the assumption of Gaussian statistics was never rejected. This demonstrates, with a good confidence and in agreement with previous works (Dayaratnam and Ranganathan, 1976; Neville, 2004; Unanwa and Mahan, 2014; Wright, 1954), that compressive strengths of concrete are distributed according to Gaussian statistics, at odds with the extreme value statistics associated with the weakest-link assumption. This also implies that a knowledge of the evolution of the mean strength $\langle \sigma_f \rangle$ and the associated standard deviation $\delta(\sigma_f)$ with external (sample) and internal (disorder) sizes will be sufficient to fully describe the size effects on the distributions of compressive strength (see section 6.6). Please note however that, at this stage, Gaussian statistics for strength appear as a robust, but empirical, fact. The theoretical framework described below argues for a power law dependence of the mean value of the strength and its standard deviation. However, it does not give a hint for a precise form of the strength distribution, which may have, particularly in the low strength probability range, a strong impact on reliability-based design rules. Hence, understanding the size effects on the mean and standard deviation alone might not be always sufficient for such reliability-based structural design.

Table 6.1. Compressive strength of concrete samples

Concrete group	Specimen size, $\phi \times h$ (mm x mm)	Compressive strength, σ_f (MPa)			
		Mean	SD	Skewness	Kurtosis
F	40x80	56.4	7.9	-0.21	-0.74
	70x140	49.7	5.3	0.08	-0.88
	110x220	44.3	2.4	-0.12	0.06
	160x320	41.9	2.4	0.29	-0.94
M	40x80	49.6	6.2	0.31	-0.73
	70x140	45.2	4.2	-0.58	-0.64
	110x220	41.9	1.9	0.04	-0.62
	160x320	39.2	1.8	-0.14	-0.66
C	40x80	39.5	4.6	0.47	-0.27
	70x140	40.0	6.3	-0.05	-0.86
	110x220	37.1	2.7	-0.35	-0.66
	160x320	36.7	1.4	-0.59	-0.05

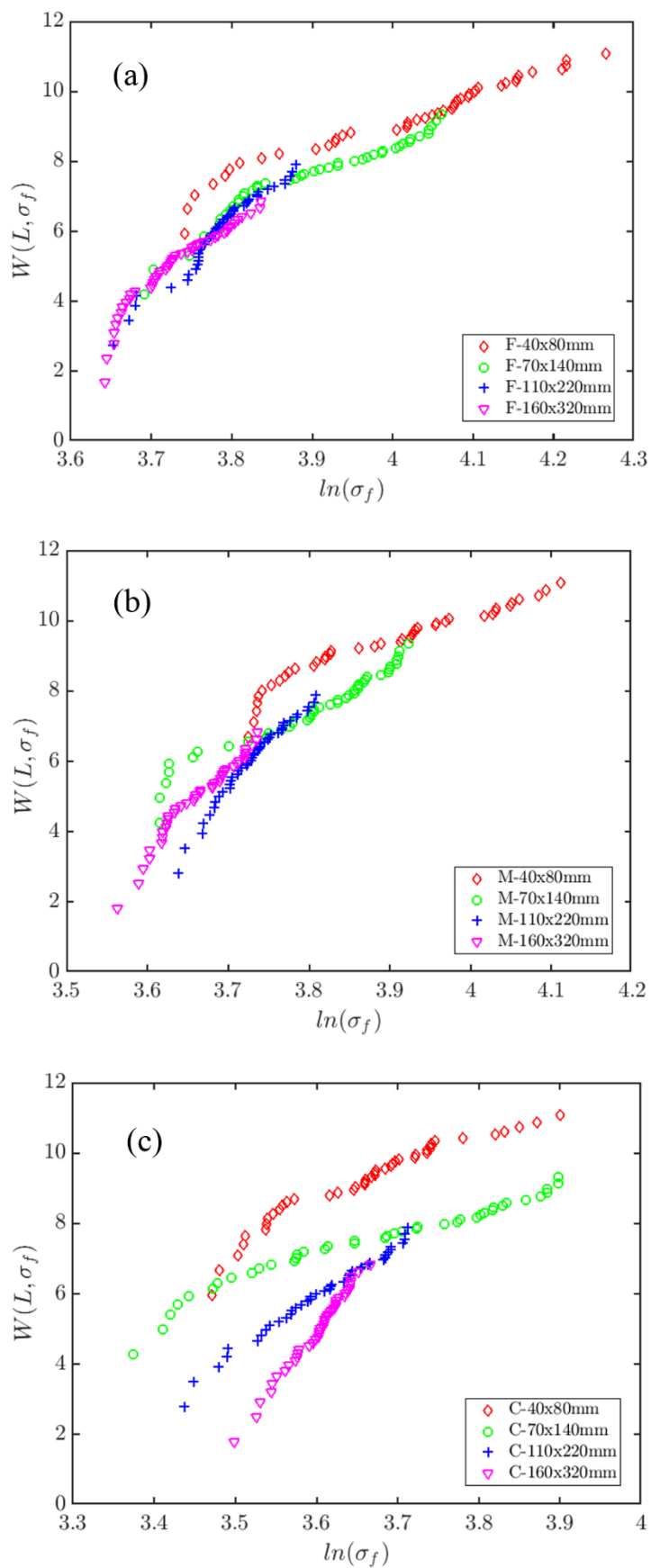


Fig. 6.3. Rescaled Weibull distributions of compressive failure strength of concrete; (a) F-concrete; (b) M-concrete ; and (c) C-concrete.

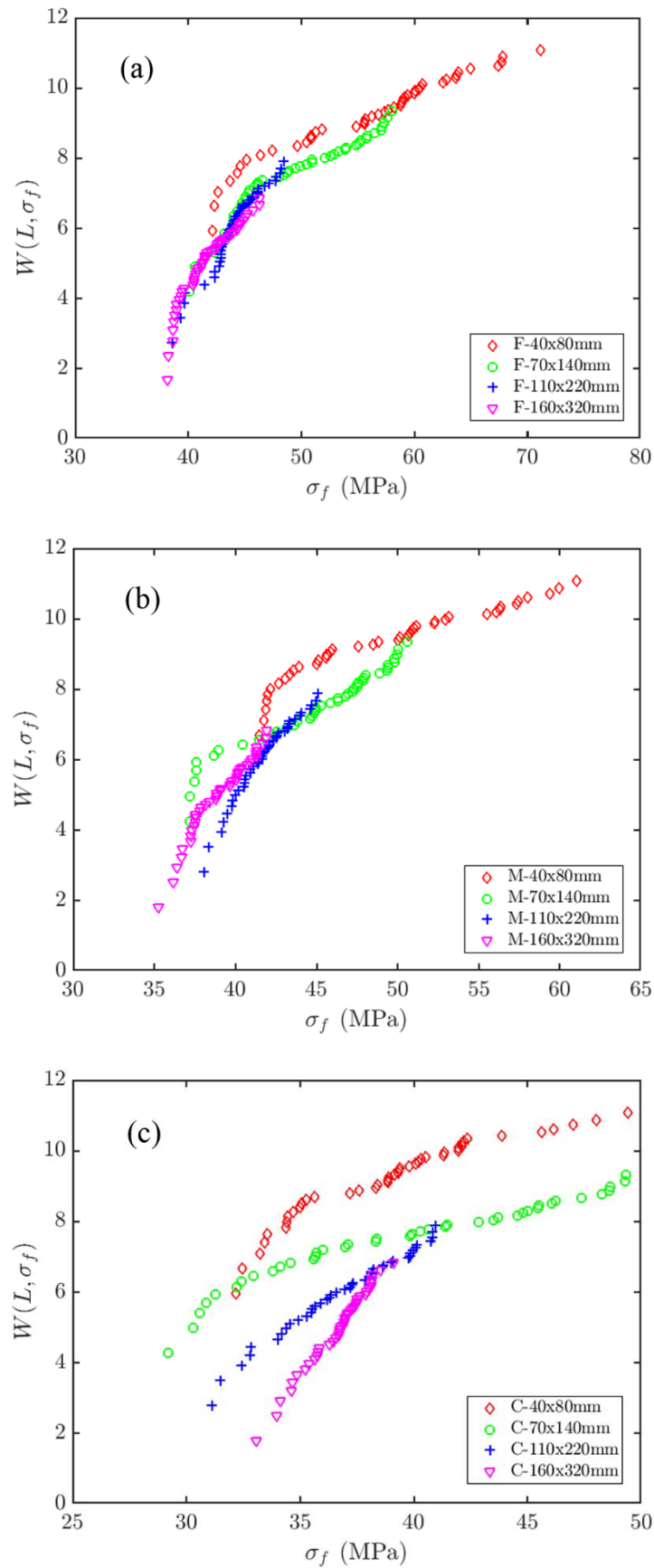


Fig. 6.4. Rescaled Gumbel distributions of compressive strength of concrete; (a) F-concrete; (b) M-concrete; and (c) C-concrete.

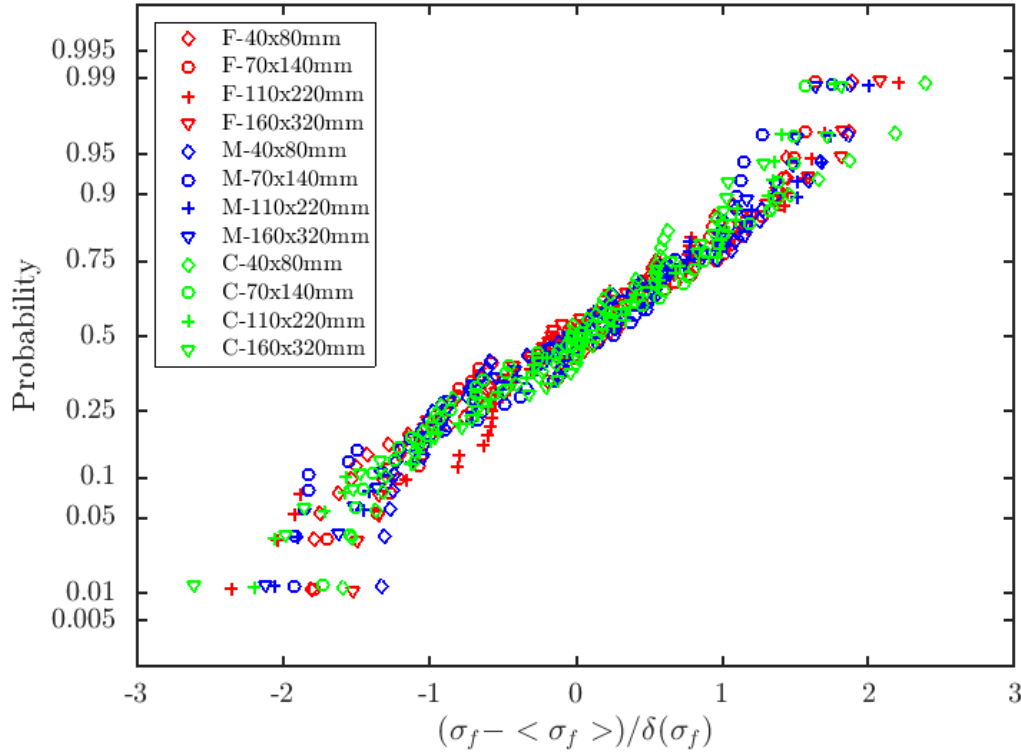


Fig. 6.5. Normal probability plot of the distributions of compressive strength for the different sample sizes and the three different concrete mixtures.

6.3 Compressive failure interpreted as a critical transition and associated finite size scaling

Tensile fracture of disordered materials has been widely studied in the context of statistical models identifying failure to a critical transition (Alava et al., 2006; Hansen et al., 2015; Herrmann and Roux, 1990). In (Weiss et al., 2014a), we argued that the compressive failure of heterogeneous materials can also be considered as a critical transition through a mapping onto the depinning transition of an elastic manifold. Indeed, the two phenomena share three fundamental ingredients, namely the (i) the presence of initial disorder (aggregates and pores in our case), (ii) a local threshold mechanism allowing to bypass an obstacle (depinning transition) or to initiate microcracking and damage from local disorder (our current problem), and (iii) long-ranged elastic interactions. Closely related approaches have been used to study crack propagation in heterogeneous materials (Bonamy and Bouchaud, 2011), plastic and brittle deformation in disordered solids (Dahmen et al., 2009; Talamali et al., 2012). However, significant differences were stressed recently between the two problems, owing to the nature of the elastic interaction kernel, which is convex in the case of classical elastic depinning but non-convex for plasticity, damage and failure, hence allowing localization in this last case

(Démery et al., 2017; Lin et al., 2014; Tyukodi et al., 2016). Nevertheless, we will see below that the analogy proposed in (Weiss et al., 2014a) is strong enough to provide powerful predictions in terms of correlation length evolution for damage and finite-size effects on failure.

In this previous work, damage was represented by a scalar field D at a mesoscopic scale ξ_d , which typically corresponds to the correlation length of the structural disorder of the material (see Chapter 3). In the context of compressive failure, the Coulomb criterion sets the local threshold mechanism, $|\tau| - \mu\sigma_N = \tau_C$, where τ and σ_N are the shear and normal stress, respectively, and μ is an internal friction coefficient. The heterogeneous nature of the material was accounted for by a statistical variability of the cohesion τ_C , $\delta(\tau_C)$. Once the local (Coulomb) threshold is reached locally, a damage event occurs, characterized by a local decrease of the elastic modulus over the mesoscopic scale, hence generating a redistribution of elastic stresses. This internal stress field induced by progressive damage plays a key role in the development of depinning models. To account for interactions between damaged “inclusions” in the material, a two-step strategy was developed to compute the internal stress field (see (Weiss et al., 2014b) for details). This allowed a complete mapping onto a depinning model, with the evolution of the damage field (playing the role of the deformed manifold) being given by:

$$M \frac{\partial D}{\partial t}(r) = \Re \left[\sigma_s^{ext} + \sigma_s^{el} \left(\{D\}, \bar{E}(\{D\}), \frac{r}{\xi_d} \right) - 2 \cos(\varphi) \tau_C(r, D) \right] \quad (6.2)$$

where \Re denotes the positive part, r is the position, M is a mobility coefficient, σ_s^{ext} is the external forcing (stress) term, σ_s^{el} is the internal stress induced by the damage field D , \bar{E} is the damage-dependent effective modulus and ξ_d is the characteristic length scale of the disorder τ_C .

From this mapping, several theoretical predictions obtained in the framework of the generic depinning transition can be tentatively extended to our problem. First of all, in the “thermodynamic limit” corresponding to an infinite system size ($L \rightarrow +\infty$), the asymptotic strength does not vanish, i.e. $\sigma_\infty > 0$. In addition, this mapping naturally entails a finite-size scaling for both the mean value of the compressive strength, $\langle \sigma_f \rangle$, and its associated variability, $\delta(\sigma_f)$ (Weiss et al., 2014a; Zapperi, 2012):

$$\frac{\langle \sigma_f \rangle}{\sigma_\infty} = \left(\frac{L}{L_m} \right)^{-\frac{1}{\nu_{FS}}} + 1 \quad (6.3)$$

$$\frac{\delta(\sigma_f)}{\sigma_\infty} = \left(\frac{L}{L_\delta} \right)^{-\frac{1}{\nu_{FS}}} \quad (6.4)$$

in which ν_{FS} is the finite-size exponent. The classical assumption is $\nu_{FS} = \nu$ (Bolech and Rosso, 2004), where ν is the exponent describing the divergence of the correlation length of damage as approaching failure, $\xi \sim \Delta^{-\nu}$, and Δ a reduced control parameter (e.g. $\Delta = (\sigma_f - \sigma)/\sigma_f$ for a stress-controlled loading). The mean-field (material-independent) prediction for depinning models is $\nu = 1$ (Ertas and Kardar, 1994), in full agreement with simulations from a progressive damage model giving $\nu = 1.0 \pm 0.1$ (Girard et al., 2012, 2010). The prefactors of the scaling laws (6.3) and (6.4) are here expressed as the length scales L_m and L_δ are constants, which are expected to be positively correlated with the microstructural disorder following the scaling:

$$L_{m,\delta} \sim \xi_d \left(\frac{\delta(\tau_c)}{\langle \tau_c \rangle} \right) \quad (6.5)$$

where $\delta(\tau_c)/\langle \tau_c \rangle$ represents the normalized variability of the local disorder (Weiss et al., 2014b). These length scales define the internal scales below which the fluctuations as well as the finite-size corrections become important compared with the asymptotic strength σ_∞ .

As both the mean and the standard deviation of the strength distribution are defined, this depinning framework implies that the statistical distribution falls within the Gaussian basin of attraction, without, however, a precise prediction for the form of the distribution. Numerical simulations of the classical depinning transition of an elastic manifold showed that the distributions vary between a Gaussian and a Gumbel form, depending on the disorder (Bolech and Rosso, 2004). We have demonstrated above very robust Gaussian statistics for the compressive strength of concrete, in agreement with previous work (Dayaratnam and Ranganathan, 1976; Neville, 2004; Unanwa and Mahan, 2014; Wright, 1954). This is also consistent with numerical results obtained for frictional granular media under multiaxial compression simulated from a discrete-element model (Weiss et al., 2014a), as well as for the yield stress in a depinning model of amorphous plasticity (Talamali et al., 2011). We can therefore speculate that the Gaussian form is quite general, showing a ‘‘universal’’ character in this failure/yielding context, whose origin, however, remains to be theoretically explained.

This finite-size scaling above entails (i) an apparent power law decay of the mean strength at small sizes ($L \ll L_{\delta,m}$), (ii) a non-vanishing strength for a system of infinite size ($L \rightarrow +\infty$), and (iii) a strength variability vanishing for ($L \rightarrow +\infty$) but increasing towards small sizes. If the points (i) and (ii) are superficially similar to size effect formulations proposed from deterministic approaches (see Chapter 1 and (Bazant, 1998; Carpinteri et al., 1995)), it is worth stressing that our approach is fundamentally different, deeply rooted in a generic, statistical physics framework (the critical depinning transition), and gives as well predictions for the scaling of the strength variability (point (iii)), for the finite-size exponent ν (which is material-independent and not empirical), and for the transition scales L_δ and L_m in relation with the microstructural characteristics of the material. We showed previously an excellent agreement between the predicted scale effect on mean strength (Eq. (6.3)) and available published data on various materials (different rocks, coal, ice, concrete,...) over a wide range of scales (Weiss et al., 2014a). However, it was not possible to test the two other scaling predictions (Eqs. (6.3) and (6.4)), owing to the limited statistics for a given material, and an absence of detailed microstructural characterization. We show below that our present results on concrete are in remarkable agreement with the scaling predictions (Eq. (6.3)) and (Eq. (6.4)), and in reasonable agreement with Eq. (6.5), thus providing a complete description of statistical extrinsic- and intrinsic-size effects on the compressive strength of concrete.

6.4 Finite size effects on compressive strength of concrete

Fig. 6.6 shows the best-fitted finite-size scaling (Eq. (6.3)) for the mean compressive strength of our concrete specimens, taking L as the sample diameter (ϕ) and using the AE-derived exponent $\nu_{FS} = \nu = 1.1$ (Table 5.2). Hence, non-linear fits were performed to extract the asymptotic strength σ_∞ as well as the length scale L_m , with values for the three different concrete mixtures presented in Table 6.2. Experimental data are in excellent agreement with the scaling prediction for the F-concrete (Fig. 6.6a) and the M-concrete (Fig. 6.6b), whereas the average strength of the 40x80 mm C-concrete specimens appears anomalously low compared with 70x140mm specimens of the same material, inducing a weaker agreement in this case. The finite-size scaling of the standard deviation (Eq. (6.4)) is shown on Fig. 6.7. Note that the condition $\delta(\sigma_f) \rightarrow 0$ when $L \rightarrow +\infty$ gives an additional constrain for the determination of the length scale L_δ (see insets in Fig. 6.7), which was performed using the asymptotic strengths σ_∞ obtained previously from the fitting of the mean strength. Once again, the agreement between the scaling prediction and the experimental data is remarkable for F- and

M-concretes, but weaker for C-concrete specimens. This weaker agreement for the C-concrete might be partly related to an imperfect casting procedure, owing to the relatively small ratio of scales between the maximum aggregate size of 25 mm, and the cardboard mold diameters used to prepare the 40x80 mm and 70x140 mm samples. We recall that we obtained slightly anomalously low P-wave velocities for the 40x80 mm samples of C-concrete (see Chapter 3 and Fig. 4.6). On the other hand, we were unable to detect any significant anomaly for these samples in terms of microstructural properties (Fig. 3.4 and Fig. 3.10).

The standard error, $\delta(\delta(\sigma_f))$, of the standard deviation of compressive strength, $\delta(\sigma_f)$, for each sample size of each concrete mixture shown in Fig. 6.7 was estimated from a bootstrap analysis. For this work, the following procedure was applied:

- 1- For each sample size of each concrete group (ϕ_i), we generated a number of n random strength values from a normal distribution with a mean and standard deviation given by the corresponding values of $\langle\sigma_f\rangle$ and $\delta(\sigma_f)$ reported in Table 6.1. We then calculated the standard deviation of this generated strength dataset. n is taken as the number of strength data for each sample size and each concrete mixture obtained from the compression tests ($n \geq 42$).
- 2- Repeating step 1 n times, we got a series of n values $\delta(\sigma_f)$. The standard deviation of this series was considered as the standard error of $\delta(\sigma_f)$ for a given concrete sample size of a given concrete mixture (ϕ_i).

The values of σ_∞ as well as of the two length scales L_m and L_δ obtained from the fit of equations (6.3) and (6.4) on the compressive strength statistics for the three materials are summarized on Table 6.2. The results show that, as expected, L_m and L_δ significantly vary with the concrete mixture; the relationship between these length scales and the microstructural characteristics of the materials is discussed in more details below. On the reverse, the asymptotic strength σ_∞ seems to only weakly depend on microstructural disorder. This is once again consistent with our depinning-like framework, as long as the average disorder strength $\langle\tau_C\rangle$ remains similar for the three materials: at very large scales, the disorder length scale ξ_d does no longer play any role on strength. Note that, taking $r=1.1$ and $D_b = L_m$, Eq. (1.2) would fit our mean strength data as well. However, the associated deterministic framework does not give any prediction for the associated variability $\delta(\sigma_f)$ and the probability of failure at stress σ_f , $P_F(\sigma_f)$.

Assuming an essentially material-independent asymptotic strength σ_∞ and $\nu_{FS} = 1.1$, the finite-size effects on both the mean strength (Eq. (6.3)) and the associated variability (Eq. (6.4)) should resume to a collapse of all data (all sample sizes, all materials) on a $[\langle\sigma_f\rangle \text{ vs. } (L/L_m)^{-1/\nu_{FS}}]$ or a $[\delta(\sigma_f) \text{ vs. } (L/L_\delta)^{-1/\nu_{FS}}]$ plot, respectively. Using a material-independent value of $\sigma_\infty \approx 36.2$ MPa, the excellent collapses obtained (Fig. 6.8) are a further confirmation of the pertinence of the underlying theoretical framework.

Using a mean-field prediction for the exponent, $\nu_{FS} = 1$ (Bolech and Rosso, 2004; Ertas and Kardar, 1994; Roux and Hild, 2002), we have also achieved a good agreement between our experimental data and the theoretical predictions of mean strength (Eq. (6.3)) and associated variability (Eq. (6.4)) (see (Vu et al., 2018b) for more details).

Table 6.2. Finite-size scaling parameters obtained for the three concrete mixtures

Concrete group	σ_∞ (MPa)		L_m (mm)		L_δ (mm)	
	Mean	SD	Mean	SD	Mean	SD
F	36.5	4.0	21.1	0.3	7.5	0.2
M	35.9	4.3	14.3	0.5	5.8	0.2
C	36.0	6.2	3.6	2.4	5.7	0.7

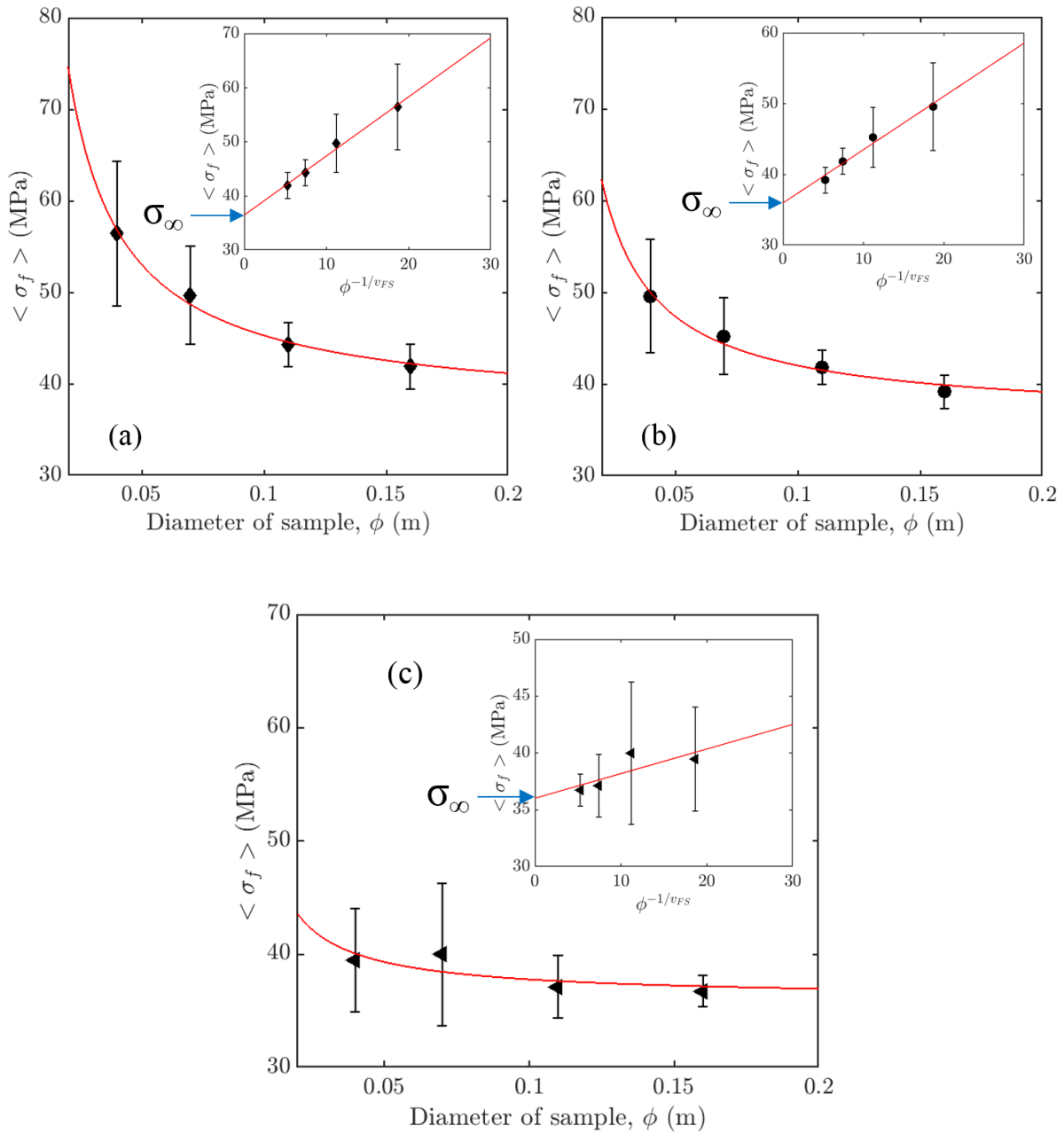


Fig. 6.6. Finite-size effect on the mean value of uniaxial compressive strength. (a) F-concrete; (b) M-concrete; (c) C-concrete. Main graphs show the mean compressive strength, $\langle \sigma_f \rangle$ as a function of specimen size. Black symbols are the experimental data obtained from the uniaxial compressive tests, with the associated standard deviation $\delta(\sigma_f)$. Red curve is the fitting by Eq. (6.3). Insets show the same data and fits in a $[\langle \sigma_f \rangle$ vs. $\phi^{-1/v_{FS}}$] graph. In this smaller graph, the fitting by Eq. (6.3) becomes a straight line and the asymptotic strength σ_∞ is determined.

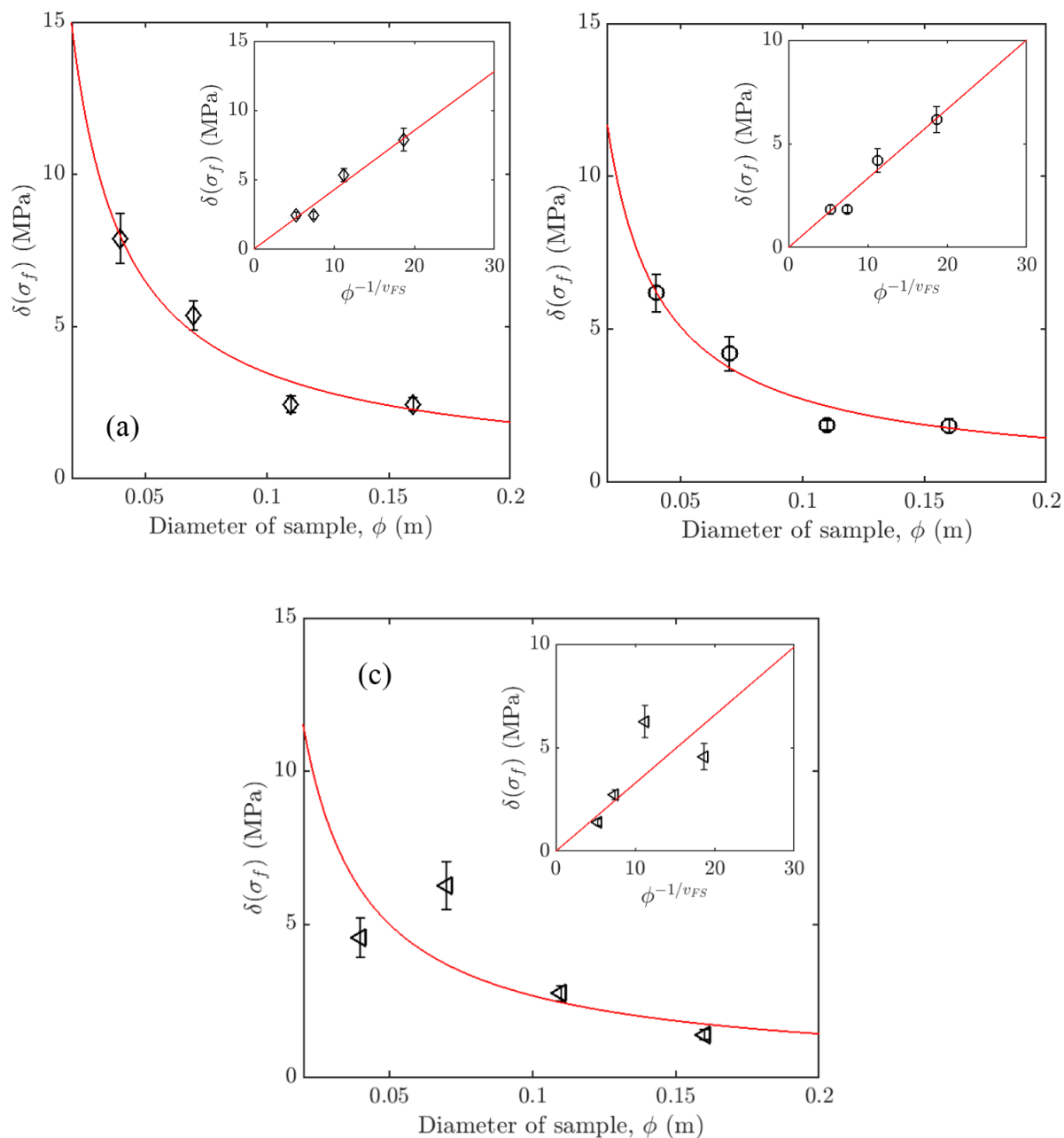


Fig. 6.7. Finite-size effect on the standard deviation of uniaxial compressive strength. (a) F-concrete; (b) M-concrete; (c) C-concrete. Main graphs show the standard deviation of compressive strength, $\delta(\sigma_f)$ as a function of specimen size. Black symbols are the experimental data obtained from the uniaxial compressive tests. Red curve is the fitting by Eq. (6.4). Insets show the same data and fits in a $[\delta(\sigma_f) \text{ vs. } \phi^{-1/v_{FS}}]$ graph where Eq. (6.4) is a straight line.

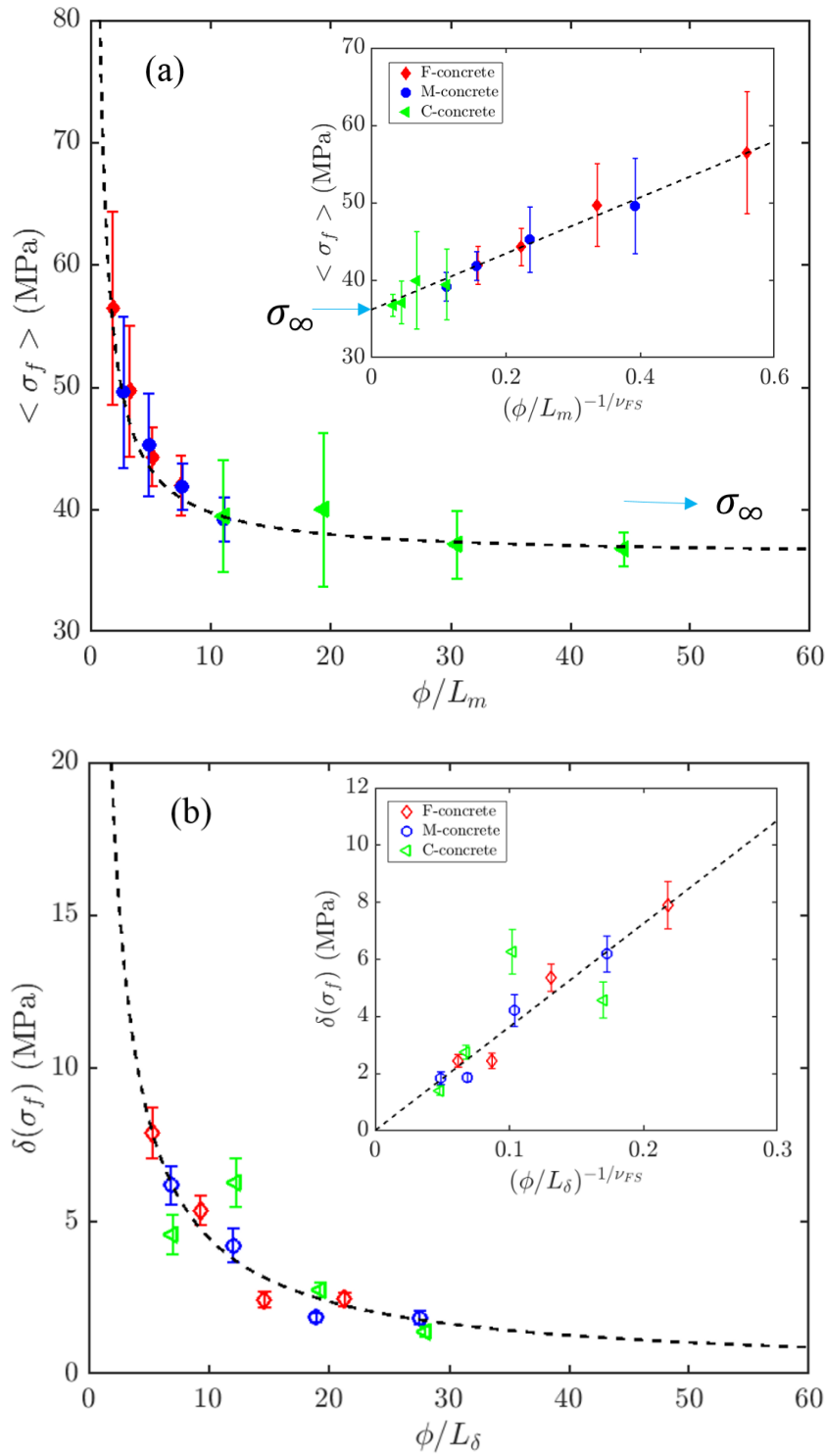


Fig. 6.8. Finite-size effects on the uniaxial compressive strength of concrete: (a) for the mean strength, $\langle \sigma_f \rangle$ and (b) for the standard deviation of strength, $\delta(\sigma_f)$. Main graphs show the relationship between $\langle \sigma_f \rangle$ and $\delta(\sigma_f)$ with the ratio of sample size (ϕ) to the length scales L_m and L_δ , respectively. Black dashed-lines are the fits by Eq. (6.3) for the mean strength (a), and Eq. (6.4) for the standard deviation of strength (b). Insets show the same data and fits on $[\langle \sigma_f \rangle vs. (\phi/L_m)^{-1/\nu_{FS}}]$ and $[\delta(\sigma_f) vs. (\phi/L_\delta)^{-1/\nu_{FS}}]$ plots where the fits by Eq. (6.3) and Eq. (6.4) are the straight lines.

6.5 The role of microstructural disorder on finite-size effects

As explained in section 6.3, we expect, from our theoretical framework (Weiss et al., 2014a), the length scales L_m and L_δ to depend on disorder following Eq. (6.5). As detailed in Chapter 3, the microstructural disorder of our concrete materials can be decomposed into two main categories, the aggregates and sand particles in one hand, pores in the other hand. At first glance, one might expect the aggregates/sand, which shape the global autocorrelation length ξ_g (see section 3.4), to control L_m and L_δ as well, i.e. $\xi_d \approx \xi_g$. This would imply a positive correlation between L_m and L_δ in one hand, and ξ_g on the other hand. Unexpectedly, Fig. 6.9 shows instead in both cases an affine dependence with a negative slope: the coarser the aggregates, the smaller the length scales L_m and L_δ . This anticorrelation is at odds with our initial naive expectation of the role of the concrete mix on the finite size effect.

We now discuss the role of pores. To consider the possible impact of the pore structure on the finite size effects on strength, we first set down $\xi_d = \xi_p$. The next step would be to estimate the variability of the local stress threshold, $\delta(\tau_c)/\langle\tau_c\rangle$. However, we have shown in section 3.5 and Fig. 3.6 that pores have a roughly spherical shape. It is well known from (Kirsch, 1898) that the stress concentration factor K_t resulting from the presence of a spherical hole in an elastic matrix, which will drive local damage initiation, is independent of hole size, as long as the hole diameter is small compared with sample size (a condition fulfilled for our samples, see section 3.5). Hence, we can reasonably assume that $\xi_d \left(\frac{\delta(\tau_c)}{\langle\tau_c\rangle} \right)$ will be essentially set by the pore correlation length ξ_p . Fig. 6.10a and b show the relationship between ξ_p and the scales L_m and L_δ , respectively. This time, positive correlations are observed in both cases. For the size effect on strength variability $\delta(\sigma_f)$, the data suggest a non-vanishing L_δ for ξ_p , which might be the fingerprint of the experimental scatter, independent of material properties but resulting from measurement error, imperfections of the samples geometry, etc.. Overall, however, owing to the limited number of different materials analyzed and the simplifying assumptions considered for the description of the internal disorder, we can conclude that (i) the finite size effects on strength are mainly controlled by the pore structure and (ii) the impact of this microstructural disorder is in reasonable agreement with our theoretical framework. An extension of this work to other concrete materials with various microstructures would be necessary to refine this analysis. Finally, the negative correlation observed between the aggregate/sand disorder length scale ξ_g and the scales L_m and L_δ (Fig. 6.9a and b) appears as

an indirect consequence of the fact that both the porosity and ξ_p decrease with increasing aggregate size (see section 3.5), a likely consequence of the casting procedure.

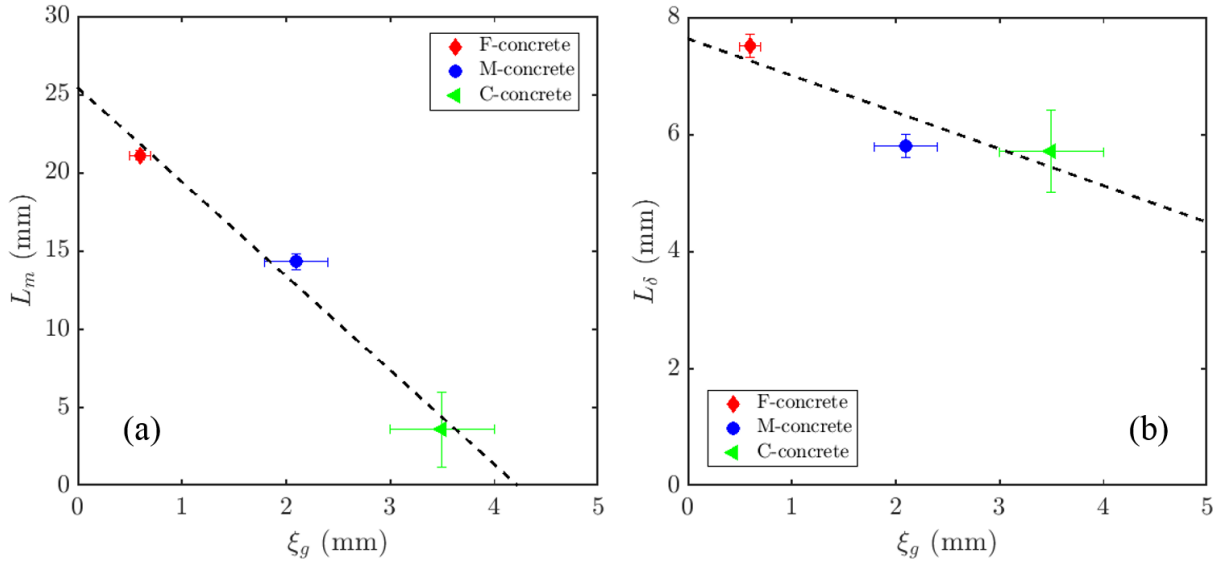


Fig. 6.9. Relationship between the global autocorrelation length, ξ_g and the length scales (a) L_m ; and (b) L_δ . Black dashed-lines are the linear fits.

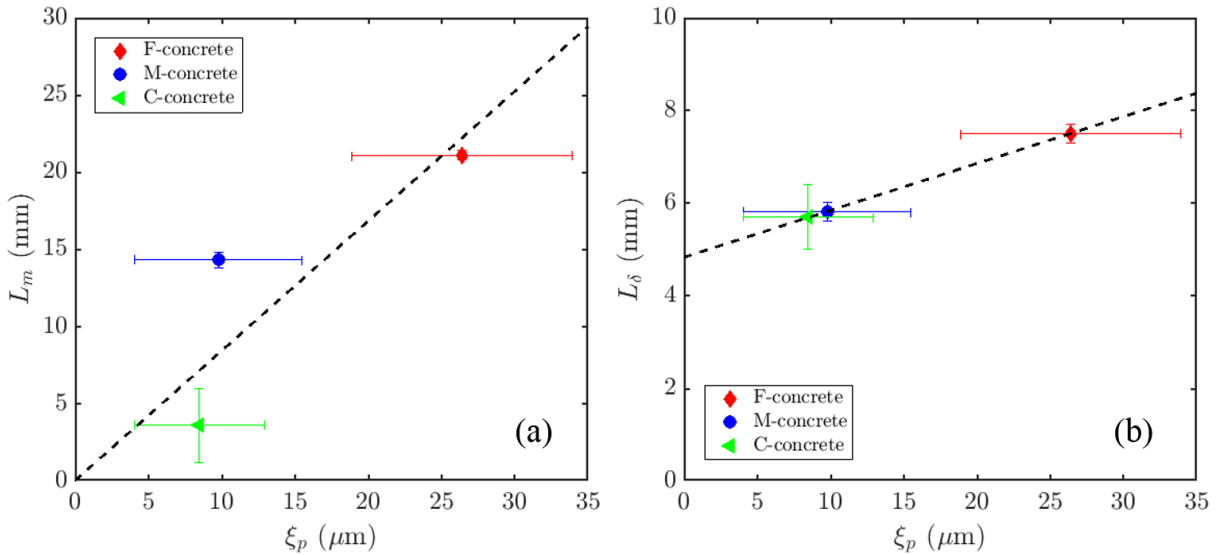


Fig. 6.10. Relationship between the autocorrelation length of the pore structure, ξ_p and the length scales (a) L_m ; and (b) L_δ . Black dashed-lines are the linear fits.

6.6 Discussion and Conclusion

From an interpretation of compressive failure of heterogeneous materials as a critical transition from an intact to a failed state (Amitrano, 2012; Girard et al., 2012; Weiss et al., 2014a), and mapping this problem to the depinning transition of an elastic manifold (Weiss et al., 2014a), we derived finite-size scaling laws for the mean strength (Eq. (6.3)) as well as the associated variability (Eq. (6.4)). Using an extensive dataset of compression tests on four sample sizes and three different concretes, we demonstrated the irrelevance of the weakest-link theory to account for statistical size effects on compressive strength of quasibrittle materials. We instead obtained a remarkable agreement between our experimental results and the predictions of our theoretical framework. A combination of Eqs. (6.3) and (6.4) with Gaussian statistics (see section 6.2 and Fig. 6.5) gives a complete description of the failure probability under an applied stress σ for a system of size L (Weiss et al., 2014a):

$$P_F(\sigma, L) = \frac{1}{2} \left[1 + \operatorname{erf} \left(\frac{\sigma - \sigma_\infty \left(1 + \left(\frac{L}{L_m} \right)^{-1/\nu_{FS}} \right)}{\sqrt{2} \sigma_\infty \left(\frac{L}{L_\delta} \right)^{-1/\nu_{FS}}} \right) \right] \quad (6.6)$$

, where the two length scales L_m and L_δ are linked to the correlation length of the microstructural disorder (Eq. (6.5)), although the current dataset does not allow to show if the associated proportionality constants are material-dependent parameters, or would exhibit some sort of universality. We recall however that (i) Gaussian strength statistics is an empirical fact, not a prediction of our theoretical framework and (ii) the exact shape of the strength distribution, particularly in the low strength probability range, may have a significant impact on reliability-based structural design.

In this framework, the asymptotic strength σ_∞ becomes the only relevant, material-dependent parameter for the dimensioning of large-scale structures from an upscaling of small-scale laboratory mechanical tests. At those large scales, the intrinsic strength variability is expected to vanish, leaving only a variability related to the loading configuration and the geometry of the structure, and/or with measurement noise.

Surprisingly, for the materials studied here (classical concretes made of water, cement, sand and aggregates), the concrete mix does not have a significant impact on this asymptotic strength σ_∞ . We also obtained a similar conclusion from applying the scaling (6.3) to describe sample size effect on the mean compressive strengths of three different concrete mixtures

reported by (Blanks and McNamara, 1935) (see Appendix C for more details). This material-independent of σ_∞ can be interpreted as follows: in such composite material, as long as the nature of the matrix and of the inclusions remains the same and the size of the structure/sample is much larger than the microstructural disorder correlation length ($L \gg \xi_d$), the failure stress will be mostly insensitive to the mix proportions. However, changing the nature of the matrix or of the inclusions (e.g. lightweight (Babu et al., 2006) or high-strength (del Viso et al., 2008) concretes) will, of course, significantly modify σ_∞ .

In our tests, the concrete mix did not control either the length scales L_m and L_δ that materialize the scales below which finite-size corrections becomes significant relatively to the asymptotic mean strength. Instead, our results argue that L_m and L_δ are mainly set by the pore structure. In our theoretical framework where microstructural disorder controls damage nucleation within an elastic matrix, this is not entirely surprising, as the contrast of elastic stiffness (and so the intensity of stress concentrations (Weiss et al., 2014b)) is obviously much larger between the cement matrix and air voids than between the matrix and sand particles or aggregates. When large enough, porosity is known to significantly impact the failure strength of concrete (Chen et al., 2013; Koliass, 1994; Kumar and Bhattacharjee, 2003; Lian et al., 2011). However, as the porosity of our samples always remained below 5% (Table 3.1), its role on σ_∞ was not significant. Hence, the disordered pore structure only affected the length scales L_m and L_δ (see section 6.5). The combination of those effects might lead to some counter-intuitive results: At small sizes, the F-concrete, which exhibits the largest porosity (Table 3.1) and the lowest Young's modulus (Table 4.2), is the strongest material under compressive loading (Fig. 6.11).

More globally, the results presented here, as well as the consequences of our framework in terms of size effects on both the mean strength, the associated variability, and the probability of failure at a given stress, of the determination of an asymptotic strength, of the role of the microstructural disorder, call for a re-evaluation of classical design rules and of the establishment of safety regulations from laboratory tests.

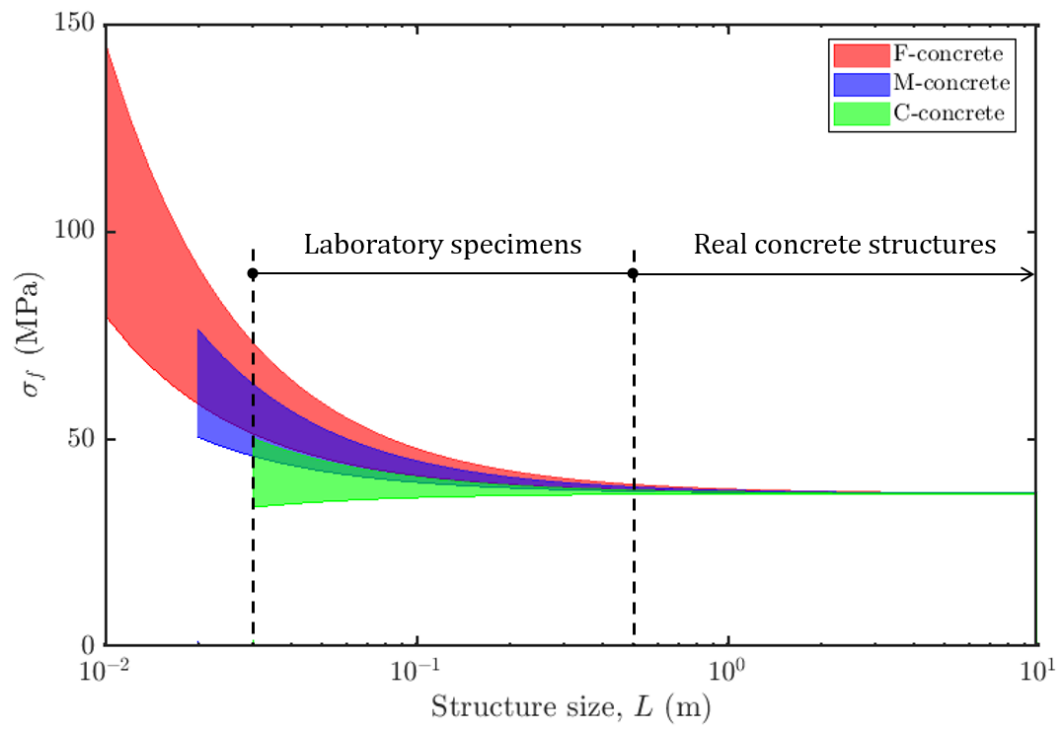


Fig. 6.11. Illustration of size effect on the compressive failure strength for the different concrete mixtures.

Chapter 7

Revising the concept of characteristic compressive strength of concrete

Based on

Vu, C. C., Plé, O., Weiss, J., Amtrano, D. (2018), Revisiting the concept of characteristic compressive strength of concrete, submitted to *Cement and Concrete Research*.

7.1 Introduction

In civil engineering, concrete is mostly used under compression loading configurations since its compressive strength is much larger than its tensile and/or flexural strengths. Generally, the tensile and flexural strengths of concrete are of the order of respectively ~10% and ~15%, of the compressive strength (Mehta and Monteiro, 2006). Furthermore, the compressive strength is often considered as a marker of the concrete quality because it is directly related to the structure of the hydrated cement paste (Neville, 2004). For these reasons, the compressive strength is usually used as the basic for taking decisions regarding the strength and serviceability of concrete members and structures (Mehta and Monteiro, 2006).

For the purpose of structural design, concrete is classified into several strength classes based on the so-called characteristic compressive strength (f_{ck}) in most of European standards (e.g. (EN 1992, 2004) and (NF EN 206-1, 2004)) or on the specified compressive strength (f'_c) in the American standard (ACI 318-05, 2005). Hereafter, both f_{ck} and f'_c are referred as the characteristic strength (f_{ck}). For example, in the standard (EN 1992, 2004), the concrete strength class ranges from C12/15 to C90/105, meaning that the characteristic strength of

cylinders and that of cubic specimens are respectively in a range 12-90MPa and 15-105MPa. During the design stage, designers must size the dimensions of the concrete members to resist the imposed loads based on some compressive strength classes. These chosen strength grades are then used to define the concrete mix to be used for construction. In the construction stage, the concrete used must be in conformity with the strength requirements previously specified from the characteristic strength by the designers. Therefore, the characteristic strength can be considered as a key property for structural design, concrete mix design and quality control of concrete.

Implicitly assuming a normal distribution for the compressive strength of concrete samples, in agreement with experimental data (ACI 318-05, 2005; EN 1992, 2004; Mehta and Monteiro, 2006; Neville, 2004), the characteristic strength of concrete (f_{ck}) is calculated from the corresponding mean value (f_{cm}) and standard deviation (s) as follows:

$$f_{ck} = f_{cm} - \lambda \cdot s \quad (7.1)$$

, where the constant λ sets the acceptable percentage of tests that will fail under a stress lower than f_{ck} (e.g. a fractile of 5% is used in (EN 1992, 2004)). These two statistical parameters (f_{cm} and s) are obtained from an adequate number of uniaxial compression tests (e.g. ≥ 30 tests recommended in (ACI 318-05, 2005)), carried out on standard concrete specimens at a minimum age of 28 days. Different standard samples are used in different countries and sometimes even in the same country. For instance, both 150x300-mm (or 6x12-in.) cylinders and 150-mm (or 6-in.) cubes are used as standard specimens in the United States (ACI 318-05, 2005; ASTM C39/C39M-14, 2014; Mehta and Monteiro, 2006) and in most European countries (EN 1992, 2004), while 160x320-mm cylinders are used in France (NF EN 12390-3, 2012; NF EN 206-1, 2004). However, quasibrittle materials in general, and concrete in particular, exhibit a size-dependent behavior on the nominal compressive strength (Bazant and Planas, 1998). Precisely, the mean compressive strength (f_{cm} in Eq. (7.1)) decreases with increasing specimen size (Bazant, 1999, 1998; Burtscher and Kollegger, 2003; del Viso et al., 2008; Muciaccia et al., 2017; Ozbolt and Eligehausen, 1995). This has been confirmed from our experimental results (see Chapter 6). In addition, we also demonstrate that the strength variability of concrete (s in Eq. (7.1)) decreases with increasing sample size (see Chapter 6). These size effects on both f_{cm} and s imply, from relation (7.1) that the characteristic compressive strength (f_{ck}) will depend on the size of tested concrete samples, an effect generally not taken into account in concrete mix and structural design. Such size dependence implies that f_{ck} is actually not a characteristic of the material.

In the preceding chapter, we have indicated that (i) a very large system ($L \rightarrow +\infty$) will have a non-vanishing asymptotic strength ($f_{cm(L \rightarrow +\infty)} \rightarrow \sigma_\infty$) but a vanishing strength variability ($s_{(L \rightarrow +\infty)} \rightarrow 0$), and (ii) the pore structure in hardened concrete samples, rather than the concrete mix, plays a key role in controlling the size effects on compressive strength. These results suggest two important points in terms of estimating the characteristic compressive strength of concrete as follows:

- 1- In this framework, the asymptotic strength (σ_∞), which is by construction independent of system size, appears as the genuine characteristic compressive strength of concrete;
- 2- A laboratory concrete specimen can only be considered as a standard specimen if its size is very large compared with the characteristic size of its pore structure.

Following this statistical size effect analysis of the compressive strength of concrete detailed in Chapter 6, we will here revisit the concept of characteristic strength by taking account the two points noted above, through a comparison with the classical expressions of characteristic strength proposed in concrete design codes ((EN 1992, 2004) and (ACI 318-05, 2005)).

From the point of view of the design and behavior of concrete structures, not only the compressive strength but also the modulus of elasticity is important (Zhou et al., 1995). While the compressive strength is used for calculating structures following the requirements of ultimate limit states, the elastic modulus is used for estimating the deformation as well as for the design of sections of structural concrete elements according to the serviceability limit state (ACI 318-05, 2005; EN 1992, 2004). In most concrete design codes, the modulus of elasticity is estimated from empirical expressions that assume a direct dependence of the elastic modulus on the compressive strength. According to these expressions, as the compressive strength increases, the modulus of elasticity also increases but at a decreasing rate (Neville, 2004). Therefore, the sample size dependence of compressive strength implies that the elastic modulus will depend on the size of the concrete sample. However, as demonstrated in section 4.4, for a given concrete mixture, there is no significant sample size effect on the elastic properties, including the static and dynamic elastic moduli. This observation, a consequence of size effects on compressive strength, calls for a re-examination of the expressions of elastic modulus in terms of compressive strength.

Before presenting the results and discussion about the characteristic compressive strength by taking into account statistical size effects (section 7.3), in the next section, we will

discuss the relationship between the compressive strength and elastic modulus of our concretes and also compare it with those given by the empirical expressions of EN 1992 and ACI 318 codes. Some overall conclusions of this chapter are given in section 7.4.

7.2 Relationship between compressive strength and Young's modulus

Current building codes (e.g. (ACI 318-05, 2005); (EN 1992, 2004)) and many authors (see reviews in (Mehta and Monteiro, 2006; Neville, 2004; Noguchi et al., 2009; Vilanova et al., 2011)) proposed several empirical formulas relating the elastic modulus to the compressive strength and/or the density of concrete.

According to (EN 1992, 2004), the static modulus of normal-weight concrete can be calculated from:

$$Y_s = 22 \left(\frac{f_{cm}}{10} \right)^{0.3} \quad (7.2)$$

where Y_s is the secant modulus of elasticity (in GPa) and f_{cm} is given in MPa.

In the standard (ACI 318-05, 2005), the modulus of elasticity, Y_s (in MPa), can be estimated from:

$$Y_s = \rho^{1.5} 0.043 \sqrt{f'_c} \quad (7.3)$$

where ρ is the density (in kg/m³) and f'_c (in MPa) is the specified compressive strength of cylindrical concrete samples.

We first note that these empirical formulas are dimensionally inconsistent (e.g. Pa vs. Pa^{0.3} in Eq. (7.2)). Besides this, Fig. 7.1, which shows the correlations between the compressive strength, σ_f , and the static (Y_t and Y_s) and dynamic (Y_d) elastic moduli for all of our concrete samples, epitomizes several problems while using such empirical relations. In this figure, we compare our experimental results with the expressions (7.2) and (7.3), taking ($\langle \sigma_f \rangle = f_{cm}$) and ($\langle \sigma_f \rangle = f'_c$). From this, we observed that:

(i) the values of both Y_t and Y_s are systematically much smaller than the empirical predictions, whatever the concrete samples. For the dynamic elastic moduli, Y_d , experimental data are below the empirical predictions for F-concrete but above the predictions for M- and C-concretes.

(ii) for a given dataset (fixed sample size and material), the correlations of static moduli Y_t and Y_s with σ_f are either very weak or insignificant (see Table 7.1). Merging strength data for all sample sizes of a given material, the absence of correlation is clear as well (see Fig. 7.1a, b and c). This is expected, as we observed a size effect on strength (see Chapter 6) but not on the elastic modulus (section 4.4).

(iii) considering now all samples (all sizes, all materials), the disagreement with the empirical formulas (7.2) and (7.3) is even more striking (Fig. 7.1d). Indeed, increasing the aggregate size implies an increase of the elastic modulus, as expected, while F-concrete showed, in average, larger strengths than M- and C-concretes. As explained in more details above, this last point is a consequence of the size effects on strength, in relation with the pore content of our materials.

This demonstrates the absence of significant and meaningful link between elastic modulus (either static or dynamic) and compressive strength. This, we argue, is not surprising, given that the elastic modulus is directly related to elastic (linear) deformation, while the compressive strength is affected by the non-linear behavior due to the progressive development of damage and microcracking (Mehta and Monteiro, 2006; Neville, 2004). For a perfect crystalline material without defects, the ultimate (tensile) strength, resulting from pure brittle failure, would be proportional to the elastic modulus (Miannay, 1998). For a disordered material like concrete under compression, such scenario is unrealistic.

In many cases (e.g. F-concrete samples in this study), using empirical laws such as Eq. (7.2) or Eq. (7.3) to estimate elastic properties from the compressive strength would lead to an overestimation (an unsafe result). Therefore, to measure the elastic modulus from the static load test, rather than from such empirical relations, appears much safer for concrete structural design.

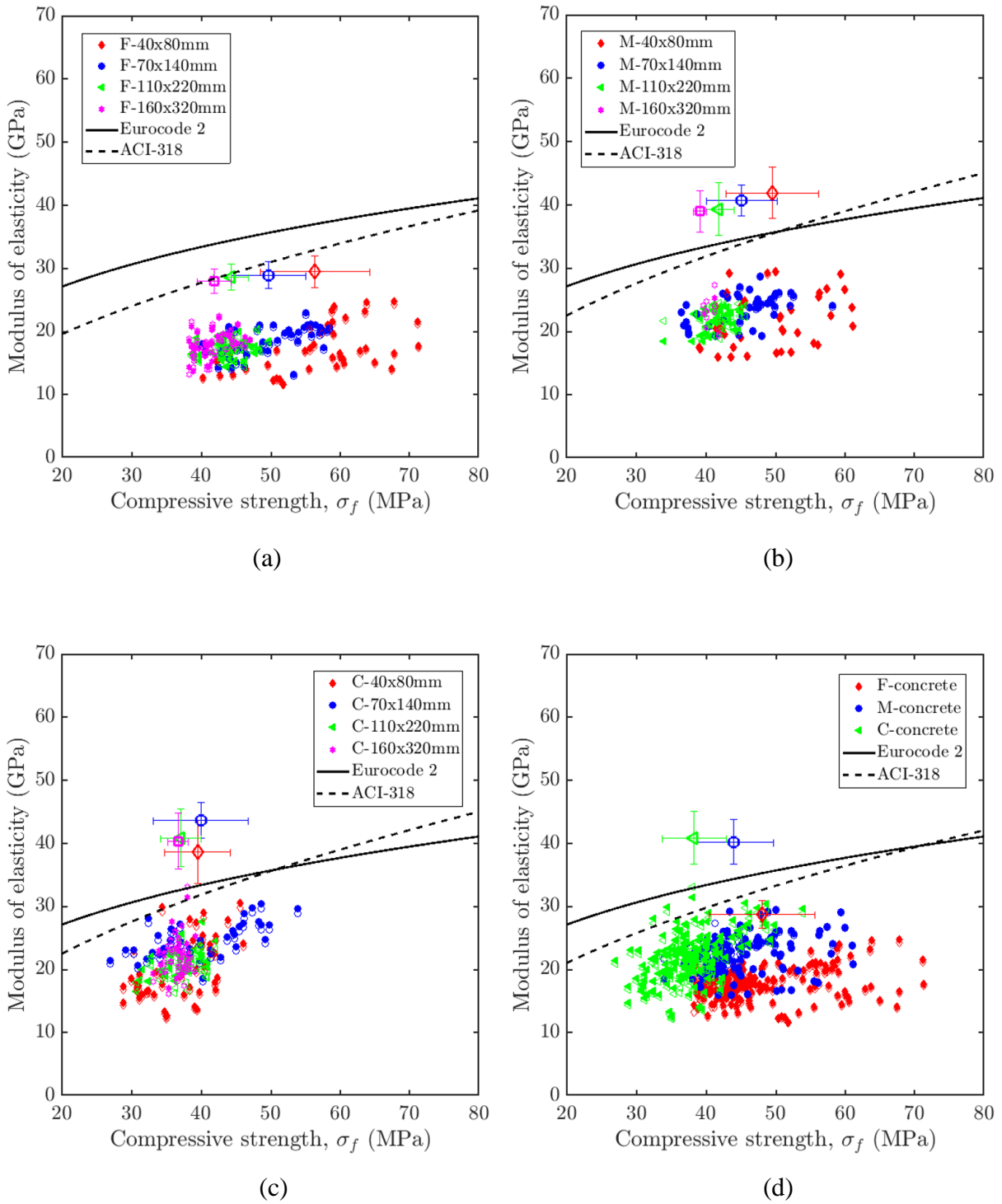


Fig. 7.1. Relationships between the compressive strength and elastic modulus of concrete samples: (a) for F-concrete; (b) for M-concrete; (c) for C-concrete and (d) for all of concrete samples. Closed symbols are the static elastic moduli (Y_t), open symbols are the secant moduli (Y_s) and unfilled symbols with error bars are the dynamic elastic moduli (Y_d).

Table 7.1. Correlation coefficient between the compressive strength (σ_f) and static moduli (Y_t and Y_s) for different concrete samples.

Concrete mixture	Sample sizes, (mm x mm)	σ_f vs. Y_t	σ_f vs. Y_s
F	40x80	0.42	0.42
	70x140	0.43	0.43
	110x220	0.19	0.09
	160x320	0.27	0.21
M	40x80	0.21	0.21
	70x140	0.38	0.38
	110x220	0.41	0.20
	160x320	-0.06	-0.36
C	40x80	0.40	0.40
	70x140	0.48	0.48
	110x220	0.45	0.15
	160x320	0.12	0.03

7.3 Characteristic compressive strength of concrete

Concrete design codes evaluate the characteristic compressive strength from subtracting the strength variability from the mean compressive strength obtained from a set of tested concrete specimens with a unique size (see Eq. (7.1)). However, due to the sample size effects on both the mean value and the associated variability of compressive strength (see Chapter 6), this traditional estimation necessarily leads to size effects on the characteristic compressive strength f_{ck} as estimated from Eq. (7.1). This questions the concept of characteristic strength itself, which should be representative of the material only and independent of external size. In this section, we show that the asymptotic strength, deduced from the external size effects towards the limit $L \rightarrow +\infty$, represents the genuine characteristic strength of concrete. We also propose some recommendations to determine accurately this asymptotic strength as well as to check the conformity of concrete with strength requirements.

7.3.1 Asymptotic versus characteristic compressive strength

Owing to the vanishing strength variability for a system of infinite size ($L \rightarrow +\infty$), the asymptotic strength σ_∞ can be considered as the genuine characteristic strength of concrete to be used to design large scale structures. As mentioned in section 7.1, the characteristic strength is instead classically calculated from the mean value and the standard deviation of compressive strength from the relation (7.1). In (EN 1992, 2004), the characteristic strength (f_{ck}) is defined as that strength value below which only 5% of the compression tests are expected to fall. This corresponds to $\lambda = 1.645$ in Eq. (7.1) (see Fig. 7.2). In (ACI 318-05, 2005), the tolerance is larger (10%), corresponding to $\lambda = 1.34$ (see Fig. 7.2).

Hence, from the mean strengths $\langle \sigma_f \rangle$ and standard deviations $\delta(\sigma_f)$ reported in Table 6.1, we can compute the characteristic strengths for each concrete mixture and sample size, as defined by the EN 1992 and the ACI 318 codes, using respectively $\lambda = 1.645$ and $\lambda = 1.34$ in Eq. (7.1).

Fig. 7.3 shows that the so-defined ‘‘characteristic’’ strength differs for the three different concrete mixtures, and is sample size dependent. This is in full contrast with the fact that the asymptotic strength σ_∞ is, by construction, sample size independent, but also independent of the concrete mix for the three materials prepared for this study (of course, this does not mean that σ_∞ should be the same for all types of concrete) (see Chapter 6). In addition, we note that

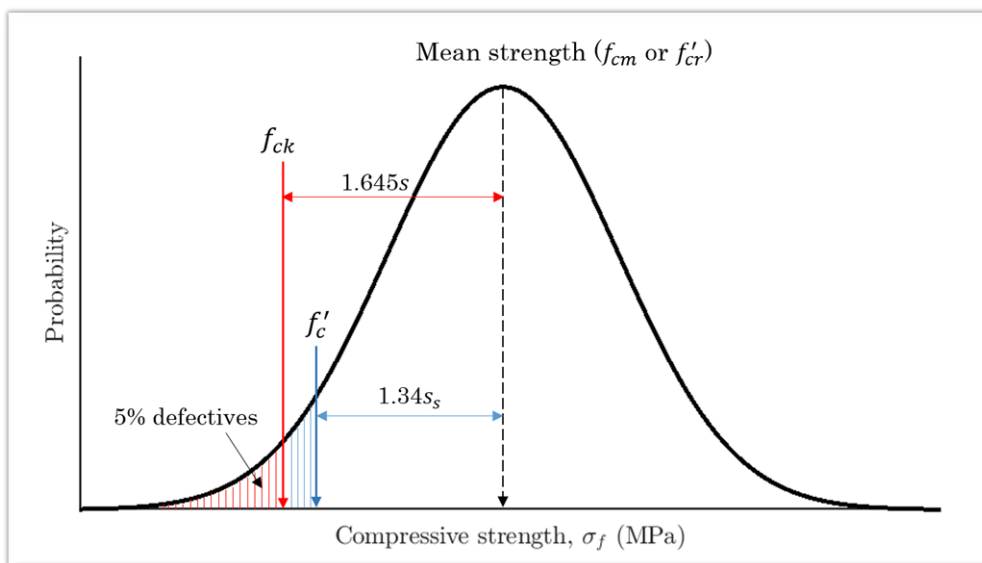


Fig. 7.2. Normal distribution curve for the compressive strength of concrete samples (modified from (Pillai and Menon, 2009)).

for most of the F-concrete and M-concrete dataset (one material, one sample size) the characteristic strength (f_{ck}) calculated from the structural design codes are larger than the asymptotic strength σ_∞ , while an opposite result is observed for the C-concrete. This illustrates that the use of classical structural design codes and small concrete samples can lead to unreliable estimations of the asymptotic strength, relevant for large scale structures. These classical methods give sometimes unsafe estimations (e.g. F- and M-concretes) (see Fig. 7.3a and b), or occasionally too conservative ones (C-concrete) (see Fig. 7.3c).

In most structural design codes, 150x300mm cylindrical samples (ACI 318-05, 2005; ASTM C39/C39M-14, 2014; EN 1992, 2004) (or 160x320mm in France (NF EN 12390-3, 2012)) are used as a standard to determine the characteristic compressive strength. Here, even though the 160x320-mm samples provide the values of the characteristic strength that are the closest to σ_∞ , the accuracy of the estimation of σ_∞ depends on the confidence level chosen (i.e. the constant λ in Eq. (7.1)), as well as on the concrete mix. Taking $f_{cm} = \langle \sigma_f \rangle$, $s = \delta(\sigma_f)$, $\nu_{FS} = 1$, a combination of Eq. (6.3) and Eq. (6.4) with Eq. (7.1) yields the following scaling for the characteristic strength (f_{ck}):

$$f_{ck} = \sigma_\infty \left(\frac{L_i}{L} \right) + \sigma_\infty \quad (7.4)$$

where $L_i = L_m - \lambda L_\delta$. Considering the corresponding strength σ_∞ for each concrete mixture (Table 6.2), Eq. (7.4) fits well the f_{ck} values for all concrete mixtures, and for both the EN 1992 and ACI 318 design codes (Fig. 7.3). For a given concrete mixture, the minimum sample size (L_{\min}) that would allow a correct estimation of the asymptotic strength ($\sigma_\infty \pm 0.01\sigma_\infty$) while using classical design codes are reported in Table 7.2. These sample sizes are always larger than 160mm and depend on the concrete mixture as well as the constant λ , i.e. on the code. In some cases, e.g. F-concrete, to perform compression tests on samples large enough to give a correct estimate of σ_∞ would require an unusually large loading capacity for laboratory testing (e.g., $36.5 \frac{N}{mm^2} \times \left(\pi \times \frac{897^2}{4} \right) mm^2 \approx 23.1 \times 10^6 N$ for F-concrete with the ACI 318 code).

This raises important problems while trying to estimate a reliable characteristic strength of concrete for large scales structural design from classical codes and a unique series of tests with a single sample size. To avoid sample size effects on strength, the sample size L should be much larger than L_m which itself depends on the microstructural characteristics (i.e. pore structure) of the hardened concrete.

On the other hand, the asymptotic strength (σ_∞) could be approximately determined by the mean strength ($\langle\sigma_f\rangle$) of samples whose the size (L) is much larger than the characteristic size of the pore structure (L_m) (see Fig. 6.8a and section 6.5). Based on this idea, some recommendations for predicting the characteristic strength of concrete are presented in the following section.

Table 7.2. The estimated parameters of the finite-size scaling of characteristic strength expressed according to equation (7.4).

Concrete mixture	EN 1992			ACI 318		
	L_i (mm)		L_{\min} (mm)	L_i (mm)		L_{\min} (mm)
	Mean	SD		Mean	SD	
F	6.3	2.0	631.0	9.0	1.7	897.0
M	3.1	2.5	305.0	5.2	2.5	517.0
C	-7.8	6.2	319.0	-5.0	4.7	224.0

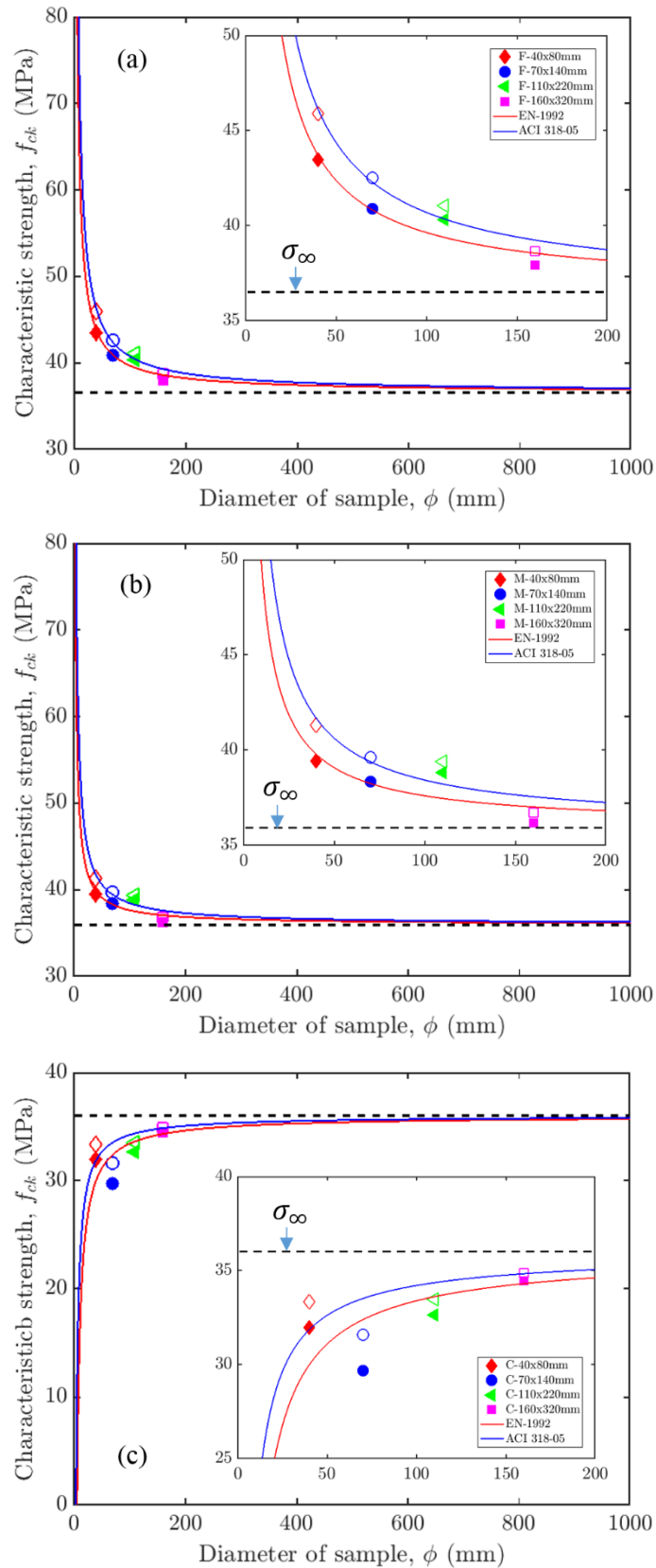


Fig. 7.3. Comparison between the asymptotic strength, σ_∞ , determined from the finite-size scaling of the mean strength (Eq. (6.3)), and the estimated values of characteristic strength, f_{ck} , following the Eurocode 2 (filled symbols) and ACI-318 (open symbols): (a) F-concrete; (b) M-concrete and (c) C-concretes. The red and blue curves are the fits by Eq. (7.4) for the f_{ck} values of all concrete mixtures according to the EN 1992 and ACI 318 design codes, respectively.

7.3.2 Recommendations for the determination of the asymptotic compressive strength

As discussed above, the form of the finite-size scaling laws for both the mean strength (Eq. (6.3)), with a non-vanishing asymptotic strength (σ_∞), and the associated variability ($\delta(\sigma)$) vanishing at large scales, implies that σ_∞ can be considered as the genuine characteristic strength (f_{ck}) of concrete. We have also stressed that using a single concrete sample size for laboratory testing leads to different estimations of the characteristic strength from classical codes. Therefore, performing a series of compression tests with different sample sizes is highly recommended to reliably estimate the characteristic (asymptotic) compressive strength of concrete. We suggest below an experimental procedure:

- 1- Prepare cylindrical concrete samples with a length-to-diameter ratio of 2 and at least four different sizes. This condition is required to perform a good fit of the finite-size scaling laws (Eq. (6.3) and Eq. (6.4)) to the data in order to estimate the length scales L_m and L_δ as well as the asymptotic strength σ_∞ . The number of test specimens in each size should be as large as possible, and not less than 30 specimens, following the standard ACI 318 (ACI 318-05, 2005).
- 2- The diameter of the smallest concrete cylinders should be at least 3 times the nominal maximum size of the coarse aggregate, following the regulations (ASTM C31/C31M-03, 2003), (NF EN 206-1, 2004) and (NF EN 12390-1, 2012). This condition allows to reduce the “*wall effect*” that might happen when the maximum aggregate size is large relatively to the size of the mold, and to ensure the quality of the compaction procedure and the uniformity of the aggregate distribution in the samples.
- 3- The largest sample size should be as large as possible depending on the laboratory loading capacity. However, it should not be less than 160mm.
- 4- All the concrete samples must be cast, cured and tested under the same conditions.
- 5- Using $\nu_{FS} = 1$ in Eq. (6.3), the asymptotic strength (σ_∞) is determined by a linear regression in a [$\langle\sigma_f\rangle$ vs. L^{-1}] graph. The pertinence of the finite-size scaling can then be checked by plotting the strength variability $\delta(\sigma)$ as a function of L^{-1} (see Eq. (6.4)).

A crucial advantage of such experimental program is that it provides a well-defined value of the characteristic (asymptotic) compressive strength of concrete which is no more affected by the sample size or the chosen λ -value. However, this requires a larger number of tests with samples of different sizes, making this procedure lengthy and costly. To circumvent this

problem, a simple analysis of the pore structure of the concrete should be performed. Indeed, Eq. (6.3) implies that the asymptotic strength will be correctly estimated from $\langle\sigma_f\rangle$ if $\frac{L_m}{L} \rightarrow 0$.

In the preceding chapter, we have shown that the length scale L_m mainly depends on the intrinsic characteristic of the pore structure in the hardened concrete. Fig. 7.4 shows the positive correlation between L_m and the the maximum pore diameter ($d_{p,max}$) times the porosity (p_o in (%)). A good linear regression ($R^2 = 0.85$) is obtained:

$$L_m = 70 \left(\frac{p_o}{100} \times d_{p,max} \right) \quad (7.5)$$

This suggests an acceptance criterion for the minimum sample size with respect to the pore structure characteristics. Combining Eq. (6.3) with $v_{FS} = 1$ and Eq. (7.5), this condition reads:

$$L \geq \frac{0.7(p_o \times d_{p,max})}{k} \quad (7.6)$$

where k can be seen as the acceptance constant, corresponding to the expected deviation of the average strength $\langle\sigma_f\rangle$ from the asymptotic strength σ_∞ . For example, to determine the characteristic asymptotic strength of C-concrete with an acceptance constant of $k = 5\%$, using the values of p_o and $d_{p,max}$ reported in Table 3.1, the minimum sample size required is $L_{min} = 120\text{mm}$. This means that the mean compressive strength obtained on the cylindrical samples with a diameter larger 120-mm can be regarded as an estimation of characteristic strength of C-concrete with a confidence level of 95%. On the other hand, with the same acceptance constant k , samples with a diameter of at least 464mm would be needed to determine the characteristic strength of F-concrete. Although the asymptotic strength σ_∞ is very similar for the three different concrete mixtures (see Table 6.2 and Fig. 6.8), the sample size required for its estimation with the same accuracy, from a single series of tests, strongly varies with the material. This is another illustration of the role of the internal pore structure on the size effects on strength, while its impact on the asymptotic strength appears limited in our low-porosity concretes (see Chapter 6). Consequently, if one use only one sample size to estimate the characteristic strength of the material from laboratory testing, the sample size criterion (Eq. (7.6)) should be taken into account.

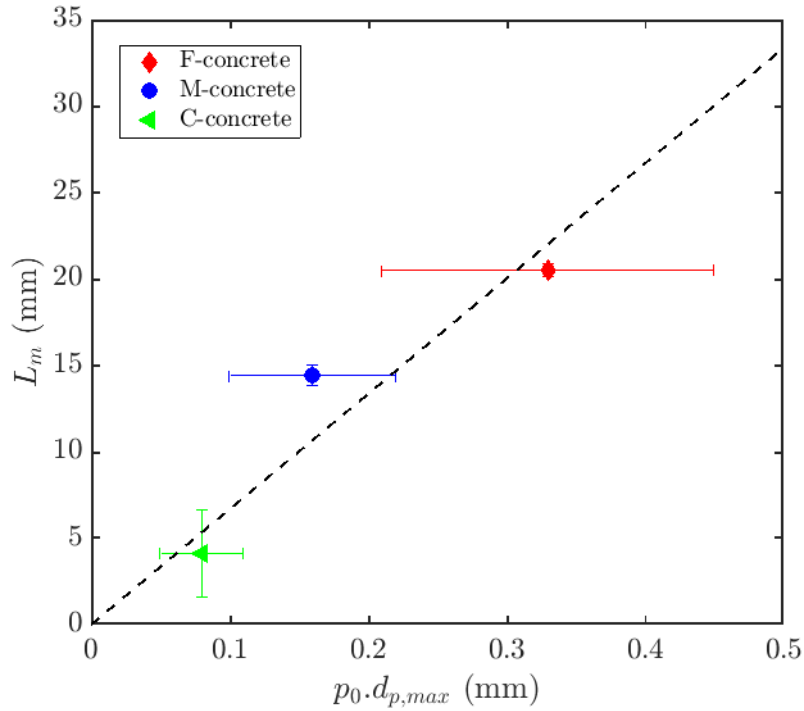


Fig. 7.4. Relationship between the length scale (L_m) and the product ($p_o \times d_{p,max}$) where the porosity, p_o , is expressed in absolute value.

Quality control during construction is required to check the conformity of concrete to the strength requirements posed at the design stage. Usually, the acceptance strength criterion is derived from the characteristic strength determined from standard procedures (ACI 318-05, 2005; EN 1992, 2004; NF EN 206-1, 2004), without paying attention to sample size effects or to the internal pore structure. However, based on the above discussion, we argue that, besides the strength criterion, an additional condition on the sample size for laboratory test should be examined for the final acceptance decision. Hence, we propose the following step-by-step checking procedure:

- 1- Assign the strength grade of concrete (f_{ck}), specified at the design stage, to the asymptotic strength (σ_∞) of the considered concrete.
- 2- Obtain the mean value $\langle \sigma_f \rangle$ and the standard deviation $\delta(\sigma_f)$ of the compressive strength of the considered concrete from a series of at least 30 compression tests carried out on sample cylinders of diameter L .
- 3- Perform an image analysis of internal sections on virgin concrete samples to estimate the porosity (p_o) and the pore maximum diameter ($d_{p,max}$). A minimum of three sections including one vertical and two horizontal sections (see Fig. 3.1) for each

sample are recommended. In the case of concrete samples fabricated from different batches, one sample in each batch has to be selected and analyzed.

- 4- Calculate the minimum required average strength (f_{mr}) of the considered concrete at the sample size L from the equations (6.3) and (7.5) with $v_{FS} = 1$, based on the values of the required asymptotic strength, σ_∞ (step 1), of the porosity, p_o (step 3) and of the pore maximum diameter, $d_{p,max}$ (step 3), yielding:

$$f_{mr} = \sigma_\infty \left[\frac{0.7(p_o \times d_{p,max})}{L} + 1 \right] \quad (7.7)$$

where the porosity p_o is expressed in %.

- 5- Compare the experimental mean strength $\langle \sigma_f \rangle$ (obtained at the step 2) with the minimum required average strength f_{mr} (calculated by using the Eq. (7.7)). If $\langle \sigma_f \rangle \geq f_{mr}$, we can state that the examined concrete complies with the strength requirements.

We note that the relation between the length scale L_m and the characteristics of the pore structure (Fig. 7.4) has only been validated for our low-porosity concrete. It is doubtful that it would hold for large porosity concretes, for which the pore structure is much more complex (non-spherical, interconnected pores) and the direct impact of porosity on strength is strong (Chen et al., 2013; Koliass, 1994; Kumar and Bhattacharjee, 2003; Lian et al., 2011). Therefore, the above procedure should be applied only for normal-weight concretes with a total porosity of less than 10%. In addition, a smaller sample diameter ϕ implies a larger “correcting factor” k in equation (7.6) as well as a larger strength variability $\delta(\sigma)$ at this size. We therefore recommend using cylindrical samples with a diameter larger than 110mm. Two examples illustrating the application of this procedure are presented in Appendix D.

7.4 Conclusion

From the experimental studies of the statistical size effects on the compressive strength of concrete, in this chapter: we (i) explored the relationship between the compressive strength and elastic modulus; (ii) discussed the definition of the characteristic compressive strength of concrete; and (iii) proposed to revise the procedures to estimate this characteristic strength and to check the conformity of concrete to the strength requirements defined at the design stage. The following main conclusions can be drawn:

- 1- There is no significant correlation between the modulus of elasticity and the compressive strength of concrete, which precludes an estimation of the elastic modulus from strength data.
- 2- Owing to the vanishing intrinsic fluctuations of strength at large scales ($\delta(\sigma_f)_{L \rightarrow +\infty} \rightarrow 0$), the asymptotic strength (σ_∞) can be considered as the genuine characteristic compressive strength of concrete. Therefore, an experimental study conducted on a series of at least four different sample sizes is strongly recommended to allow an accurate determination of the size effects on strength, hence of the characteristic compressive strength of concrete.
- 3- For low-porosity concretes, the pore structure of the hardened concrete samples plays a key role in controlling the size effects on strength but does not have a significant impact on the asymptotic compressive strength. A concrete with a lower porosity will be less affected by size effects on compressive strength than a concrete with a larger porosity. Another important consequence is that, if one wants to estimate the characteristic (asymptotic) strength of the material from a series of tests with a single sample size, a condition on this size with respect to the characteristic scale of the pore structure should be fulfilled.
- 4- The characteristic scale of the pore structure in a hardened concrete sample can be estimated from the product of the maximum pore diameter and the total porosity. In order to determine these two parameters, we proposed a simple image analysis procedure on internal sections of concrete samples. This procedure was tested so far only on a limited number of different concrete mixtures. An extension of this work to other concrete materials with various microstructures would be necessary to refine this estimation.

Chapter 8

Conclusion and perspectives

8.1 Conclusions and main results

The research presented in this thesis was undertaken to investigate the statistical size effects on the compressive strength of concrete, which is a typical heterogeneous material of tremendous importance in civil engineering. To do so, a campaign of different experimental programs was carried out on a large number of concrete specimens with four different cylindrical sizes and three different microstructures. The main findings from experimentation and data analysis of each of the main issues and the links between them have already been presented and discussed at the end of the previous chapters. In the following paragraphs, we summarize the main conclusions drawn from the experimental studies conducted throughout this thesis.

A first series of conclusions relates to the analysis of microstructural characteristics (Chapter 3) and elastic properties (Chapter 4) of all our three types of concretes:

- The associated characteristic length scales of microstructural disorder can be simply quantified via two autocorrelation lengths: ξ_g for describing the internal microstructure as a whole and ξ_p for representing the pore structure within the hardened concrete sample. The global autocorrelation length, ξ_g is strongly affected by the aggregate size, while the pore autocorrelation length, ξ_p is directly related to the number and the size of pores existing in the material. Precisely, ξ_g increases, whereas ξ_p decreases with the increase of aggregate size in our concretes.

- For each given concrete group, both the autocorrelation lengths ξ_g and ξ_p are independent of the sample size and smaller than the smallest sample size. This means that there is no significant sample size effect on the microstructural characteristics. This also allows to confirm that all our tested samples are larger than the RVE of the corresponding concrete in terms of microstructure and disorder.
- The finer concretes have a larger porosity than the coarser ones. However, for each type of concrete, both the pore size distribution and porosity are similar for different sample sizes. In other words, there is no dependence of the pore structure on the concrete sample size.
- The coarser concrete shows a larger elastic modulus than the finer ones. This is consistent with the fact that the elastic modulus of concrete is affected by the modulus of elasticity of the aggregate and by the volumetric proportion of aggregate in the concrete. However, for a specified concrete mixture, the modulus of elasticity is independent of the sample size.

A second series of conclusions concerning the interpretation of compressive failure as a critical phase transition are achieved from the Acoustic Emission (AE) experiments (Chapter 5):

- The associated durations and energies of AE events released by the fracturing events are distributed according to a power law which presents a cut-off diverging as approaching the failure.
- The failure behavior of concrete under compression loading is preceded by an acceleration of the rate of fracturing events and of the energy released, and a divergence of the fracturing correlation length as well as the associated duration towards failure. These results are strong evidences to support an interpretation of the compressive failure of low-porosity disordered materials as a critical phase transition between an intact state and a failed state.
- The associated critical exponents, which were found to be independent of sample size and of concrete mixture, and very close to mean-field depinning values, provide a further confirmation for a critical interpretation and also demonstrate that the critical behavior of compressive failure of heterogeneous materials is not affected by either system size or microstructural disorder.

A prominent consequence obtained from the critical interpretation of compressive failure is to provide finite-size scaling laws for the mean value of compressive strength and its associated

variability. These scaling laws have been used to describe the statistical size effects on compressive strength of our concrete in Chapter 6. The main outcomes of this chapter are:

- The weakest-link approach based on the hypotheses of pure brittleness and the independence of damage events is irrelevant to explain size effects on the compressive strength of quasibrittle materials like concrete. As a result, for this kind of material, the statistical size effects and the failure probability of strength under compression loading could not quantify in the framework of extreme value statistics.
- The compressive strength of concrete exhibits clearly the dependence on both the sample size and the associated internal microstructure size. Precisely, (i) the increase of both the mean strength and its variability towards small system size follow a power law scaling of the sample size with a power-law exponent close to the mean-field prediction ($\nu_{FS} = 1$); and (ii) when the sample size increases, the mean strength decreases and reaches a non-vanishing asymptotic strength ($\sigma_\infty > 0$) for a system of infinite size ($L \rightarrow +\infty$), while the associated variability of strength vanishes for ($L \rightarrow +\infty$).
- For a low-porosity heterogeneous material like the concretes used in this study, the pore structure plays a key role to control the finite size effects on compressive strength, but it does not have a significant impact on the asymptotic strength (σ_∞).
- Owing to the vanishing strength variability at large-sizes, the non-vanishing asymptotic strength σ_∞ becomes the most relevant, material-dependent parameter for dimensioning large-scale structures from an upscaling of small-scale laboratory mechanical tests.

Finally, Chapter 7 presented a study revisiting the two most popular design codes of concrete structures, EN 1992 and ACI-318, by taking into account the statistical size effects on compressive strength. This study focus on the concept of characteristic compressive strength and the prediction of elastic modulus, that are commonly expressed through the mean compressive strength obtained on laboratory-scale concrete samples. The main conclusions of this chapter are:

- There is no direct proportionality between the elastic modulus (linear property) and the compressive strength (non-linear property) of concrete.
- The asymptotic compressive strength σ_∞ can be considered as the genuine characteristic compressive strength of concrete. Therefore, an experimental program

conducted on a range of at least four different sample sizes, rather than on only one kind of sample size, is extremely recommended to achieve a highly accurate value of the characteristic strength of concrete.

- For the same targeted characteristic strength, a concrete with a lower porosity will be less affected by size effects on compressive strength than a concrete with a larger porosity.
- Besides the strength criteria, an additional condition of sample size much greater than the internal length scale of the pore structure must be satisfied in the case of using only one sample size for predicting the characteristic strength and examining the conformity with the acceptance strength requirement of concrete.

The two last points are the consequence of the principal role of the pore structure on the statistical size effects on compressive strength of concrete.

Overall, linking these findings above, we can conclude that the three major research objectives posed in the introduction of this thesis were met.

8.2 Perspectives

Because the critical behavior of failure of heterogeneous materials is not affected by the loading condition and microstructural disorder, we thus believe that the finite-size scaling laws, derived from the critical interpretation of failure, can provide a powerful formulation to fit the size effect of whatever type of strength data for other quasibrittle materials.

Although the leading role of pore structure for the size effects on compressive strength were addressed in the present research, there still remains several possible extensions.

- The first possible improvement is refining the relationship between the characteristic length scales of the pore structure and the associated size effect length scales ($L_{m,\delta}$). This work can be accomplished by following the same strategy of experimentation used in this thesis on other normal weight concrete mixtures (different shape and sizes of aggregates).
- The second refinement could be based on investigating the statistical size effects on compressive strength of lightweight and high-strength concretes (HSC). The former are highly porous materials, while the latter are very dense materials with a minimal volume of pores and very fine aggregate particles (Mehta and Monteiro, 2006; Neville,

2004). Therefore, studying these two types of concrete would allow to get more insight into the role of (i) pore structure, and (ii) changing the nature of the aggregate or of the mortar matrix, for the size effect on compressive strength.

Concerning the extension of this critical interpretation of failure from the laboratory scale to geophysical field scales, an application to seismic signals before a chalk cliff collapse (Amitrano et al., 2005) has been presented in (Vu et al., 2018a). In this work, the acceleration of the seismic activity and the evolution of the seismic energies are in agreement with our critical interpretation. This strongly suggests an extension of our critical framework to large scale geophysical situations, and identifies the associated scaling laws as precursory signals of catastrophic failure, hence potentially opens the way towards forecasting tools.

Appendix A

Weibull-type size effect

The weakest link concept assumes that a structure is considered as being equivalent to a chain of N independent links (Fig. A.1a). All the elements (or links) have the same distribution of strength σ , characterized by the cumulative distribution function (*cdf*), $P_1(s_i < \sigma)$, which represents the probability of failure of an element i whose strength, s_i , is less than the applied stress σ . The survival probability of one element for this stress level is $1 - P_1(\sigma)$. If the whole chain should survive, all of its elements must survive. This condition can be expressed in mathematical terms as follows:

$$1 - P_f(\sigma) = \prod_{i=1}^N (1 - P_1(s_i < \sigma)) = (1 - P_1(\sigma))^N \quad (\text{A.1})$$

where $P_f(\sigma)$ is the failure probability of the chain as a whole. Taking natural logarithms of these expressions, we have:

$$\ln(1 - P_f(\sigma)) = N \cdot \ln(1 - P_1(\sigma)) \quad (\text{A.2})$$

Since $P_1(\sigma)$ is extremely small in practical situations, we can approximate it as $\ln(1 - P_1(\sigma)) \approx -P_1$. Therefore, after solving for $P_f(\sigma)$, the equation (A.2) reduces to:

$$P_f(\sigma) = 1 - e^{-N \cdot P_1(\sigma)} \quad (\text{A.3})$$

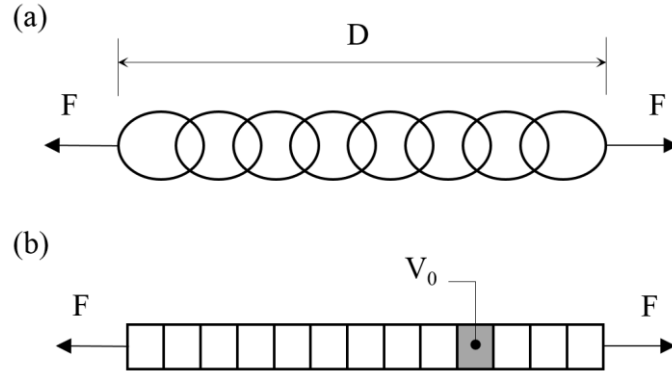


Fig. A.1. Various cases on which the weakest-link theory is applied: (a) one-dimensional discrete chain; (b) unidimensional bar (after (Bazant and Planas, 1998; Torrenti et al., 2013)).

The last equation can be extended to a continuous bar as shown in Fig. A.1b by setting $N = V/V_0$, where V is the volume of the bar and V_0 is a representative volume of the material. Substituting this expression into the equation (A.3), we finally obtain:

$$P_f(\sigma) = 1 - \exp\left[-\frac{V}{V_0}P_1(\sigma)\right] \quad (\text{A.4})$$

Equation (A.4) can be regarded as a simple statement of the weakest-link theory.

(Weibull, 1951, 1939a) introduced an empirical formula for the failure probability $P_i(\sigma)$ as follows:

$$P_1(\sigma) = \left(\frac{\sigma - \sigma_u}{\sigma_0}\right)^m \quad (\text{A.5})$$

where σ_u is the strength threshold, normally assumed to be equal to zero, σ_0 is a reference strength that can be interpreted as the mean strength for a volume V_0 , and m is called the shape parameter or Weibull's modulus. With $\sigma_u = 0$, substitution of Eq. (A.5) into Eq. (A.4) leads to the following statistical probability distribution of strength known as the Weibull distribution:

$$P_f(\sigma) = 1 - \exp\left[-\frac{V}{V_0}\left(\frac{\sigma}{\sigma_0}\right)^m\right] \quad (\text{A.6})$$

From the last equation, the mean failure strength $\langle\sigma_f\rangle$ on a structure of volume V is:

$$\langle \sigma_f \rangle = \int_{-\infty}^{+\infty} \sigma \cdot dP_f(\sigma) = \frac{V \cdot m}{V_0 \sigma_0^m} \int_0^{+\infty} \sigma^m \exp\left(-\frac{V \sigma^m}{V_0 \sigma_0^m}\right) d\sigma = \sigma_0 \Gamma\left(1 + \frac{1}{m}\right) \left(\frac{V_0}{V}\right)^{1/m} \quad (\text{A.7})$$

where the integration has been solved by using the substitution $u = \left(\frac{V}{V_0}\right) \left(\frac{\sigma}{\sigma_0}\right)^m$, and $\Gamma(p)$ is the gamma function:

$$\Gamma(p) = \int_0^{+\infty} u^{p-1} e^{-u} du \quad (\text{A.8})$$

The relation (A.7) clearly shows the dependence of the mean failure strength of a uniformly stressed sample on the volume of sample as $\langle \sigma_f \rangle \sim V^{-\frac{1}{m}}$.

Also based on the equation (A.6), the strength variance is given by:

$$s^2 = \int_{-\infty}^{+\infty} [\sigma^2 \cdot dP_f(\sigma)] - \langle \sigma_f \rangle^2 = \Gamma\left(1 + \frac{2}{m}\right) \left(\frac{V_0}{V}\right)^{\frac{2}{m}} \sigma_0^2 - \langle \sigma_f \rangle^2 \quad (\text{A.9})$$

From Eq. (A.7), we have:

$$\sigma_0 = \frac{\langle \sigma_f \rangle}{\Gamma\left(1 + \frac{1}{m}\right) \left(\frac{V_0}{V}\right)^{1/m}} \quad (\text{A.10})$$

Substituting the last expression into Eq. (A.9), the strength variance is computed as follows:

$$s^2 = \langle \sigma_f \rangle^2 \left[\frac{\Gamma\left(1 + \frac{2}{m}\right)}{\Gamma^2\left(1 + \frac{1}{m}\right)} - 1 \right] \quad (\text{A.11})$$

As mentioned above, the mean failure strength depends on the volume of sample V , thus, following to the equation (A.11), the associated strength variability also depends on V . Considering $V = L^n$ with L is the characteristic dimension of the sample, and n is the topological dimension (1, 2 or 3), the simple form of statistical size effect according to the weakest-link and Weibull theories can be finally derived (Bazant et al., 1991) as:

$$\langle \sigma_f \rangle(L) \sim s(L) \sim L^{-n/m} \quad (\text{A.12})$$

Appendix B

Results of Acoustic Emission experiments

In this appendix, several additional tables and figures can be found to give a detailed view on the results of Acoustic Emission (AE) experiments which are presented in Chapter 5.

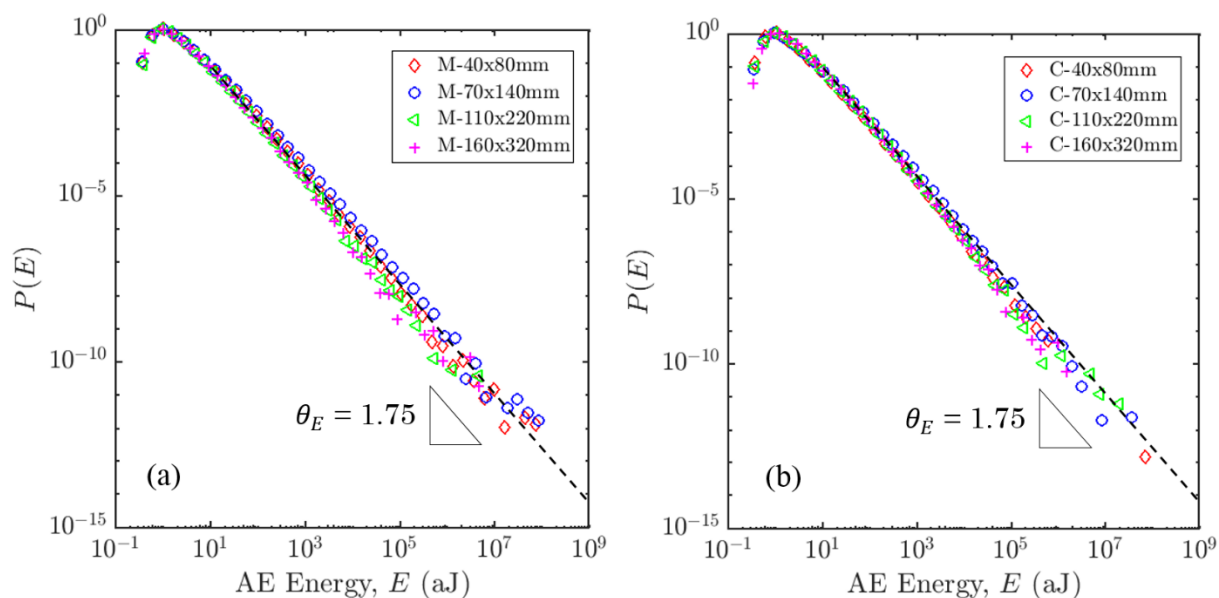


Fig. B.1. Probability density functions of AE energy for the whole AE events dataset for four different sample sizes of (a) M-concrete and (b) C-concrete. The *pdfs* were normalized by their maximum value. Curves were averaged over all sensors and all samples of a given sample size.

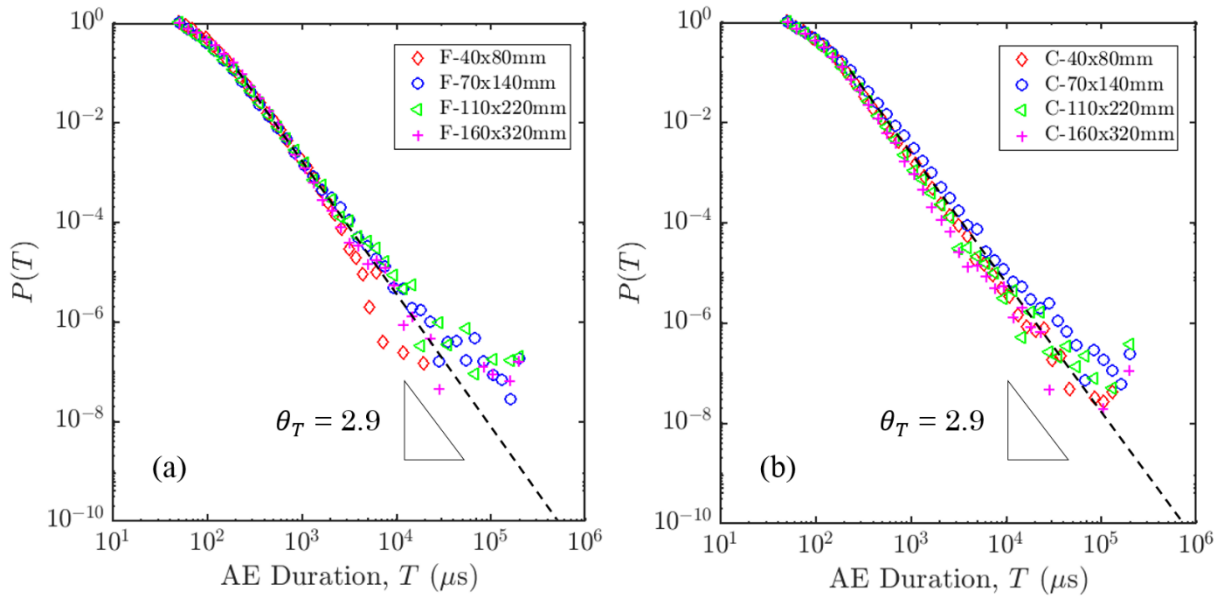


Fig. B.2. Probability density functions of AE duration of the whole AE events catalog for four different sample sizes of (a) F-concrete and (b) C-concrete. The functions were normalized by their maximum value. Curves were averaged over all sensors and all samples of a given sample size.

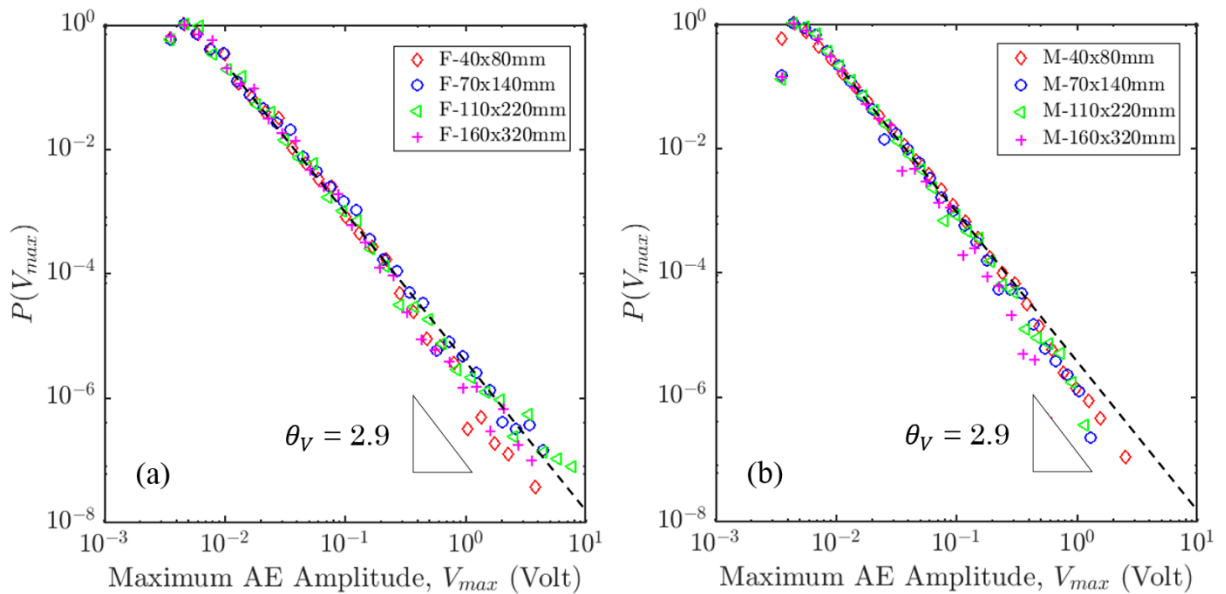


Fig. B.3. Probability density functions of AE amplitude for four different sample sizes of (a) F-concrete and (b) M-concrete. The functions were normalized by their maximum value. Curves were averaged over all sensors and all samples of a given sample size.

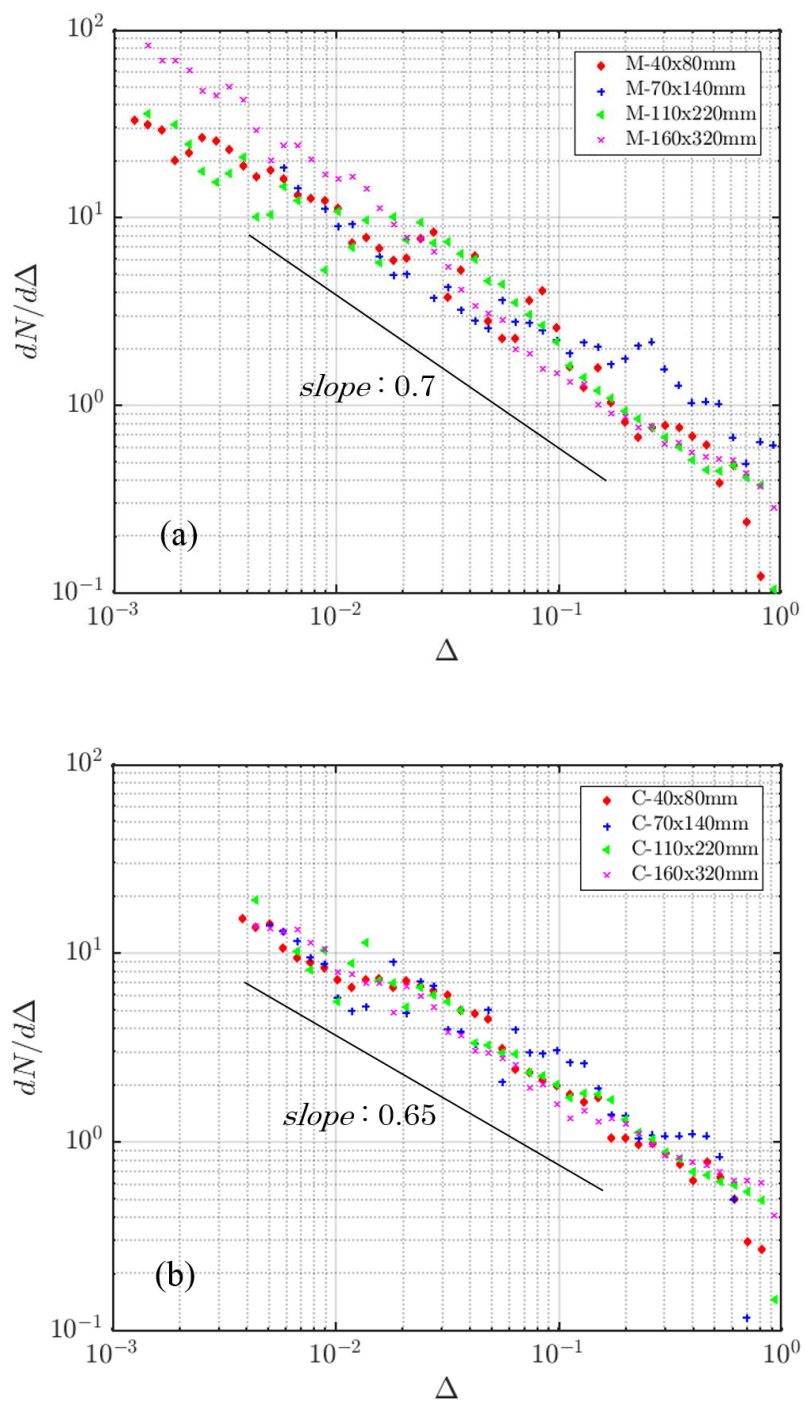


Fig. B.4. Evolution of AE event rate $dN/d\Delta$ for different sample sizes of (a) M-concrete; and (b) C-concrete. Curves were averaged over all sensors and all samples of a given sample size.

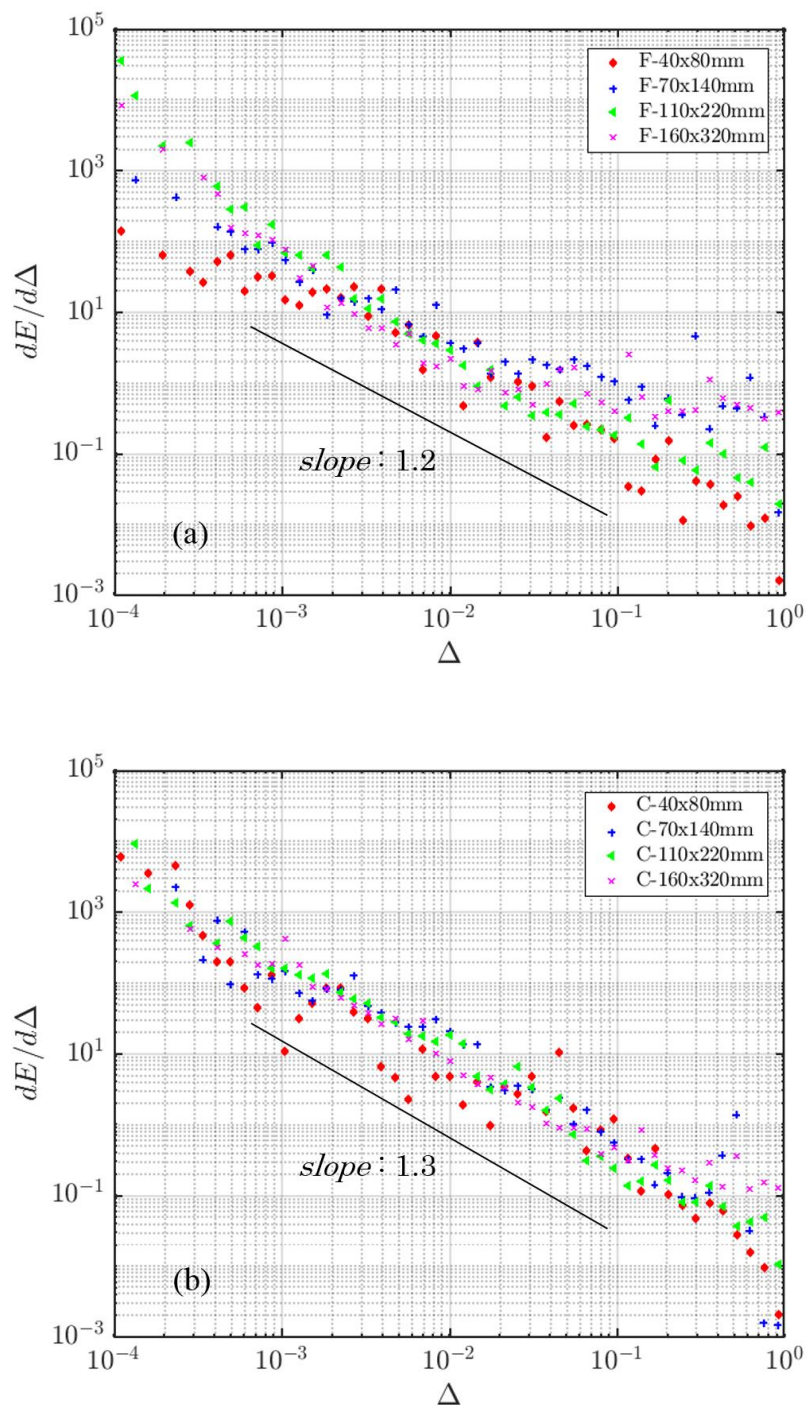


Fig. B.5. The AE energy release rate $dE/d\Delta$ for different sample sizes of (a) F-concrete, and (b) C-concrete. Curves were averaged over all sensors and all samples of a given sample size.

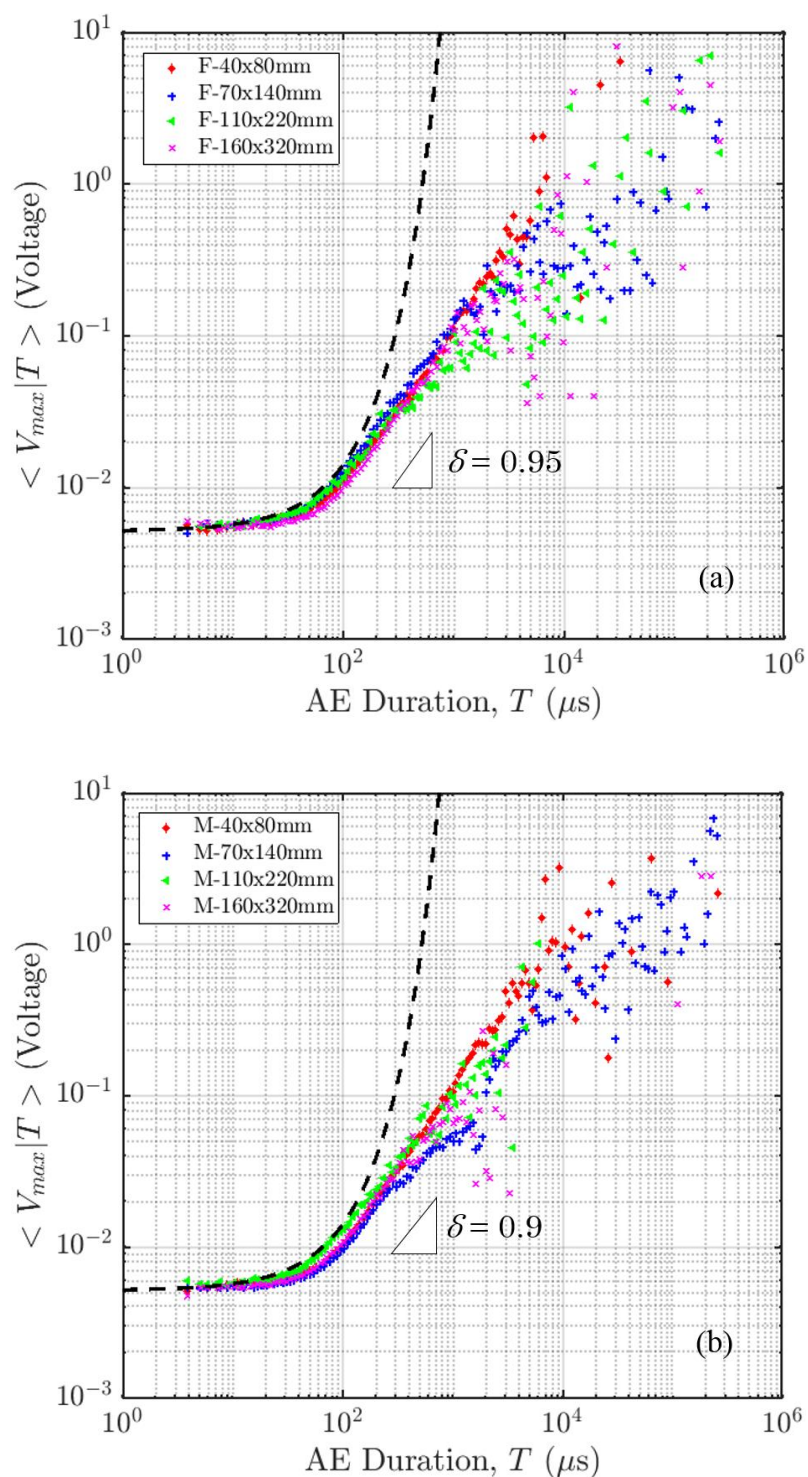


Fig. B.6. Conditional average maximum AE amplitude $\langle V_{max}|T \rangle$ for different sample sizes of (a) F-concrete, and (b) M-concrete. Curves of data points were averaged over all sensors and all samples of a given size (a). Black dashed lines are the reference curves according to the equation: $\langle V_{max}|T \rangle = V_{th} \exp(T/\tau)$ (Eq. (5.22)), with $V_{th} = 34dB$ and $\tau = 100\mu s$.

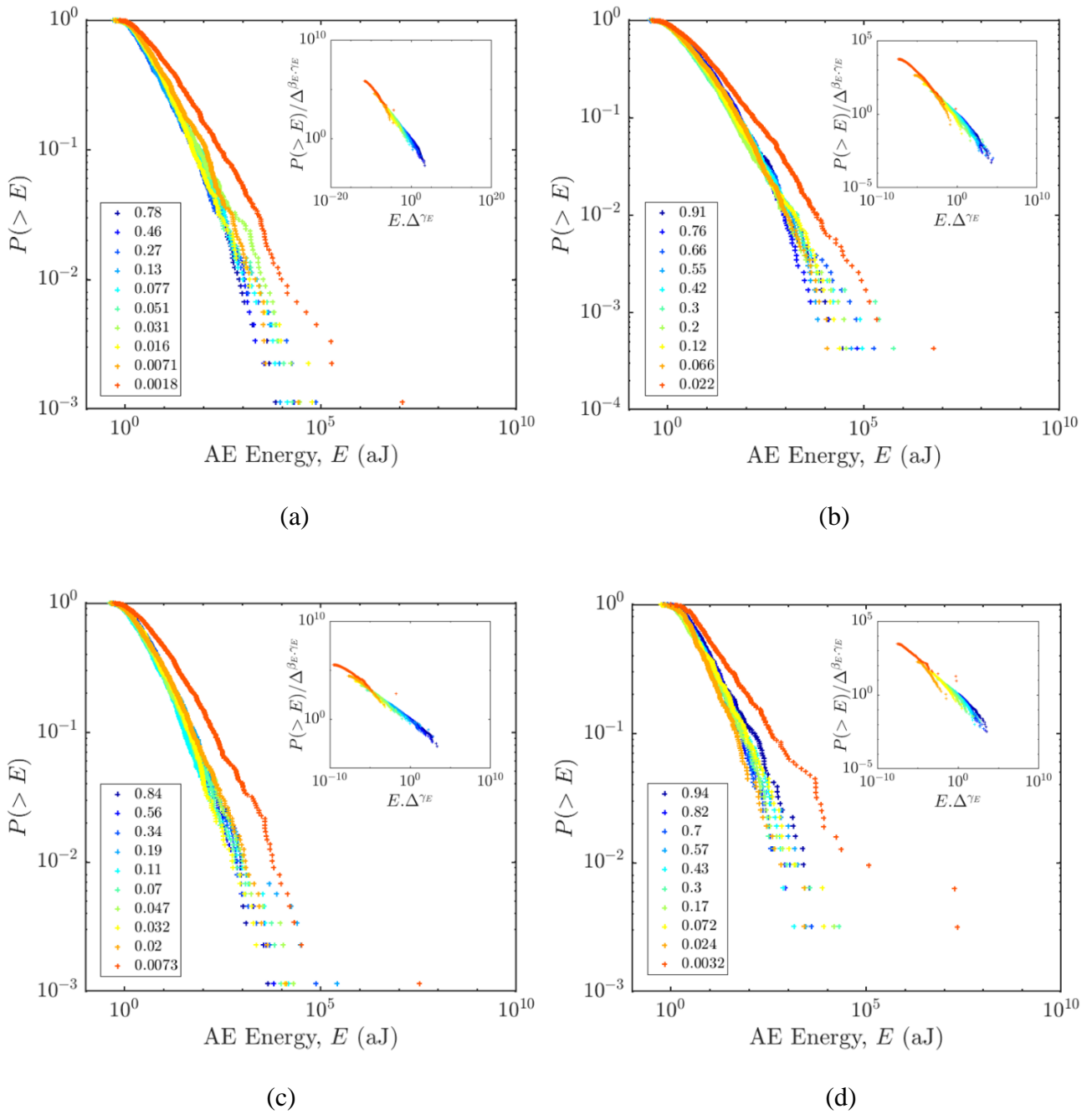


Fig. B.7. Cumulative distribution (*cdf*) of AE energies, E , at different distances to failure (Δ) for tests on four different sample sizes of **F-concrete**: (a) 40x80 mm; (b) 70x140 mm; (c) 110x220 mm; and (d) 160x320 mm. Insets: data collapses of the same data, presented in the corresponding main graph, in a rescaled plot.

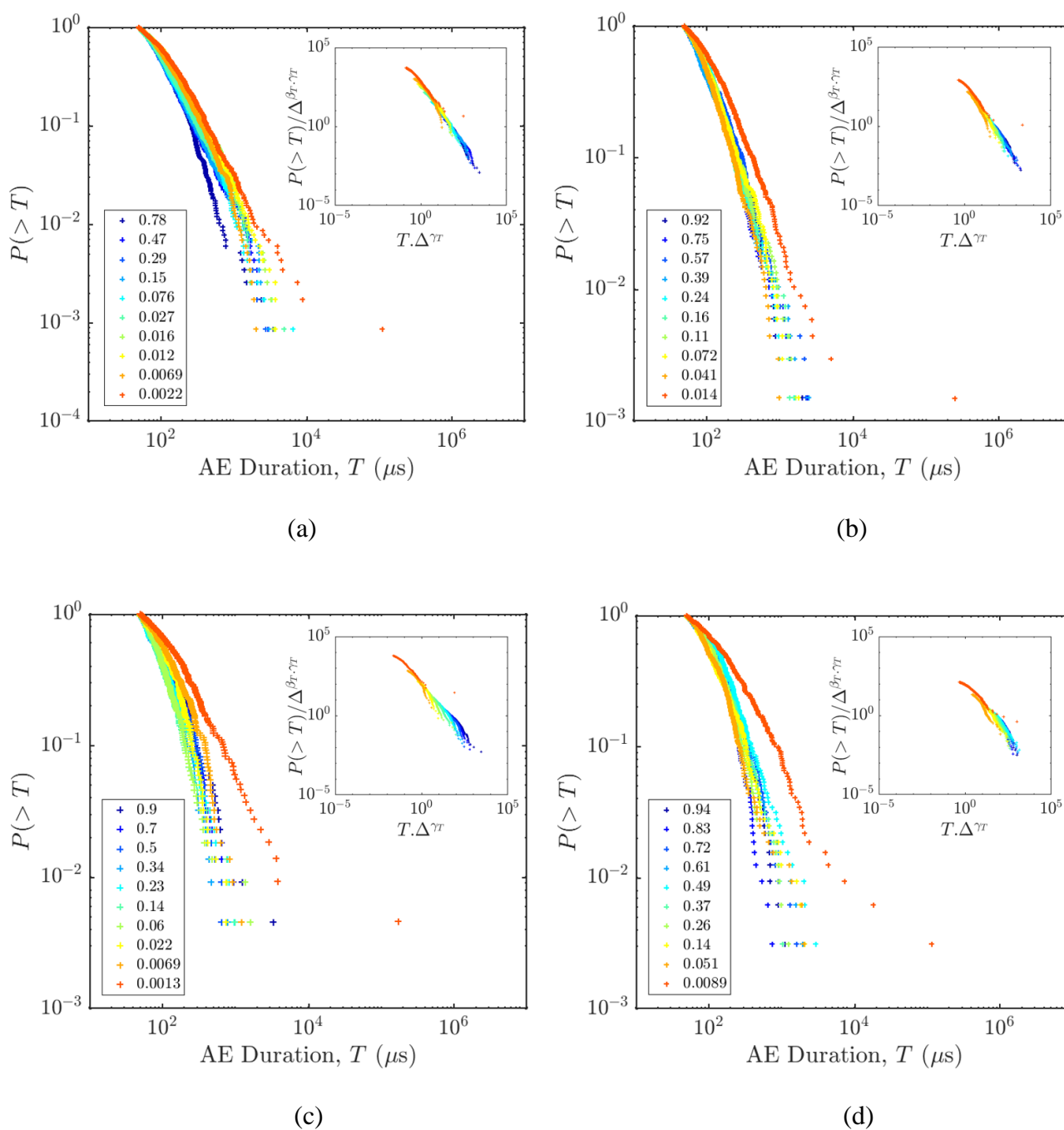


Fig. B.8. Cumulative distribution (*cdf*) of AE durations, T , at different distances to failure (Δ) for tests on four different sample sizes of **F-concrete**: (a) 40x80 mm; (b) 70x140 mm; (c) 110x220 mm; and (d) 160x320 mm. Insets: data collapses of the same data, presented in the corresponding main graph, in a rescaled plot.

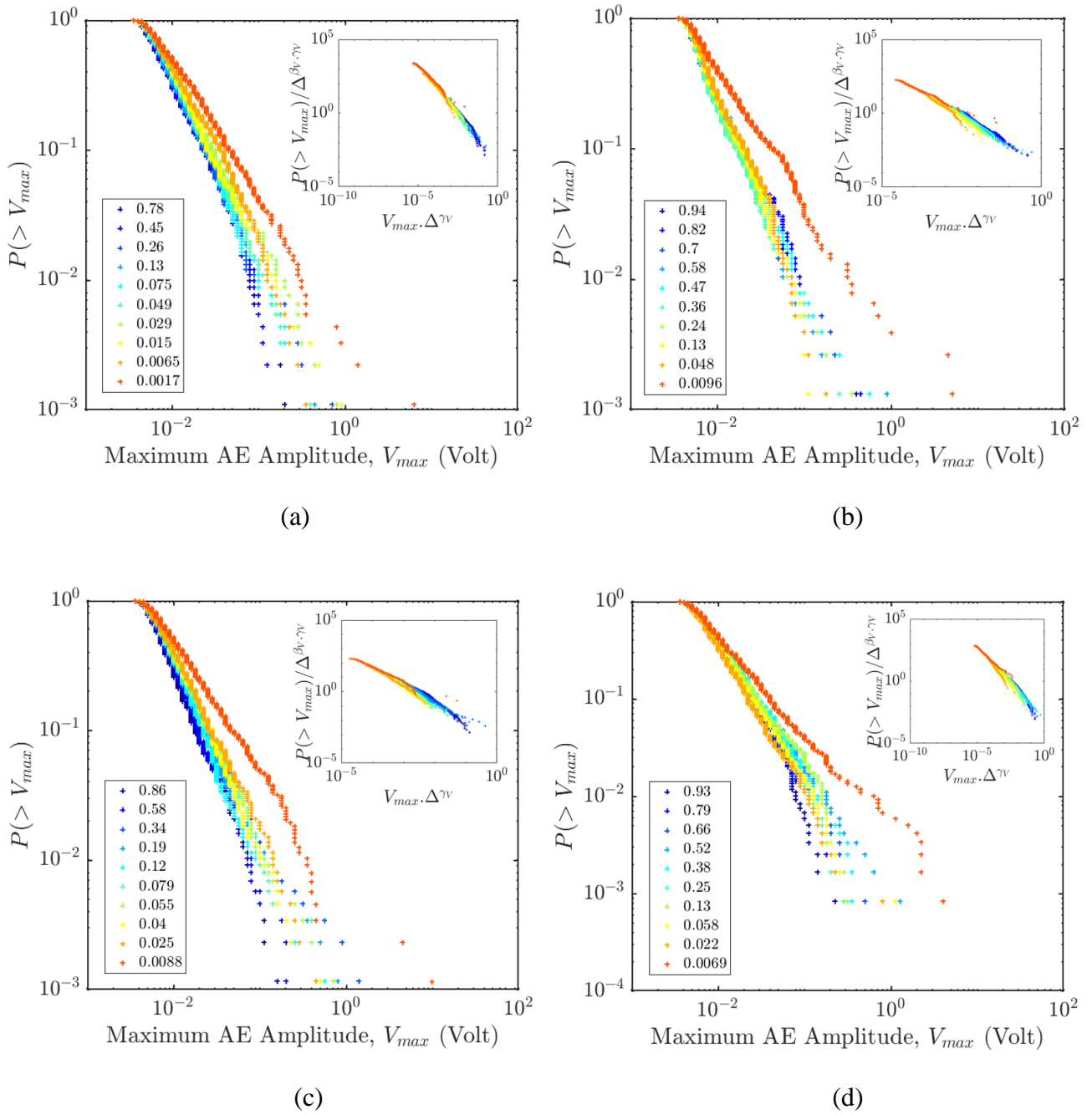


Fig. B.9. Cumulative distribution (*cdf*) of peak AE Amplitudes, V_{max} , at different distances to failure (Δ) for tests on four different sample sizes of **F-concrete**: (a) 40x80 mm; (b) 70x140 mm; (c) 110x220 mm; and (d) 160x320 mm. Insets: data collapses of the same data, presented in the corresponding main graph, in a rescaled plot.

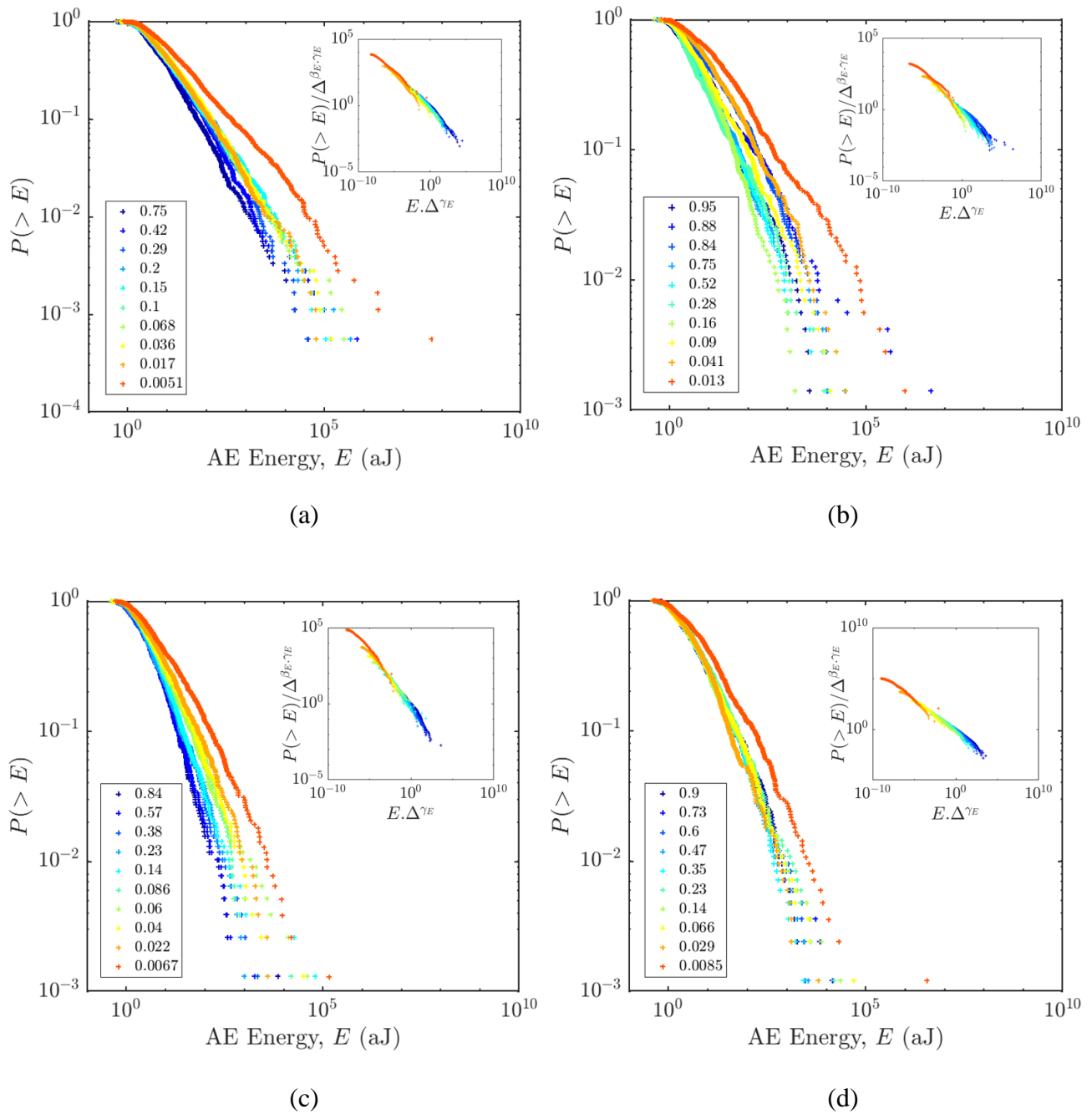


Fig. B.10. Cumulative distribution (*cdf*) of AE energies, E , at different distances to failure (Δ) for tests on four different sample sizes of **M-concrete**: (a) 40x80 mm; (b) 70x140 mm; (c) 110x220 mm; and (d) 160x320 mm. Insets: data collapses of the same data, presented in the corresponding main graph, in a rescaled plot.

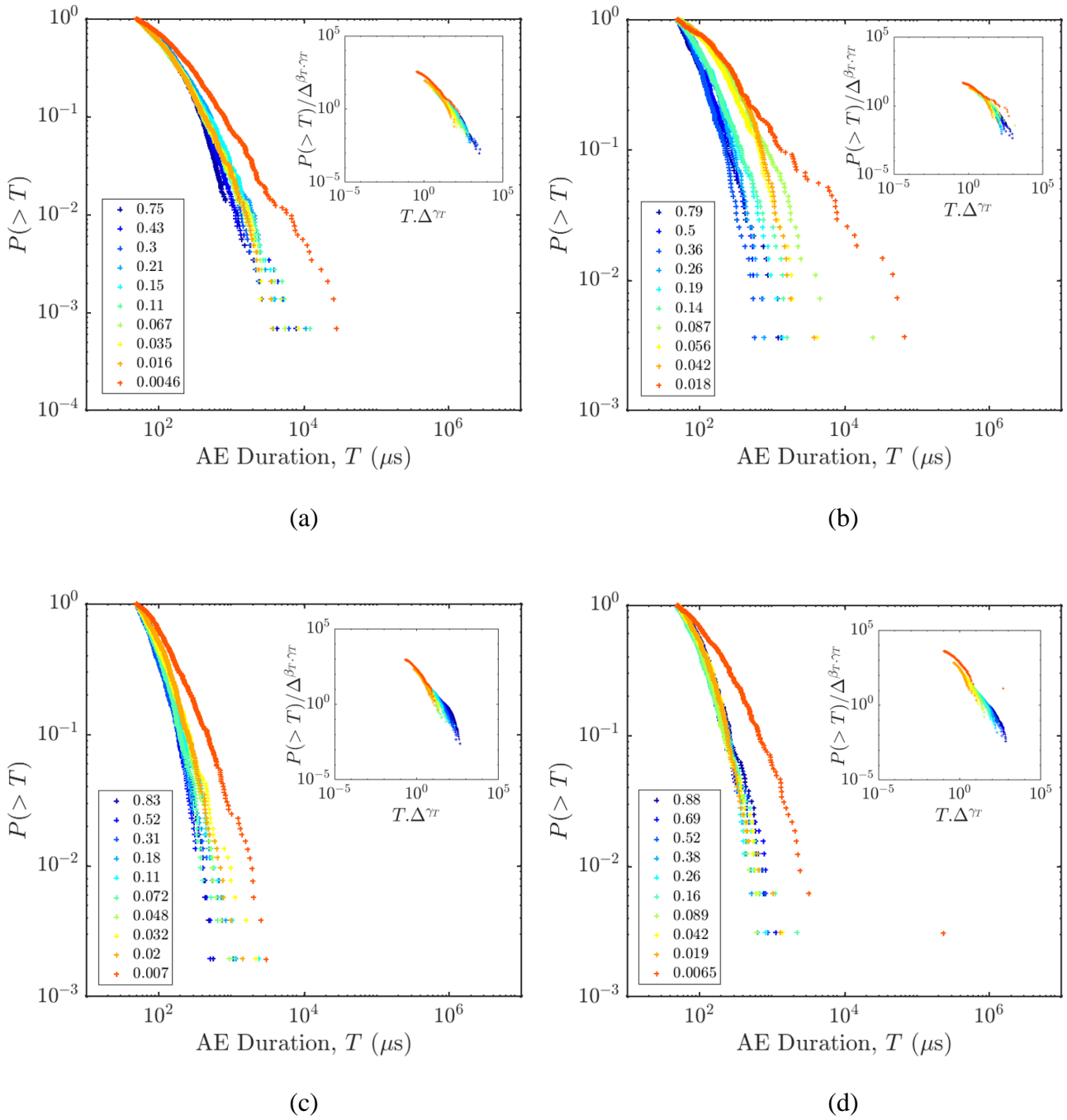


Fig. B.11. Cumulative distribution (*cdf*) of AE durations, T , at different distances to failure (Δ) for tests on four different sample sizes of **M-concrete**: (a) 40x80 mm; (b) 70x140 mm; (c) 110x220 mm; and (d) 160x320 mm. Insets: data collapses of the same data, presented in the corresponding main graph, in a rescaled plot.

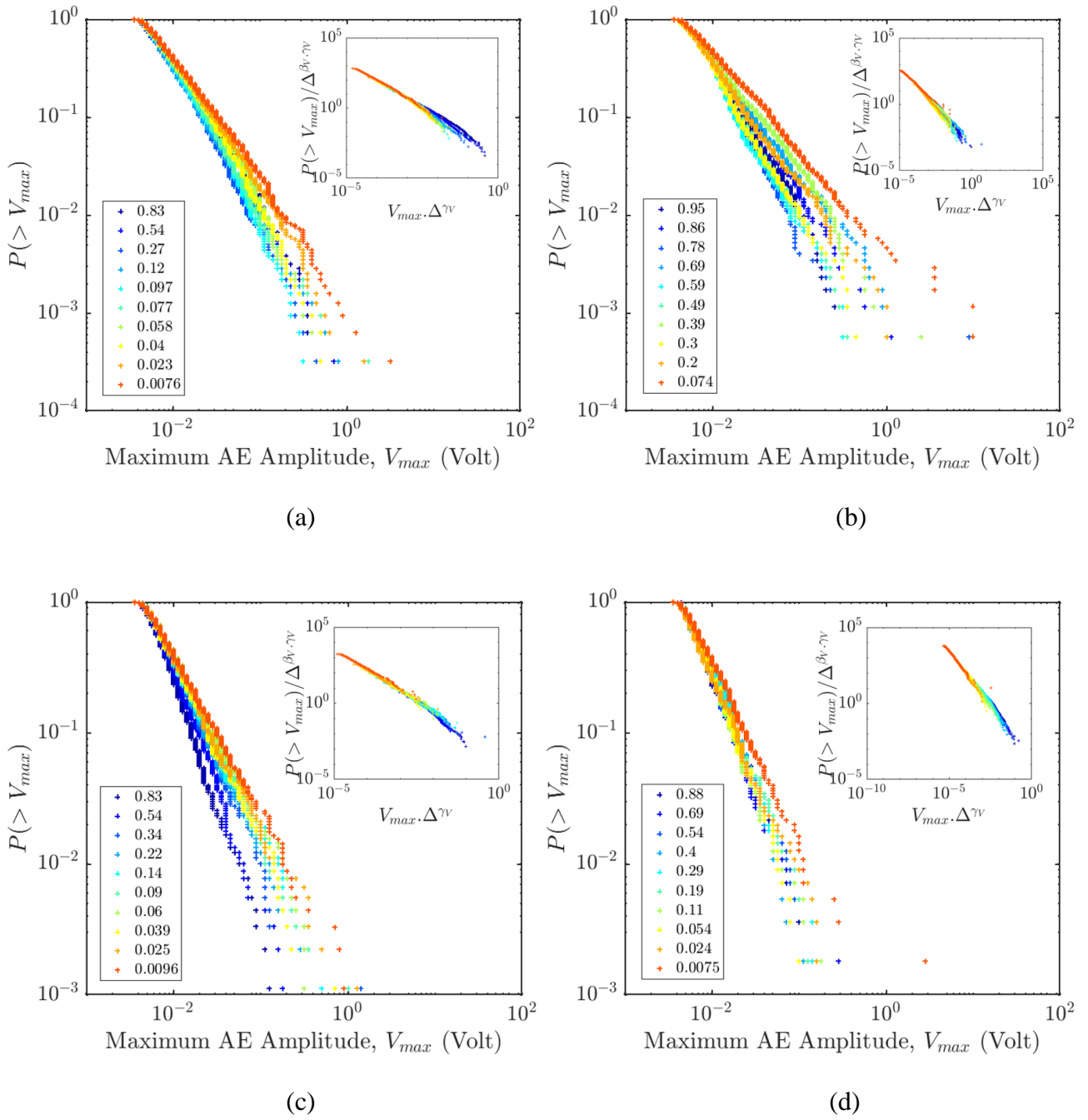


Fig. B.12. Cumulative distribution (*cdf*) of peak AE Amplitudes, V_{max} , at different distances to failure (Δ) for tests on four different sample sizes of **M-concrete**: (a) 40x80 mm; (b) 70x140 mm; (c) 110x220 mm; and (d) 160x320 mm. Insets: data collapses of the same data, presented in the corresponding main graph, in a rescaled plot.

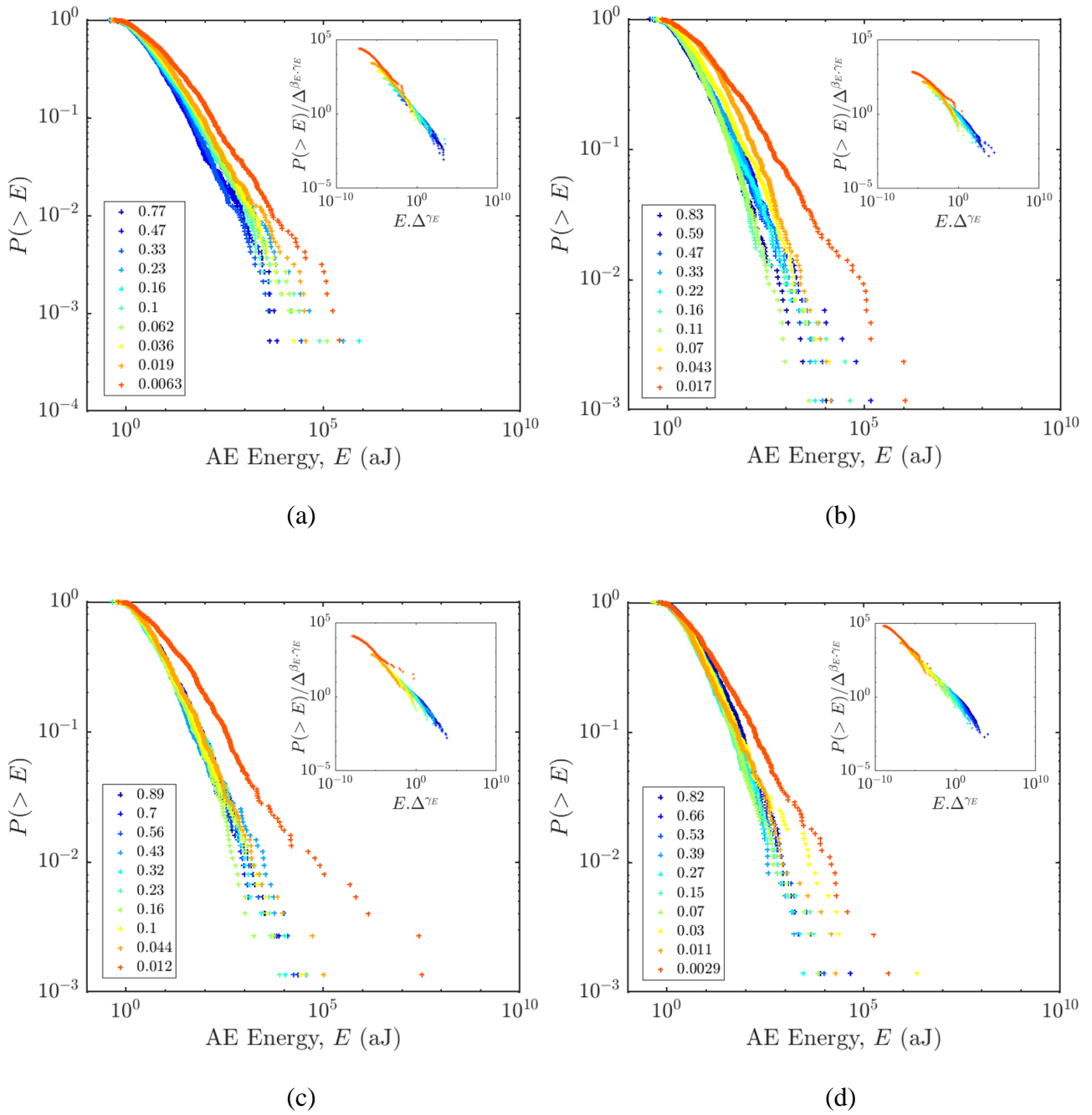


Fig. B.13. Cumulative distribution (*cdf*) of AE energies, E , at different distances to failure (Δ) for tests on four different sample sizes of **C-concrete**: (a) 40x80 mm; (b) 70x140 mm; (c) 110x220 mm; and (d) 160x320 mm. Insets: data collapses of the same data, presented in the corresponding main graph, in a rescaled plot.

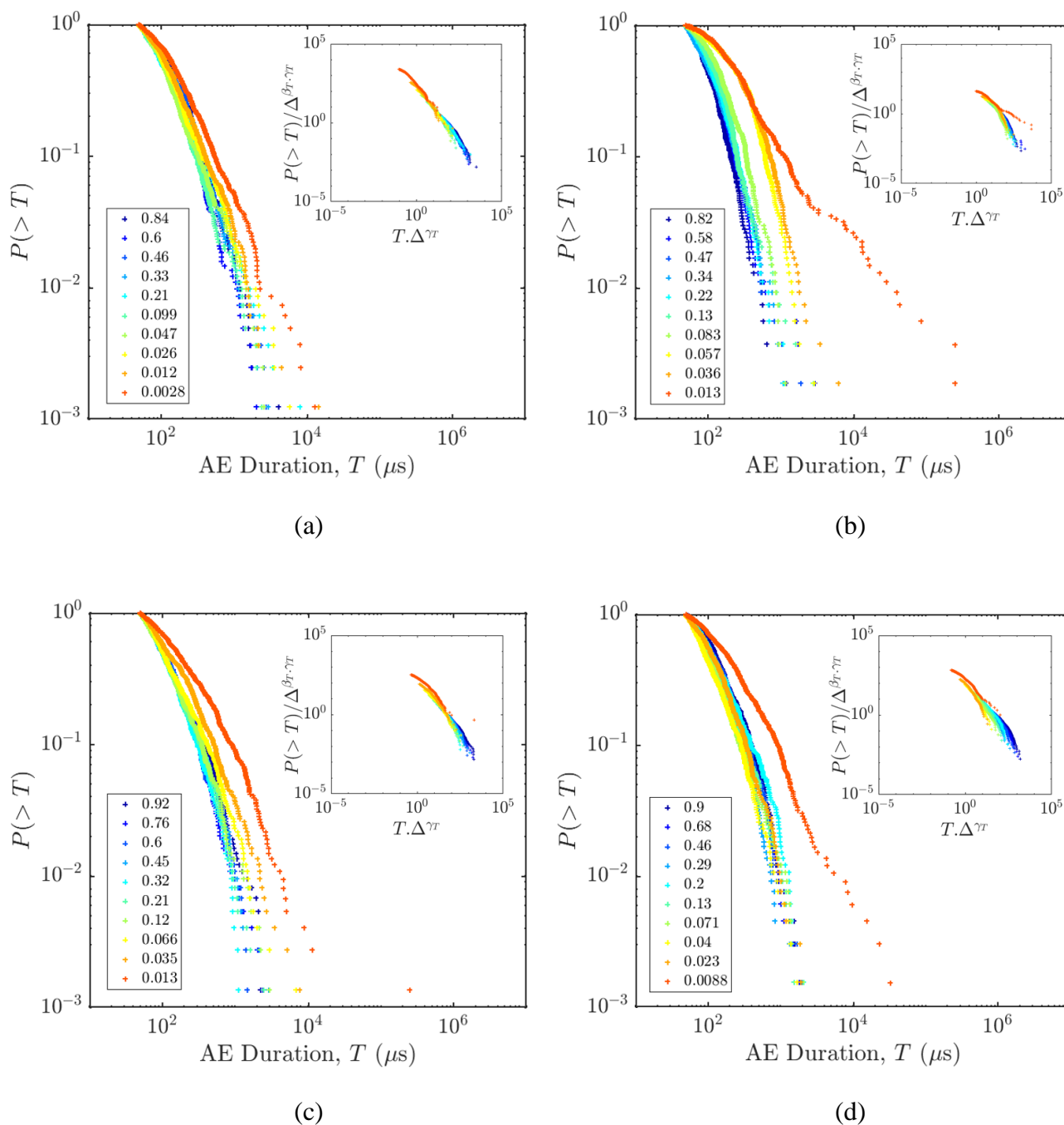


Fig. B.14. Cumulative distribution (*cdf*) of AE durations, T , at different distances to failure (Δ) for tests on four different sample sizes of **C-concrete**: (a) 40x80 mm; (b) 70x140 mm; (c) 110x220 mm; and (d) 160x320 mm. Insets: data collapses of the same data, presented in the corresponding main graph, in a rescaled plot.

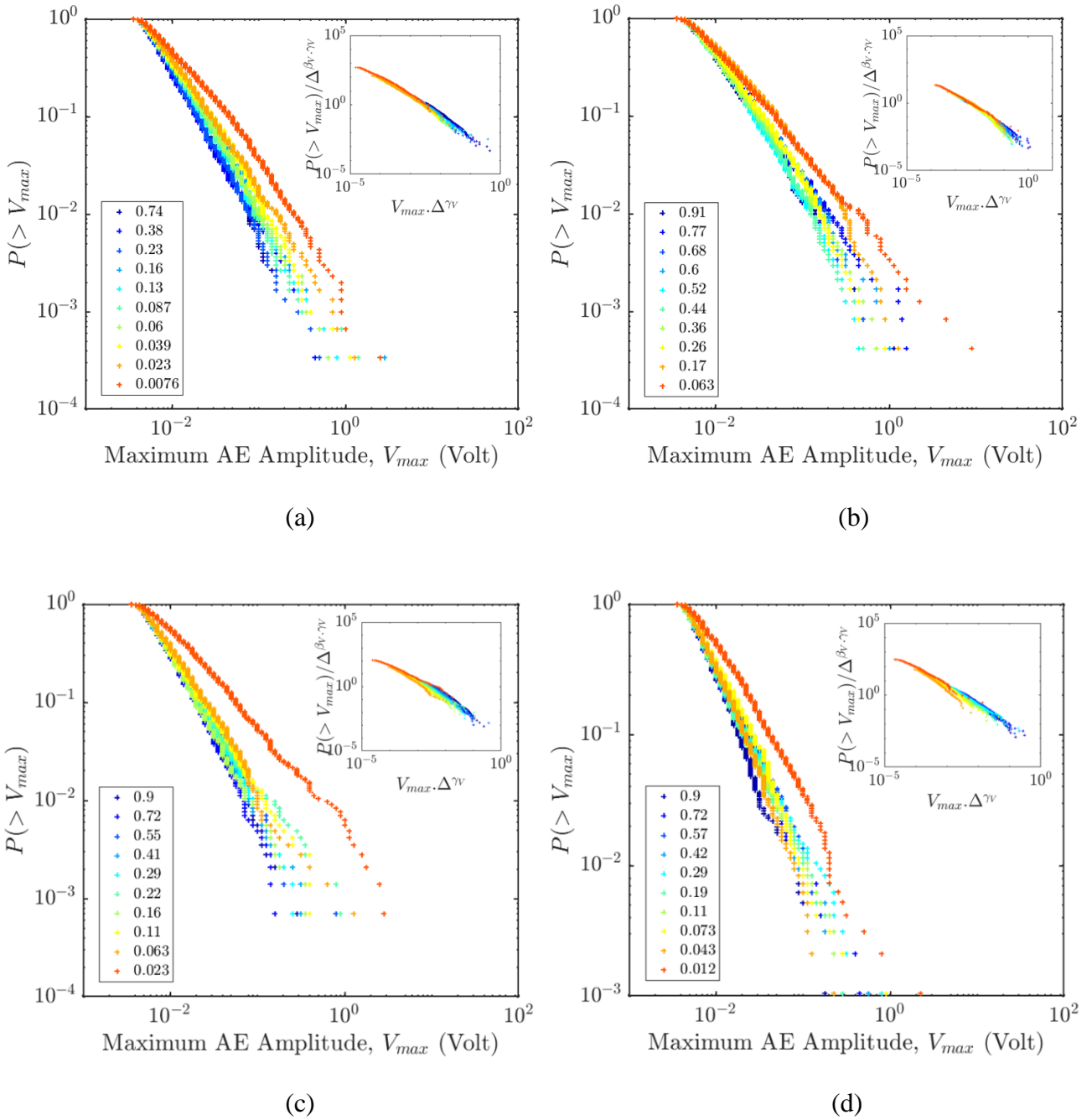


Fig. B.15. Cumulative distribution (*cdf*) of peak AE Amplitudes, V_{max} , at different distances to failure (Δ) for tests on four different sample sizes of **C-concrete**: (a) 40×80 mm; (b) 70×140 mm; (c) 110×220 mm; and (d) 160×320 mm. Insets: data collapses of the same data, presented in the corresponding main graph, in a rescaled plot.

Table. B.1. Summary of the scaling exponents for the distributions of AE durations, of AE energies released, and of AE amplitudes as well as for the rate of AE events, and of AE energy release for four different sample sizes of **F-concrete** and comparison with the corresponding values of Mean-Field Depinning/Stick-Slip (Baro et al., 2018; Dahmen, 2017; Ertas and Kardar, 1994; Leblanc et al., 2013; Salje and Dahmen, 2014).

Quantity	Form	Exponent	Sample size								All sizes	Mean-field values
			40x80mm		70x140mm		110x220mm		160x320mm			
Duration distribution	$P(T) \sim T^{-\beta_T} g(\Delta^{\gamma_T} T)$	β_T	2.1 ± 0.2	2.0 ± 0.2	2.1 ± 0.3	2.1 ± 0.3	2.1 ± 0.3	2.1 ± 0.3	2.1 ± 0.3	2.1 ± 0.3	2.1 ± 0.2	2
		γ_T	1.2 ± 0.6	1.2 ± 0.4	1.2 ± 0.5	1.1 ± 0.3	1.2 ± 0.5	1.1 ± 0.3	1.2 ± 0.5	1.1 ± 0.3	1.2 ± 0.5	1
Stress-integrated duration distribution	$P_{int}(T) \sim T^{-\theta_T}$	θ_T	2.9 ± 0.4	2.9 ± 0.2	2.9 ± 0.2	3.0 ± 0.2	2.9 ± 0.2	3.0 ± 0.2	2.9 ± 0.2	2.9 ± 0.2	2.9 ± 0.2	3
Energy distribution	$P(E) \sim E^{-\beta_E} f(\Delta^{\gamma_E} E)$	β_E	1.5 ± 0.1	1.5 ± 0.1	1.5 ± 0.1	1.5 ± 0.1	1.5 ± 0.1	1.5 ± 0.1	1.5 ± 0.1	1.5 ± 0.1	1.5 ± 0.1	4/3
		γ_E	3.5 ± 1.3	3.1 ± 0.8	3.0 ± 0.9	3.1 ± 1.0	3.2 ± 1.1	3.1 ± 1.0	3.2 ± 1.1	3.1 ± 1.0	3.2 ± 1.1	3
Stress-integrated energy distribution	$P_{int}(E) \sim E^{-\theta_E}$	θ_E	1.7 ± 0.1	1.8 ± 0.1	1.8 ± 0.1	1.8 ± 0.1	1.8 ± 0.1	1.8 ± 0.1	1.8 ± 0.1	1.8 ± 0.1	1.8 ± 0.1	5/3
Amplitude distribution	$P(V) \sim V^{-\beta_V} g(\Delta^{\gamma_V} V)$	β_V	2.1 ± 0.2	2.0 ± 0.1	1.9 ± 0.1	2.0 ± 0.1	2.0 ± 0.1	2.0 ± 0.1	2.0 ± 0.1	2.0 ± 0.1	2.0 ± 0.1	2
		γ_V	1.1 ± 0.5	1.1 ± 0.7	1.1 ± 0.6	1.2 ± 0.4	1.2 ± 0.5	1.2 ± 0.4	1.2 ± 0.5	1.2 ± 0.4	1.2 ± 0.5	1
Stress-integrated amplitude distribution	$P_{int}(V) \sim V^{-\theta_V}$	θ_V	2.9 ± 0.3	2.9 ± 0.5	2.8 ± 0.4	2.8 ± 0.3	2.9 ± 0.4	2.8 ± 0.3	2.9 ± 0.4	2.9 ± 0.4	2.9 ± 0.4	3
Conditional average maximum amplitude vs duration	$\langle V_{max} T \rangle \sim T^\delta$	δ	1.00 ± 0.05	1.00 ± 0.05	0.85 ± 0.10	1.00 ± 0.05	0.95 ± 0.05	1.00 ± 0.05	0.95 ± 0.05	0.95 ± 0.05	0.95 ± 0.05	1
Rate of AE event	$dN/d\Delta \sim \Delta^{-p}$	p	0.7 ± 0.1	0.6 ± 0.1	0.9 ± 0.1	0.8 ± 0.1	0.70 ± 0.05	0.8 ± 0.1	0.70 ± 0.05	0.70 ± 0.05	0.70 ± 0.05	None
Rate of AE Energy	$dE/d\Delta \sim \Delta^{-\alpha}$	α	1.1 ± 0.1	1.0 ± 0.1	1.3 ± 0.1	1.3 ± 0.1	1.2 ± 0.1	1.3 ± 0.1	1.2 ± 0.1	1.2 ± 0.1	1.2 ± 0.1	2
Derived exponents												
Correlation length	$\xi \sim \Delta^{-\nu}$	ν									1.1 ± 0.3	1
Dynamic exponent	$T^* \sim \xi^z$	z									1.1 ± 0.5	1

Table. B.2. Summary of the scaling exponents for the distributions of AE durations, of AE energies released, and of AE amplitudes as well as for the rate of AE events, and of AE energy release for four different sample sizes of **M-concrete** and comparison with the corresponding values of Mean-Field Depinning/Stick-Slip (Baro et al., 2018; Dahmen, 2017; Ertas and Kardar, 1994; Leblanc et al., 2013; Salje and Dahmen, 2014).

Quantity	Form	Exponent	Sample size				All sizes	Mean-field values
			40x80mm		70x140mm			
Duration distribution	$P(T) \sim T^{-\beta_T} g(\Delta^{\gamma_T} T)$	β_T	2.0 ± 0.3	2.0 ± 0.2	2.0 ± 0.4	2.0 ± 0.3	2.0 ± 0.3	2
		γ_T	1.1 ± 0.3	1.3 ± 0.5	1.1 ± 0.5	1.1 ± 0.4	1.1 ± 0.5	1
Stress-integrated duration distribution	$P_{int}(T) \sim T^{-\theta_T}$	θ_T	2.9 ± 0.1	2.8 ± 0.3	2.9 ± 0.2	2.9 ± 0.2	2.9 ± 0.2	3
Energy distribution	$P(E) \sim E^{-\beta_E} f(\Delta^{\gamma_E} E)$	β_E	1.4 ± 0.1	1.4 ± 0.1	1.5 ± 0.1	1.4 ± 0.1	1.4 ± 0.1	4/3
		γ_E	3.3 ± 0.7	3.9 ± 1.2	3.3 ± 1.0	2.6 ± 0.5	3.4 ± 0.9	3
Stress-integrated energy distribution	$P_{int}(E) \sim E^{-\theta_E}$	θ_E	1.7 ± 0.1	1.7 ± 0.1	1.8 ± 0.1	1.8 ± 0.1	1.75 ± 0.10	5/3
Amplitude distribution	$P(V) \sim V^{-\beta_V} g(\Delta^{\gamma_V} V)$	β_V	2.0 ± 0.1	2.0 ± 0.2	2.0 ± 0.2	2.1 ± 0.2	2.0 ± 0.1	2
		γ_V	1.1 ± 0.7	1.1 ± 0.8	1.2 ± 0.8	1.3 ± 0.8	1.2 ± 0.6	1
Stress-integrated amplitude distribution	$P_{int}(V) \sim V^{-\theta_V}$	θ_V	2.9 ± 0.5	2.9 ± 0.6	2.8 ± 0.4	2.9 ± 0.4	2.9 ± 0.4	3
Conditional average maximum amplitude vs duration	$\langle V_{max} T \rangle \sim T^\delta$	δ	1.00 ± 0.05	0.85 ± 0.05	0.95 ± 0.05	0.90 ± 0.05	0.95 ± 0.05	1
Rate of AE event	$dN/d\Delta \sim \Delta^{-p}$	p	0.7 ± 0.1	0.6 ± 0.1	0.7 ± 0.1	1.0 ± 0.1	0.65 ± 0.05	None
Rate of AE Energy	$dE/d\Delta \sim \Delta^{-\alpha}$	α	1.1 ± 0.2	1.3 ± 0.2	1.5 ± 0.1	1.4 ± 0.1	1.3 ± 0.1	2
Derived exponents								
Correlation length	$\xi \sim \Delta^{-\nu}$	ν					1.1 ± 0.3	1
Dynamic exponent	$T^* \sim \xi^z$	z					1.0 ± 0.5	1

Table. B.3. Summary of the scaling exponents for the distributions of AE durations, of AE energies released, and of AE amplitudes as well as for the rate of AE events, and of AE energy release for four different sample sizes of **C-concrete** and comparison with the corresponding values of Mean-Field Depinning/Stick-Slip (Baro et al., 2018; Dahmen, 2017; Ertas and Kardar, 1994; Leblanc et al., 2013; Salje and Dahmen, 2014).

Quantity	Form	Exponent	Sample size				All sizes	Mean-field values
			40x80mm	70x140mm	110x220mm	160x320mm		
Duration distribution	$P(T) \sim T^{-\beta_T} g(\Delta^{\gamma_T} T)$	β_T	2.0 ± 0.2	1.9 ± 0.3	2.0 ± 0.4	1.9 ± 0.2	2.0 ± 0.3	2
		γ_T	1.1 ± 0.4	1.2 ± 0.6	1.1 ± 0.6	1.0 ± 0.3	1.1 ± 0.5	1
Stress-integrated duration distribution	$P_{int}(T) \sim T^{-\theta_T}$	θ_T	3.0 ± 0.2	2.7 ± 0.3	2.9 ± 0.2	2.9 ± 0.1	2.9 ± 0.2	3
Energy distribution	$P(E) \sim E^{-\beta_E} f(\Delta^{\gamma_E} E)$	β_E	1.4 ± 0.1	1.4 ± 0.1	1.5 ± 0.1	1.5 ± 0.1	1.4 ± 0.1	4/3
		γ_E	3.2 ± 0.7	3.5 ± 0.8	3.3 ± 0.9	3.5 ± 1.0	3.4 ± 0.8	3
Stress-integrated energy distribution	$P_{int}(E) \sim E^{-\theta_E}$	θ_E	1.7 ± 0.1	1.7 ± 0.1	1.8 ± 0.1	1.8 ± 0.1	1.75 ± 0.05	5/3
Amplitude distribution	$P(V) \sim V^{-\beta_V} g(\Delta^{\gamma_V} V)$	β_V	2.0 ± 0.1	1.9 ± 0.1	2.0 ± 0.1	2.1 ± 0.2	2.0 ± 0.1	2
		γ_V	1.1 ± 0.6	1.1 ± 0.2	1.2 ± 0.8	1.2 ± 0.7	1.2 ± 0.6	1
Stress-integrated amplitude distribution	$P_{int}(V) \sim V^{-\theta_V}$	θ_V	2.9 ± 0.5	2.8 ± 0.1	2.8 ± 0.6	2.9 ± 0.5	2.9 ± 0.4	3
Conditional average maximum amplitude vs duration	$\langle V_{max} T \rangle \sim T^\delta$	δ	1.00 ± 0.05	0.90 ± 0.05	0.90 ± 0.05	0.90 ± 0.05	0.95 ± 0.05	1
Rate of AE event	$dN/d\Delta \sim \Delta^{-p}$	p	0.7 ± 0.1	0.6 ± 0.1	0.7 ± 0.1	0.7 ± 0.1	0.65 ± 0.05	None
Rate of AE Energy	$dE/d\Delta \sim \Delta^{-\alpha}$	α	1.3 ± 0.1	1.3 ± 0.1	1.4 ± 0.1	1.3 ± 0.1	1.3 ± 0.1	2
Derived exponents								
Correlation length	$\xi \sim \Delta^{-\nu}$	ν					1.1 ± 0.3	1
Dynamic exponent	$T^* \sim \xi^z$	z					1.0 ± 0.5	1

Appendix C

Application to published experimental strength data

In this appendix, we use the finite-size scaling for the mean compressive strength (Eq. (6.3)) to fit the experimental strength data reported by (Blanks and McNamara, 1935). In their work, different concrete mixtures obtained by simply varying the maximum aggregate size d_{\max} were tested for various sizes of the length-to-diameter ratio ($h/\phi = 2$) cylinders. We consider here only three concrete mixtures termed B-8, B-9 and B-10 as they were associated with the widest range of sample size. The mix data, the geometrical specimen sizes and the corresponding mean 28-days compressive strength $\langle\sigma_f\rangle$ are reported in Table C.1.

Fig. C.1 shows the best-fitted finite-size scaling (Eq. (6.3)) for the mean compressive strength of the three considered concrete mixtures, taking L as the diameter of sample (ϕ). The mean-field prediction $\nu_{FS} = 1$ was used in this work. We performed non-linear fits to extract the asymptotic strength σ_∞ as well as the length scale L_m for the three considered concrete mixtures. These values are presented in Table C.1. We observe that the scaling prediction (6.3) is in remarkable agreement with the published experimental data of (Blanks and McNamara, 1935). Due to the absence of reported values of strength variability and microstructural characteristics, the scaling (6.4) and the role of heterogeneities on size effect compressive strength for these concrete mixtures above were not examined.

Using $\nu_{FS} = 1$ and the values of L_m in Table C.1, we plot all strength data on $[\langle\sigma_f\rangle \text{ vs. } (L/L_m)^{-1/\nu_{FS}}]$ plot. As shown in Fig. C.1d, a good collapse of all data (all sample size, all considered concrete mixtures) onto the fit of scaling (6.3) is achieved. From the non-linear fits, the asymptotic strength $\sigma_\infty \approx 22.4$ MPa is found to be independent of sample size

and concrete mixture. This observation, consistent with our results (see section 6.4), allows to validate the rationality of the underlying theoretical framework.

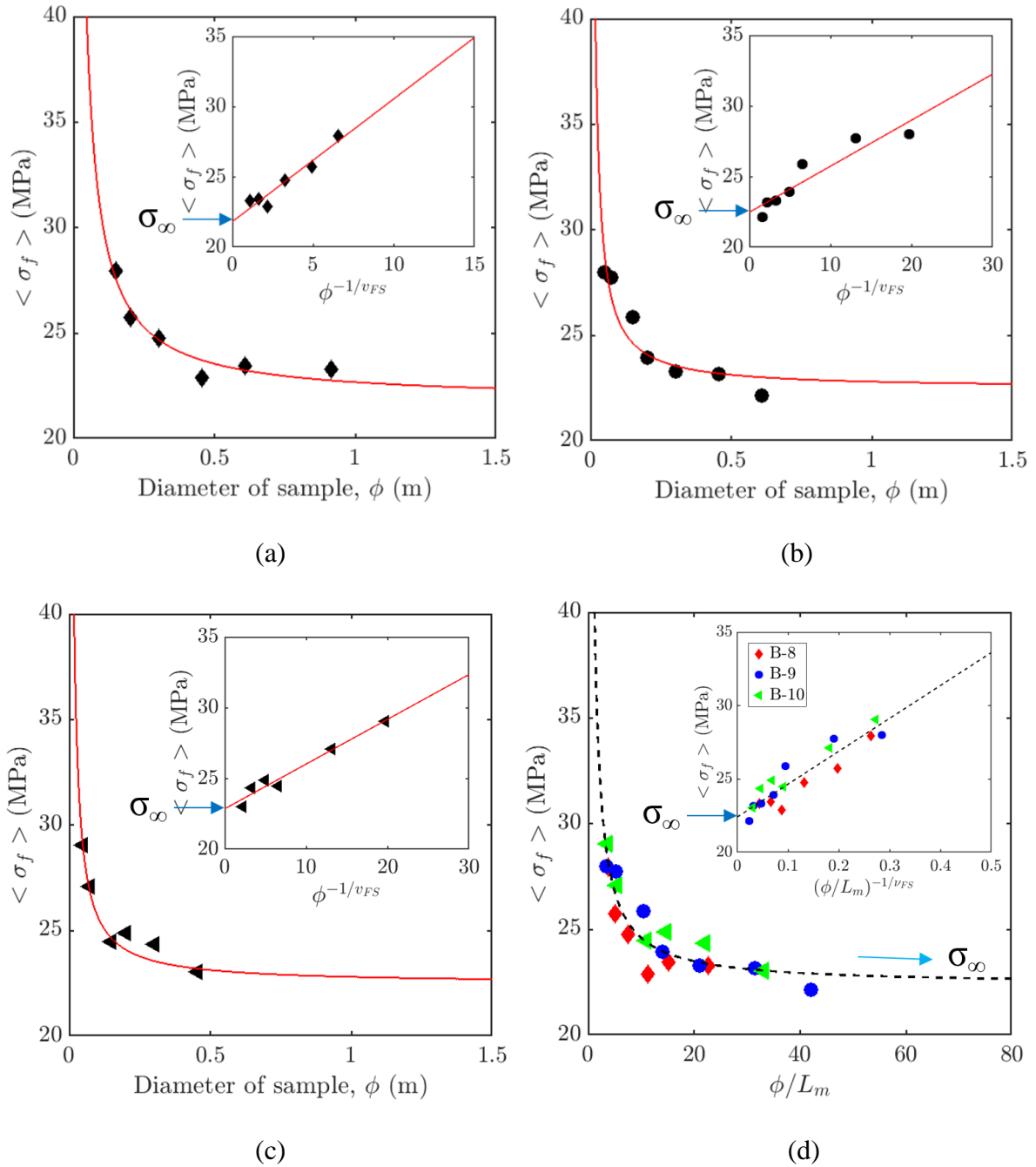


Fig. C.1. Finite-size effect on the mean compressive strength. (a) B-8 concrete mixture; (b) B-9 concrete mixture; (c) B-10 concrete mixture. Main graphs show the mean compressive strength, $\langle \sigma_f \rangle$ as a function of specimen size. Black symbols are the experimental data reported by (Blanks and McNamara, 1935). Red curve is the fitting by Eq. (6.3). Insets show the same data and fits in a $[\langle \sigma_f \rangle vs. \phi^{-1/v_{FS}}]$ graph. In this smaller graph, the fitting by Eq. (6.3) becomes a straight line and the asymptotic strength σ_∞ is determined.

Table C.1. Concrete mixture data, geometrical specimen sizes and mean compressive strengths for the experiments reported by (Blanks and McNamara, 1935).

Concrete mix data			Cylinders ($h/\phi = 2$)	Compressive strength, $\langle \sigma_f \rangle$ (MPa)	Asymptotic strength, σ_∞ (MPa)		L_m (mm)	
No.	W/C	d_{\max} (mm)	ϕ (mm)		Mean	SD	Mean	SD
B-8	0.53	38.10	152.4	27.92	21.8	1.3	40.1	5.2
			203.2	25.72				
			304.8	24.75				
			457.2	22.89				
			609.6	23.44				
			914.4	23.30				
B-9	0.55	19.05	50.8	27.99	22.5	1.4	14.5	2.1
			76.2	27.72				
			152.4	25.86				
			203.2	23.92				
			304.8	23.30				
			457.2	23.17				
B-10	0.54	9.52	50.8	29.03	22.9	0.8	13.8	1.3
			76.2	27.10				
			152.4	24.48				
			203.2	24.89				
			304.8	24.34				
			457.2	23.03				

Appendix D

Examples of application for Chapter 7

We present here two examples of application of the checking procedure proposed in section 7.3.2 to verify the conformity of concrete with the strength requirements.

In the first example (Table D.1), we check the conformity of our three concrete mixtures with the strength class C35/45 expressed in the standard (EN 1992, 2004). The values of parameters obtained for the 160x320-mm samples are used for this example.

Table D.1. Example of application of the checking procedure proposed in section 7.3.2 for our three concrete mixtures

Parameter		F-concrete	M-concrete	C-concrete
Compressive strength class C35/45	$\sigma_\infty = f_{ck} = 35 \text{ MPa}$			
Mean compressive strength (MPa)	$\langle \sigma_f \rangle$	41.9	39.2	36.7
Sample size (mm)	L	160	160	160
Porosity (%)	p_o	4.8	1.6	1.5
Maximum pore diameter (mm)	$d_{p,max}$	6.9	6.7	5.4
Minimum required average strength ³ (MPa)	$f_{mr} = \sigma_\infty \left[\frac{0.7(p_o \times d_{p,max})}{L} + 1 \right]$	40.1	36.6	36.2
Acceptance condition	$\langle \sigma_f \rangle \geq f_{mr}$	passed	passed	passed

As shown in Table D.1, all of the three concrete mixtures have an experimental mean compressive strength $\langle \sigma_f \rangle$, which is larger than the minimum required average strength (f_{mr})

³ The porosity p_o expressed in %.

estimated from the proposed procedure,. Therefore, we can conclude that these three mixtures comply with the strength requirements for the strength class C35/45. In this example, the C-mixture provides the closest mean strength value to the required value of strength class C35/45 in comparison to the other mixtures. This means that a coarser concrete mixture, having a lower porosity in its hardened form, will comply better the target characteristic strength than the finer mixtures.

For the second example (Table D.2), based on the original data of the C-160x320mm samples (Case 1), two additional cases are considered after changing either the value of porosity (Case 2) or the value of the mean compressive strength (Case 3).

Table D.2. Example of application of the checking procedure proposed in section 7.3.2 for three assumed cases of C-concrete

Parameter		Case 1	Case 2	Case 3
Compressive strength class C35/45	$\sigma_{\infty} = f_{ck} = 35 \text{ MPa}$			
Mean compressive strength (MPa)	$\langle \sigma_f \rangle$	36.7	36.7	35.7
Sample size (mm)	L	160	160	160
Porosity (%)	p_o	1.5	3.5	1.5
Maximum pore diameter (mm)	$d_{p,max}$	5.4	5.4	5.4
Minimum required average strength ⁴ (MPa)	$f_{mr} = \sigma_{\infty} \left[\frac{0.7(p_o \times d_{p,max})}{L} + 1 \right]$	36.2	37.9	36.2
Acceptance condition	$\langle \sigma_f \rangle \geq f_{mr}$	passed	failed	failed

As the results presented in Table D.2, the two last cases do not comply with the strength requirement for the strength class C35/45. Although Case 2 has the same mean strength for 160x320mm samples as experimental Case 1, the strength requirement is not satisfied for Case 2, owing to a larger porosity. This results from the fact that a larger porosity means stronger size effects on strength, hence a larger value of the minimum average strength required at a fixed sample size. The production of normal-weight concrete with a porosity as small as possible is an important goal to achieve a good quality of concrete as well as to be able to correctly estimate the asymptotic strength for laboratory samples. Case 3, characterized by an unchanged porosity but a smaller mean strength than Case 1, also fails the strength

⁴ The porosity p_o expressed in %.

requirement. This illustrates the fact that both the strength and the sample size criteria must be examined for the acceptance decision.

Bibliography

- ACI 318-05, 2005. Building Code Requirements for Structural Concrete and Commentary. Am. Concr. Inst.
- Alava, M.J., Nukala, P.K.V.V., Zapperi, S., 2006. Statistical models of fracture. *Adv. Phys.* 55, 349–476. doi:10.1080/00018730300741518
- Alava, M.J., Nukala, P.K.V. V, Zapperi, S., 2009. Size effects in statistical fracture. *J. Phys. D Applied Phys.* 42, 214012. doi:10.1088/0022-3727/42/21/214012
- Amitrano, D., 2012. Variability in the power-law distributions of rupture events. *Eur. Phys. J. - Spec. Top.* 205, 199–215. doi:10.1140/epjst/e2012-01571-9
- Amitrano, D., Grasso, J.R., Hantz, D., 1999. From diffuse to localised damage through elastic interaction. *Geophys. Res. Lett.* 26, 2109–2112. doi:10.1029/1999GL900388
- Amitrano, D., Grasso, J.R., Senfaute, G., 2005. Seismic precursory patterns before a cliff collapse and critical point phenomena. *Geophys. Res. Lett.* 32, 1–5. doi:10.1029/2004GL022270
- Andersons, J., Joffe, R., Hojo, M., Ochiai, S., 2002. Glass fibre strength distribution determined by common experimental methods. *Compos. Sci. Technol.* 62, 131–145. doi:10.1016/S0266-3538(01)00182-8
- Asloun, E.M., Donnet, J.B., Guilpain, G., Nardin, M., Schultz, J., 1989. On the estimation of the tensile strength of carbon fibres at short lengths. *J. Mater. Sci.* 24, 3504–3510. doi:10.1007/BF02385732
- ASTM C 457/C 457M-16, 2016. Standard Test Method for Microscopical Determination of Parameters of the Air-Void System in Hardened Concrete. ASTM Int.
- ASTM C31/C31M-03, 2003. Standard Practice for Making and Curing Concrete Test Specimens in the Field. ASTM Int. 1–5.
- ASTM C39/C39M-14, 2014. Standard Test Method for Compressive Strength of Cylindrical Concrete Specimens. ASTM Int. 1–7. doi:10.1520/C0039_C0039M-14
- ASTM C469/C469M-14, 2014. Standard Test Method for Static Modulus of Elasticity and Poisson's Ratio of Concrete in Compression. ASTM Int. West Conshohocken, PA. doi:10.1520/C0469_C0469M
- ASTM C597-02, 2002. Standard Test Method for Pulse Velocity Through Concrete. ASTM International, West Conshohocken, PA.
- ASTM E1316-06a, 2006. Standard Terminology for Nondestructive Examinations. ASTM Int. West Conshohocken, PA.
- ASTM E650–97, 1997. Standard Guide for Mounting Piezoelectric Acoustic Emission Sensors,. ASTM Int. West Conshohocken, PA.
- ASTM E976-10, 2010. Standard Guide for Determining the Reproducibility of Acoustic Emission Sensor Response. ASTM Int. West Conshohocken, PA.

- Babu, D.S., Babu, K.G., Tiong-Huan, W., 2006. Effect of polystyrene aggregate size on strength and moisture migration characteristics of lightweight concrete. *Cem. Concr. Compos.* 28, 520–527. doi:10.1016/j.cemconcomp.2006.02.018
- Bao, Y., Jin, Z., 1993. Size effects and a mean-strength criterion for ceramics. *Fatigue Fract. Eng. Mater. Struct.* 16, 829–835. doi:10.1111/j.1460-2695.1993.tb00122.x
- Baran, G.R., Mccool, J.I., Boberick, K.G., 1999. Size effect in resin/glass composite flexure strengths. *J. Oral Rehabil.* 26, 775–780. doi:10.1046/j.1365-2842.1999.00451.x
- Barés, J., Barbier, L., Bonamy, D., 2013. Crackling versus continuumlike dynamics in brittle failure. *Phys. Rev. Lett.* 111, 1–5. doi:10.1103/PhysRevLett.111.054301
- Baró, J., Corral, Á., Illa, X., Planes, A., Salje, E.K.H., Schranz, W., Soto-Parra, D.E., Vives, E., 2013. Statistical similarity between the compression of a porous material and earthquakes. *Phys. Rev. Lett.* 110, 1–5. doi:10.1103/PhysRevLett.110.088702
- Baro, J., Dahmen, K.A., Planes, A., Pedro, C.O., Nataf, G.F., Salje, E.K.H., Vives, E., 2018. Experimental evidence of accelerated seismic release without critical failure in acoustic emissions of compressed nanoporous materials. 1–7.
- Bartlett, F.M., MacGregor, J.G., 1994. Effect of Moisture Condition on Concrete Core Strengths. *ACI Mater. J.* 91, 227–236.
- Bazant, Z.P., 2004a. Scaling theory for quasibrittle structural failure. *Proc. Natl. Acad. Sci. U. S. A.* 101, 13400–13407. doi:10.1073/pnas.0404096101
- Bazant, Z.P., 2004b. Probability distribution of energetic-statistical size effect in quasibrittle fracture. *Probabilistic Eng. Mech.* 19, 307–319. doi:10.1016/j.probengmech.2003.09.003
- Bazant, Z.P., 1999. Size Effect on Structural Strength: A Review. *Arch. Appl. Mech.* 69, 703–725. doi:10.1007/s004190050252
- Bazant, Z.P., 1998. Size effect in tensile and compression fracture of concrete structures: Computational modeling and design. *Fract. Mech. Concr. Struct. Proceeding*, 1905–1922.
- Bazant, Z.P., 1984. Size Effect in Blunt Fracture: Concrete, Rock, Metal. *J. Eng. Mech.* 110, 518–535. doi:10.1061/(ASCE)0733-9399(1984)110:4(518)
- Bazant, Z.P., Chen, E.P., 1997. Scaling of structural failure. *Appl. Mech. Rev.* 50, 593–627.
- Bazant, Z.P., Kazemi, M.T., 1990. Determination of fracture energy, process zone length and brittleness number from size effect, with application to rock and concrete. *Int. J. Fract.* 44, 111–131. doi:10.1007/BF00047063
- Bazant, Z.P., Planas, J., 1998. Fracture and size effect in concrete and other quasibrittle materials. CRC Press, Boca Raton, Florida, USA.
- Bazant, Z.P., Vorechovsky, M., Novak, D., 2007. Asymptotic Prediction of Energetic-Statistical Size Effect from Deterministic Finite-Element Solutions. *J. Eng. Mech.* 133, 153–162. doi:10.1061/(ASCE)0733-9399(2007)133:2(153)
- Bazant, Z.P., Xi, Y., Reid, S.G., 1991. Statistical size effect in quasi-brittle structures: I. Is Weibull theory applicable? *J. Eng. Mech.* 117, 2609–2622. doi:10.1061/(ASCE)0733-9399(1991)117:11(2609)
- Bazant, Z.P., Xiang, Y., 1997. Size Effect in Compression Fracture: Splitting Crack Band Propagation. *J. Eng. Mech.* 123, 162–172. doi:10.1061/(ASCE)0733-9399(1997)123:2(162)
- Bazant, Z.P., Yavari, A., 2005. Is the cause of size effect on structural strength fractal or energetic-statistical? *Eng. Fract. Mech.* 72, 1–31. doi:10.1016/j.engfracmech.2004.03.004
- Bertalan, Z., Shekhawat, A., Sethna, J.P., Zapperi, S., 2014. Fracture Strength: Stress Concentration, Extreme Value Statistics, and the Fate of the Weibull Distribution. *Phys. Rev. Appl.* 2, 1–8. doi:10.1103/PhysRevApplied.2.034008

- Blanks, R.F., McNamara, C., 1935. Mass concrete tests in large cylinders. *J. Am. Concr. Inst.* 31, 280–303.
- Bolech, C.J., Rosso, A., 2004. Universal statistics of the critical depinning force of elastic systems in random media. *Phys. Rev. Lett.* 93, 1–4. doi:10.1103/PhysRevLett.93.125701
- Bonamy, D., Bouchaud, E., 2011. Failure of heterogeneous materials: A dynamic phase transition? *Phys. Rep.* 498, 1–44. doi:10.1016/j.physrep.2010.07.006
- Bonamy, D., Santucci, S., Ponson, L., 2008. Crackling dynamics in material failure as the signature of a self-organized dynamic phase transition. *Phys. Rev. Lett.* 101, 1–4. doi:10.1103/PhysRevLett.101.045501
- Burtscher, S.L., Kollegger, J., 2004. Size effect experiments on granular materials in compression, in: 5th International Conference on Fracture Mechanics of Concrete and Concrete Structures – FraMCoS-5. p. 8.
- Burtscher, S.L., Kollegger, J., 2003. Size-effect experiments on concrete in compression. *Struct. Concr.* 4, 163–174.
- Carpinteri, A., 1994a. Scaling laws and renormalization groups for strength and toughness of disordered materials. *Int. J. Solids Struct.* 31, 291–302. doi:10.1016/0020-7683(94)90107-4
- Carpinteri, A., 1994b. Fractal nature of material microstructure and size effects on apparent mechanical properties. *Mech. Mater.* 18, 89–101. doi:10.1016/0167-6636(94)00008-5
- Carpinteri, A., Chiaia, B., Ferro, G., 1995. Size effects on nominal tensile strength of concrete structures: multifractality of material ligaments and dimensional transition from order to disorder. *Mater. Struct.* 28, 311–317. doi:10.1007/BF02473145
- Carpinteri, A., Ferro, G., Monetto, I., 1999. Scale effects in uniaxially compressed concrete specimens. *Mag. Concr. Res.* 51, 217–225. doi:10.1680/mac.1999.51.3.217
- Carpinteri, A., Pugno, N., 2005. Fractal fragmentation theory for size effects of quasi-brittle materials in compression. *Mag. Concr. Res.* 57, 309–313. doi:10.1680/mac.2005.57.6.309
- Chen, X., Wu, S., Zhou, J., 2013. Influence of porosity on compressive and tensile strength of cement mortar. *Constr. Build. Mater.* 40, 869–874. doi:10.1016/j.conbuildmat.2012.11.072
- Clauset, A., Shalizi, C.R., Newman, M.E., 2009. Power-law distributions in empirical data. *SIAM Rev.* 51, 661–703.
- Crosta, G.B., Agliardi, F., 2003. Failure forecast for large rock slides by surface displacement measurements. *Can. Geotech. J.* 40, 176–191. doi:10.1139/t02-085
- Dahmen, K.A., 2017. Mean Field Theory of Slip Statistics, in: Salje, E.K.H., Saxena, A., Planes, A. (Eds.), *Avalanches in Functional Materials and Geophysics*. Springer International Publishing, Cham, Switzerland, p. 310. doi:10.1007/978-3-319-45612-6
- Dahmen, K.A., Ben-Zion, Y., Uhl, J.T., 2009. Micromechanical model for deformation in solids with universal predictions for stress-strain curves and slip avalanches. *Phys. Rev. Lett.* 102, 1–4. doi:10.1103/PhysRevLett.102.175501
- Dayaratnam, P., Ranganathan, R., 1976. Statistical analysis of strength of concrete. *Build. Environ.* 11, 145–152.
- de Arcangelis, L., Godano, C., Grasso, J.R., Lippiello, E., 2016. Statistical physics approach to earthquake occurrence and forecasting. *Phys. Rep.* 628, 1–91. doi:10.1016/j.physrep.2016.03.002
- del Viso, J.R., Carmona, J.R., Ruiz, G., 2008. Shape and size effects on the compressive strength of high-strength concrete. *Cem. Concr. Res.* 38, 386–395. doi:10.1016/j.cemconres.2007.09.020
- Démery, V., Dansereau, V., Berthier, E., Ponson, L., Weiss, J., 2017. Elastic interactions in damage models of brittle failure. *ArXiv e-prints 2017arXiv1*, 1–16.

- Deschanel, S., Ben Rhouma, W., Weiss, J., 2017. Acoustic emission multiplets as early warnings of fatigue failure in metallic materials. *Sci. Rep.* 7, 1–10. doi:10.1038/s41598-017-13226-1
- EN 1992, 2004. Eurocode 2: Design of concrete structures - Part 1-1 : General rules and rules for buildings, European Committee for Standardization.
- Ertas, D., Kardar, M., 1994. Critical dynamics of contact line depinning. *Phys. Rev. E* 49, 2532–2535. doi:10.1103/PhysRevE.49.R2532
- Evans, A.G., 1979. Acoustic emission sources in brittle solids, in: Ono, K. (Ed.), *Fundamentals of Acoustic Emission*. Los Angeles, pp. 209–227.
- Ferro, G., Carpinteri, A., 2008. Effect of Specimen Size on the Dissipated Energy Density in Compression. *J. Appl. Mech.* 75, 041003. doi:10.1115/1.2910899
- Fib Mode Code, 2013. *fib Mode Code for Concrete Structures 2010*. Wilhelm Ernst & Sohn. doi:10.1002/9783433604090
- Fisher, D.S., 1998. Collective transport in random media: from superconductors to earthquakes. *Phys. Rep.* 301, 113–150.
- Fisher, D.S., Dahmen, K., Ramanathan, S., Ben-Zion, Y., 1997. Statistics of Earthquakes in Simple Models of Heterogeneous Faults. *Phys. Rev. Lett.* 78, 4885–4888. doi:10.1103/PhysRevLett.78.4885
- Fisher, R.A., Tippett, L.H.C., 1928. Limiting forms of the frequency distribution of the largest or smallest member of a sample. *Math. Proc. Cambridge Philos. Soc.* 24, 180–190. doi:10.1017/S0305004100015681
- Fonseca, P.C., Scherer, G.W., 2015. An image analysis procedure to quantify the air void system of mortar and concrete. *Mater. Struct.* 48, 3087–3098. doi:10.1617/s11527-014-0381-9
- Girard, L., Amitrano, D., Weiss, J., 2010. Failure as a critical phenomenon in a progressive damage model. *J. Stat. Mech. Theory Exp.* 2010, P01013. doi:10.1088/1742-5468/2010/01/P01013
- Girard, L., Weiss, J., Amitrano, D., 2012. Damage-cluster distributions and size effect on strength in compressive failure. *Phys. Rev. Lett.* 108, 1–5. doi:10.1103/PhysRevLett.108.225502
- Gonzalez, R.C., Woods, R.E., 2002. *Digital image processing*, 2nd ed. Prentice Hall.
- Grosse, C.U., Ohtsu, M., 2008. *Acoustic Emission Testing: Basics for Research - Applications in Civil Engineering*. Springer-Verlag Berlin Heidelberg, Leipzig, Germany. doi:10.1007/978-3-540-69972-9
- Grosse, C.U., Reinhardt, H.W., Finck, F., 2003. Signal-Based Acoustic Emission Techniques in Civil Engineering. *J. Mater. Civ. Eng.* 15, 274–279. doi:10.1061/(ASCE)0899-1561(2003)15:3(274)
- Guarino, A., Garcimartín, A., Ciliberto, S., 1998. An experimental test of the critical behaviour of fracture precursors. *Eur. Phys. J. B* 6, 13–24. doi:10.1007/s100510050521
- Gumbel, E.J., 2004. *Statistics of Extremes*, Dover books on mathematics. Dover Publications.
- Gumbel, E.J., 1958. *Statistics of Extremes*. Columbia University Press, New York.
- Gurvich, M.R., DiBenedetto, A.T., Ranade, S. V., 1997. A new statistical distribution for characterizing the random strength of brittle materials. *J. Mater. Sci.* 32, 2559–2564. doi:10.1023/A:1018594215963
- Hanks, T.C., 1977. Earthquake stress drops, ambient tectonic stresses and stresses that drive plate motions. *Pure Appl. Geophys.* 115, 441–458. doi:10.1007/BF01637120
- Hansen, A., Hemmer, P.C., Pradhan, S., 2015. *The Fiber Bundle Model: Modeling Failure in Materials*. Wiley-VCH Verlag GmbH & Co, KGaA, Boschstr. 12, 69469 Weinheim, Germany. doi:10.1002/9783527671960

- Heilbronner, R., 2002. Analysis of bulk fabrics and microstructure variations using tessellations of autocorrelation functions. *Comput. Geosci.* 28, 447–455. doi:10.1016/S0098-3004(01)00088-7
- Heilbronner, R., 1992. The autocorrelation function: an image processing tool for fabric analysis. *Tectonophysics* 212, 351–370. doi:10.1016/0040-1951(92)90300-U
- Heilbronner, R., Barrett, S., 2014. *Image analysis in earth sciences: Microstructures and Textures of Earth Materials*, 1st ed. Springer-Verlag Berlin Heidelberg. doi:10.1007/978-3-642-10343-8
- Herrmann, H.J., Roux, S., 1990. *Statistical models for the fracture of disordered media*, North-Holland, Elsevier Science Publishers, Amsterdam. doi:10.1002/crat.2170260821
- Hilsdorf, H.K., 1967. A method to estimate the water content of concrete shields. *Nucl. Eng. Des.* 6, 251–263. doi:10.1016/0029-5493(67)90022-2
- Ifsttar, 1994. *Caractérisation du béton durci: Essais liés à a corrosion des armatures*.
- Jahne, B., 2005. *Digital Image Processing*, 6th ed. Springer.
- Jakobsen, U.H., Pade, C., Thaulow, N., Brown, D., Sahu, S., Magnusson, O., De Buck, S., De Schutter, G., 2006. Automated air void analysis of hardened concrete - a Round Robin study. *Cem. Concr. Res.* 36, 1444–1452. doi:10.1016/j.cemconres.2006.03.005
- Jaumé, S.C., Sykes, L.R., 1999. Evolving Towards a Critical Point: A Review of Accelerating Seismic Moment/Energy Release Prior to Large and Great Earthquakes. *Pure Appl. Geophys.* 155, 279–305. doi:10.1007/s000240050266
- Jeulin, D., Ostoja-Starzewski, M., 2001. *Mechanics of random and multiscale microstructures*, 1st ed. Springer-Verlag Wien. doi:10.1007/978-3-7091-2780-3
- Jiao, Y., Stillinger, F.H., Torquato, S., 2008. Modeling heterogeneous materials via two-point correlation functions. II. Algorithmic details and applications. *Phys. Rev. E - Stat. Nonlinear, Soft Matter Phys.* 77, 1–15. doi:10.1103/PhysRevE.77.031135
- Kanit, T., Forest, S., Galliet, I., Mounoury, V., Jeulin, D., 2003. Determination of the size of the representative volume element for random composites : statistical and numerical approach. *Int. J. Solids Struct.* 40, 3647–3679. doi:10.1016/S0020-7683(03)00143-4
- Kirsch, G., 1898. *Die Theorie der Elastizität und die Bedürfnisse der Festigkeitslehre*. Springer.
- Kocur, G.K., 2012. Time reverse modeling of acoustic emissions in structural concrete. ETH Zurich. doi:10.3929/ethz-a-007319340
- Kolias, S., 1994. Investigation of the possibility of estimating concrete strength by porosity measurements. *Mater. Struct.* 27, 265–272. doi:10.1007/BF02473043
- Kumar, R., Bhattacharjee, B., 2003. Porosity, pore size distribution and in situ strength of concrete. *Cem. Concr. Res.* 33, 155–164. doi:10.1016/S0008-8846(02)00942-0
- Leblanc, M., Angheluta, L., Dahmen, K., Goldenfeld, N., 2013. Universal fluctuations and extreme statistics of avalanches near the depinning transition. *Phys. Rev. E* 87, 1–13. doi:10.1103/PhysRevE.87.022126
- Lian, C., Zhuge, Y., Beecham, S., 2011. The relationship between porosity and strength for porous concrete. *Constr. Build. Mater.* 25, 4294–4298. doi:10.1016/j.conbuildmat.2011.05.005
- Lin, J., Lerner, E., Rosso, A., Wyart, M., 2014. Scaling description of the yielding transition in soft amorphous solids at zero temperature. *Proc. Natl. Acad. Sci. U. S. A.* 111, 14382–14387. doi:10.1073/pnas.1406391111
- Linger, D.A., 1963. Effect of stress on the dynamic modulus of concrete. *Highw. Res. Rec. - Prop. Concr.* 62–73.
- Lockner, D.A., Byerlee, J.D., Kuksenko, V., Ponomarev, A., Sidorin, A., 1991. Quasi-static fault growth and shear fracture energy in granite. *Nature* 350, 39–42.

- Lydon, F.D., Balendran, R. V., 1986. Some observations on elastic properties of plain concrete. *Cem. Concr. Res.* 16, 314–324.
- Mäkinen, T., Miksic, A., Ovaska, M., Alava, M.J., 2015. Avalanches in Wood Compression. *Phys. Rev. Lett.* 115, 1–5. doi:10.1103/PhysRevLett.115.055501
- Mansur, M.A., Wee, T.H., Chin, M.S., 1995. Derivation of the complete stress - strain curves for concrete in compression. *Mag. Concr. Res.* 47, 285–290. doi:10.1680/mac.1995.47.173.285
- Mariotte, E., 1686. *Traité du mouvement des eaux et des autres corps fluides*. Chez J. Jombert.
- Masad, E., Muhunthan, B., Shashidhar, N., Harman, T., 1999. Internal Structure Characterization of Asphalt Concrete Using Image Analysis. *J. Comput. Civ. Eng.* 13, 88–95. doi:10.1061/(ASCE)0887-3801(1999)13:2(88)
- Matheron, G., 1971. *The theory of regionalized variables and its applications*. Ecole Nationale Supérieure des Mines de Paris.
- Mazars, J., Pijaudier-Cabot, G., Saouridis, C., 1991. Size effect and continuous damage in cementitious materials. *Int. J. Fract.* 51, 159–173. doi:10.1007/BF00033976
- Mehta, P.K., Monteiro, P.J.M., 2006. *Concrete: microstructure, properties, and materials*, Third. ed. McGraw-Hill. doi:10.1036/0071462899
- Miannay, D.P., 1998. *Fracture Mechanics*. Springer, Berlin, Germany. doi:10.1007/978-1-4612-1740-4
- Mindess, S., 2004. Acoustic Emission Methods, in: Malhotra, V.M., Carino, N.J. (Eds.), *Handbook on Nondestructive Testing of Concrete*. &_3UHVV_//&, Boca Raton, Florida, USA, pp. 348–365.
- Mistras, 2001. *MISTRAS 2001 - AEDSP-32/16: Users Manual*, 1st ed. Princeton, New Jersey, USA.
- Moon, K.H., Falchetto, A.C., Jeong, J.H., 2014. Microstructural analysis of asphalt mixtures using digital image processing techniques. *Can. J. Civ. Eng.* 41, 74–86. doi:10.1139/cjce-2013-0250
- Muciaccia, G., Rosati, G., Luzio, G. Di, 2017. Compressive failure and size effect in plain concrete cylindrical specimens. *Constr. Build. Mater.* 137, 185–194. doi:10.1016/j.conbuildmat.2017.01.057
- Nataf, G.F., Castillo-Villa, P.O., Sellappan, P., Kriven, W.M., Vives, E., Planes, A., Salje, E.K.H., 2014. Predicting failure: Acoustic emission of berlinite under compression. *J. Phys. Condens. Matter* 26. doi:10.1088/0953-8984/26/27/275401
- Neville, A.M., 2004. *Properties of Concrete*, 4th ed. Pearson Education Limited.
- NF EN 12390-1, 2012. *Essais pour béton durci - Partie 1 : Forme , dimensions et autres exigences relatives*. Association Française de Normalisation (AFNOR).
- NF EN 12390-13, 2014. *Essais pour béton durci — Partie 13 : Détermination du module sécant d'élasticité en compression*. Association Française de Normalisation (AFNOR).
- NF EN 12390-3, 2012. *Essais pour béton durci - Partie 3 : Résistance à la compression des éprouvettes*. Association Française de Normalisation (AFNOR).
- NF EN 12390-4, 2000. *Essais pour béton durci - Partie 4 : Résistance à la compression - Caractéristiques des machines d'essai*. Association Française de Normalisation (AFNOR). doi:10.1017/CBO9781107415324.004
- NF EN 12390-7, 2012. *Essais pour béton durci - Partie 7 : Masse volumique du béton durci*. Association Française de Normalisation (AFNOR).
- NF EN 12620, 2008. *Granulats pour béton*. Association Française de Normalisation (AFNOR).
- NF EN 197-1, 2012. *Ciment -Partie 1: Compostition, spécifications et critères de conformité des*

- ciments courants. Association Française de Normalisation (AFNOR).
- NF EN 206-1, 2004. Béton - Partie 1 : Spécification, performances, production et conformité. Association Française de Normalisation (AFNOR).
- NF EN 933-1, 2012. Essais pour déterminer les caractéristiques géométriques des granulats - Partie 1 : détermination de la granularité - Analyse granulométrique par tamisage. Association Française de Normalisation (AFNOR).
- Noguchi, T., Tomosawa, F., Nemati, K.M., Chiaia, B.M., Fantilli, A.R., 2009. A practical equation for elastic modulus of concrete. *ACI Struct. J.* 106, 690–696. doi:10.14359/51663109
- Nukala, P.K.V.V., Zapperi, S., Āimunović, S., 2005. Statistical properties of fracture in a random spring model. *Phys. Rev. E - Stat. Nonlinear, Soft Matter Phys.* 71, 1–11. doi:10.1103/PhysRevE.71.066106
- Nukala, P.K.V. V, Šimunović, S., Zapperi, S., 2004. Percolation and localization in the random fuse model. *J. Stat. Mech. Theory Exp.* 08001, 1–23. doi:10.1088/1742-5468/2004/08/P08001
- Ohtsu, M., 2015. *Acoustic Emission (AE) and Related Non-destructive Evaluation Techniques in the Fracture Mechanics of Concrete: Fundamentals and Applications*. Elsevier, Cambridge, CB22 3HJ, UK. doi:http://dx.doi.org/10.1016/B978-1-78242-327-0.00008-8
- Ohtsu, M., 2010. Recommendation of RILEM TC 212-ACD: acoustic emission and related NDE techniques for crack detection and damage evaluation in concrete: Measurement method for acoustic emission signals in concrete. *Mater. Struct.* 43, 1177–1181. doi:10.1617/s11527-010-9638-0
- Ojala, I.O., Main, I.G., Ngwenya, B.T., 2004. Strain rate and temperature dependence of Omori law scaling constants of AE data: Implications for earthquake foreshock-aftershock sequences. *Geophys. Res. Lett.* 31, 1–5. doi:10.1029/2004GL020781
- Ouyang, C., Landis, E., Shah, S.P., 1991. Damage assessment in concrete using quantitative acoustic emission. *J. Eng. Mech.* 117, 2681–2698. doi:10.1061/(ASCE)0733-9399(1991)117:11(2681)
- Ozbolt, J., Eligehausen, R., 1995. Size effect in concrete and reinforced concrete structures. *Fract. Mech. Concr. Struct.* 665–674.
- Papanikolaou, S., Bohn, F., Sommer, R.L., Durin, G., Zapperi, S., Sethna, J.P., 2011. Universality beyond power laws and the average avalanche shape. *Nat. Phys.* 7, 316–320. doi:10.1038/nphys1884
- Pfleiderer, S., Ball, D.G.A., Bailey, R.C., 1993. AUTO: A computer program for the determination of the two-dimensional autocorrelation function of digital images. *Comput. Geosci.* 19, 825–829. doi:10.1016/0098-3004(93)90053-8
- Phani, K.K., 1987. A new modified Weibull distribution function. *J. Am. Ceram. Soc.* 70, 182–184.
- Pihlajavaara, S.E., 1974. A review of some of the main results of a research on the ageing phenomena of concrete: Effect of moisture conditions on strength, shrinkage and creep of mature concrete. *Cem. Concr. Res.* 4, 761–771. doi:10.1016/0008-8846(74)90048-9
- Pillai, S.U., Menon, D., 2009. *Reinforced Concrete Design*, 3rd ed. Tata McGraw-Hill Education Pvt. Ltd.
- Pollock, A.A., 1989. *Acoustic emission inspection*, Technical report, TR-103-96-12/89. Physical Acoustics Corporation.
- Pradhan, S., Hansen, A., Chakrabarti, B.K., 2010. Failure processes in elastic fiber bundles. *Rev. Mod. Phys.* 82, 499–555. doi:10.1103/RevModPhys.82.499
- Prosser, W.H., 2001. Acoustic Emission, in: Shull, P.J. (Ed.), *Nondestructive Evaluation: Theory, Techniques, and Applications*. Marcel Dekker, Inc, pp. 369–446.
- Reches, Z., Lockner, D.A., 1994. Nucleation and growth of faults in brittle rocks. *J. Geophys. Res.* 99,

- 18,159-18,173. doi:10.1029/94JB00115
- Renard, F., Cordonnier, B., Kobchenko, M., Kandula, N., Weiss, J., Zhu, W., 2017. Microscale characterization of rupture nucleation unravels precursors to faulting in rocks. *Earth Planet. Sci. Lett.* 476, 69–78. doi:10.1016/j.epsl.2017.08.002
- Renard, F., Weiss, J., Mathiesen, J., Ben-Zion, Y., Kandula, N., Cordonnier, B., 2018. Critical Evolution of Damage Toward System-Size Failure in Crystalline Rock. *J. Geophys. Res. Solid Earth* 123, 1969–1986. doi:10.1002/2017JB014964
- RILEM TC 148-SSC, 2000. Strain softening of concrete: Test method for measurement of the strain-softening behaviour of concrete under uniaxial compression.
- Roux, S., Hansen, A., Herrmann, H., Guyon, E., 1988. Rupture of heterogeneous media in the limit of infinite disorder. *J. Stat. Phys.* 52, 237–244. doi:10.1007/BF01016411
- Roux, S., Hild, F., 2002. On the relevance of mean field to continuum damage mechanics. *Int. J. Fract.* 116, 219–229. doi:10.1023/A:1020131031404
- Salje, E.K.H., Dahmen, K.A., 2014. Crackling Noise in Disordered Materials. *Annu. Rev. Condens. Matter Phys.* 5, 233–254. doi:10.1146/annurev-conmatphys-031113-133838
- Saltykov, S.A., 1967. The determination of the size distribution of particles in an opaque material from a measurement of the size distribution of their sections, *Proceedings of the Second International Congress for Stereology, Chicago-April 8-13, 1967.* Springer Berlin Heidelberg. doi:10.1007/978-3-642-88260-9_31
- Scholz, C.H., 2002. *The mechanics of Earthquakes and faulting*, 2nd ed. Cambridge University Press, Cambridge, UK.
- Schubnel, A., Thompson, B.D., Fortin, J., Guéguen, Y., Young, R.P., 2007. Fluid-induced rupture experiment on Fontainebleau sandstone: Premonitory activity, rupture propagation, and aftershocks. *Geophys. Res. Lett.* 34, 1–5. doi:10.1029/2007GL031076
- Sener, S., Barr, B. i G., Abusiaf, H.F., 1999. Size-effect tests in unreinforced concrete columns. *Mag. Concrete Res.* 51, 3–11.
- Shen, H., Oppenheimer, S.M., Dunand, D.C., Brinson, L.C., 2006. Numerical modeling of pore size and distribution in foamed titanium. *Mech. Mater.* 38, 933–944. doi:10.1016/j.mechmat.2005.06.027
- Sornette, D., 1994. Sweeping of an instability: an alternative to self-organized criticality to get powerlaws without parameter tuning. *J. Phys. I* 4, 209–221. doi:10.1051/jpl1:1994133
- Talamali, M., Petäjä, V., Vandembroucq, D., Roux, S., 2012. Strain localization and anisotropic correlations in a mesoscopic model of amorphous plasticity. *Comptes Rendus - Mec.* 340, 275–288. doi:10.1016/j.crme.2012.02.010
- Talamali, M., Petäjä, V., Vandembroucq, D., Roux, S., 2011. Avalanches, precursors, and finite-size fluctuations in a mesoscopic model of amorphous plasticity. *Phys. Rev. E* 84, 1–12. doi:10.1103/PhysRevE.84.016115
- Theobald, P., Zeqiri, B., Avison, J., 2008. Couplants and their influence on AE sensor sensitivity. *J. Acoust. Emiss.* 26, 91–97.
- Tippett, L.H.C., 1925. On the extreme individuals and the range of samples taken from a normal population. *Biometrika* 17, 364–387. doi:10.1093/biomet/17.3-4.355
- Torquato, S., 1991. Random heterogeneous media: Microstructure and improved bounds on effective properties. *Appl. Mech. Rev.* 44, 37–76. doi:10.1115/1.3119494
- Torrenti, J.M., Pijaudier-Cabot, G., Reynouard, J.M., 2013. *Mechanical Behavior of Concrete.* ISTE and Wiley. doi:10.1002/9781118557587
- Tyukodi, B., Patinet, S., Roux, S., Vandembroucq, D., 2016. From depinning transition to plastic

- yielding of amorphous media: A soft-modes perspective. *Phys. Rev. E* 93, 1–13. doi:10.1103/PhysRevE.93.063005
- Unanwa, C., Mahan, M., 2014. Statistical Analysis of Concrete Compressive Strengths for California Highway Bridges. *J. Perform. Constr. Facil.* 28, 157–167. doi:10.1061/(ASCE)CF.1943-5509.0000404
- Underwood, E.E., 1970. Quantitative stereology. Addison-Wesley Pub. Co.
- Utsu, T., Ogata, Y., S, R., Matsu'ura, 1995. The Centenary of the Omori Formula for a Decay Law of Aftershock Activity. *J. Phys. Earth* 43, 1–33. doi:10.4294/jpe1952.43.1
- Van Vliet, M.R.A., 2000. Size effect in tensile fracture of concrete and rock. Delft University Press.
- VandenBorn, I.C., Santen, A., Hoekstra, H.D., DeHosson, J.T.M., 1991. Mechanical strength of highly porous ceramics. *Phys. Rev. B* 43, 3794–3796. doi:10.1103/PhysRevB.43.3794
- Vilanova, A., Fernandez-Gomez, J., Landsberger, G.A., 2011. Evaluation of the mechanical properties of self compacting concrete using current estimating models: Estimating the modulus of elasticity, tensile strength, and modulus of rupture of self compacting concrete. *Constr. Build. Mater.* 25, 3417–3426. doi:10.1016/j.conbuildmat.2011.03.033
- Vives, E., Ortin, J., Rafois, I., Perez-Magrane, R., Planes, A., 1994. Distributions of Avalanches in Martensitic Transformations. *Phys. Rev. Lett.* 72, 1694–1697.
- Vu, C.C., Amitrano, D., Plé, O., Weiss, J., 2018a. Compressive failure as a critical transition: Experimental evidences and applications. *arXiv Prepr. arXiv1807.06386*.
- Vu, C.C., Weiss, J., Plé, O., Amitrano, D., Vandembroucq, D., 2018b. Revisiting statistical size effects on compressive failure of heterogeneous materials, with a special focus on concrete. *J. Mech. Phys. Solids* 121, 47–70. doi:10.1016/j.jmps.2018.07.022
- Wang, F., Shao, J., 2014. Modified Weibull distribution for analyzing the tensile strength of bamboo fibers. *Polymers (Basel)*. 6, 3005–3018. doi:10.3390/polym6123005
- Wang, L., Ma, S., Ma, L., 2008. Accelerating moment release of acoustic emission during rock deformation in the laboratory. *Pure Appl. Geophys.* 165, 181–199. doi:10.1007/s00024-008-0305-0
- Weibull, W., 1951. A Statistical Distribution Function of Wide Applicability. *J. Appl. Mech.* 18, 293–297.
- Weibull, W., 1939a. A statistical theory of the strength of materials. *R. Swedish Inst. Eng. Res.* 151, 45.
- Weibull, W., 1939b. The phenomenon of rupture in solids. *R. Swedish Inst. Eng. Res.* 153, 55.
- Weiss, J., Girard, L., Gimbert, F., Amitrano, D., Vandembroucq, D., 2014a. (Finite) statistical size effects on compressive strength. *Proc. Natl. Acad. Sci. U. S. A.* 111, 6231–6236. doi:10.1073/pnas.1403500111
- Weiss, J., Girard, L., Gimbert, F., Amitrano, D., Vandembroucq, D., 2014b. (Finite) statistical size effects on compressive strength. Supporting Information. *Proc. Natl. Acad. Sci. U. S. A.* 111, 1–7. doi:10.1073/pnas.1403500111 SI
- Wevers, M., Lambrihs, K., 2009. Applications of acoustic emission for SHM: A review, in: Christian Boller, F.-K.C. and Y.F. (Ed.), *Encyclopedia of Structural Health Monitoring*. John Wiley & Sons, Ltd, pp. 1–13.
- Wright, P.J.F., 1954. Statistical methods in concrete research. *Mag. Concr. Res.* 5, 139–149. doi:10.1680/mac.1954.5.15.139
- Xu, J., He, X., 1990. Size effect on the strength member. *Eng. Fract. Mech.* 35, 687–695.
- Yi, S.T., Yang, E.I., Choi, J.C., 2006. Effect of specimen sizes, specimen shapes, and placement

-
- directions on compressive strength of concrete. *Nucl. Eng. Des.* 236, 115–127. doi:10.1016/j.nucengdes.2005.08.004
- Yin, X.C., Yu, H.Z., Kukshenko, V., Xu, Z.Y., Wu, Z., Li, M., Peng, K., Elizarov, S., Li, Q., 2004. Load-Unload Response Ratio (LURR), Accelerating Moment/Energy Release (AM/ER) and state vector saltation as precursors to failure of rock specimens. *Pure Appl. Geophys.* 161, 2405–2416. doi:10.1007/s00024-004-2572-8
- Yu, Z., Clapp, P.C., 1987. Quantitative analysis of acoustic emission signals. *J. Appl. Phys.* 62, 2212. doi:10.1063/1.339525
- Zapperi, S., 2012. Current challenges for statistical physics in fracture and plasticity. *Eur. Phys. J. B* 85, 329. doi:10.1140/epjb/e2012-30471-9
- Zhou, F.P.P., Lydon, F.D.D., Barr, B.I.G.I.G., College, W., Iyf, C.F., 1995. Effect of coarse aggregate on elastic modulus and compressive strength of high performance concrete. *Cem. Concr. Res.* 25, 177–186. doi:10.1016/0008-8846(94)00125-I